Development of Superconducting Josephson Junction Travelling Wave Parametric Amplifiers

Javier Navarro Montilla

Balliol College

University of Oxford

A thesis submitted for the degree of

Doctor of Philosophy

Michaelmas 2024

"La science est révolutionnaire et contribue à l'affranchissement de l'humanité."

— Georges Politzer
Principes Élémentaires de Philosophie

Abstract

Recent progress in physics has increased the necessity for ultra-low noise amplifiers capable of operating at the quantum limit performance. These amplifiers are essential to enhance astronomical detection, dark-matter search, and qubit readout in quantum computing, among other applications. Superconducting Josephson junction Travelling Wave Parametric Amplifiers (JTWPAs) operated in the microwave range, have demonstrated high gain over several gigahertz (GHz) bandwidth, with quantum-limited noise performance and minimal heat dissipation. These excellent properties make JTWPAs an ideal solution for ultra-low noise amplification. This thesis delves into the design, fabrication and characterisation of JTWPAs operated in the microwave (1-16 GHz) and the W-band (70-115 GHz) regimes.

A generalised coupled-mode equations (CME) framework describing JTWPAs based on Josephson junctions and DC superconducting quantum interference devices (SQUIDs) is introduced. This framework can be combined with electromagnetic (EM) simulation softwares to model the JTWPAs, facilitating their design. It is therefore used to model two microwave JTWPA designs, using parallel plate capacitors (PPCs) and interdigitated capacitors (IDCs). The fabrication and characterisation of both designs are presented, and possible fabrication and design issues are carefully discussed. Despite these issues, we observed broadband gain in the JTWPA with PPCs, achieving $> 20\,\mathrm{dB}$ gain at several frequency points, and a measured $P_{1\mathrm{dB}} = -95.8\,\mathrm{dBm}$ when operated at 17.3 dB.

The RF properties of a 500-junction Josephson array are also presented in this manuscript. The device creates a Fabry-Perot cavity, leading to non-travelling wave parametric effects, such as narrow-band gain. We also observed indications of efficient phase-sensitive amplification. The thesis is concluded with the first — to the best of our knowledge — experimental attempt to extend the operational frequency of a JTWPA to the W-band. The novel design, fabrication techniques and characterisation of the W-band JTWPA are discussed in detail in this manuscript, leading to promising results suggesting that JTWPA could operate at high frequencies.

Statement of Originality

I carried out the work presented in this thesis at the Department of Astrophysics, University of Oxford between October 2020 and October 2024, under the supervision of Dr. Boon Kok Tan. My DPhil was funded by a Science Technology Facilities Council (STFC) Studentship and the Foley-Bejar Scholarship from Balliol College. I hereby declare that no part of this thesis has been submitted in support of another degree, diploma or other qualification at the University of Oxford or other higher learning institute. Except where otherwise stated or where reference is made to the work of others, the work in this thesis is entirely my own. The total length of this thesis does not exceed 250 pages.

All the devices presented in this thesis were fabricated by myself at the fabrication facilities from the Institut de Radioastronomie Millimétrique (IRAM), St. Martin d'Hères (France), under the guidance and supervision of Dr. Eduard F.C. Driessen and Arnaud Barbier. Part of the work presented in Chapter. 5, was published in the Proceedings of the International Symposium of Space Terahertz Technologies 2022 [1]. The works presented in Sec. 5.4 and Sec. 9.2, were published in the Proceedings of the International Symposium of Space Terahertz Technologies 2024 [2, 3].

Javier Navarro Montilla
(*October 2024*)

COVID-19 Disclaimer

A significant portion of the work presented in this thesis was carried out during the global COVID-19 pandemic or delayed due to its impact. As a consequence, all the measurements and experimental works discussed in this thesis were conducted after July 2022.

Since I started my DPhil in October 2020, England went though different phases of total and partial lockdown until June 2021. During this period, access to the laboratory was limited, resulting in delays in the experimental aspects of my project. International travel was also limited, preventing me from travelling to IRAM to fabricate the devices I had designed. My first visit did not take place until June 2022. Similarly, these travel restrictions delayed the visit of an engineer who was supposed to install one of the main cryogenic systems used to characterise the devices in this thesis. The system sat in its crate for over a year, before finally being commissioned at the end of 2021.

Additionally, this project is our research group's first attempt at fabricating and testing JTWPAs, which required the acquisition of numerous new components for the experimental setups. However, global supply chain disruptions caused significant delays in the delivery of these components — some taking more than six months to arrive. As a result, it was not until the Summer of 2022 that we had enough equipment to begin implementing the initial experimental setups.

List of Publications

Javier M. Navarro, and Boon-Kok Tan. "Optimising the design of a broadband Josephson junction TWPA for axion dark matter search experiments." *Proc. SPIE 11881, Quantum Technology: Driving Commercialisation of an Enabling Science II*, 1188115, 2021.

Boon-Kok Tan, Faouzi M. Boussaha, Christine Chaumont, Joseph C. Longden, and **Javier Navarro Montilla**. "Engineering the thin film characteristics for optimal performance of superconducting kinetic inductance amplifiers using a rigorous modelling technique." *Open Research Europe*, 2:88, 2022.

Javier Navarro Montilla, Eduard F.C. Driessen, Arnaud Barbier, Faouzi M. Boussaha, Christine Chaumont, and Boon-Kok Tan. "Exploring the limits of the tunnel junction fabrication technique for Josephson junctions TWPA and the preliminary characterisation results." *Proceedings of the 32nd International Symposium on Space Terahertz Technology*, 2022.

Javier Navarro Montilla, and Boon-Kok Tan. "Design of high compression point Josephson junction travelling wave parametric amplifiers for readout of millimetre and sub-millimetre astronomical receivers." *Proc. SPIE 12190, Millimeter, Submillimeter, and Far-Infrared Detectors and Instrumentation for Astronomy XI*, 1219030 2022.

Javier Navarro Montilla, Nikita Klimovich, Arnaud Barbier, Eduard F.C. Driessen, and Boon-Kok Tan. "Investigating Pin-Holes Issues in Josephson Junction Travelling Wave Parametric Amplifiers Requiring Large Area of Dielectric Layer." *Proceedings of the 33rd International Symposium on Space Terahertz Technology*, 2024.

Javier Navarro Montilla, Arnaud Barbier, Eduard F.C. Driessen, and Boon-Kok Tan. "Design considerations for a W-band Josephson junction travelling wave parametric amplifier." *Proceedings of the 33rd International Symposium on Space Terahertz Technology*, 2024.

Joseph C. Longden, **Javier Navarro Montilla** and Boon-Kok Tan. "Balanced travelling-wave parametric amplifiers for practical applications" *Phys. Scr.* 99 065046.

2024.

Javier Navarro Montilla, and Boon-Kok Tan. "Generalising the Coupled-Mode Framework for Symmetric Travelling Wave Parametric Amplifiers with $\chi^{(3)}$ nonlinearity." In Preparation, 2024.

Javier Navarro Montilla, Arnaud Barbier, Nikita Klimovich, Eduard F.C. Driessen, and Boon-Kok Tan. "Preliminary Characterisation of Microwave Travelling Wave Parametric Amplifiers Comprising Josephson Junction Meta-material Line." In preparation, 2024.

Javier Navarro Montilla, Ryan C. Stephenson, Arnaud Barbier, Nikita Klimovich, Eduard F.C. Driessen, Peter K. Day, and Boon-Kok Tan. "Investigating the Nonlinearity of Josephson Arrays for Travelling-Wave Parametric Amplification in the W-band." In preparation, 2024.

Acknowledgements

The past four years have been an incredible intellectual journey. When I started my DPhil, very little literature existed on JTWPAs, but as my DPhil progressed, I had the privilege of witnessing a remarkable growth in global interest in the field. I feel immensely fortunate to have been part of this exciting period, which has not only brought me joy but also fuelled my curiosity to unprecedented levels.

All of this would not have been possible without the support and guidance from my supervisor Dr. Boon-Kok Tan. Since I met him in 2019, Boon has been a fantastic mentor, motivating me to enhance my scientific skills every day and become an independent researcher. I will always be grateful for his tireless willingness to help, inside and outside the workspace, and his ability to motivate his students to pursue their ideas and projects. Over my DPhil, there has not been a single time when Boon was not available for a chat when I was stuck on my project. He has always made me feel better through our discussions and his priceless advice.

I would also like to extend my deepest gratitude to Dr. Eduard F.C Driessen from IRAM. Since my master's thesis in Grenoble, Eduard has also been a fantastic mentor, shaping me into an independent researcher. I am very glad we got to collaborate during my DPhil project, for which he has given extremely valuable advice and guidance at many stages. Thank you for being so friendly and making my visits to Grenoble such nice experiences. Although, you still owe me a visit to the Plateau de Bure!

I would like to thank Prof. Ghassan Yassin for the interesting discussions and valuable lessons from his long experience in academia. I would also like to thank our lab technician, Rik Elliot, the magician who makes everything work in the lab. Sorry for ever changing my mind about the wiring that I needed for my experiments over the past years. I owe you a lot! I would also like to extend my gratitude to our group's postdoc, Dr. Nikita Klimovich. Since he joined the group, Nikita has been a fantastic colleague and friend. He has helped me through the most stressful period of my DPhil, advising me on my experiments and helping me to develop a better theoretical understanding through many hours of discussions in the lab. He is a brilliant and inspiring scientist, with whom I am very glad to have crossed paths. I wish you all the best in the future! I would also like to thank my ex fellow DPhil students, now Dr. Joseph Longden and Dr. Jakob Wenninger. Thank you very much for paving the way for me in the lab, and for being so supportive, fun, and helpful.

I will always cherish the camaraderie in the lab — often with Jakob's questionable music taste playing in the background — and our lunch breaks at Balliol College. The pork ribs did not taste the same in my last year without you! Thanks also to Arnaud Barbier and Dominique Billon-Pierron from IRAM for their support during the fabrication of the devices. I would not have been able to fabricate a single device without their help. I would also like to thank the new DPhil student in the group Jee-Ho Kim, and the master's student Samuel Wood, for contributing to the great lab atmosphere in the past year. I wish you the best in your projects!

I am also very grateful to the fantastic friends I have made over the past four years in Oxford, including those from Balliol College (Hrushi, Aston, Robbie, Kristine, Jiarui, Andres, etc.), who made the start of my DPhil experience as fun as lockdown allowed, and those from outside university (Silvia, Alexis, Alex, Ken, etc.) who made my stressful days so much easier to deal with. I would also like to thank all my friends from Seville. Despite having left the city nine years ago to pursue my professional projects, they always make me feel at home when I come back.

Most importantly, I would like to extend my deepest gratitude to my parents, José and Mila, who have always supported my dreams and projects. They have taught me the value of effort and passion, and none of my life achievements would have been possible without them. Additionally, I am extremely grateful to my sister Marina who has always been a reference of excellence to me, demonstrating that everything is possible with hard work. She is also the kindest and most supportive sister anyone could ask for. Last, but by no means least, I would like to thank my wonderful partner Caroline for enlightening me with her love and kindness. The world is brighter with you, and I cannot wait to walk by your side and hold your hand along the whole path. I love you.

Contents

List of Figures

List of Tables

Chapter 1

Introduction

The extreme physical conditions in black holes have made them the subject of fascination for both physicist and the general public. The modern concept of black holes, based on Einstein's theory of general relativity, emerged in the early 20$^{\text{th}}$ century. However, it was not until 2019 that the first black hole — located at the center of the M87 galaxy — image was published [4]. This unprecedented achievement was made possible only by a global network of interconnected millimetre-wave telescopes, using a technique called aperture synthesis interferometry to achieve high angular resolution images [5].

That same year, Google® made headlines in the scientific field of quantum computing by claiming 'quantum supremacy' [6]. Their Sycamore quantum processor completed a task in 200 second that would have taken classical supercomputers 10,000 years to complete[1]. Quantum processors like Sycamore, based on superconducting materials, exploit the unique properties of quantum mechanics to tackle complex computational problems. This milestone was the result of decades of progress in cryogenics, microwave engineering, and related fields.

Although these two breakthroughs may seem unrelated, they share a common technical requirement: the high-sensitivity measurement of extremely faint signals. Whether measuring the down-converted signal from the event horizon of a black hole 55 million light-years away, or the ultra-feeble signal encoding the state of a quantum bit (qubit), both require amplification to be observed. Consequently, these two achievements were made possible, in part, by the advancements in cryogenic low-noise amplifiers (LNAs) developed over recent decades.

This thesis delves into the development of superconducting Josephson Travelling Wave Parametric Amplifiers (JTWPAs), a novel cryogenic broadband amplifier tech-

[1]This claim was contested by IBM® arguing that using optimised algorithms a classical supercomputer could perform the same task in about 2.5 days. [7]

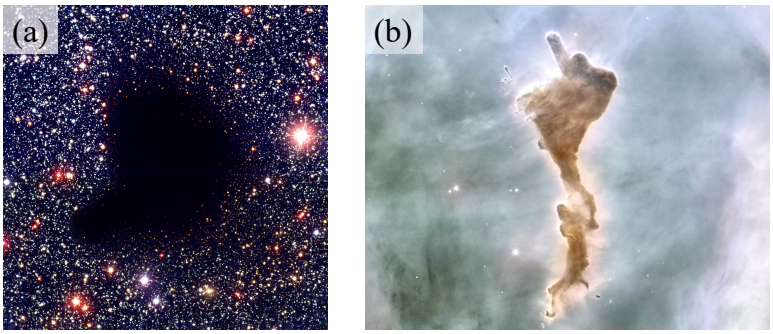

Figure 1.1: Giant Molecular Clouds (GMCs) images. (a) Colour composite of visible and near-infrared images of the dark cloud Barnard 68. The picture was obtained with the 8.2-m VLT ANTU telescope. No visible or near-infrared light is emitted by the cloud.[2](b) Image of a molecular cloud at Carina nebula taken with the Hubble Space Telescope in 1999. The bright spots are stellar formation regions. The radiation generated by these new stars is destroying the molecular cloud.[3]

nology with quantum-limited noise performance. In this chapter, I will discuss the scientific motivation for the quantum-limited amplification, as well as the their fundamental properties and a non-exhaustive survey of the existing technologies.

1.1 Scientific motivation

Millimetre (mm) and sub-millimetre (sub-mm) wavelengths ($\sim 30\,\mathrm{GHz}$ to $\sim 3\,\mathrm{THz}$) is a window with rich information for astronomical observation. One of the most explored fields in mm/sub-mm wave astronomy is the star formation process in galaxies and the interstellar medium (ISM). In the coldest regions inside the galaxies, clouds of molecular gas are formed. These clouds are essentially composed of hydrogen molecules (H_2) and the biggest of them are called Giant Molecular Clouds (GMCs). The GMCs diameter can reach ~ 300 light years and their mass can be larger than 10^6 times the mass of our sun. The temperature of these molecular clouds is around $T \sim 10$ K; as a consequence, they barely emit in the visible light spectrum. As shown in Fig. 1.1(a), the GMC appears as a black spot at visible and near-infrared light. GMCs can however be observed at mm-wavelengths and emission lines of chemical compounds like carbon monoxyde (CO) can be tracked. The molecular gas within the GMCs collapses due to its own gravity and forms stars. The radiation generated by these stars breaks down the molecular cloud, a process currently occurring

[2]Credit: ESO.
[3]Credit: N. Smith (University of California, Berkeley) and NOAO/AURA/NSF.

at the Carina nebula as shown in Fig. 1.1(b) — which can be observed in the visible spectrum. Studying the chemical properties of GMCs is crucial to understand stellar formation [8] and galaxy evolution [9].

Other scientific applications in the mm-wave range include studying the Cosmic Microwave Background (CMB). The CMB is the first light emitted by the universe, 379,000 years after the big Bang, and it has a peak emission at 160.2 GHz. The analysis of the CMB radiation has been fundamental to establishing the standard cosmological model [10]. Millimetre and sub-mm telescopes have also been used to study protoplanetary disks [11], the chemical composition of Venus atmosphere[4] [13], the dust in interestellar medium [14], the kinematics of galactic nuclei [15], testing the strong-field general relativity theory [16], and many other astronomical topics.

Numerous mm and sub-mm wave telescopes employ heterodyne detection techniques to measure the astronomical signals. In heterodyne detection, the high-frequency astronomical signal (f_{RF}) is mixed with a local oscillator frequency (f_{LO}) to generate an intermediate frequency (f_{IF}) at a lower frequency that can be easily analysed using existing room-temperature electronics, retaining the information of the astronomical signal. This detection technique can achieve extremely high spectral resolving powers[5], on the order of $R \sim 10^3 - 10^8$. Furthermore, the signal from different telescopes can be combined — since the heterodyne detection technique preserves both the amplitude and phase information of the incoming signal — using aperture synthesis interferometry to increase the angular resolution of the observations. Some examples of observatories implementing this technique include the Atacama Large Millimeter/Submillimeter Array (ALMA) in Chile, and the Northern Extended Millimeter Array (NOEMA) in France.

The standard receiver system for a heterodyne detection scheme is shown in Fig. 1.2(a). Each component in the receiver chain contributes to the total noise of the system. Assuming a chain of N cascaded components, each one with a noise temperature T_{i} and gain G_{i}, where $i = \{1, 2, 3, ..., N\}$, the total noise temperature of the system is given by the Friis equation [17]:

$$T_{\mathrm{sys}} = T_1 + \frac{T_2}{G_1} + \frac{T_3}{G_1 G_2} + ... + \frac{T_{\mathrm{N}}}{G_1 G_2 ... G_{\mathrm{N}-1}}. \tag{1.1}$$

[4]In 2020, researchers claimed the detection of phosphine (PH_3) in the atmosphere of Venus, a gas associated with life on Earth. Although further analysis of the data highlighted issues with the telescope's calibration process, which after correction weakened the PH_3 signal [12], it shows the multidisciplinary applications of mm-waves telescopes.

[5]The spectral resolving power is defined as $R = \nu/\Delta\nu$, where ν is the centre frequency and $\Delta\nu$ is the frequency resolution.

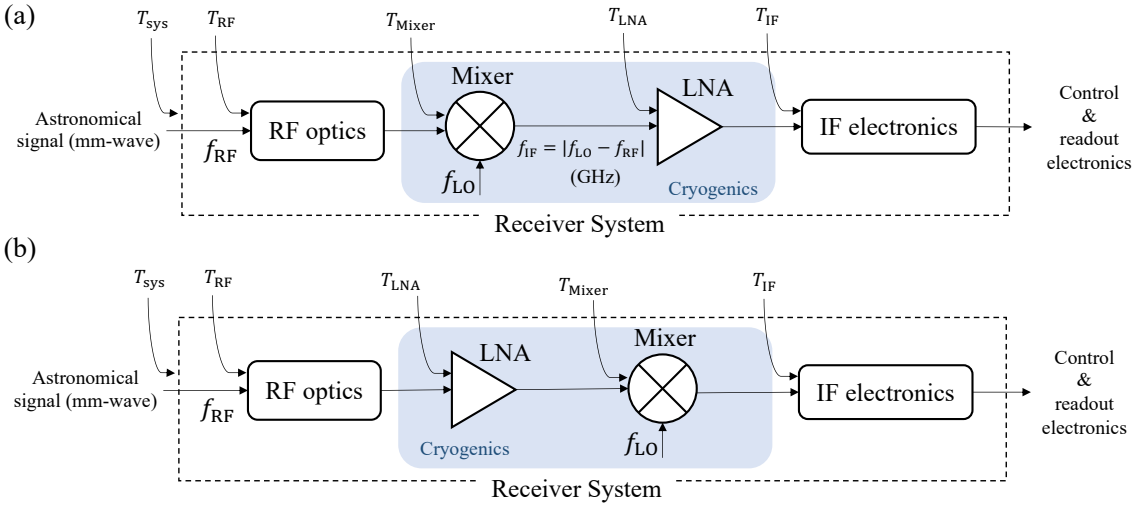

Figure 1.2: Schematics of a conventional astronomical mm/sub-mm wave heterodyne receiver system. (a) The LNA is placed after the mixer for the readout of the down-converted IF signal. The LNA operates in the microwave frequency range. (b) The LNA is placed before the mixer, as a first-stage pre-amplifier, substantially reducing the noise of the system. The LNA operates in the mm/sub-mm wave frequency range.

Note that a lossy component ($G_{\rm i} < 1$) amplifies the noise contribution from all the subsequent components in the chain ($T_{\rm i+1}$, $T_{\rm i+2}$, etc.). Conversely, a component with high gain ($G_{\rm i} \gg 1$) can mask the noise contribution from components further down the chain. For this reason, any receiver chain should ideally start with an LNA, as illustrated in Fig. 1.2(b). However, the performance of current LNA technologies quickly deteriorates above 120 GHz. Therefore, at mm and sub-mm waves, the heterodyne mixer often comes first in the receiver chain.

Current cryogenic LNAs used in astronomical applications are based on high electron mobility transistors (HEMTs). Despite achieving high gains over a broad range of frequencies, the added noise of even the state-of-the-art HEMT amplifiers is 5-10 times larger than the minimum added noise allowed by quantum mechanics, known as the quantum limit [18]. Since HEMT LNAs are implemented using semiconductor materials, they unavoidably have large heat dissipation in the order of milliwatts [19].

The observation efficiency/speed of a mm/sub-mm wave telescope is proportional to the number of pixels in the receiver, therefore, large pixel arrays offer significant advantages. Nevertheless, using superconductor-insulator-superconductor (SIS) mixers as an example, a sideband-separated, dual-polarisation SIS mixer requires 4 LNAs per pixel. Therefore, a $\sim$1,000 pixel array, as the one targeted by the Atacama Large Aperture Submillimeter Telescope (AtLAST) [20], would require 4,000

LNAs. Assuming a typical power consumption of $\sim 2-30\,\mathrm{mW}$ for HEMT amplifiers operated at the optimal cryogenic noise performance [18], this would mean a total power consumption of $8-120\,\mathrm{W}$. Standard cryocolers operated at $4\,\mathrm{K}$, such as the Gifford-McMahon (GM) coolers (see Sec. 4.8), generate $1-2\,\mathrm{W}$ of cooling power. Therefore, the heat dissipation of HEMT amplifiers creates a bottleneck with current cryogenic technologies. This challenge extends to other technologies, such as hot-electron bolometers (HEB) mixers, and direct detector arrays such as microwave kinetic inductance detectors (MKIDs); all of which need a readout LNA.

Despite the obvious advantages of replacing the readout HEMT amplifiers with a quantum-limited noise and low-heat dissipation alternative, an even more advantageous detection scheme is illustrated in Fig. 1.2(b). Using the LNA as a pre-amplifier before the astronomical receiver can further reduce the noise of the system, relaxing the requirement for high-sensitivity mixers. This detection scheme has been the preferred choice for the upgrade of ALMA Band 2 & 3 (67-116 GHz), currently under development [21]. Although this upgrade will use HEMT LNAs, as demonstrated in the '*Cycle 5 NRAO ALMA Development Study Report*' by O. Noroozian [22] using a quantum-limited amplifiers for Band 3 (84-116 GHz) could lead to a factor of ~ 5 improvement in the receiver noise temperature. This would double the system sensitivity and increase the observation efficiency/speed of the telescope by a factor of four.

Beyond astronomy, cryogenic LNAs are essential components for emerging fields such as Quantum Computing (QC). Unlike classical computers based on binary bits, quantum computers use qubits, which can exist in a superposition of states simultaneously. Leveraging the properties of qubits, calculations for certain tasks can be performed with an immense computation advantage compared with classical computers. Quantum computers can be used for cryptography [23], drug discovery [24], to simulate molecular structures and chemical reactions for material science [25], and to enhance artificial intelligence capabilities [26], among other applications. The strategic, economic and national security implications of QC have been recognised by numerous governments, with extensive plans to develop the field in the upcoming years [27, 28, 29].

One of the most mature QC technologies is based on superconducting qubits. These qubits use the properties of Josephson junctions to create a well isolated two-level system. Arguably, the dispersive readout [30] is the most popular technique to measure the state of a superconducting qubit. In this technique, the qubit is coupled to a microwave resonator, whose resonant-frequency phase shift indicates

the quantum state of the qubit. The power of the readout signal needs to be kept extremely weak, otherwise disturbing the qubit quantum state. Therefore, cryogenic LNAs are essential for the accurate qubit readout. For instance, the use of quantum-limited amplifiers, such as Josephson Parametric Amplifiers (JPAs), has demonstrated to improve the qubit readout signal signal-to-noise ratio (SNR) by a factor of 1,000 compared to the HEMT LNAs [31].

Despite focusing on astrophysics and QC, LNAs are indispensable in a wide range of technologies and experiments such as nano-electromechanical systems (NEMS) [32], electron spin resonance detection [33], the detection of spontaneous photon decay in Josephson junctions [34], and the search for dark-matter candidates [35].

1.2 Amplifiers and quantum limit of noise

Fundamentally, an amplifier takes an input signal and generates a correlated enlarged output signal. Numerous properties, or figures of merit, can be used to quantify the performance of an amplifier. In this section, I shall define the main amplifier figures of merit relevant to this thesis, introduce the different types of amplifiers, and discuss the origins of the quantum limit for added noise.

1.2.1 Amplifiers figures of merit

A non-exhaustive list of the amplifiers' figures of merit include:

Gain — Considering an input signal with amplitude A_{in} that goes through an amplifier generating an output signal with larger amplitude A_{out}. The power gain G is defined as $G = (A_{\text{in}}/A_{\text{out}})^2 \Leftrightarrow \sqrt{G} = A_{\text{in}}/A_{\text{out}}$. This coefficient quantises the growth that the input signal amplitude/power experiences going through the amplifier, as illustrated in Fig. 1.3(a). Hereafter, the term gain will be used to refer to the power gain and will be expressed in decibels (dB). Therefore, $G = 20\,\text{dB}$ corresponds to a linear gain of $G = 100$.

Bandwidth — The gain value in an amplifier depends on the frequency of the input signal f_{s}. The bandwidth (B) is defined as the frequency range where $G(f_{\text{s}}) > G_{\text{max}}/2$, where G_{max} is the maximum gain of the amplifier in linear units ($G(f_{\text{s}}) > G_{\text{max}} - 3$, when G_{max} in dB). A representation of the bandwidth is given in Fig. 1.3(b).

Dynamic Range — The gain also depends on the power of the input signal, denoted P_{s}. The dynamic range is the difference between the smallest ($P_{\mathrm{s}}^{\mathrm{min}}$) and the largest ($P_{\mathrm{s}}^{\mathrm{max}}$) input signal power that the amplifier can amplify linearly without resulting in gain compression and signal distortion. The amplifier is linear, i.e., independent of the input power, when $P_{\mathrm{s}}^{\mathrm{min}} < P_{\mathrm{s}} < P_{\mathrm{s}}^{\mathrm{max}}$. In this thesis, the upper limit of the dynamic range is given by the compression point P_{1dB}, defined as the P_{s} value resulting in a 1 dB compression of the gain, i.e., $G = G_{\mathrm{max}} - 1$ in dB or $G = 0.8G_{\mathrm{max}}$ in linear units. The compression point is illustrated in Fig. 1.3(c).

Noise — Undesired random disturbance added to the amplified signal in the amplification process. Noise is often measured in power units (P_{n}) over a certain bandwidth B (usually 1 Hz for convenience). However, a more intuitive approach consist of referring the noise as a noise temperature $T_{\mathrm{n}} = P_{\mathrm{n}}/(Bk_{\mathrm{B}})$, where k_{B} is the Boltzmann constant, at the input of the device. Therefore, T_{n} corresponds to the physical temperature of a 'fictive' black-body source that would generate the same amount of noise power as the amplifier, referred to its input. Apart from the noise generated by the amplifier, other sources of noise will add to the input signal getting amplified by the amplifier along the signal. The different noise contributions in the amplification process are shown in Fig. 1.3(a). The signal-to-noise ratio (SNR) is the ratio between the signal amplitude and noise amplitude, expressed in dB. When the SNR < 0 dB, the signal is masked by the noise and requires long integration times[6] to be measured. Designing measurement setups that maximise the SNR is essential for the measurement of any signal.

From these definitions, an ideal amplifier would produce gain as high as possible, over a bandwidth as large as possible, with a dynamic range as high as possible and the lowest possible added noise.

1.2.2 Quantum limits of noise

In quantum mechanics, measurable physical quantities (observables) — such as momentum, energy, or position — are represented using operators. Considering the position $\hat{x}$ and momentum $\hat{p}$ operators, two operators are non-commuting if:

$$[\hat{x}, \hat{p}] = \hat{x}\hat{p} - \hat{p}\hat{x} \neq 0 \tag{1.2}$$

[6] Assuming that the noise is purely stochastic.

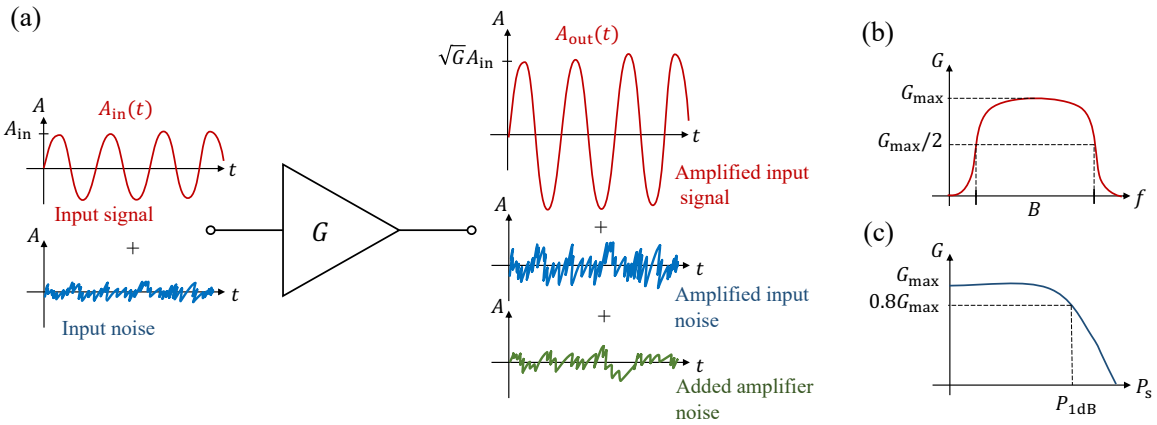

Figure 1.3: (a) Amplification process in a linear amplifier. The input noise (blue) gets amplified along with the signal (red), and some extra noise is added by the amplifier (green). (b) Representation of the bandwidth B of an amplifier. (c) Representation of the $P_{1\mathrm{dB}}$ determining the dynamic range of an amplifier.

which is the case for $\hat{x}$ and $\hat{p}$, and as a consequence, the Heisemberg uncertainty principle imposes the following relationship between the position and momentum uncertainties ($\Delta\hat{x}$ and $\Delta\hat{p}$ respectively):

$$\Delta\hat{x}\Delta\hat{p} \geq \hbar/2 \tag{1.3}$$

implying that position and momentum cannot be measured simultaneously with arbitrary precision, where the precision limit is set by Eq. 1.3.

A classical electromagnetic signal $V(t)$ at an angular frequency of ω can be written as a function of the quadratures I and Q,

$$V(t) = I\cos(\omega t) + Q\sin(\omega t), \tag{1.4}$$

where I is the in-phase component, and Q is the quadrature-phase component. In quantum mechanics, the quadratures of an electromagnetic signal can be expressed as a function of the ladder operators $\hat{a}$ and $\hat{a}^\dagger$ of the electromagnetic field as,

$$\hat{I} = \frac{1}{\sqrt{2}}(\hat{a}^\dagger + \hat{a}), \quad \hat{Q} = \frac{i}{\sqrt{2}}(\hat{a}^\dagger - \hat{a}), \tag{1.5}$$

where $\left[\hat{a}, \hat{a}^\dagger\right] = 1$, and therefore $\left[\hat{I}, \hat{Q}\right] = i$. This implies that the quadratures must also obey the Heisenberg uncertainty principle, and they cannot be known simultaneously with arbitrary precision.

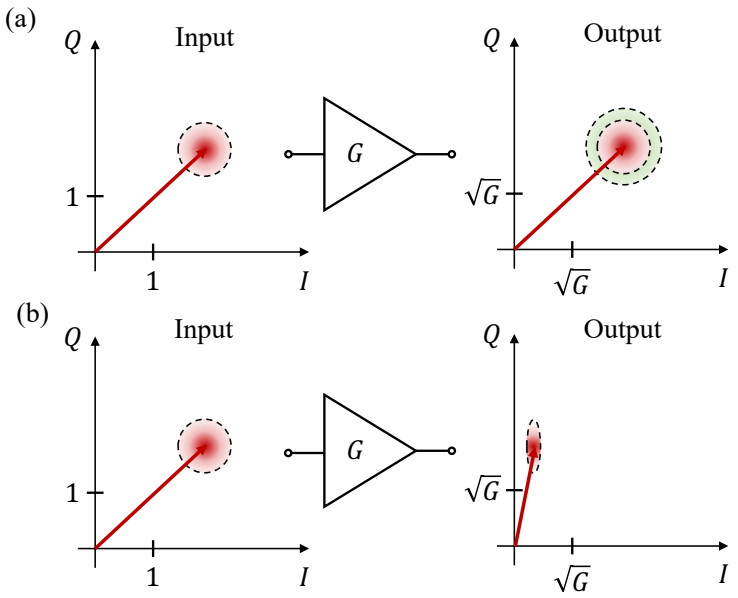

Figure 1.4: IQ plane representation of a coherent state vector, where the circle at the end of the vector represents the uncertainty (noise) associated with vacuum fluctuations. (a) Phase-preserving amplification process. The vector is enlarged and the phase is preserved while the uncertainty is further increased at the output by the addition of at least half a photon of noise (green circle). (b) Phase-sensitive amplification process. The input vector is amplified by $\sqrt{G}$ along the Q quadrature, while deamplified (or squeezed) by $1/\sqrt{G}$ along the I quadrature.

1.2.2.1 Phase-preserving amplification

The amplification process takes an input signal and creates a correlated output signal with a higher amplitude. In a phase-preserving linear amplifier, both quadratures are equally amplified to preserve the phase information of the signal, as illustrated in Fig. 1.4(a). Since the input signal $\hat{I}$ and $\hat{Q}$ cannot be known with arbitrary precision, this translates to some minimum added noise in the amplification process. This minimum noise value is referred to as the quantum limit of noise.

The initial theoretical investigations of the nature of the quantum limit of noise in amplifiers date from the early 60's [36, 37]. Later, in 1982, Carlton M. Caves reviewed these theoretical concepts resulting in a more comprehensive and extended analysis [38]. In short, from these theoretical studies, the number of added noise photons N_{n} created during the linear amplification process is given by,

$$N_{\mathrm{n}} \geqslant \frac{|1 - 1/G|}{2}. \tag{1.6}$$

Therefore, in the unity-gain case ($G = 1$), the number of added noise photons can be zero, i.e., transmission can occur without the addition of extra noise. In the case of high gain, i.e., $G \gg 1$, the right-hand side of Eq. 1.6 becomes 1/2. Therefore, the minimum added noise for a linear phase-preserving amplifier is half a photon. This limit is known as the quantum limit of added noise, and amplifiers approaching this lowest bound of added noise are generally termed as quantum-limited amplifiers.

1.2.2.2 Phase-sensitive amplification

When only a single quadrature component of the signal, e.g., $\hat{Q}$, is of interest, the measurement (amplification) can be performed with arbitrary precision, at the expense of increasing the uncertainty in the opposite quadrature, e.g., $\hat{I}$. In this context, the amplification process yields:

$$\hat{Q}_{\mathrm{out}} = \sqrt{G}\hat{Q}_{\mathrm{in}} \quad \hat{I}_{\mathrm{out}} = \hat{I}_{\mathrm{in}}/\sqrt{G}. \tag{1.7}$$

An amplifier that performs this process is known as a phase-sensitive amplifier, since the amplification process is different depending on the phase of the input signal, i.e., the amplification process does not preserve the phase information of the signal. In this example, $\hat{Q}$ is the amplified quadrature and $\hat{I}$ is the de-amplified (or squeezed) quadratrue. The phase-sensitive amplification process is illustrated in Fig. 1.4(b).

When the input signal is the vacuum noise fluctuations[7], the fluctuations will get amplified in one quadrature and de-amplified in the opposite one, hence achieving noise levels below the vacuum noise. This extraordinary property can be used to enhance the sensitivity of detection schemes for extremely weak signals. Following the example given by D.F Wals in [39], a bar detector used in gravitational waves detection can be treated as a harmonic oscillator. The displacement of the bar associated with a gravitational wave is in the order of 10^{-19} cm, the same order of magnitude that the quantum mechanical uncertainty of the bar position. By squeezing the state of the oscillator and measuring the displacement on the squeezed quadrature, one can increase the sensitivity of the detection. Since 1985, squeezed states of light have been widely demonstrated and used in quantum optics experiments [40], and from 2019 it is used by the Laser Interferometer Gravitational-Wave Observatory (LIGO) to enhance the detection sensitivity of gravitational waves [41].

1.3 Parametric amplification

Amplifiers generating gain through the periodic modulation of one of their system's parameters are know as parametric amplifiers. A useful analogy to understand the amplification mechanism in a parametric amplifier is the movement of a skater in a half-pipe, as introduced by J. Aumentado in his review article [42]. As shown in Fig. 1.5, the oscillation of the skater can be described with the angle parameter θ, which oscillate at an angular frequency ω_s. Periodically changing the center of gravity g (internal system parameter) at a frequency $2\omega_s$, by bending or extending the skater's knees, the amplitude of the oscillation θ increases. This analogy highlights two important effects in parametric amplification: first, the skater needs to bend and extend their knees synchronised with the oscillations to maximise the energy exchange. This is an intuitive representation of the phase-matching condition that will be introduced in Chapter 2. Secondly, for the amplification process to occur, the skater needs to start with at least a small oscillation θ, and the longer the skater modulates their center of gravity, the largest the resulting θ. This intuitively showcases the importance of the interaction time to increase the gain in a parametric amplifier.

This concept can be implemented in electrical circuits, achieving amplification though the periodic modulation of the reactive properties of the circuit. The first

[7]Inherent quantum fluctuations present in the electromagnetic field even in the absence of photons.

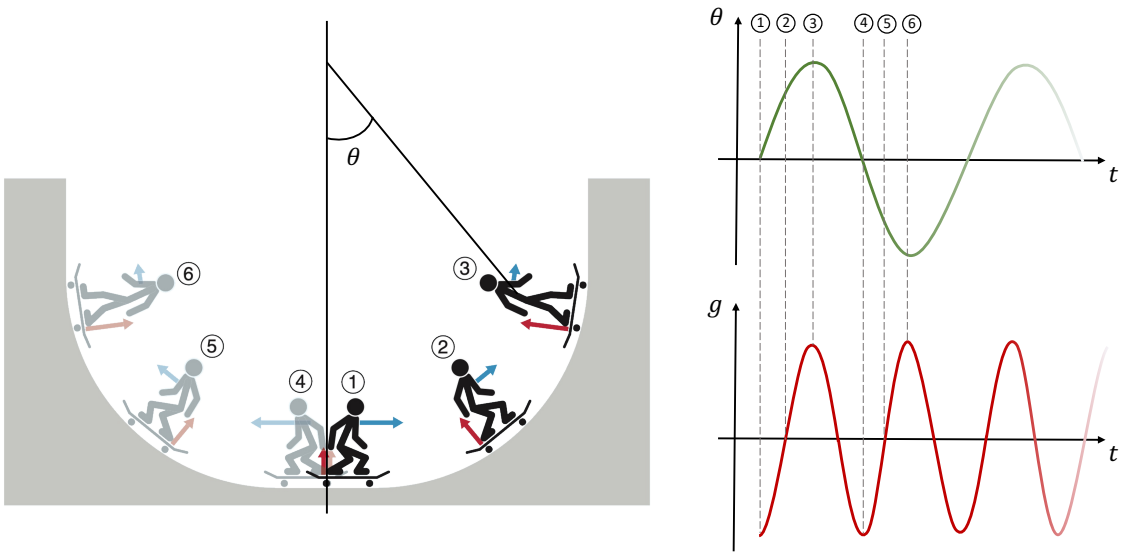

Figure 1.5: The oscillation θ and velocity (blue arrow) of a skater in a half-pipe experiences parametric amplification through the periodic modulation of the skater's centre of gravity g (red arrow). For optimal amplification, g needs to oscillate at twice the frequency of θ, and the phase needs to be synchonised as illustrated in the plots[8].

implementation dated back to 1916 [43], and the development of semiconductor components in the late 1950s promoted the use of diode varactors as the reactive components in a resonant circuit for parametric amplification purposes [44, 45]. However, due to their fairly limited bandwidth and noise performance compared with other semiconductor-based amplifiers [46], particularly HEMT amplifiers, the technology did not gain further traction.

1.3.1 Josephson Parametric Amplifiers (JPAs)

Two superconductors separated by a thin dielectric layer form a Josephson junction. The intrinsic inductance of a Josephson junction is current-dependent (as derived in Sec. 2.1.2), hence it can be modulated to generate parametric amplification in devices known as Josephson Parametric Amplifiers (JPAs). The development of Josephson junction's fabrication techniques in the 1960s fostered the first studies on their applications for parametric amplification [47, 48, 49]. However, the limited performance from the first JPA implementations resulted in decline on the interest for this technology. Later, in the 1980s, a renewed interest for quantum-limited amplifiers, owing to their potential applications in gravitational waves detection, resulted in the

[8]Credits of the half-pipe figure: J. Aumentado [42]

first demonstration of a near quantum-limited JPA [50], squeezing thermal [51] and vacuum noise [52]. Recently, the development of circuit quantum electrodynamics (cQED) in the past decades has seen a resurged interest on JPAs, with the fundamental work of Manuel A. Castellanos-Beltran et al. establishing the contemporary resonant design of JPAs [53], and achieving noise levels below the standard quantum limit via squeezing [54].

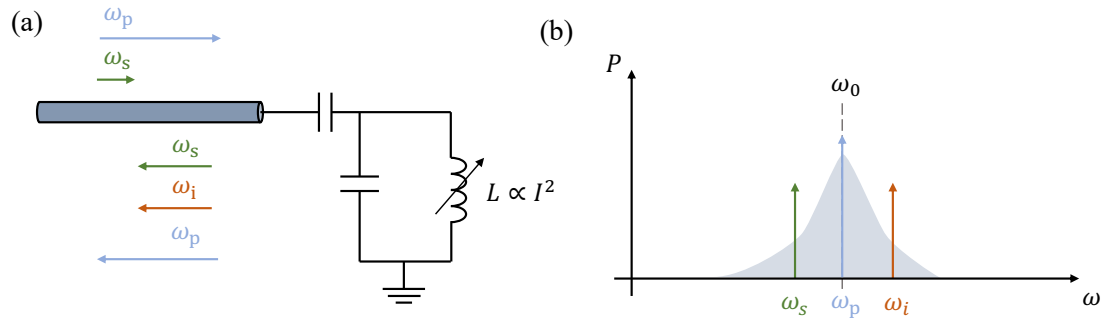

Figure 1.6: (a) Circuit diagram of a single-port JPA. The nonlinear inductance originates from a Josephson junction. (b) Power spectrum of the four-wave mixing gain process in a JPA. The grey area indicates the narrow-band region of gain around the resonance frequency of the device. When a signal frequency within that region is injected to the JPA, it gets amplified and generates an idler tone to conserve energy and momentum.

Although different designs exist, current JPAs often consist of single-port devices comprising an LC resonator, where the inductance is replaced by a Josephson junction, as illustrated in Fig. 1.6(a). Since the nonlinear inductance of the junction $L_\mathrm{j} \propto I(t)^2$, when a pump tone at frequency ω_p is applied, this modulates the inductance at $2\omega_\mathrm{p}$. By pumping at $\omega_\mathrm{p} \sim \omega_0$, where ω_0 is the resonance frequency of the LC resonator, this results in a narrow-band gain generated around ω_0. Therefore, if a signal at a frequency ω_s in the amplification band is injected into the JPA, it gets reflected out with an enhanced amplitude, and an idler frequency at $\omega_\mathrm{i} = 2\omega_\mathrm{p} - \omega_\mathrm{s}$ is generated for energy and momentum conservation, as illustrated in Fig. 1.6(b). This process is known as four-wave mixing (see Sec. 2.2.1). Often JPAs are implemented using superconducting quantum interference devices (SQUIDs) — more details in Sec. 2.1.2 — which allow tuning ω_0 with an applied external magnetic field ϕ_ext. Furthermore, since the SQUID inductance $L_\mathrm{SQUID} \propto \phi_\mathrm{ext}(t)$, a time-dependent sinusoidal modulation of ϕ_ext results in a three-wave mixing scheme (see Sec. 2.2.1), permitting the operation of the JPA in the degenerated parametric amplification regime ($\omega_\mathrm{s} = \omega_\mathrm{i}$), which yields phase-sensitive gain [55].

The precise physics behind the JPAs operation are beyond the scope of this thesis; more information on the JPA classical formalism can be found in [56], and a quantum approach in [57]. In order to reach high gain values in a JPA, the quality factor of the resonance Q needs to be increased to enhance the interaction time of the different frequency tones in the resonator. However, a high Q comes at the price of reducing the bandwidth; this trade-off is known as the gain-bandwidth product, and can be expressed as,

$$B\sqrt{G} \propto \frac{1}{Q}, \tag{1.8}$$

where B is the bandwidth and the gain G is given in linear terms. Standard gain-bandwidth products of JPAs are in the order of 100 MHz, implying $B = 10\,\text{MHz}$ with 20 dB gain [58, 59]. Recent efforts have focused on extending the bandwidth through impedance matching techniques, reaching values as high as $\sim 700\,\text{MHz}$ [60, 61, 62]. Another active field of research focuses on increasing the compression point of JPAs, often limited to values around $-130\,\text{dBm}$ [63, 64]. Despite these limitations, JPAs have been widely used for the measurement of qubits [65], nano-mechanical resonators [32], and dark-matter search [66], among many other applications.

1.3.2 Travelling Wave Parametric Amplifiers (TWPAs)

In order to lift the gain-bandwidth limitation of early varactor-diode parametric amplifiers, in the late 1950s travelling-wave circuits with similar nonlinear reactive elements were extensively explored [67, 68]. However, the physical implementations yielded limited gain and poor noise performance. On the other side of the electromagnetic spectrum, the invention of laser in 1960 [69], motivated the rapid development of Optical Parametric Amplifiers (OPAs) [70], followed by the development of optical fibers, which permitted the efficient confinement and manipulation of light signals. The low loss and inherent Kerr nonlinearity of certain fibers quickly positioned them as an ideal medium for implementing optical traveling wave parametric amplifiers. In 2001, the significance of phase-matching in optimising the performance of these devices was demonstrated for the first time [71], leading to the introduction of several phase-matching techniques in subsequent years [72].

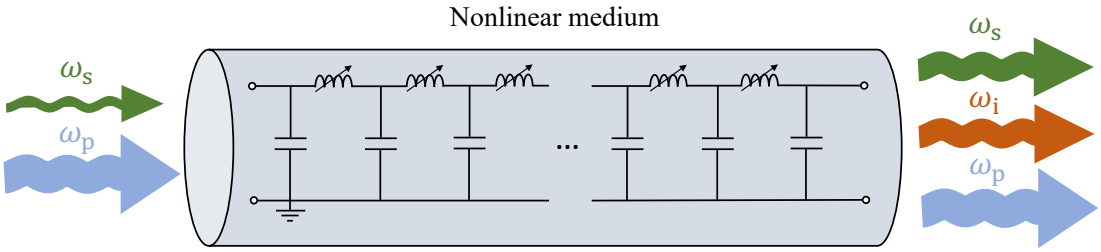

Figure 1.7: Circuit representation of a TWPA. A transmission line with high nonlinear inductance is formed by using high-kinetic-inductance films (KTWPA), or Josephson junctions (JTWPA). A weak signal tone ω_s gets amplified while co-propagating along the line with a strong pump tone ω_p. An idler tone ω_i is generated in this process to preserve the energy and momentum of the system.

In 2013, these phase-matching techniques were applied to the field of microwave superconducting circuits, yielding the first superconducting travelling wave parametric amplifier (TWPA) [73]. This implementation used NbTiN — a high kinetic inductance superconducting film — where the kinetic inductance has a nonlinear dependence with the applied current and can be modulated with a strong pump tone to generate parametric gain. The resulting device showcased $> 10\,\mathrm{dB}$ gain over $\sim 4\,\mathrm{GHz}$ bandwidth. This technology, named kinetic inductance (K-)TWPAs, has been the subject of many recently published scientific studies [74, 75, 76, 77].

Around the same time, the perfection of Josephson junction fabrication techniques permitted the implementation of superconducting transmission lines with thousands of junctions creating a travelling wave geometry[9]. In these transmission lines, assuming propagating tones with wavelengths much larger than the separation between the junctions, the line acts as a metamaterial with high nonlinear inductance, equivalent to the Kerr effect in optical fibers. As illustrated in Fig. 1.7, when a strong pump at amplitude ω_p and a weak signal at frequency ω_s co-propagate in the transmission line, there is exchange of energy between the pump and the signal through the parametric modulation of the inductance, leading to the amplification of the signal tone. In this process an idler tone at frequency ω_i is also generated for momentum conservation. The first demonstration of this device, termed Josephson (J-)TWPA, used novel microwave phase-matching techniques leading to a $\sim 20\,\mathrm{dB}$ gain with $\sim 3\,\mathrm{GHz}$ bandwidth, approaching the quantum limit of added noise [79]. Ever since, development of JTWPAs accelerated, leading to implementations using SQUIDs [80]

[9]Note that using Josephson junction arrays for travelling wave parametric amplification was first suggested in 1985 [78].

and nonlinear asymmetric inductive elements (SNAILs) [81, 82]; as well as several schemes improving their directionality [83, 84, 85, 86], dynamic range [87], quantum efficiency [88], among other aspects.

1.4 Thesis outline

This thesis delves into the development of JTWPAs, from the theoretical design, to the fabrication and characterisation. In Chapter 2, I shall introduce the theoretical concepts required for understanding the functioning of JTWPAs. This chapter includes the description of basic superconductivity concepts and the mathematical framework, based on transmission line theory, describing signal propagation in a JTWPA. Chapter 3 gives a detailed presentation of the methodology used to design the JTWPAs presented in this thesis. First, I demonstrate the validity of the novel mathematical framework I co-developed to predict and optimise the performance of JTWPAs. Then, the simulated performance of four amplifier designs — two using parallel plate capacitors (PPCs), and two using interdigitated capacitors (IDCs) — fabricated and tested in this thesis is presented. Chapter 4 gives an overview of the fabrication and mounting techniques used, as well as the different cryogenic systems and experimental setups employed for this work. Before fabricating the JTWPAs, I fabricated a series of test devices to explore the limits of the fabrication process. Chapter 5 summarises the experimental results and insights obtained from these measurements. Chapter 6 discusses the experimental results obtained for the JTWPA designed using PPCs, while Chapter 7 summarises the experimental results from the JTWPA with IDCs. Chapter 8 presents various interesting observations of the behaviour of a 500-junctions' Josephson array. Finally, Chapter 9 presents my efforts in developing a JTWPA operating in the W-band (75-110 GHz) range. In that chapter, I present the design considerations to extend the operational frequency of JTWPAs, concluding with two designs optimised for operation in the W-band that I subsequently fabricated and characterised. I conclude the thesis with a summary of the results and the possible strategies to improve the performance of the JTWPA designs in the near future.

Throughout the thesis, black boxes have been included with additional information that is potentially useful for the reader to better understand the topic discussed. These boxes can be omitted without impacting the arguments in the main text.

Chapter 2

TWPA theory

A good understanding of TWPA's operation requires some knowledge in superconductivity and nonlinear optics. In this chapter, I introduce some key concepts of superconductivity that are needed for TWPAs, leading to the derivation of the nonlinear inductance for the different types of nonlinear medium used for contructing a TWPA, with particular emphasis on Josephson junctions. Subsequently, I present a generalised coupled-mode equations (CME) framework we developed to describe the propagation of different frequency tones in a nonlinear superconducting transmission line (STL). This framework, not only describes TWPAs with different sources of nonlinearity, but it also captures different wave-mixing regimes. The chapter concludes with an exploration of techniques used to optimise the parametric gain through dispersion engineering.

2.1 Superconductivity

Superconductivity is a property of certain materials for which below a certain temperature T_c they experience no resistance to DC current and the magnetic field is totally expelled from the bulk of the material (Meissner effect). Superconductivity was first observed in 1911 by H. Kamerlingh Onnes, noticing that the electrical resistance of mercury disappeared at temperatures below $\sim 4.2\,\mathrm{K}$ [89]. In the following years, numerous theories arose providing a better understanding of superconductivity; leading to the publication of the first microscopic theory of superconductivity [90] (BCS theory) in 1957 by John Bardeen, Leon Cooper, and John Robert Schrieffer.

Superconductivity is also at the origin of the Josephson effect, used in numerous devices with applications in metrology and beyond. The Josephson effect is the fundamental phenomena behind the nonlinear behaviour of Josephson junctions at the origin of Josephson TWPAs.

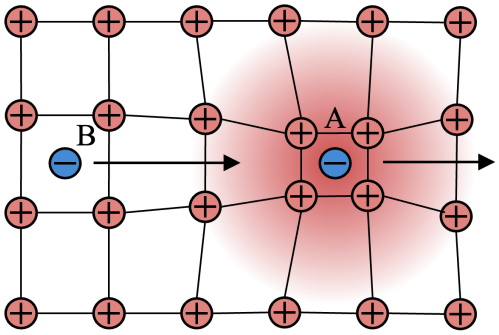

Figure 2.1: Cooper pair formation in BCS theory. The positively-charged ions in the crystal lattice are shown in red and the two quasi-particles forming the Cooper pair are marked in blue. The red area around quasi-particle '1' indicates a positively-charged region.

2.1.1 Fundamental concepts from BCS theory

BCS theory states that the charge carriers in a superconductor are formed by pairs of electrons bonded together by the interaction with phonons in the crystalline lattice, forming a Cooper pair. Although the origin of this effect arises from the quantum mechanical properties of the system, the following classical description helps to understand the underlying physics of Cooper pair formation. At temperatures close to the absolute zero, the ions in a superconducting metallic lattice do not experience vibrations. As a consequence, when an electron moves in the lattice, Coulomb forces attract the positive ions deforming the lattice as illustrated with 'A' in Fig. 2.1. This lattice deformation produces an excess of positive charges in the electron environment, resulting in an attractive Coulomb force exerts in a nearby electron ('B' in Fig. 2.1). This weak-interacting force overcomes the Coulomb repulsion from both electrons, hence bonding together in the form of a Cooper pair.

Because at low temperatures there is an important electron-lattice interaction, electrons are usually referred as quasi-particles, with an effective mass m_{qp}. Quasi-particles are Fermions and must obey the Pauli exclusion principle, however, Cooper pairs behave as Bosons which can condense into the same energy level. This Bose-Einstein condensate state can be described with a single wave-function $\Psi(r) = \sqrt{n_{\mathrm{s}}}e^{i\varphi(r)}$ where r denotes position, n_{s} is the density of Cooper pairs and the phase $\varphi(r)$ is coherent over macroscopic distances. $\Psi(r)$ does not interact with the lattice defects and phonons at the origin of electrical resistivity, hence, the observation of zero resistance for DC current in superconductors.

For temperatures $T < T_c$ in a superconductor, the binding of quasi-particles into Cooper pairs become energetically favourable. One of the key predictions from BCS theory is the need of a minimum binding energy $E_g = 2\Delta(T)$ to break a Cooper pair, creating two quasi-particle excitations. The superconducting gap $\Delta(T)$ increases from non-existance at T_c to a limiting value:

$$E_g = 2\Delta(0) = 3.528 k_B T_c, \tag{2.1}$$

where k_B is the Boltzmann constant. Therefore, at $T \ll T_c$, photons with energy $h\nu > 2\Delta(0)$ will break the Cooper pairs and result in quasi-particles excitation, and hence dissipation in the superconductor. For example, niobium has a $T_c \sim 9.2\,\mathrm{K}$, and therefore, $2\Delta(0) \approx 2.8\,\mathrm{meV}$, which result in $\nu \approx 676\,\mathrm{GHz}$. On the other hand, aluminium has a $T_c \sim 1.2\,\mathrm{K}$, hence $2\Delta(0) \approx 0.37\,\mathrm{meV}$, resulting in $\nu \approx 89\,\mathrm{GHz}$; limiting the applications of aluminium beyond this frequency.

Kinetic inductance

Kinetic inductance (L_k) is a type of inductance arising from the inertia of moving charges in a conductor, and can be prominent in some superconducting materials [91]. Assuming a varying electric field E is applied to a superconductor, as a consequence of the mass of the Cooper pairs, a finite time is required to accelerate them. This phase lag between E and the Cooper pairs' movement results in energy storage in the carrier, giving rise to kinetic inductance. This effect can be only noticed in materials with high carrier mobility, such as superconductors, graphene, gallium nitride (GaN) or indium phosphide (InP).

The kinetic inductance has a complex behaviour with applied current (I), however, it can be approximated with the following Taylor expansion [92]:

$$L_k = L_{k,0}\left[1 + \frac{I^2}{I_*^2} + O(I^4)\right] \tag{2.2}$$

where $L_{k,0}$ is the intrinsic inductance at the material and I_* sets the scale of nonlinearity. This equation has been extensively investigated experimentally and confirmed using high-Q superconducting resonators made with high kinetic inductance [93].

2.1.2 The Josephson junction

In 1962, Bryan Josephson predicted the tunnelling of cooper-pairs between two superconducting electrodes separated by a thin insulating barrier [94]; a device referred

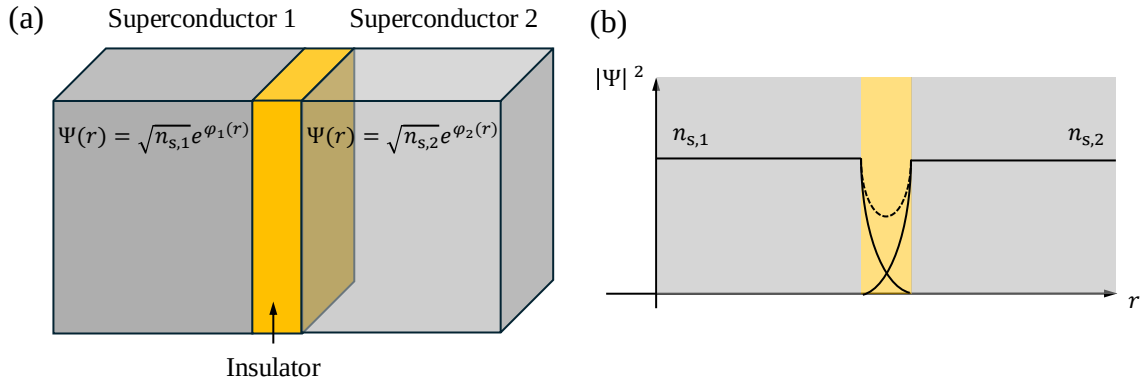

Figure 2.2: (a) Physical representation of a Josephson junction. (b) Representation of the amplitude of the superconducting wave functions across the junction. The amplitudes decay and overlap in the insulator. The addition of both amplitudes is marked with a dashed line.

as Josephson junction which is illustrated in Fig. 2.2(a). This 'super-current' can be expressed as:

$$I = I_c \sin \phi, \tag{2.3}$$

where $\phi = \varphi_2 - \varphi_1$ is the phase difference in the superconducting condensate wavefunction[1] of the two electrodes, and I_c is the critical current setting the maximum current a junction can support. This expression indicates that at zero-voltage, current can flow between the two electrodes without dissipation, as a result of a phase-difference across the junction. This remarkable effect, known as the DC Josephson effect, results from the overlapping of the wavefunctions from both superconducting electrodes inside the barrier due to the proximity effect. Therefore, resulting in a finite probability of Cooper-pairs tunnelling, as shown in Fig. 2.2(b).

Furthermore, Josephson predicted that the voltage across the junction (V) is related to a time variation of ϕ by the following expression:

$$\frac{d\phi}{dt} = \frac{2eV}{\hbar}, \tag{2.4}$$

where e is the electron charge and $\hbar$ is the reduced Plank constant. Therefore, when a voltage is applied across the junction, the phase varies linearly with time, resulting in an oscillating current at frequency $\omega = 2eV/\hbar$. This effect, known as the AC Josephson effect, has been, among other applications, used for the definition of the

[1]More precisely, it is the difference in the phase of the Ginzburg-Landau (GL) wavefunction. For further details on GL theory we refer the reader to [95].

voltage standard[2] [96].

The RCSJ model and Josephson inductance

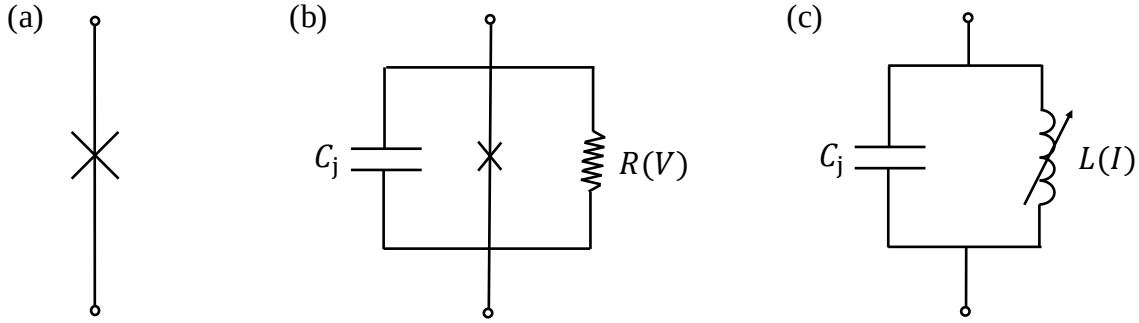

Figure 2.3: (a) Standard circuit representation of a Josephson junction. (b) RCSJ model. The cross indicate an ideal Josephson junction. (c) Modified RCSJ model for the $V = 0$ case.

A Josephson junction is generally represented with the circuit symbol illustrated in Fig. 2.3(a). To describe the AC and DC effects, a Josephson junction is often modelled using the resistively and capacitively shunted junction (RCSJ) model. The circuit diagram of this model is shown in Fig. 2.3(b), where the capacitance C_j originates from the geometric shunting capacitance between the two electrodes, the cross indicates an ideal junction described by Eq. 2.3 and R takes into account the finite dissipation in the finite voltage regime without affecting the lossless case. The value of R is highly depending on the temperature and voltage regime of the junction, and needs to be chosen accordingly in the model.

In this thesis, we use a modified RCSJ model to describe the junctions. From the definition of the inductance $\left(v(t) = L\frac{di}{dt}\right)$ and Eq.2.3 & 2.4, the inductance of a Josephson junction can be written as:

$$L_j = \frac{\Phi_0}{2\pi I_c \cos\phi}, \tag{2.5}$$

where Φ_0 is the magnetic flux quantum. Given the trigonometry identity $\sin^2\phi + \cos^2\phi = 1$, we can rewrite $\cos\phi = \sqrt{1-\sin^2\phi} = \sqrt{1-\left(\frac{I}{I_c}\right)^2}$. By replacing this expression in Eq. 2.5, we obtain:

[2]The inverse process, where an AC current generates a DC voltage across the junction, is the actual mechanism used for the definition of the voltage standard.

$$L_{\mathrm{j}} = \frac{L_0}{\sqrt{1 - \left(\frac{I}{I_c}\right)^2}}, \tag{2.6}$$

where $L_0 = \frac{\phi_0}{I_c}$. Applying a Taylor expansion to the first order of the denominator in the above equation, we can rewrite the inductance of a junction as:

$$L_{\mathrm{j}} = L_0 \left[1 + \frac{1}{2}\left(\frac{I}{I_{\mathrm{c}}}\right)^2 + O\left(I^4\right)\right]. \tag{2.7}$$

Therefore, the Josephson inductance is nonlinear with the applied current and we can replace the junction in the original RCSJ model with a nonlinear inductor. This nonlinear property of the inductance is the key for parametric amplification, as we will discuss in Sec. 2.2. Furthermore, all the devices presented in this thesis are designed for operation in the $V = 0$ regime where the junction is lossless, and therefore R can be neglected, resulting in the equivalent circuit presented in Fig. 2.3(c).

The tilted-washboard potential and the current-voltage characteristics

The current-voltage (IV) characteristics of a Josephson junction provide crucial information about the junction. A popular and intuitive description of Josephson junctions IV characteristics is given by a semiconductor-like energy bands model, as presented in [97]. Nevertheless, this model assumes the suppression of the DC and AC Josephson current, only describing the quasi-particles tunnelling in the junction. Therefore, for a more complete image of the junctions IV characteristics required for the understanding of the measurements presented in this thesis, I opt for a description based on the tilted-washboard potential.

Using Kirchhoff's current law in the original RCSJ model, the expression of a current I injected in the junction can be written as:

$$\begin{aligned} I &= I_{\mathrm{c}} \sin\phi + V/R + C_{\mathrm{j}} \frac{dV}{dt} \\ &= I_{\mathrm{c}} \sin\phi + \frac{\Phi_0}{2\pi R}\dot{\phi} + \frac{\Phi_0 C_{\mathrm{j}}}{2\pi}\ddot{\phi}. \end{aligned} \tag{2.8}$$

Rearranging the terms,

$$\frac{\Phi_0}{2\pi} C_{\mathrm{j}} \ddot{\phi} + \frac{\Phi_0}{2\pi R}\dot{\phi} = -I_{\mathrm{c}} \sin\phi + I \equiv -\frac{2\pi}{\Phi_0}\frac{\partial U_{\mathrm{j}}}{\partial \phi}, \tag{2.9}$$

where $U_\mathrm{j} = E_\mathrm{j}\left[1 - \cos\phi - \frac{I}{I_\mathrm{c}}\phi\right]$ is the potential field and $E_\mathrm{j} = \frac{I_\mathrm{c}\Phi_0}{2\pi}$ is the Josephson energy. Eq. 2.9 is often referred as the equation of motion for ϕ. As shown in Fig. 2.4(a), without applied current the potential $U_\mathrm{j}(\phi)$ follows a $1 - \cos\phi$ function, oscillating at a period of 2π with a $2E_\mathrm{j}$ amplitude. As the applied current increases, the curve tilts, and the local minima begin to fade away.

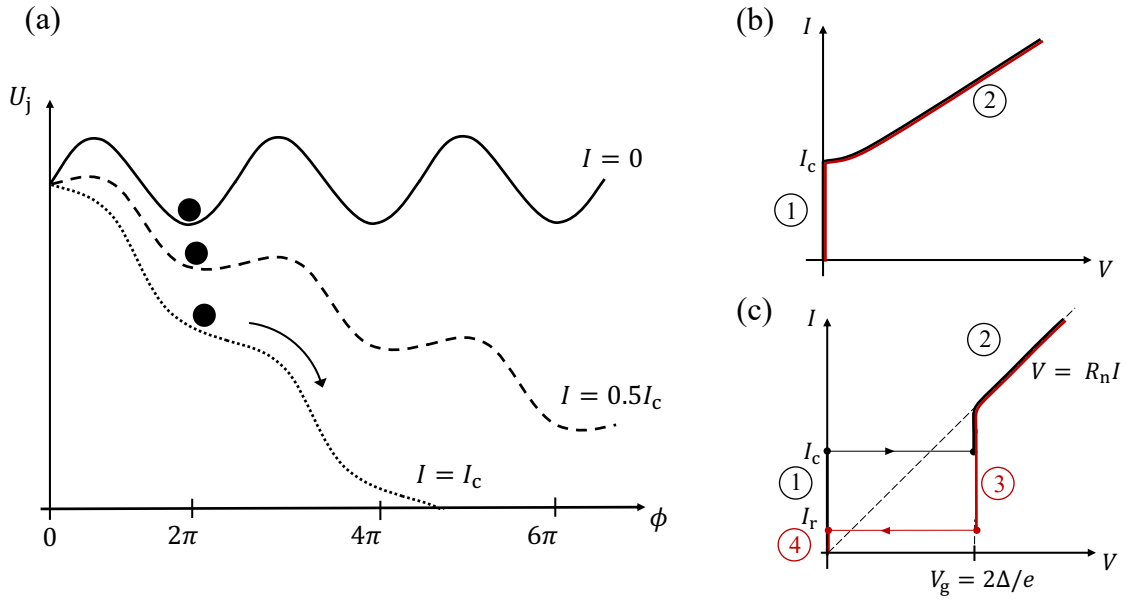

Figure 2.4: (a) Representation of the tilted-washboard potential model of a Josephson junction. The three $U_\mathrm{j}(\phi)$ curves indicate results from different values of I. The particle' is represented with a black dot. The system is in a static state when the particle is trapped in a local minima e.g., $I = 0$ curve, and a running state when the particle falls down the curve e.g., $I = I_\mathrm{c}$ curve. (b) Representation of the IV curve of an overdamped Josephson junction. (c) Representation of the IV curve of an underdamped Josephson junction. In (b) and (c) the black and red line indicates an upward and downward current sweep respectively.

The dynamics of the system described with Eq. 2.9 are analogous to a point-like particle in a tilted washboard gravitational potential, hence the name of the model. The motion of this point-like particle is described by the following equation:

$$m\ddot{x} + \xi\dot{x} = -\frac{\partial\left[W(x) - F_\mathrm{d}x\right]}{\partial x}, \tag{2.10}$$

where x is the position, m is the particle mass, ξ is the friction coefficient, F_d is the external force and $W(x)$ is a cosine gravitational potential. Comparing Eq. 2.10 and Eq. 2.9, we notice that in a Josephson junction, C_j is analogous to the mass, R^{-1} to the friction coefficient, I to the external force, and $\frac{\Phi_0}{2\pi}\dot{\phi} = V$ to the velocity.

If C_j is small, the friction term $\frac{\Phi_0}{2\pi R}$ dominates Eq. 2.9 and we are in the overdamped regime. In this regime, the IV curve of the junction resembles that presented in Fig. 2.4(b), where the upwards and downwards current sweep are indicated in black and red lines respectively. For the case of $I \ll I_c$ (region 1 in Fig. 2.4(b)) the 'particle' is trapped in a local minima of the potential field, and supercurrent flows through the junction without developing a voltage across it. We shall refer to this as the static state. When $I \geqslant I_c$, the local minimas in the potential disappear as a consequence of the tilt, forcing the 'particle' to roll down, i.e., increasing ϕ (dotted line in Fig. 2.4(a)). We shall refer to this case as the running state. From Eq. 2.4, a time variation of ϕ results in a voltage across the junction, hence the shape of the current with finite voltage as shown in the IV curve (region 2 in Fig. 2.4(b)). In the running state, the voltage across the junction is proportional to I, following Ohm's law[3]. When sweeping down the current, for $I < I_c$, the minimas in the potential reappear, trapping the 'particle' resulting in the static state again.

If C_j is large, the inertia term $\frac{\Phi_0}{2\pi}C$ dominates Eq. 2.9 and we are in the underdamped regime. The IV curve in this regime becomes hysteretic and resembles Fig. 2.4(c). As we increase the current below I_c (region 1 in Fig. 2.4(c)), the system is in the static state. When $I = I_c$, we enter the running state and the voltage jumps to the gap voltage $V_g = 2\Delta/e$ due to the tunneling of quasi-particles. If we further increase I, the voltage across the junction follows Ohm's law $V = R_n I$, where R_n is known as the normal resistance (region 2 in Fig. 2.4(c)). If we now decrease the applied current, the system will get to the static state at a retrapping current (I_r) lower than I_c, resulting in a hysteresis effect (region 3 in Fig. 2.4(c)). The hysteresis effect can be explained in the potential pictures as follows: at $I > I_c$ the heavy particle is moving down the potential curve; when we reduce I just below I_c, the local minima in the potential start forming but they are shallow. Therefore, due to its inertia, the particle keeps falling down the potential curve jumping over the barriers. This state corresponds to the region 3 in Fig. 2.4(c). If the current is further reduced, the potential curve gets more horizontal and the minimas get deeper. Eventually, when the retrapping current value $I = I_r$ is reached, the local minimas are deep enough to trap the particle, reaching the steady state (region 4 in Fig. 2.4(c)).

[3]This is a simplified description; in reality, in the running state, $V = R\left(I^2 - I_c^2\right)^{1/2}$. Therefore, only for $I \gg I_c$ we find the Ohm's law [95].

DC Superconducting quantum interference devices (SQUIDs)

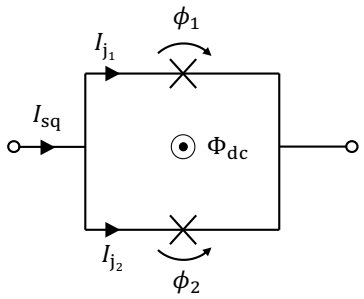

Figure 2.5: Circuit diagram of a DC-SQUID. The DC-SQUID effectively behaves as a Josephson junction where the I_c can be modified with an external magnetic field Φ_{dc}.

The DC superconducting quantum interference device (DC-SQUID) consists of two junctions in parallel in a superconducting loop. For symmetric DC-SQUIDs, where both the junctions in parallel are identical — as shown in Fig. 2.5 — the total current in the DC-SQUID is given by:

$$\begin{aligned} I_{sq} &= I_{j_1} + I_{j_2} \\ &= I_c \sin\phi_1 + I_c \sin\phi_2 \\ &= 2I_c \sin\left(\frac{\phi_1+\phi_2}{2}\right)\cos\left(\frac{\phi_1-\phi_2}{2}\right). \end{aligned} \tag{2.11}$$

Given the geometry of the DC-SQUID, when applying an external DC magnetic flux Φ_{dc}, it induces an opposite phase change ϕ_M in each junction of the DC-SQUID, i.e., $\phi_1 = \phi + \phi_M$ and $\phi_2 = \phi - \phi_M$ where ϕ is the Josephson phase of a single junction. Therefore,

$$\phi_1 - \phi_2 = 2\phi_M = 2\pi\frac{\Phi_{dc}}{\Phi_0}. \tag{2.12}$$

Hence, we can rewrite the current in a DC-SQUID as:

$$I_{sq} = 2I_c \cos\left(\pi\frac{\Phi_{dc}}{\Phi_0}\right)\sin\phi \quad = I_{c,sq}\sin\phi, \tag{2.13}$$

where $I_{c,sq} = 2I_c\cos\left(\pi\frac{\Phi_{dc}}{\Phi_0}\right)$.

The inductance of the DC-SQUID is given by the equivalent inductance of both

junctions in parallel:

$$\begin{aligned} L_{\mathrm{sq}} &= \frac{L_{\mathrm{j}_1} L_{\mathrm{j}_2}}{L_{\mathrm{j}_1} + L_{\mathrm{j}_2}} = \frac{\left(\frac{\phi_0}{I_{\mathrm{c}} \cos\phi_1} \times \frac{\phi_0}{I_{\mathrm{c}} \cos\phi_2}\right)}{\left(\frac{\phi_0}{I_{\mathrm{c}} \cos\phi_1} + \frac{\phi_0}{I_{\mathrm{c}} \cos\phi_2}\right)} \\ &= \frac{\phi_0}{I_{\mathrm{c}}} \left[\frac{1}{\cos\phi_1 + \cos\phi_2}\right] \\ &= \frac{\phi_0}{I_{\mathrm{c,sq}} \cos\phi}. \end{aligned} \tag{2.14}$$

From Eq. 2.13, $\sin\phi = \frac{I_{\mathrm{sq}}}{I_{\mathrm{c,sq}}}$, hence using the same trigonometry identity used in the Josephson junction case, we can rewrite $\cos\phi = \sqrt{1 - \left(\frac{I_{\mathrm{sq}}}{I_{\mathrm{c,sq}}}\right)^2}$. Applying the first order Taylor expansion and replacing $\cos\phi$ in Eq. 2.14:

$$L_{\mathrm{sq}} = L_{0,\mathrm{sq}} \left[1 + \frac{1}{2}\left(\frac{I_{\mathrm{sq}}}{I_{\mathrm{c,sq}}}\right)^2 + O\left(I^4\right)\right] \tag{2.15}$$

where $L_{0,\mathrm{sq}} = \frac{\phi_0}{I_{\mathrm{c,sq}}}$. Therefore, the inductance of a SQUID is nonlinear with current, and the amplitude can be modified with an external magnetic field, since $I_{\mathrm{c,sq}}$ depends on Φ_{dc}. Similar to the single Josephson junction case, the nonlinear inductance demonstrates that SQUIDs can be used for parametric amplification.

SQUID variations with physical asymmetry such as the RF-SQUID [98] or the nonlinear asymmetric inductive element (SNAIL) [82], equally result in nonlinear inductance and have been employed for parametric amplification. However, the mathematical framework introduced in this chapter to describe TWPAs, is currently limited to components and transmission lines with spatial centrosymmetry[4]. Therefore, these SQUIDs variations will not be covered in this section.

2.2 Travelling-wave parametric amplification in $\chi^{(3)}$ nonlinear materials

In this section, I will explain how the nonlinear inductance of the components introduced in the previous section can be used to build nonlinear transmission lines resulting in parametric amplification, particularly for TWPAs.

[4]The framework could be potentially extended to non-centrosymmetric transmission lines provided a generalised inductance equation that includes the linear and quadratic current term with the external applied magnetic field.

2.2.1 Wave-mixing regimes

Wave-mixing occurs in a nonlinear medium when two or more electromagnetic waves of different frequencies propagate through it. As these waves — often referred to as frequency tones — interact, they generate new frequency components and exchange energy. Various wave-mixing regimes can arise from this process depending on the nature of the nonlinear medium, e.g., $\chi^{(2)}$ or $\chi^{(3)}$ nonlinear materials.

Four-wave mixing (4WM)

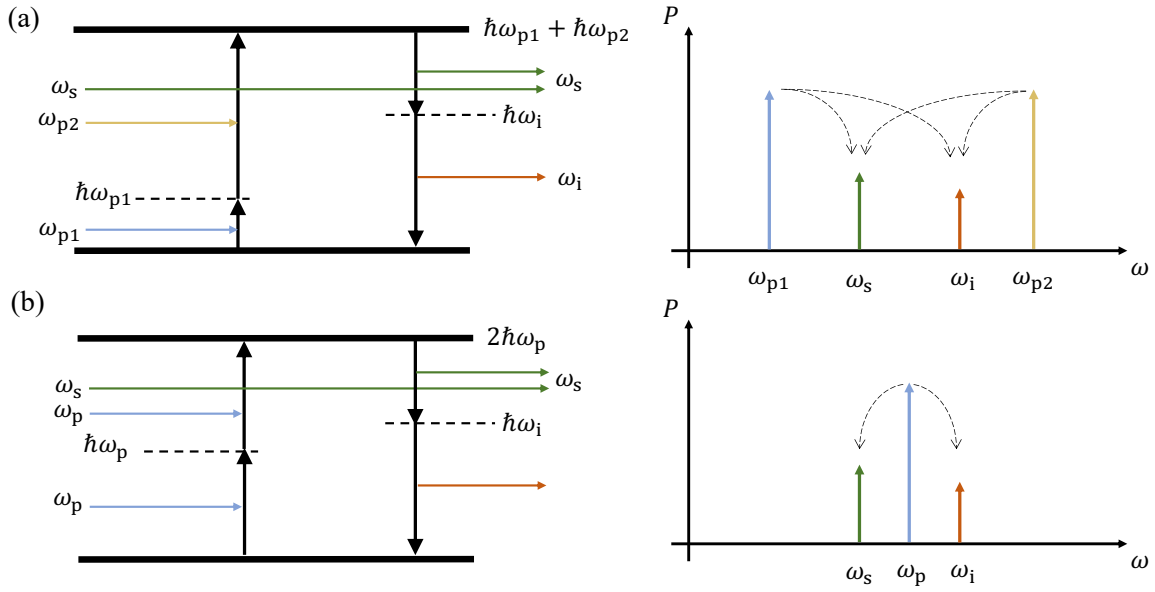

Figure 2.6: Four-wave mixing process for (a) non-degenerated pump (NP4WM) and (b) degenerated pump (DP4WM) device. The left panel illustrates the energy diagram and the right panel illustrates the frequency power spectrum, where the dashed lines indicate energy transfer.

Four-wave mixing (4WM) is the natural wave-mixing process in a $\chi^{(3)}$ nonlinear material[5]. It consists of the interaction of two pump photons at frequency ω_{p_1} and ω_{p_2}, and a signal photon at frequency ω_s, generating an idler photon at frequency ω_i. To preserve the momentum and energy of the system, the following frequency relation needs to be satisfied:

$$\omega_{p_1} + \omega_{p_2} = \omega_s + \omega_i. \tag{2.16}$$

[5]This terminology originated from the field of optics, where $\chi^{(3)}$ nonlinearity refers to materials with a quadratic electro-optic dependence, at the origin of the Kerr effect.

The energy diagram and frequency power spectrum from this process are illustrated in Fig. 2.6(a).

When the two pump photons have different frequencies, as discussed above, the process is known as non-degenerated pump 4WM (NP4WM). A special case in 4WM is where both pump photons have the same frequency $\omega_{\mathrm{p}_1} = \omega_{\mathrm{p}_2} = \omega_{\mathrm{p}}$, known as degenerated-pump 4WM (DP4WM). In DP4WM, the following frequency relation is satisfied:

$$2\omega_{\mathrm{p}} = \omega_s + \omega_i. \tag{2.17}$$

This process is illustrated in Fig. 2.6(b). In this case, only one pump tone is required for the TWPA operation.

Three-wave mixing (3WM)

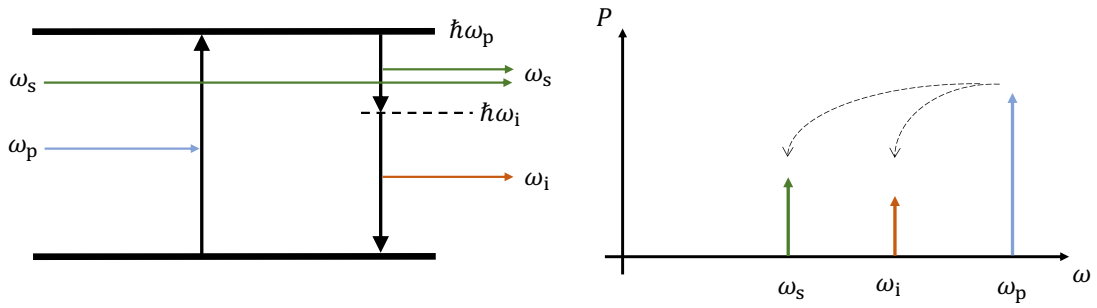

Figure 2.7: Three-wave mixing process. The left panel illustrates the energy diagram and the right panel illustrates the frequency power spectrum, where the dashed lines indicate energy transfer.

Three-wave mixing (3WM) is the natural wave-mixing process in $\chi^{(2)}$ nonlinear materials[6]. In this process, a single pump photon at frequency ω_{p} interacts with a signal photon at frequency ω_{s} to create an idler photon at frequency ω_{i}, such that the energy conservation relation obeys,

$$\omega_{\mathrm{p}} = \omega_{\mathrm{s}} + \omega_{\mathrm{i}}. \tag{2.18}$$

Fig. 2.7 illustrates the energy diagram and frequency power spectrum. Materials with only $\chi^{(2)}$ nonlinearity for microwave parametric amplification have been suggested using RF-SQUIDs [98] and successfully implemented using SNAILs [82], under a particular magnetic bias configuration[7]. 3WM can also be generated in a $\chi^{(3)}$

[6]In optics, $\chi^{(2)}$ nonlinearity describes materials with a linear electro-optic dependence, at the origin of the Pockels effect.

[7]Note that without the right magnetic bias, RF-SQUID and SNAIL JTWPAs are $\chi^{(3)}$ nonlinear materials or a combination of $\chi^{(3)}$ and $\chi^{(2)}$ nonlinear materials.

nonlinear material by breaking the nonlinear symmetry[8]. For example, in a superconducting line with a quadratic nonlinear inductance, applying a DC signal will break the symmetry adding a linear term in the current dependence of the inductance. This linear term results in 3WM generation. It needs to be noticed that in the mentioned example, both 3WM and 4WM processes will take place, therefore, to differentiate this regime from the case of materials with only $\chi^{(2)}$ nonlinearity and 3WM, we shall refer to it as DC3WM. This wave-mixing regime has been extensively explored for KTWPAs [99, 74], however, it has not yet been experimentally demonstrated in JTWPAs.

2.2.2 Coupled-Mode Equations (CME) framework

In this section, I derive the equations describing the propagation of current tones in an STL with quadratic nonlinear inductance, i.e., $\chi^{(3)}$ nonlinear materials. Different from the general approach presented in the literature, I generalise the mathematical framework to include different $\chi^{(3)}$ nonlinear materials and provide solutions for the different wave-mixing regimes. This novel framework is extensively used to predict the performance of the JTWPA designs presented in this thesis.

Transmission line theory and the Telegrapher equations

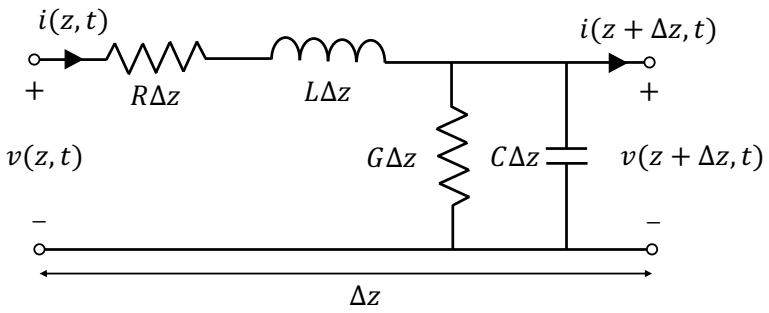

Figure 2.8: Lumped-element circuit model of a transmission line, often referred as the RLGC model.

Transmission line theory describes the current and voltage changes in distributed circuits where the dimensions of individuals components, e.g., resistors, inductors or capacitors, are non-negligible compared with the electrical wavelengths, otherwise

[8]In the TWPA case, the nonlinear symmetry refers to the property of the inductance $L(I) = L(-I)$.

	Kinetic Inductance	Josephson Junctions	DC-SQUID
β_{nl}	1	0.5	0.5
L_0	$\hbar R_{\mathrm{N}}/\pi\Delta$	ϕ_0/I_*	ϕ_0/I_*
I_*	αI_{c}	I_{c}	$2I_{\mathrm{c}}\cos\left(\pi\frac{\Phi_{\mathrm{dc}}}{\Phi_0}\right)$

Table 2.1: Key parameters in Eq.2.21 for the different sources of nonlinear inductance in a TWPA.

described by circuit theory for lumped-element circuits. For an infinitesimal length Δz, a transmission line can be modelled with the lumped-element circuit presented in Fig. 2.8, where R, L, G and C correspond to the series resistance, series inductance, shunt conductance and shunt capacitance per unit length respectively. The voltage (V) and current (I) variation in space (z) and time (t) in a transmission line is given by the Telegrapher equations [100]:

$$\begin{aligned}\frac{\partial V(z,t)}{\partial z} &= -RI(z,t) - L\frac{\partial I(z,t)}{\partial t}\\ \frac{\partial I(z,t)}{\partial z} &= -GV(z,t) - C\frac{\partial V(z,t)}{\partial t}.\end{aligned} \tag{2.19}$$

Combining both equations, we derive the current propagation in a transmission line:

$$\frac{\partial^2 I(z,t)}{\partial z^2} = RG\cdot I + (RC+LG)\frac{\partial I}{\partial t} + C\frac{\partial}{\partial t}L\frac{\partial I(z,t)}{\partial t}. \tag{2.20}$$

Nonlinear propagation equation

As we have introduced earlier, the kinetic inductance (Eq. 2.2), the Josephson junction inductance (Eq. 2.7) and the DC-SQUIDs inductance (Eq. 2.15) have a quadratic dependence with current. In these three cases, the inductance expression can be generalised as:

$$L(I) = L_0\left[1+\beta_{\mathrm{nl}}\left(\frac{I}{I_*}\right)^2\right], \tag{2.21}$$

where L_0 is the intrinsic inductance, I_* sets the scale of nonlinearity and β_{nl} is a constant describing the different sources of nonlinearity. The values for these parameters for the kinetic inductance, Josephson junctions, and DC-SQUIDs are tabulated in Table 2.1. Replacing the inductance L in Eq. 2.20 with Eq. 2.21, we obtain the nonlinear propagation equation,

$$\begin{aligned}\frac{\partial^2 I}{\partial z^2} - RG\cdot I(z,t) - (RC+L_0G)\frac{\partial I(z,t)}{\partial t} - L_0C\frac{\partial^2 I}{\partial t^2}\\ -\frac{\beta_{\mathrm{nl}}L_0C}{I_*^2}\frac{\partial}{\partial t}\left(I^2\frac{\partial I}{\partial t}\right) - \frac{\beta_{\mathrm{nl}}L_0G}{I_*^2}\left(I^2\frac{\partial I}{\partial t}\right) = 0,\end{aligned} \tag{2.22}$$

where the fifth and sixth terms are the mixing terms. This equation describes the waves' propagation in a nonlinear STL assuming that the nonlinear inductance is much larger than the geometric inductance of the transmission line ($L_0 \gg L_{\text{geo}}$).

Negligible effect of C_j in the STL

From Sec. 2.1.2, the modified RCSJ model includes a capacitance C_j which is not included in the STL lumped-element circuit model used in this derivation. The equivalent impedance of the capacitor (Z_C) and inductor (Z_L) in the modified RCSJ model is defined as:

$$\begin{aligned} Z_\text{L} &= i\omega L_\text{j} \\ Z_\text{C} &= \frac{1}{i\omega C_\text{j}}. \end{aligned} \tag{2.23}$$

For all the JTWPAs published to date, the order of magnitude in the international units (IU) system is $10^{-14}\,\text{F} \lesssim C_\text{j} \lesssim 10^{-13}\,\text{F}$ and $10^{-11}\,\text{H} \lesssim L_\text{j} \lesssim 10^{-10}\,\text{H}$. Therefore, $|Z_\text{L}| \ll |Z_\text{C}|$, hence most of the current flows through L_j, and C_j can be safely neglected.

Coupled-Mode Equations

To derive the coupled-mode equations describing the system, I follow the same procedure introduced by J.C. Longden in [101]. I start by assuming that the solution to Eq. 2.22 are forward propagating waves in the form of

$$I(z,t) = \sum_\text{m} \frac{1}{2} A_\text{m}(z) e^{i\omega_\text{m} t - \gamma_\text{m} z} + c.c, \tag{2.24}$$

where $c.c$ denotes the complex conjugate, A_m denotes the slowly varying amplitude of the waves, $\gamma_\text{m} = \alpha_\text{m} + ik_\text{m} = \sqrt{(R + i\omega_\text{m} L)(G + i\omega_\text{m} C)}$ is the complex propagation constant where α_m is the attenuation constant, k_m is the wavevector, and ω_m is the angular frequency. Considering operation in the NP4WM regime, $\text{m} = \{\text{p}_1, \text{p}_2, \text{s}, \text{i}\}$ denotes the two pump tones (p_1 and p_2), a signal (s) and an idler (i) tone.

Next, we inject Eq. 2.24 in Eq. 2.22, and simplify the resulting expression using the slowly varying envelope approximation $\left|\frac{d^2 A_\text{m}(z)}{dz^2}\right| \ll \left|k_\text{m} \frac{dA_\text{m}(z)}{dz}\right|$. This results in a large number of mixing frequency terms. By separating the terms that oscillate at the pumps, signal and idler frequencies, including any frequency combination that satisfies the NP4WM energy conservation equation (Eq. 2.16), we obtain the following coupled-mode equations:

$$\gamma_{\mathrm{p}_1}\frac{\partial A_{\mathrm{p}_1}(z)}{\partial z} =\xi_{\mathrm{p}_1}\Bigg[A_{\mathrm{p}_1}\Bigg(\eta_{\mathrm{p}_{11}}A_{\mathrm{p}_1}A^*_{\mathrm{p}_1}e^{-2\alpha_{\mathrm{p}_1}z}+2\eta_{\mathrm{p}_{22}}A_{\mathrm{p}_2}A^*_{\mathrm{p}_2}e^{-2\alpha_{\mathrm{p}_2}z} + 2A_{\mathrm{s}}A^*_{\mathrm{s}}e^{-2\alpha_{\mathrm{s}}z}+2A_{\mathrm{i}}A^*_{\mathrm{i}}e^{-2\alpha_{\mathrm{i}}z}\Bigg)+2A^*_{\mathrm{p}_2}A_{\mathrm{s}}A_{\mathrm{i}}e^{(2\alpha_{\mathrm{p}_1}-\Delta_\alpha)z}e^{-i\Delta_k z}\Bigg] \tag{2.25a}$$

$$\gamma_{\mathrm{p}_2}\frac{\partial A_{\mathrm{p}_2}(z)}{\partial z} =\xi_{\mathrm{p}_2}\Bigg[A_{\mathrm{p}_2}\Bigg(2\eta_{\mathrm{p}_{11}}A_{\mathrm{p}_1}A^*_{\mathrm{p}_1}e^{-2\alpha_{\mathrm{p}_1}z}+\eta_{\mathrm{p}_{22}}A_{\mathrm{p}_2}A^*_{\mathrm{p}_2}e^{-2\alpha_{\mathrm{p}_2}z} + 2A_{\mathrm{s}}A^*_{\mathrm{s}}e^{-2\alpha_{\mathrm{s}}z}+2A_{\mathrm{i}}A^*_{\mathrm{i}}e^{-2\alpha_{\mathrm{i}}z}\Bigg)+2A^*_{\mathrm{p}_1}A_{\mathrm{s}}A_{\mathrm{i}}e^{(2\alpha_{\mathrm{p}_2}-\Delta_\alpha)z}e^{-i\Delta_k z}\Bigg] \tag{2.25b}$$

$$\gamma_{\mathrm{s}}\frac{\partial A_{\mathrm{s}}(z)}{\partial z} =\xi_{\mathrm{s}}\Bigg[A_{\mathrm{s}}\Bigg(2A_{\mathrm{p}_1}A^*_{\mathrm{p}_1}e^{-2\alpha_{\mathrm{p}_1}z}+2A_{\mathrm{p}_2}A^*_{\mathrm{p}_2}e^{-2\alpha_{\mathrm{p}_2}z} + A_{\mathrm{s}}A^*_{\mathrm{s}}e^{-2\alpha_{\mathrm{s}}z}+2A_{\mathrm{i}}A^*_{\mathrm{i}}e^{-2\alpha_{\mathrm{i}}z}\Bigg)+2A_{\mathrm{p}_1}A_{\mathrm{p}_2}A^*_{\mathrm{i}}e^{(2\alpha_{\mathrm{s}}-\Delta_\alpha)z}e^{-i\Delta_k z}\Bigg] \tag{2.25c}$$

$$\gamma_{\mathrm{i}}\frac{\partial A_{\mathrm{i}}(z)}{\partial z} =\xi_{\mathrm{i}}\Bigg[A_{\mathrm{i}}\Bigg(2A_{\mathrm{p}_1}A^*_{\mathrm{p}_1}e^{-2\alpha_{\mathrm{p}_1}z}+2A_{\mathrm{p}_2}A^*_{\mathrm{p}_2}e^{-2\alpha_{\mathrm{p}_2}z} + 2A_{\mathrm{s}}A^*_{\mathrm{s}}e^{-2\alpha_{\mathrm{s}}z}+A_{\mathrm{i}}A^*_{\mathrm{i}}e^{-2\alpha_{\mathrm{i}}z}\Bigg)+2A_{\mathrm{p}_1}A_{\mathrm{p}_2}A^*_{\mathrm{s}}e^{(2\alpha_{\mathrm{i}}-\Delta_\alpha)z}e^{-i\Delta_k z}\Bigg], \tag{2.25d}$$

where $\xi_{\mathrm{m}} = \eta_{\mathrm{m}}\frac{\beta_{\mathrm{nl}}\omega_{\mathrm{m}}^2 L_0 C}{8I_*^2}$, $\eta_{\mathrm{m}} = \left(1+i\frac{G}{\omega_{\mathrm{m}}C}\right)$, $\Delta_k = k_{\mathrm{p}_1}+k_{\mathrm{p}_2}-k_{\mathrm{s}}-k_{\mathrm{i}}$ and $\Delta_\alpha = \alpha_{\mathrm{p}_1}+\alpha_{\mathrm{p}_2}+\alpha_{\mathrm{s}}+\alpha_{\mathrm{i}}$. $\eta_{\mathrm{p}_{11}}$ and $\eta_{\mathrm{p}_{22}}$ are two coefficients introduced here to generalise the set of equations for different wave-mixing regimes. In the NP4WM case, $\eta_{\mathrm{p}_{11}}=1$ and $\eta_{\mathrm{p}_{22}}=1$.

This set of equations is the most generic expression of the CMEs for STLs with spatial centrosymmetry, extending the framework presented in [101] to further include different sources of $\chi^{(3)}$ nonlinearity. Therefore, it can be used to model both KTWPAs and JTWPA based on either bare Josephson junctions or DC-SQUIDs. Often, TWPAs operate in the 'low-loss' limit, where $R \ll \omega_{\mathrm{m}}L$ and $G \ll \omega_{\mathrm{m}}C$ and,

$$\gamma_{\mathrm{m}} \approx \frac{1}{2}\left(R\sqrt{\frac{C}{L_0}}+G\frac{L_0}{C}\right)+i\omega_{\mathrm{m}}\sqrt{L_0 C}, \tag{2.26}$$

therefore, $\eta_{\mathrm{m}} \approx 1$ and $\xi_{\mathrm{m}} \approx \frac{\beta_{\mathrm{nl}}k_{\mathrm{m}}^2}{8I_*^2}$, further simplifying Eq. 2.25. Since we only deal superconducting lines in this thesis, I only consider operation in the 'low-loss' limit for the rest of this section. Next, I shall demonstrate the special cases derived from this generalised CMEs, showing how the conventional DP4WM and DC3WM operation can be easily derived.

Degenerated-pump four-wave mixing (DP4WM)

Assuming a degenerated pump tone is applied to the transmission line, i.e., $f_{\mathrm{p}} = f_{\mathrm{p_1}} = f_{\mathrm{p_2}}$, and to preserve the total energy in the system:

$$\begin{aligned} P_{\mathrm{p_1}} + P_{\mathrm{p_2}} &= P_{\mathrm{p}} \\ I_{\mathrm{p_1}}^2 R + I_{\mathrm{p_2}}^2 R &= I_{\mathrm{p}}^2 R \\ I_{\mathrm{p_1}}^2 + I_{\mathrm{p_2}}^2 &= I_{\mathrm{p}}^2, \end{aligned} \tag{2.27}$$

where P denotes the power and R the resistance of the transmission line. Therefore,

$$A_{\mathrm{p_1}}^2(z)e^{2(i\omega_{\mathrm{p_1}}t-\gamma_{\mathrm{p_1}}z)} + A_{\mathrm{p_2}}^2(z)e^{2(i\omega_{\mathrm{p_2}}t-\gamma_{\mathrm{p_2}}z)} = A_{\mathrm{p}}^2(z)e^{2(i\omega_{\mathrm{p}}t-\gamma_{\mathrm{p}}z)}.$$

This condition can only be met if $A_{\mathrm{p_1}} = A_{\mathrm{p_2}} = A_{\mathrm{p}}/\sqrt{2}$, $\omega_{\mathrm{p_1}} = \omega_{\mathrm{p_2}} = \omega_{\mathrm{p}}$, $\gamma_{\mathrm{p_1}} = \gamma_{\mathrm{p_2}} = \gamma_{\mathrm{p}}$, i.e., $\alpha_{\mathrm{p_1}} = \alpha_{\mathrm{p_2}} = \alpha_{\mathrm{p}}$ and $k_{\mathrm{p_1}} = k_{\mathrm{p_2}} = k_{\mathrm{p}}$. Replacing these values in Eq.2.25, we can rewrite the CMEs as:

$$\begin{aligned} \gamma_{\mathrm{p}}\frac{\partial A_{\mathrm{p}}(z)}{\partial z} = \frac{\beta_{\mathrm{nl}}k_{\mathrm{p}}^2}{8I_*^2}\Bigg[A_{\mathrm{p}}\Big(A_{\mathrm{p}}A_{\mathrm{p}}^*e^{-2\alpha_{\mathrm{p}}z} + 2A_{\mathrm{s}}A_{\mathrm{s}}^*e^{-2\alpha_{\mathrm{s}}z} + 2A_{\mathrm{i}}A_{\mathrm{i}}^*e^{-2\alpha_{\mathrm{i}}z}\Big) \\ + 2A_{\mathrm{p}}^*A_{\mathrm{s}}A_{\mathrm{i}}e^{-(\alpha_{\mathrm{s}}+\alpha_{\mathrm{i}})z}e^{-i\Delta_{\mathrm{k}}z}\Bigg] \end{aligned} \tag{2.28a}$$

$$\begin{aligned} \gamma_{\mathrm{s}}\frac{\partial A_{\mathrm{s}}(z)}{\partial z} = \frac{\beta_{\mathrm{nl}}k_{\mathrm{s}}^2}{8I_*^2}\Bigg[A_{\mathrm{s}}\Big(2A_{\mathrm{p}}A_{\mathrm{p}}^*e^{-2\alpha_{\mathrm{p}}z} + A_{\mathrm{s}}A_{\mathrm{s}}^*e^{-2\alpha_{\mathrm{s}}z} + 2A_{\mathrm{i}}A_{\mathrm{i}}^*e^{-2\alpha_{\mathrm{i}}z}\Big) \\ + A_{\mathrm{p}}^2A_{\mathrm{i}}^*e^{-(2\alpha_{\mathrm{p}}-\alpha_{\mathrm{s}}+\alpha_{\mathrm{i}})z}e^{i\Delta_{\mathrm{k}}z}\Bigg] \end{aligned} \tag{2.28b}$$

$$\begin{aligned} \gamma_{\mathrm{i}}\frac{\partial A_{\mathrm{i}}(z)}{\partial z} = \frac{\beta_{\mathrm{nl}}k_{\mathrm{i}}^2}{8I_*^2}\Bigg[A_{\mathrm{i}}\Big(2A_{\mathrm{p}}A_{\mathrm{p}}^*e^{-2\alpha_{\mathrm{p}}z} + 2A_{\mathrm{s}}A_{\mathrm{s}}^*e^{-2\alpha_{\mathrm{s}}z} + A_{\mathrm{i}}A_{\mathrm{i}}^*e^{-2\alpha_{\mathrm{i}}z}\Big) \\ + A_{\mathrm{p}}^2A_{\mathrm{s}}^*e^{-(2\alpha_{\mathrm{p}}+\alpha_{\mathrm{s}}-\alpha_{\mathrm{i}})z}e^{i\Delta_{\mathrm{k}}z}\Bigg], \end{aligned} \tag{2.28c}$$

where $\Delta_k = 2k_{\mathrm{p}} - k_{\mathrm{s}} - k_{\mathrm{i}}$ and $\Delta_\alpha = 2\alpha_{\mathrm{p}} + \alpha_{\mathrm{s}} + \alpha_{\mathrm{i}}$. This result implies $\eta_{\mathrm{p}_{11}} = 0$ and $\eta_{\mathrm{p}_{22}} = 1$.

DC three-wave mixing (DC3WM)

For the DC3WM case, we replace $\frac{1}{2}A_{\mathrm{p_1}}(z)e^{(i\omega_{\mathrm{p_1}}t-\gamma_{\mathrm{p_1}}z)} = \frac{1}{2}A_{\mathrm{p}}(z)e^{(i\omega_{\mathrm{p}}t-\gamma_{\mathrm{p}}z)}$ and the second pump tone by a DC current, i.e., $|A_{\mathrm{p_2}}(z)| = 2I_{\mathrm{dc}}$. The factor of 2 is added to account for the conjugate of $A_{\mathrm{p_2}}(z)$ ensuring the total energy in the system is conserved. Furthermore, since there is no oscillation of the current in a DC signal, $\gamma_{\mathrm{p_2}} = \omega_{\mathrm{p_2}} = \alpha_{\mathrm{p_2}} = 0$. Hence Eq.2.25 becomes:

$$\gamma_{\mathrm{p}}\frac{\partial A_{\mathrm{p}}(z)}{\partial z} = \frac{\beta_{\mathrm{nl}}k_{\mathrm{p}}^2}{8I_*^2}\Bigg[A_{\mathrm{p}}\Big(A_{\mathrm{p}}A_{\mathrm{p}}^* e^{-2\alpha_{\mathrm{p}}z} + 2A_{\mathrm{s}}A_{\mathrm{s}}^* e^{-2\alpha_{\mathrm{s}}z} + 2A_{\mathrm{i}}A_{\mathrm{i}}^* e^{-2\alpha_{\mathrm{i}}z} + 4I_{\mathrm{dc}}^2\Big) + 4I_{\mathrm{dc}}A_{\mathrm{s}}A_{\mathrm{i}}e^{(2\alpha_{\mathrm{p}}-\Delta_\alpha)z}e^{-i\Delta_k z}\Bigg] \tag{2.29a}$$

$$\gamma_{\mathrm{s}}\frac{\partial A_{\mathrm{s}}(z)}{\partial z} = \frac{\beta_{\mathrm{nl}}k_{\mathrm{s}}^2}{8I_*^2}\Bigg[A_{\mathrm{s}}\Big(2A_{\mathrm{p}}A_{\mathrm{p}}^* e^{-2\alpha_{\mathrm{p}}z} + A_{\mathrm{s}}A_{\mathrm{s}}^* e^{-2\alpha_{\mathrm{s}}z} + 2A_{\mathrm{i}}A_{\mathrm{i}}^* e^{-2\alpha_{\mathrm{i}}z} + 4I_{\mathrm{dc}}^2\Big) + 4I_{\mathrm{dc}}A_{\mathrm{p}}A_{\mathrm{i}}^* e^{(2\alpha_{\mathrm{s}}-\Delta_\alpha)z}e^{i\Delta_k z}\Bigg] \tag{2.29b}$$

$$\gamma_{\mathrm{i}}\frac{\partial A_{\mathrm{i}}(z)}{\partial z} = \frac{\beta_{\mathrm{nl}}k_{\mathrm{i}}^2}{8I_*^2}\Bigg[A_{\mathrm{i}}\Big(2A_{\mathrm{p}}A_{\mathrm{p}}^* e^{-2\alpha_{\mathrm{p}}z} + A_{\mathrm{s}}A_{\mathrm{s}}^* e^{-2\alpha_{\mathrm{s}}z} + 2A_{\mathrm{i}}A_{\mathrm{i}}^* e^{-2\alpha_{\mathrm{i}}z} + 4I_{\mathrm{dc}}^2\Big) + 4I_{\mathrm{dc}}A_{\mathrm{p}}A_{\mathrm{s}}^* e^{(2\alpha_{\mathrm{i}}-\Delta_\alpha)z}e^{i\Delta_k z}\Bigg], \tag{2.29c}$$

where $\Delta_k = k_{\mathrm{p}} - k_{\mathrm{s}} - k_{\mathrm{i}}$ and $\Delta_\alpha = \alpha_{\mathrm{p}} + \alpha_{\mathrm{s}} + \alpha_{\mathrm{i}}$. These expressions imply $\eta_{\mathrm{p}11} = 1$ and $\eta_{\mathrm{p}22} = \frac{1}{2}$. The term $\eta_{\mathrm{p}22} = \frac{1}{2}$ results from the missing interaction in the DC current with its conjugate, i.e., there is no backwards moving wave associated with the DC current, hence the self-phase modulation (more details in Sec. 2.2.3) is half compared with conventional oscillating tones like the pump, signal or idler.

2.2.3 Analytical solution of the CME

Although Eq.2.25 can be directly solved using numerical methods, an analytical solution of the CME can be obtained under certain assumptions. This solution provides a better insight into the physics phenomena occurring in the transmission line, which are essential for the optimal design of a TWPA. In this section, I derive the analytical solution of the CME for the NP4WM regime, although a similar procedure can be applied for the DP4WM and DC3WM using the relevant coefficients for the generalised CME.

Assuming the pump tones are undepleted through the STL, i.e., $\frac{d|A_{\mathrm{p}_1}|}{dz} = \frac{d|A_{\mathrm{p}_2}|}{dz} = 0$ and the their amplitudes are much stronger than the signal and idler wave, i.e., $A_{\mathrm{p}_1}, A_{\mathrm{p}_2} \gg A_{\mathrm{s}}\,\&\,A_{\mathrm{i}}$, the pump equations reduces to

$$\frac{\partial A_{\mathrm{p}_1}(z)}{\partial z} - i\varphi'_{\mathrm{p}_1}A_{\mathrm{p}_1} = 0 \tag{2.30a}$$

$$\frac{\partial A_{\mathrm{p}_2}(z)}{\partial z} - i\varphi'_{\mathrm{p}_2}A_{\mathrm{p}_2} = 0, \tag{2.30b}$$

where

$$\varphi'_{\mathrm{p}_1} = -i\frac{\beta_{\mathrm{nl}}k_{\mathrm{p}_1}^2}{8I_*^2\gamma_{\mathrm{p}_1}}\left[\eta_{\mathrm{p}_{11}}A_{\mathrm{p}_1}A_{\mathrm{p}_1}^* e^{-2\alpha_{\mathrm{p}_1}z} + 2\eta_{\mathrm{p}_{22}}A_{\mathrm{p}_2}A_{\mathrm{p}_2}^* e^{-2\alpha_{\mathrm{p}_2}z}\right]$$
$$\varphi'_{\mathrm{p}_2} = -i\frac{\beta_{\mathrm{nl}}k_{\mathrm{p}_2}^2}{8I_*^2\gamma_{\mathrm{p}_2}}\left[2\eta_{\mathrm{p}_{11}}A_{\mathrm{p}_1}A_{\mathrm{p}_1}^* e^{-2\alpha_{\mathrm{p}_1}z} + \eta_{\mathrm{p}_{22}}A_{\mathrm{p}_2}A_{\mathrm{p}_2}^* e^{-2\alpha_{\mathrm{p}_2}z}\right].$$

The solution of these partial differential equation is in the form of a plane wave $A_{\mathrm{p}_1}(z) = Ce^{i\varphi' z}$, where C is a constant. Using the pump amplitude at $z = 0$ as a boundary condition, we can solve for C, then $A_{\mathrm{p}_1}(0) = C = A_{0,\mathrm{p}_1}$. Hence, the solution for the pump tones are:

$$A_{\mathrm{p}_1}(z) = A_{0,\mathrm{p}_1}e^{i\varphi_{\mathrm{p}_1}z} \tag{2.31a}$$
$$A_{\mathrm{p}_2}(z) = A_{0,\mathrm{p}_2}e^{i\varphi_{\mathrm{p}_2}z}, \tag{2.31b}$$

where

$$\varphi_{\mathrm{p}_1} = -i\frac{\beta_{\mathrm{nl}}k_{\mathrm{p}_1}^2}{8I_*^2\gamma_{\mathrm{p}_1}}(\varphi_{\mathrm{p}_{11}} + 2\varphi_{\mathrm{p}_{22}})$$
$$\varphi_{\mathrm{p}_2} = -i\frac{\beta_{\mathrm{nl}}k_{\mathrm{p}_2}^2}{8I_*^2\gamma_{\mathrm{p}_2}}(2\varphi_{\mathrm{p}_{11}} + \varphi_{\mathrm{p}_{22}})$$
$$\varphi_{\mathrm{p}_{11}} = A_{0,\mathrm{p}_1}A_{0,\mathrm{p}_1}^* e^{-2\alpha_{\mathrm{p}_1}z}$$
$$\varphi_{\mathrm{p}_{22}} = A_{0,\mathrm{p}_2}A_{0,\mathrm{p}_2}^* e^{-2\alpha_{\mathrm{p}_2}z}.$$

Therefore, φ_{p_1} and φ_{p_2} result in a phase-shift known as self-phase modulation (SPM) when resulting from the amplitude of the same pump tone, and cross-phase modulation (XPM) when resulting from the amplitude of the opposite pump tone. By replacing Eqs. 2.31 in the simplified signal equation resulting from the aforementioned assumptions, we obtain:

$$\frac{\partial A_{\mathrm{s}}(z)}{\partial z} = i\varphi_{\mathrm{s}}A_{\mathrm{s}} + i\varphi'_{\mathrm{s}}A_{\mathrm{i}}^* e^{(\alpha_{\mathrm{s}}-\alpha_{\mathrm{i}})z}e^{i(\Delta_k+\varphi_{\mathrm{p}_1}+\varphi_{\mathrm{p}_2})z} \tag{2.32a}$$
$$\frac{\partial A_{\mathrm{i}}(z)}{\partial z} = i\varphi_{\mathrm{i}}A_{\mathrm{i}} + i\varphi'_{\mathrm{i}}A_{\mathrm{s}}^* e^{(-\alpha_{\mathrm{s}}+\alpha_{\mathrm{i}})z}e^{i(\Delta_k+\varphi_{\mathrm{p}_1}+\varphi_{\mathrm{p}_2})z}, \tag{2.32b}$$

where

$$\varphi_{\mathrm{s}} = -i\frac{\beta_{\mathrm{nl}}k_{\mathrm{s}}^2}{4I_*^2\gamma_{\mathrm{s}}}(\varphi_{\mathrm{p}_{11}} + \varphi_{\mathrm{p}_{22}}), \quad \varphi'_{\mathrm{s}} = -i\frac{\beta_{\mathrm{nl}}k_{\mathrm{s}}^2}{4I_*^2\gamma_{\mathrm{s}}}\varphi_{\mathrm{p}_{12}},$$
$$\varphi_{\mathrm{i}} = -i\frac{\beta_{\mathrm{nl}}k_{\mathrm{i}}^2}{4I_*^2\gamma_{\mathrm{i}}}(\varphi_{\mathrm{p}_{11}} + \varphi_{\mathrm{p}_{22}}), \quad \varphi'_{\mathrm{i}} = -i\frac{\beta_{\mathrm{nl}}k_{\mathrm{i}}^2}{4I_*^2\gamma_{\mathrm{i}}}\varphi_{\mathrm{p}_{12}},$$
$$\varphi_{\mathrm{p}_{12}} = A_{0,\mathrm{p}_1}A_{0,\mathrm{p}_2}^* e^{-(\alpha_{\mathrm{p}_1}+\alpha_{\mathrm{p}_2})z}.$$

Hence, φ_{s} and φ_{i} act upon the XPM that the two pump tones apply to the signal and idler. Assuming the solution for the above coupled-mode equations in the form

of $A_{\mathrm{s}}(z) = a_{\mathrm{s}}(z)e^{i\varphi_{\mathrm{s}}z}$ and $A_{\mathrm{i}}(z) = a_{\mathrm{i}}(z)e^{i\varphi_{\mathrm{i}}z}$, replacing the Eqs. 2.32, we obtain:

$$\frac{\partial a_{\mathrm{s}}(z)}{\partial z} - i\kappa_{\mathrm{s}} a_{\mathrm{i}}^{*}(z)e^{i\Delta_{\phi}z} = 0 \tag{2.33a}$$

$$\frac{\partial a_{\mathrm{i}}(z)}{\partial z} - i\kappa_{\mathrm{i}} a_{\mathrm{s}}^{*}(z)e^{i\Delta_{\phi}z} = 0, \tag{2.33b}$$

where

$$\kappa_{\mathrm{s}} = \varphi_{\mathrm{s}}' e^{(\alpha_{\mathrm{s}}-\alpha_{\mathrm{i}})z}, \quad \kappa_{\mathrm{i}} = \varphi_{\mathrm{i}}' e^{(-\alpha_{\mathrm{s}}+\alpha_{\mathrm{i}})z},$$

$$\Delta_{\phi} = \Delta_k + \Delta_{\varphi} = k_{\mathrm{p}_1} + k_{\mathrm{p}_2} - k_{\mathrm{s}} - k_{\mathrm{i}} + \varphi_{\mathrm{p}_1} + \varphi_{\mathrm{p}_2} - \varphi_{\mathrm{s}} - \varphi_{\mathrm{i}}.$$

We shall refer Δ_{ϕ} as the total phase-mismatch, formed by the linear phase-mismatch term Δ_k, and a nonlinear term Δ_{φ} gathering the effects of SPM and XPM from the different frequency tones. Following the methods described in [102], we arrive at the solutions for the signal and idler:

$$a_{\mathrm{s}}(z) = \left\{ \left[\cosh(gz) - \frac{i\Delta_{\phi}}{2g} \sinh(gz) \right] a_{\mathrm{s}}(0) + \left[\frac{i\kappa_{\mathrm{s}}}{g} \sinh(gz) \right] a_{\mathrm{i}}(0) \right\} e^{i\Delta_{\phi}z/2} \tag{2.34a}$$

$$a_{\mathrm{i}}(z) = \left\{ \left[\cosh(gz) - \frac{i\Delta_{\phi}}{2g} \sinh(gz) \right] a_{\mathrm{i}}(0) + \left[\frac{i\kappa_{\mathrm{s}}}{g} \sinh(gz) \right] a_{\mathrm{s}}(0) \right\} e^{i\Delta_{\phi}z/2}, \tag{2.34b}$$

where $g = \sqrt{\kappa_{\mathrm{s}}\kappa_{\mathrm{i}} - \frac{\Delta_{\phi}^2}{4}}$ is the gain coefficient. Defining the signal gain as:

$$G_{\mathrm{s}} = \frac{|A_{\mathrm{s}}(z)|^2}{|A_{\mathrm{s}}(0)|^2} = \frac{|a_{\mathrm{s}}(z)|^2}{|a_{\mathrm{s}}(0)|^2}, \tag{2.35}$$

since $a_{\mathrm{i}}(0) = 0$ and the complex exponential cancel with the modulus signs, we find

$$G_{\mathrm{s}}(z) = \left| \cosh(gz) - \frac{i\Delta_{\phi}}{2g} \sinh(gz) \right|^2. \tag{2.36}$$

From this expression, we notice that G_{s} is maximised when g is maximised, i.e., when $\Delta_{\phi} = 0$. This is known as the phase-matching condition, which implies that momentum is preserved in the STL, therefore, optimising the mixing processes to maximise the signal gain[9].

The same approach can be followed for the DP4WM and DC3WM using the right coefficients in Eq. 2.25. By doing so, we will arrive at the same expression of the signal gain, where the resulting coefficients are summarised in Tab. 2.2

[9]Refer to the analogy of the skater in a half-pipe in Chapter 1, Δ_{ϕ} describes how well the signals are synchronised.

	NP4WM	DP4WM	DC3WM
$A_{\mathrm{p}_1}(z)$	$A_{0,\mathrm{p}_1}e^{i\varphi_{\mathrm{p}_1}z}$	$A_{0,\mathrm{p}}e^{i\varphi_{\mathrm{p}}z}$	$A_{0,\mathrm{p}}e^{i\varphi_{\mathrm{p}}z}$
$A_{\mathrm{p}_2}(z)$	$A_{0,\mathrm{p}_2}e^{i\varphi_{\mathrm{p}_2}z}$		
φ_{p_1}	$-i\frac{\beta_{\mathrm{nl}}k_{\mathrm{p}_1}^2}{8I_*^2\gamma_{\mathrm{p}_1}}(\varphi_{\mathrm{p}_{11}}+2\varphi_{\mathrm{p}_{22}})$	$\varphi_{\mathrm{p}}=-i\frac{\beta_{\mathrm{nl}}k_{\mathrm{p}}^2}{8I_*^2\gamma_{\mathrm{p}}}(2\varphi_{\mathrm{pp}})$	$\varphi_{\mathrm{p}}=-i\frac{\beta_{\mathrm{nl}}k_{\mathrm{p}}^2}{8I_*^2\gamma_{\mathrm{p}}}(\varphi_{\mathrm{pp}}+2\varphi_{\mathrm{dc}})$
φ_{p_2}	$-i\frac{\beta_{\mathrm{nl}}k_{\mathrm{p}_2}^2}{8I_*^2\gamma_{\mathrm{p}_2}}(2\varphi_{\mathrm{p}_{11}}+\varphi_{\mathrm{p}_{22}})$		
$\varphi_{\mathrm{p}_{11}}$	$\eta_{\mathrm{p}_{11}}A_{0,\mathrm{p}_1}A_{0,\mathrm{p}_1}^*e^{-2\alpha_{\mathrm{p}_1}z}$		$\varphi_{\mathrm{pp}}=A_{0,\mathrm{p}}A_{0,\mathrm{p}}^*e^{-2\alpha_{\mathrm{p}}z}$
$\varphi_{\mathrm{p}_{22}}$	$\eta_{\mathrm{p}_{22}}A_{0,\mathrm{p}_2}A_{0,\mathrm{p}_2}^*e^{-2\alpha_{\mathrm{p}_2}z}$	$\varphi_{\mathrm{pp}}=\frac{\lvert A_{0,\mathrm{p}}\rvert^2}{2}e^{-2\alpha_{\mathrm{p}}z}$	$\varphi_{\mathrm{dc}}=2I_{\mathrm{dc}}^2$
$\varphi_{\mathrm{p}_{12}}$	$A_{0,\mathrm{p}_1}A_{0,\mathrm{p}_2}^*e^{-(\alpha_{\mathrm{p}_1}+\alpha_{\mathrm{p}_2})z}$		$\varphi_{\mathrm{p,dc}}=2I_{\mathrm{dc}}A_{0,\mathrm{p}}e^{-\alpha_{\mathrm{p}}z}$
$\eta_{\mathrm{p}_{11}}$	1	0	1
$\eta_{\mathrm{p}_{22}}$	1	1	1/2
κ_{s}	$\varphi_s'e^{(\alpha_{\mathrm{s}}-\alpha_{\mathrm{i}})z}$	$\varphi_s'e^{(\alpha_{\mathrm{s}}-\alpha_{\mathrm{i}})z}$	$\varphi_s'e^{(\alpha_{\mathrm{s}}-\alpha_{\mathrm{i}})z}$
κ_{i}	$\varphi_i'e^{(-\alpha_{\mathrm{s}}+\alpha_{\mathrm{i}})z}$	$\varphi_i'e^{(-\alpha_{\mathrm{s}}+\alpha_{\mathrm{i}})z}$	$\varphi_i'e^{(-\alpha_{\mathrm{s}}+\alpha_{\mathrm{i}})z}$
φ_{s}'	$-i\frac{\beta_{\mathrm{nl}}k_{\mathrm{s}}^2}{4I_*^2\gamma_{\mathrm{s}}}\varphi_{\mathrm{p}_{12}}$	$\frac{\varphi_{\mathrm{s}}}{2}$	$-i\frac{\beta_{\mathrm{nl}}k_{\mathrm{s}}^2}{4I_*^2\gamma_{\mathrm{s}}}\varphi_{\mathrm{p,dc}}$
φ_{i}'	$-i\frac{\beta_{\mathrm{nl}}k_{\mathrm{i}}^2}{4I_*^2\gamma_{\mathrm{i}}}\varphi_{\mathrm{p}_{12}}$	$\frac{\varphi_{\mathrm{i}}}{2}$	$-i\frac{\beta_{\mathrm{nl}}k_{\mathrm{i}}^2}{4I_*^2\gamma_{\mathrm{i}}}\varphi_{\mathrm{p,dc}}$
φ_{s}	$-i\frac{\beta_{\mathrm{nl}}k_{\mathrm{s}}^2}{4I_*^2\gamma_{\mathrm{s}}}(\varphi_{\mathrm{p}_{11}}+\varphi_{\mathrm{p}_{22}})$	$-i\frac{\beta_{\mathrm{nl}}k_{\mathrm{s}}^2}{4I_*^2\gamma_{\mathrm{s}}}(2\varphi_{\mathrm{pp}})$	$-i\frac{\beta_{\mathrm{nl}}k_{\mathrm{s}}^2}{4I_*^2\gamma_{\mathrm{s}}}(\varphi_{\mathrm{pp}}+\varphi_{\mathrm{dc}})$
φ_{i}	$-i\frac{\beta_{\mathrm{nl}}k_{\mathrm{i}}^2}{4I_*^2\gamma_{\mathrm{i}}}(\varphi_{\mathrm{p}_{11}}+\varphi_{\mathrm{p}_{22}})$	$-i\frac{\beta_{\mathrm{nl}}k_{\mathrm{i}}^2}{4I_*^2\gamma_{\mathrm{i}}}(2\varphi_{\mathrm{pp}})$	$-i\frac{\beta_{\mathrm{nl}}k_{\mathrm{i}}^2}{4I_*^2\gamma_{\mathrm{i}}}(\varphi_{\mathrm{pp}}+\varphi_{\mathrm{dc}})$
Δ_ϕ	$\Delta_k+\Delta_\varphi$	$\Delta_k+\Delta_\varphi$	$\Delta_k+\Delta_\varphi$
Δ_k	$k_{\mathrm{p}_1}+k_{\mathrm{p}_2}-k_{\mathrm{s}}-k_{\mathrm{i}}$	$2k_{\mathrm{p}}-k_{\mathrm{s}}-k_{\mathrm{i}}$	$k_{\mathrm{p}}-k_{\mathrm{s}}-k_{\mathrm{i}}$
Δ_φ	$\varphi_{\mathrm{p}_1}+\varphi_{\mathrm{p}_2}-\varphi_{\mathrm{s}}-\varphi_{\mathrm{i}}$	$2\varphi_{\mathrm{p}}-\varphi_{\mathrm{s}}-\varphi_{\mathrm{i}}$	$\varphi_{\mathrm{p}}-\varphi_{\mathrm{s}}-\varphi_{\mathrm{i}}$
Δ_α	$\alpha_{\mathrm{p}_1}+\alpha_{\mathrm{p}_2}+\alpha_{\mathrm{s}}+\alpha_{\mathrm{i}}$	$2\alpha_{\mathrm{p}}+\alpha_{\mathrm{s}}+\alpha_{\mathrm{i}}$	$\alpha_{\mathrm{p}}+\alpha_{\mathrm{s}}+\alpha_{\mathrm{i}}$

Table 2.2: Coefficients of CME for the non-degenerated pump 4-wave mixing (NP4WM), degenerated pump 4-wave mixing (DP4WM) and the DC-bias 3-wave mixing (DC3WM) regimes of any TWPA with spatial centrosymmetry.

2.2.4 Dispersion engineering

The above shows the need for $\Delta_\phi = 0$ to maximise the gain. However, any transmission line operated far from its cutoff frequency[10], as for the case of a TWPA, is weakly dispersive, i.e., $\Delta_k \approx 0$. Therefore, in practice the condition cannot be met without extra engineering features. This effort of introducing extra circuit elements to the native STL to satisfy the $\Delta_\phi = 0$ condition is called dispersion engineering, which corrects for the phase-matching condition to achieve exponential gain.

Gain expression for $\Delta_k = 0$ and $\Delta_\phi = 0$ in lossless DP4WM

Linear dispersion case ($\Delta_k = 0$)

In the linear dispersion regime $\Delta_k = 0$, therefore $\Delta_\phi = -2\varphi_\mathrm{p}$ and $g = i\varphi_\mathrm{p}\left|1 - \frac{k_\mathrm{s}}{k_\mathrm{p}}\right| = i\varphi_\mathrm{p}\left|1 - \frac{\omega_\mathrm{s}}{\omega_\mathrm{p}}\right|$. Replacing in Eq. 2.36 and simplifying using $\sinh(ix) = i\sinh(x)$, we find:

$$G_\mathrm{s}(\omega_\mathrm{s}) = 1 + \left(\frac{1}{\left|1 - \frac{\omega_\mathrm{s}}{\omega_\mathrm{p}}\right|^2} - 1\right) \sin\left(\left|1 - \frac{\omega_\mathrm{s}}{\omega_\mathrm{p}}\right| z\varphi_\mathrm{p}\right). \tag{2.37}$$

When the signal frequency approaches ω_p, we can write:

$$\lim_{\omega_s \to \omega_p} G_s(\omega_s) \approx 1 + (z\varphi_\mathrm{p})^2. \tag{2.38}$$

Therefore, in the linear-dispersion case, the gain follows a quadratic growth with length z and input power of the pump, since $\varphi_\mathrm{p} \propto |A_\mathrm{p}|^2$.

Phase-matched case ($\Delta_\phi = 0$)

If we assume a perfect phase-match between all the tones propagating in the STL, $\Delta_\phi = 0$, then $g = \varphi_\mathrm{p}\sqrt{\frac{\omega_\mathrm{s}\omega_\mathrm{i}}{\omega_\mathrm{p}}}$, and we can rewrite Eq. 2.36 as:

$$G_\mathrm{s}(\omega_\mathrm{s}) = 1 + \sinh^2\left(\sqrt{\frac{\omega_\mathrm{s}\omega_\mathrm{i}}{\omega_\mathrm{p}^2}} z\varphi_\mathrm{p}\right) \tag{2.39}$$

When the signal frequency approaches ω_p,

$$\lim_{\omega_s \to \omega_p} G_s(\omega_s) = 1 + \sinh^2(z\varphi_\mathrm{p}) \approx 1 + \frac{e^{2z\varphi_\mathrm{p}}}{4} \tag{2.40}$$

Therefore, assuming a perfect phase-match between all the tones propagating in the line, G_s grows exponentially with length and input pump power.

[10]The cutoff frequency is defined as $f_0 = 1/2\pi\sqrt{LC}$.

Furthermore, the nonlinear STL generates harmonics of the pump as well as other unwanted intermodulation products at a combination of multiples of ω_p and ω_s, stealing energy from the pump which weaken the energy conversion into the weak signal for amplification. In JTWPAs, these higher harmonics are often suppressed with the plasma frequency of the junctions[11]. However, intermodulation products generation can be problematic for JTWPAs made of $\chi^{(2)}$ nonlinear STLs [82]. Similarly, high harmonics generation are problematic for KTWPAs, which do not naturally have the low-frequency cutoff from the junctions. To alleviate these issues, the dispersion relation of the STL can be locally altered using dispersion engineering techniques. Here, I will introduce the two most commonly used dispersion engineering techniques: the resonant phase-matching (RPM) and periodic loading modulation.

2.2.4.1 Resonant phase matching (RPM)

The resonant phase-matching (RPM) technique was first introduced by O'Brien et al. [103] to ensure $\Delta_\phi = 0$ in JTWPAs operated in the 4WM regime, but it can be extended to other operational regimes. This technique consists of adding numerous identical LC resonators shunted to the ground in the STL, as illustrated in Fig. 2.9(a). Fig. 2.9(b), shows the example of a JTWPA's dispersion relation with (red) and without (black) RPM. Near the resonators' frequency f_r, the dispersion diverges exponentially relative to the STL, creating a mean for a local modification of the dispersion curve. Assuming operation in the DP4WM regime for simplicity, by carefully placing the pump frequency below f_r, the pump wavevector k_p is increased by a factor δk_p without affecting k_s and k_i, therefore,

$$\Delta_\phi = \Delta_k + \delta_{k_\mathrm{p}} + \Delta_\varphi. \tag{2.41}$$

Hence, by carefully choosing f_p so that $\delta_{k_\mathrm{p}} = -(\Delta_k + \Delta_\varphi)$, we ensure that $\Delta_\phi \simeq 0$ at the widest frequency range, as shown in Fig. 2.9(c). This effect can be understood as adding some extra linear dispersion to compensate for the nonlinear dispersion, ensuring momentum conservation along the line.

As noticed in Fig. 2.9(b), the JTWPA dispersion is linear at low frequencies, and diverges from the linear case the closer it gets to the cutoff frequency, dominated by the plasma frequency of the junctions $\omega_\mathrm{j} = 1/\sqrt{LC_\mathrm{j}} = 2\pi \times 27.7\,\mathrm{GHz}$. This natural dispersion of the line results in the Δ_ϕ shape observed in Fig. 2.9(c), where only frequencies close to f_p lead to $\Delta_\phi \approx 0$. Since only frequency tones satisfying

[11] The cutoff frequency of the junctions, defined as $\omega_\mathrm{j} = 1/\sqrt{L_0 C_\mathrm{j}}$

$\Delta_\phi \approx 0$ are efficiently generated, the strong dispersion resulting from the plasma frequency of the junctions limits the generation of high harmonics of the pump and other unwanted parametric processes, at the expense of reducing the bandwidth of the device. Fig. 2.9(d) shows the substantial gain and bandwidth enhancement resulting from the implementation of the RPM technique.

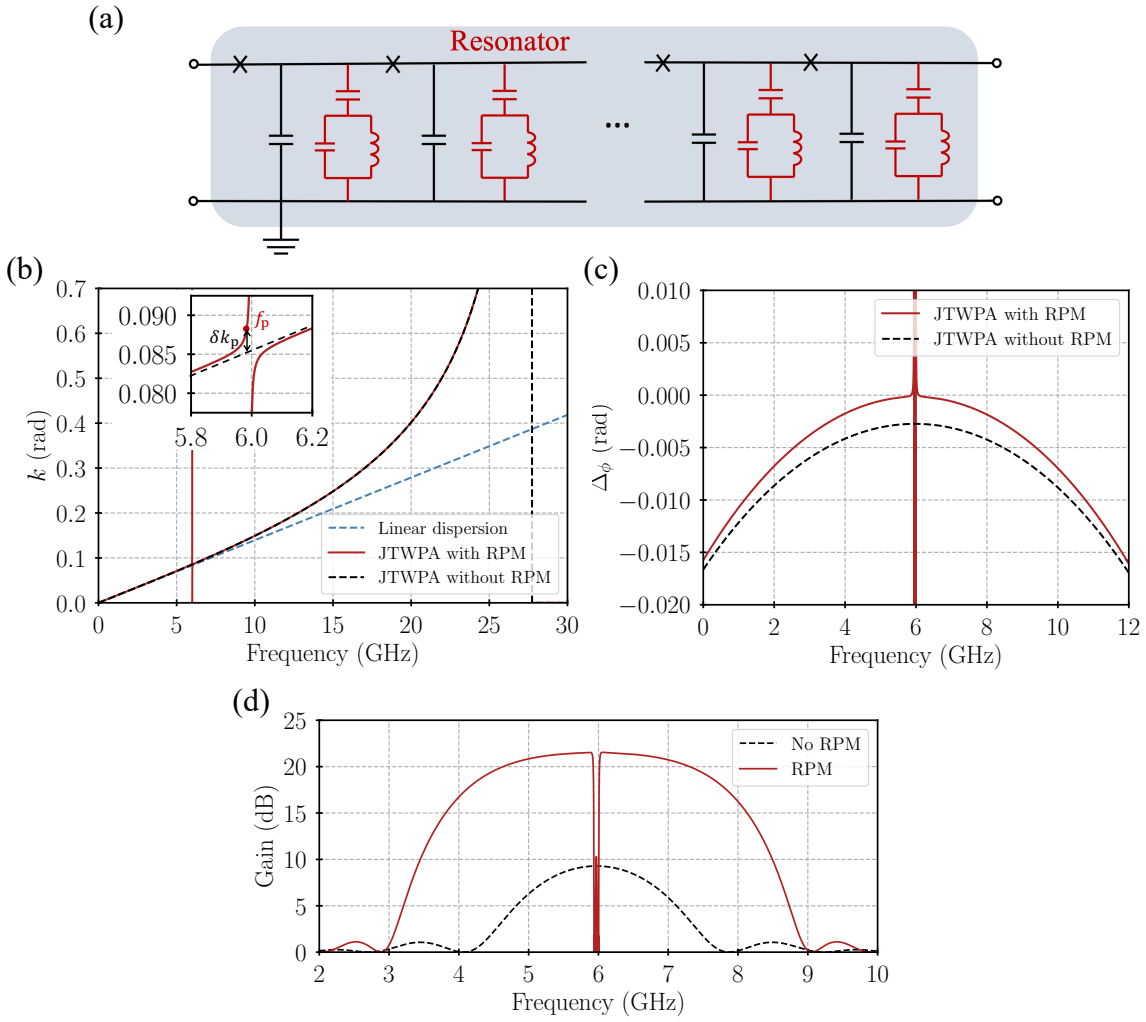

Figure 2.9: (a) Circuit diagram of a JTWPA with RPM. (b) Dispersion per unit cell, (c) phase-mismatch, and (d) gain, calculated using the analytical expression of the CME, for a JTWPA with (red) and without (black) RPM. In (b) the linear dispersion curve (blue) is added for reference and the inset shows the region around the resonator's frequency.

2.2.4.2 Periodic loading

A local modification of the dispersion relation can also be introduced by periodically changing the impedance of the line; a technique known as periodic loading. Two main

periodic loading designs have been successfully demonstrated for TWPAs so far.

Step impedance modulation

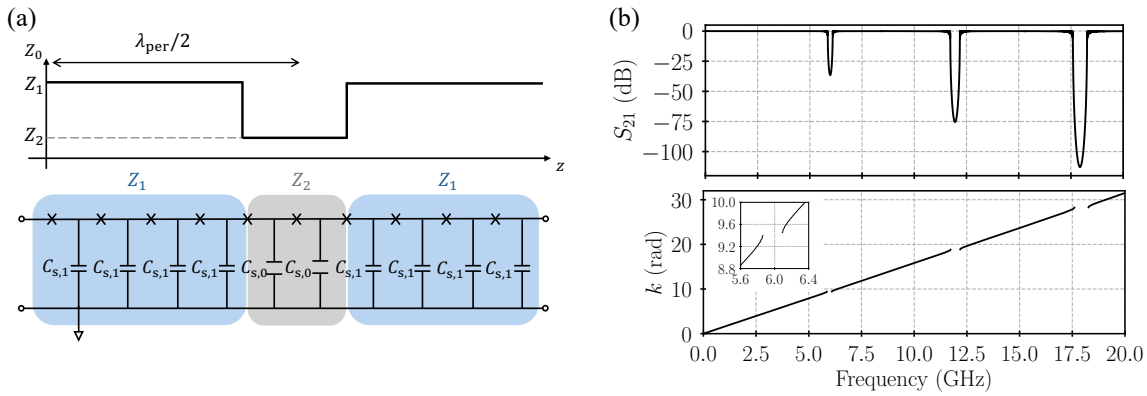

Figure 2.10: Step impedance modulation. (a) Characteristic impedance as a function of distance in a JTWPA supercell (top) and circuit diagram of a JTWPA supercell (bottom). (b) Transmission (top) and dispersion (bottom) curves for an STL with $Z_1 = 50\,\Omega$ and $Z_2 = 80\,\Omega$, and a loading sections length of $l_2 = 0.04 \times \lambda_{per}/2$, corresponding to $f_{per} = 6\,\text{GHz}$.

Let us assume a generic TWPA transmission line with characteristic impedance $Z_0 = Z_1$. Introducing short sections with $Z_0 = Z_2$ periodically at $\lambda_{per}/2$ (loading sections), it would result in a stopband formation in the transmission of the line. The line segment — including the loading section — that is repeated to form the TWPA, is known as the supercell. The supercell of a JTWPA with step impedance modulation, and the resulting transmission and dispersion are shown in Fig. 2.10(a) and (b) respectively. The stopbands form at multiples of $f_{per} = \lambda_{per} v$, where v is the phase velocity in the TWPA. As shown in the inset plot in Fig. 2.10(b), the dispersion exponentially diverges around these stopbands.

The impedance of the loading section is often altered by modifying the shunt capacitance, although in a JTWPA, the junctions' inductance can be equally altered for this purpose. Periodic loading is often used for KTWPAs, where the cutoff frequency of the line is very high ($> 100\,\text{GHz}$) and the pump harmonics can be efficiently generated. Therefore, by carefully choosing the value of f_p, the pump harmonics can fall in the stopband at multiples of f_{per} and therefore be suppressed [73].

Sinusoidal impedance modulation

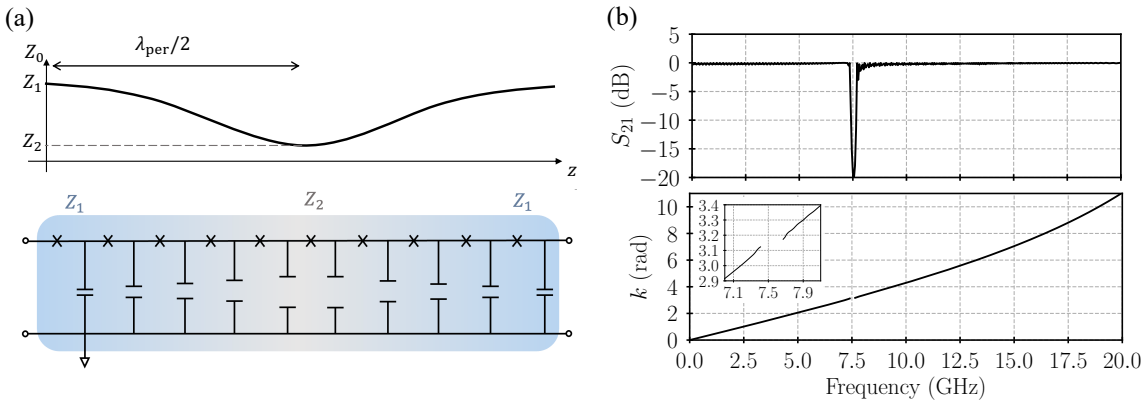

Figure 2.11: Smooth sinusoidal impedance modulation. (a) Characteristic impedance as a function of distance in a JTWPA supercell (top) and circuit diagram of a JTWPA supercell (bottom). (b) Example of the transmission and dispersion curves for a smooth sinusoidal impedance modulation. Inset: zoom-in plot around the stopband.

Another common impedance modulation technique involves varying the impedance sinusoidally along the transmission line, known as sinusoidal impedance modulation. The supercell of a JTWPA implementing this method is shown in Fig. 2.11(a), where $Z_0 \propto \cos(z)$ with z representing the position along the line. Although the modulation is demonstrated using the shunt capacitance, a similar effect can be achieved by modulating the inductance of the junctions. Compared to the step impedance modulation technique, this approach generates a single stopband at $f_{\mathrm{per}} = \lambda_{\mathrm{per}} v$, where λ_{per} is the period of the sinusoidal modulation, as shown in Fig. 2.11(b). As a result, the sinusoidal modulation technique is commonly used in TWPAs that do not require additional stopbands to suppress higher harmonics and intermodulation products [80], among other applications.

2.3 Conclusion

In this chapter, I have described the basic theoretical principles of the nonlinear inductance expressions of kinetic inductance, Josephson junctions and DC-SQUIDs needed for TWPAs. These inductances have a quadratic dependence on the current — which can be generalised under the same expression — suggesting that it can be used for all $\chi^{(3)}$ nonlinear materials with spatial centrosymmetry. Therefore, using transmission line theory, I derive a generalised CME framework describing the propagation of waves in such a material, with different wave-mixing regimes. This derivation unveils the

effect of different physical mechanisms at the origin of gain in a TWPA, highlighting the importance of the phase-matching $\Delta_\phi = 0$ for optimal amplification.

Despite the CME framework derived in this chapter only includes $\chi^{(3)}$ nonlinear materials, it can potentially be extended to $\chi^{(2)}$ materials as well, such as transmission lines formed with RF-SQUIDs and SNAILS. This would require a new generalised expression of the nonlinear inductance for $\chi^{(3)}$ and $\chi^{(2)}$ materials. Then, the same steps presented in this chapter could be followed to re-derive the framework.

Chapter 3

JTWPA modelling techniques and designs

The CME framework introduced in the previous chapter gives a mathematical description of TWPAs' performance from the circuit parameters of the transmission line. Although it allows for simulating both KTWPAs and JTWPAs, for this thesis, I will focus mainly on the latter case. In this chapter, I discuss the different JTWPA design techniques. I first validate the framework by comparing it with other CME approaches and reproducing the experimental data of a SQUID-based JTWPAs. Then, I use the framework to investigate the JTWPA circuit parameters space and their impact on the figures of merit of the amplifier, focusing only on JTWPAs formed with bare junctions, i.e., not with RF-SQUIDs or SNAILs. Finally, I introduce a novel modelling technique combining electromagnetic simulations and the CME framework to predict the performance from the physical layout of a JTWPA. I conclude the chapter by presenting four optimised JTWPA designs modelled using this technique.

3.1 JTWPA performance from circuit model

JTWPAs are formed by cascading a series of unit cells comprising one or more Josephson-based components into a long nonlinear STL. In this thesis, we focus only on the development of JTWPA with bare junctions. The junctions in a JTWPA can be represented with the modified RCSJ model presented in Sec. 2.1.2, as shown in Fig. 3.1. The main parameters in the unit cell circuit are the shunt capacitance to the ground C_s, the junction inductance L_j and capacitance C_j, and the unit cell length a. The parameters of the unit cell can be periodically modified to create a periodic loading structure, or resonators can be added to the line for RPM. In this section,

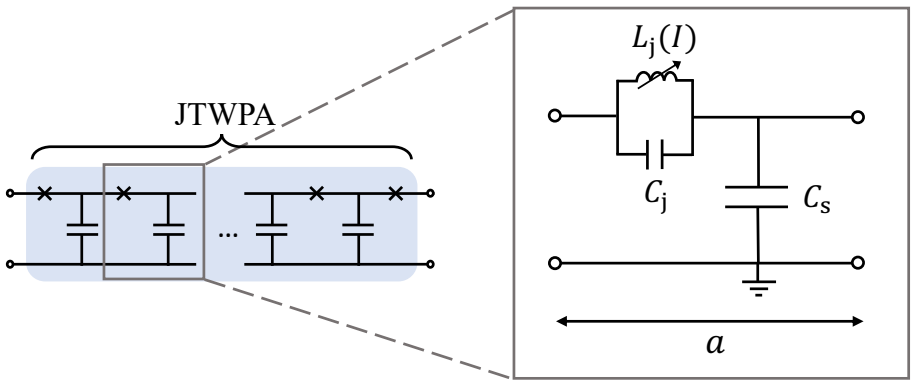

Figure 3.1: Circuit model of a JTWPA unit cell.

I will discuss different existing techniques to simulate the performance of a JTWPA using these unit cell circuit parameters.

3.1.1 Coupled-Mode Equations (CME) frameworks

CMEs are a fast and accurate technique to calculate the performance of JTWPAs. The first CME framework for JTWPAs was introduced by O. Yaakobi et al. [104] and further extended for the specific case of RPM JTWPAs by O'Brian et al. [103]. This model was derived for a particular unit cell design, and therefore, the unit cell's circuit parameters are tightly integrated in the formulation of the CME. With a specific set of the unit cell parameters values, the CME can be solved to predict the gain-bandwidth performance of the JTWPA. Similarly, L. Planat et al. [80] derived the CME for a SQUID-based JTWPA with sinusoidal impedance modulation. This framework was also constructed from first principle for this particular unit cell design. Both models show good agreements with experimental data [79, 80], however, their application is rigidly limited only to the JTWPA designs using the same unit cell as the model was constructed for, requiring a major effort to reconstruct the models from scratch for an even slightly different unit cell topology, e.g., two junctions instead of one coupled with two resonators. Hereafter, we shall refer to these frameworks as conventional CME frameworks.

On the other hand, Eom et al. [73] developed a similar CME framework for their KTWPA, which had the potential to be more flexible to include different design topologies. Although technically flexible, it was never been reconstructed to include other TWPA variants except KTWPA. Therefore, the CME framework described in the previous chapter attempted and successfully extended the CME framework to

include JTWPAs with spatial centrosymmetry, allowing us to get access to the flexibility to design a wide range of JTWPAs that are not constrained to a particular unit cell topology. This is important as it allows to explore a wide range of designs easily and rapidly using the same framework, without the need to reconstruct the CME every time we wish to explore a potential design. From Eq.,2.36, one notices that G_s depends only on the attenuation constant α_n and the wavevector k_m, in addition to operational parameters such as pump amplitude and frequency. These two parameters are grouped in the propagation constant $\gamma_\mathrm{m} = \alpha_\mathrm{m} + ik_\mathrm{m}$, which is intrinsic to the JTWPA design. Therefore, γ_m is the only information required from the STL to solve the CME equations and obtain the JTWPA performance. The γ_m of the STL can be calculated using different techniques that I shall summarise here.

γ_m assuming translation symmetry

A two-port network, such as the unit cell of a JTWPA, can be described with an `ABCD` matrix [100], which relates the input and output current and voltages,

$$\begin{pmatrix} V_\mathrm{out} \\ I_\mathrm{out} \end{pmatrix} = \begin{pmatrix} A & B \\ C & D \end{pmatrix} \begin{pmatrix} V_\mathrm{in} \\ I_\mathrm{in} \end{pmatrix}. \tag{3.1}$$

Assuming translation symmetry in the input and output voltages of a single unit cell, and considering that for reciprocal networks $AD - BC = 1$, the wavevector k can be written as

$$ka = \cos^{-1}\left(\frac{A+D}{2}\right). \tag{3.2}$$

Considering a lossless line where $\gamma_\mathrm{m} = ik_\mathrm{m}$, this expression is sufficient to solve the CMEs.

γ_m cascading `ABCD` matrices

When losses in the transmission line need to be included a better approach consists of cascading the `ABCD` matrix of the unit cell to form the `ABCD` matrix of the entire device,

$$\begin{pmatrix} A & B \\ C & D \end{pmatrix}_\mathrm{JTWPA} = \begin{pmatrix} A & B \\ C & D \end{pmatrix}^N_\mathrm{unit\ cell}, \tag{3.3}$$

where N is the number of unit cells in the JTWPA. This approach also allows to model periodic modulations on the unit cell parameters, by using a distinct `ABCD` matrix for

each variation and multiplying them together to obtain the final ABCD matrix of the device. Then, the scattering parameter S_{21} of the device can be obtained from the ABCD matrix elements of the device as,

$$S_{21} = \frac{2}{A + B/Z + CZ + D}, \tag{3.4}$$

where Z is the characteristic impedance of the line. The attenuation constant α can be calculated from the S_{21} as:

$$\alpha = -\frac{|S_{21}|}{Na}, \tag{3.5}$$

where $|S_{21}|$ is given in linear units, and the wavevector,

$$k = -\frac{\text{unwrap}(\angle \text{S}_{21})}{Na}, \tag{3.6}$$

where $\angle S_{21}$ is the phase of the complex number S_{21}. This approach allows to capture complex behaviours resulting from the cascade of numerous unit cells, especially around the stopbands, having a non-negligeable impact in the JTWPA performance. The ABCD matrix of commonly used circuits is given in [100], therefore, knowing the circuit parameters of the unit cell, we can calculate the ABCD matrix of the entire JTWPA and extract the γ_{m} needed to solve the CMEs.

3.1.2 Harmonic balance (HB) and other techniques

Harmonic Balance (HB) is a popular technique for the signal analysis of nonlinear microwave circuits with steady-state responses. A sinusoidal signal applied to a nonlinear system will generate harmonic components of the fundamental frequency. The HB technique assumes that the voltage and current solution of the system can be written as a linear combination of the input signal harmonics. Then, an iterative process is followed to adjust the voltage and current amplitudes and phases (in the frequency domain) at each harmonic until Kirchhoff's current low is satisfied at every point in the circuit. For more details on the HB technique and algorithms, I refer the reader to [105]. Current commercial circuit simulator's softwares, such as Keysight ADS®, incorporate optimised algorithms for HB simulation. This software has been used to simulate KTWPAs [106], and JTWPAs using rather complex circuit implementations and techniques [107, 108]. In this section, I will introduce a simpler method to model JTWPAs using the HB feature available in Keysight ADS®.

To demonstrate the validity of this technique, I make use of the DP4WM theoretical JTWPA design presented by O'Brien et al. [103] as an example. We start

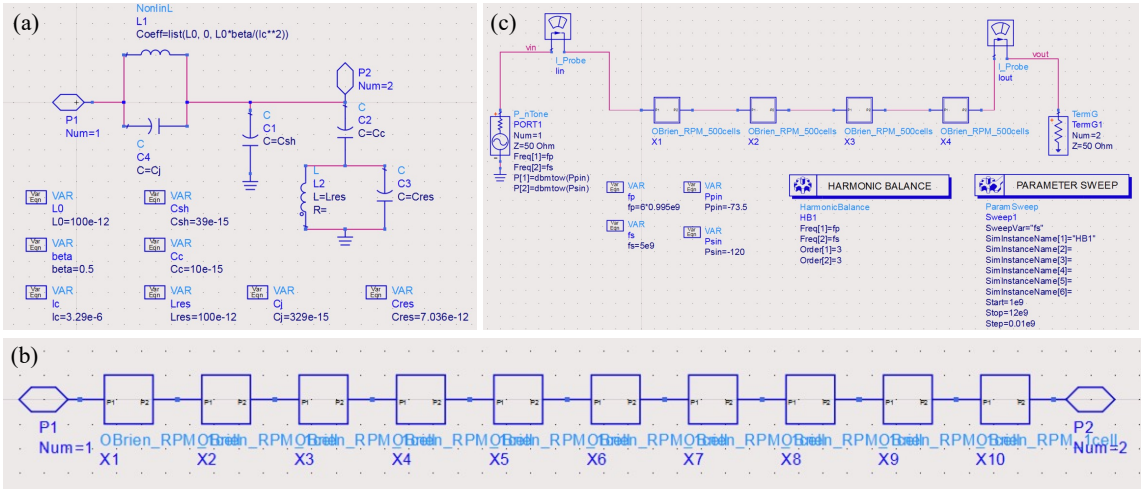

Figure 3.2: Harmonic balance implementation in Keysight ADS®. (a) Circuit model of the JTWPA unit cell. (b) Two-port network of the JTWPA unit cell cascaded 10 times to create another two-port network with 10× JTWPA unit cells. (c) Set up used for the HB simulation. The four squared circuit elements in centre of the image represent 500× unit cells each, modelling the entire JTWPA.

by implementing the unit cell's circuit in Keysight ADS® using standard circuit elements available from the build-in libraries of the software, as shown in Fig. 3.2(a). The junction inductance is modelled with a nonlinear inductor, where the nonlinear coefficients are chosen to satisfy Eq. 2.7. We define a variable for each circuit parameter, e.g., C_s, C_j and L_0. Next, we create a two-port network representation of the unit cell (Edit > Component > Create Hierarchy) that can be easily cascaded 2,000 times to create the JTWPA model. To facilitate the task, we can create two-port networks of any number of cascaded unit cells, so we do not need to manually connect 2,000 circuit elements together. An example of ten unit cell two-port networks cascaded together is shown in Fig. 3.2(b). Since all the cascaded elements are linked with the unit cell circuit, any modification of the unit cell circuit file will automatically update every cascaded element.

Once we have the 2,000 cascaded elements, we need to add some additional components to run the HB simulation, as shown in Fig. 3.2(c). First, we add a 'P_nTone' port at the input of the JTWPA, setting two frequency tones f_s and f_p with power values $P_\mathrm{s,in}$ and $P_\mathrm{p,in}$ respectively. This port is immediately followed by a current probe 'I_probe' and we label the wire connecting the port and the probe, which will allow us to access the input voltage and current value (V_in and I_in) in the simulation. Similarly, we add a current probe and a 50 Ω termination at the output of the

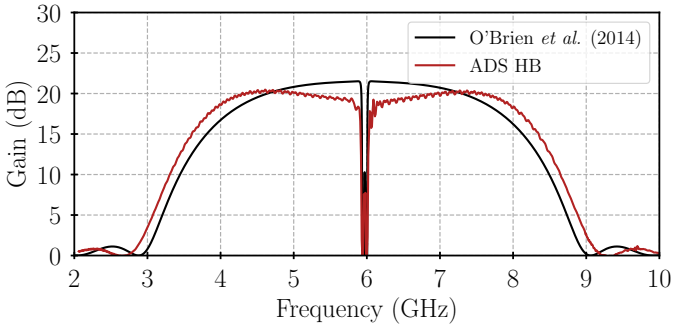

Figure 3.3: Signal gain for the JTWPA design presented in [103]. The black line used the CME framework introduced in [103] for $I_{\mathrm{p}}/I_{*} = 0.5$, and the red line used the HB simulation in Keysight ADS® for $P_{\mathrm{p,in}} = -73.9\,\mathrm{dBm}$.

JTWPA, and we label the wire connecting them to later access the output voltage and current (V_{out} and I_{out}). Next, the harmonic balance simulation needs to be set up. We add the Harmonic Balance icon to our circuit, and we double-click to open the setup window. There, we set the frequency tones for the simulation to f_{s} and f_{p}. The frequency order (N) defines how many harmonics of each individual tone are simulated, and the mixing order (M) controls how many intermodulation products between multiple tones are simulated. In our case, we set $N = 3$ for both frequency tones, and $M = 3$, to take into account the idler and other intermodulation products. To explore the gain as a function of f_{s}, we further add a parameter sweep that we set for f_{s} in the range that we want to investigate (2-10 GHz at a frequency step of 10 MHz in our case). Finally, we set $P_{\mathrm{p,in}} = -73.9\,\mathrm{dBm}$ and $P_{\mathrm{s,in}} = -140\,\mathrm{dBm}$ and we run the simulation, which takes a couple of minutes with the described set of parameters. Increasing N, M and/or the number of f_{s} points in the parameter sweep substantially increases the simulation time.

Once the simulation is finished, we can visualise the signal gain data by defining the following expression in the data visualisation interface of Keysight ADS®: $G_{\mathrm{s}} = \mathrm{mix}(v_{\mathrm{out}} I_{\mathrm{out}}/v_{\mathrm{in}} I_{\mathrm{in}}, \{0, 1\}, \mathrm{Mix})$. The result of the simulation when using $P_{\mathrm{p,in}} = -73.9\,\mathrm{dBm}$ is shown in Fig. 3.3, compared to the CME analytical gain solution provided by O'Brien et al. [103] for the same design with $I_{\mathrm{p}}/I_{*} = 0.5$. The difference between both curves is most certainly a result from the consideration of harmonics and intermodulation products in the HB simulation, which were ignored in the CME framework. This result shows the great potential of using the HB technique to simulate JTWPAs performance, which can be set to include numerous second-order processes neglected in the CME frameworks, which for certain designs could have a

substantial impact on the figures of merit. However, since HB relies on an iterative algorithm to converge to the solution, frequently when simulating JTWPAs operated at high I_{p}/I_{*} ratios, the algorithm is unstable and does not converge to the solution. Further efforts could be done in stabilising the circuit implementation in Keysight ADS®, resolving the uncertainty surrounding whether the instabilities stem from the circuit design or the solver algorithm, which is a work in progress at the time of writing. More importantly, HB is computationally heavy to simulate compared to the analytical CME solution. In summary, CME frameworks are useful in initial stages of the design, particularly to optimise the JTWPA design, while HB techniques are useful at later stage to verify the performance of the JTWPA taking into account other second-order effects to ensure the performance of the device is as expected.

Both CME and HB are frequency-domain techniques to model JTWPAs. However, there are other methods based on time-domain techniques such as Finite-Difference Time-Domain (FDTD) simulations that have been successfully implemented to simulate JTWPAs [109, 57]. Time-domain techniques are implemented in circuit-modeling softwares like WRspice, and several studies have compared their performance to standard frequency-domain methods in the context of JTWPA simulations [108, 110]. While time-domain approaches yield accurate results, these studies show that they are significantly more computationally intensive than frequency-domain alternatives, hence not suitable for designing JTWPAs in the initial phase.

3.2 Validating the CME framework for JTWPAs

The mathematical CME framework introduced in Chapter 2 is in fact extending from the CME initially derived for the lossless ($\alpha_{\mathrm{m}} = 0$) KTWPAs [73] as explained earlier. Therefore, in this section, I focus on replicating the theoretical and measured performance of a JTWPA and a SQUID-based JTWPA design respectively to further validate the framework for junction-based devices.

Josephson junction TWPA

Here, I reproduce the theoretical gain curve presented in [103] using the unit cell circuit parameters given in the manuscript. I calculate the `ABCD` matrix of the unit cell using Keysight ADS®, and I cascade it 2,000 times, the total number of cells in the design. From the cascaded `ABCD` matrix, I obtain the S_{21} parameter of the device as shown in the red line plotted in Fig. 3.4 (a). From the S_{21}, I calculate the γ_{m}

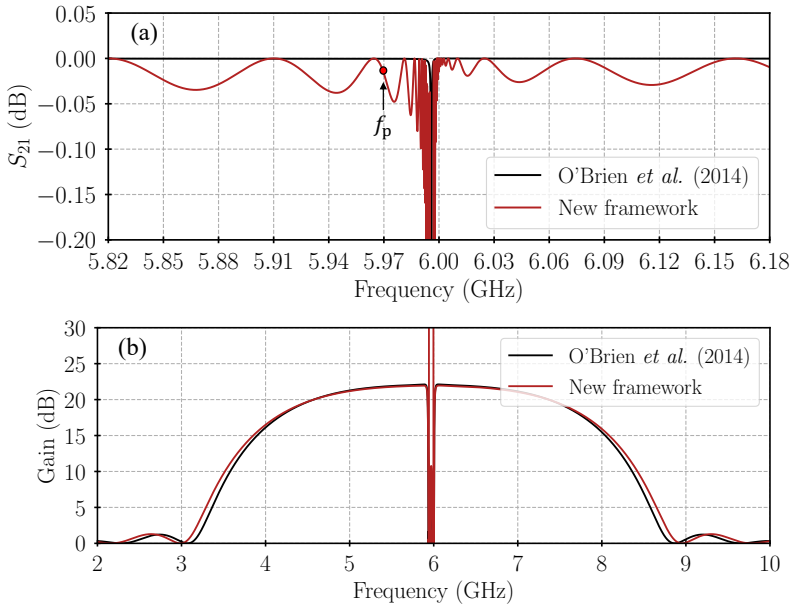

Figure 3.4: (a) Transmission profile S_{21} of the JTWPA design presented in [103] calculated using the translation symmetry assumption from the original framework (black) and the generalised CME framework (red). (b) Theoretical gain profile of the JTWPA presented in [103] calculated using the analytical solution of the conventional CME framework (black) and the generalised CME framework (red).

required to solve the CME as explained in Sec. 3.1.1. Note the ripple effect in the S_{21} calculated using this method compared to the mathematical model in [103] shown in black line in Fig. 3.4 (a), which assumes translation symmetry. These ripples are originated from the interaction between the cascaded cells[1], and play an important role in optimising the gain, since the misplacement of the pump frequency could result in unwanted attenuation of the pump [111]. However, in this particular example the pump frequency ($f_p = 5.97\,\text{GHz}$) almost coincides with a peak of transmission in the S_{21} profile of the new model, resulting in an almost optimal pumping condition for both cases.

Using the calculated γ_m, I solve the analytical solution of the generalised CME (Eqs. 2.34b) for the JTWPA in the DP4WM regime when pumping at $I_p/I_* = 0.54$, leading to the gain profile shown in Fig. 3.4 (b) (red line). We observe a near-perfect match with the gain profile obtained using the analytical expression from the conventional CME framework presented in [103] (black line). The small deviation in band-

[1]This ripple effect originates only around the stopbands structures and has been observed in numerous experimental implementations [80, 79]. It originates from the periodic disruption of the electromagnetic tones propagating in the STL and it should not be confused with the gain ripples originating from the impedance mismatch in the JTWPA.

width could result from the assumption of trivial junction capacitance not included in our model. Apart from these minor differences, the behaviour of the JTWPA is largely similar. Thereby, it demonstrates that the proposed methodology could perform almost identically to the conventional CME framework developed by O'Brien et al. [103], which has been extensively used to predict the JTWPA results [79, 112].

SQUID-based TWPA

L. Planat et al. [80] reported the first successful operation of a SQUID-based TWPA in the DP4WM regime. The design consisted of an array with symmetric SQUIDs, where the electrical parameters of the unit cell were modulated on a sinusoidal trend, creating a stop-band around 7 GHz to satisfy the phase-matching condition. Prior to that, they also fabricated and characterised similar SQUID arrays without periodic modulation [57].

Using the cell parameters presented in [57], i.e., L_0, C_j, and C_s, for the SQUID arrays without modulation — hereafter the non-modulated array — I calculate the unit cell's `ABCD` matrix[2]. Next, I cascade it 2,063 times, i.e., the total number of cell in the actual array. Given the microstrip design of the device, it experiences substantial frequency dependent losses in the dielectric layer, as measured in [57]. I further include the dielectric losses by adding a shunt resistance to the ground in the unit cell with a value of $R_\mathrm{shunt}(\omega) = 5 \times 10^{15}/\omega\,\Omega\mathrm{Hz}^{-1}$, resulting in a cascaded S_{21} that is consistent with the measured transmission profile. I extract the phase constant from the cascaded S_{21} and solve the CME, resulting in the gain profile presented in Fig. 3.5 (a). The authors in [57] acknowledge a 10% spread of the measured junctions inductance value in their wafer, therefore, this value is included as error margins in my theoretical calculation. The simulated result matches well with the measurement, where we relate the small deviation between the simulated curve and the experimental data to the several assumptions required for the CME derivation, as well as possible unknowns on the actual fabricated device characteristics and operational parameters.

I further replicate the gain of the modulated SQUID array with and without magnetic flux. First, using the cell parameters presented in [57], i.e., L_0, C_j, and C_s, I find the values of R_shunt resulting in the right attenuation of the S_{21} profile, i.e., $R_\mathrm{shunt}(\omega) = 3.2 \times 10^{15}/\omega\,\Omega\mathrm{Hz}^{-1}$ ($R_\mathrm{shunt}(\omega) = 4 \times 10^{15}/\omega\,\Omega\mathrm{Hz}^{-1}$) for the modulated

[2]The `ABCD` matrix calculation and cascading is implemented in a python script, which uses the definition of basic two-port circuits `ABCD` matrices, as introduced in [100], to build the JTWPA `ABCD` matrix.

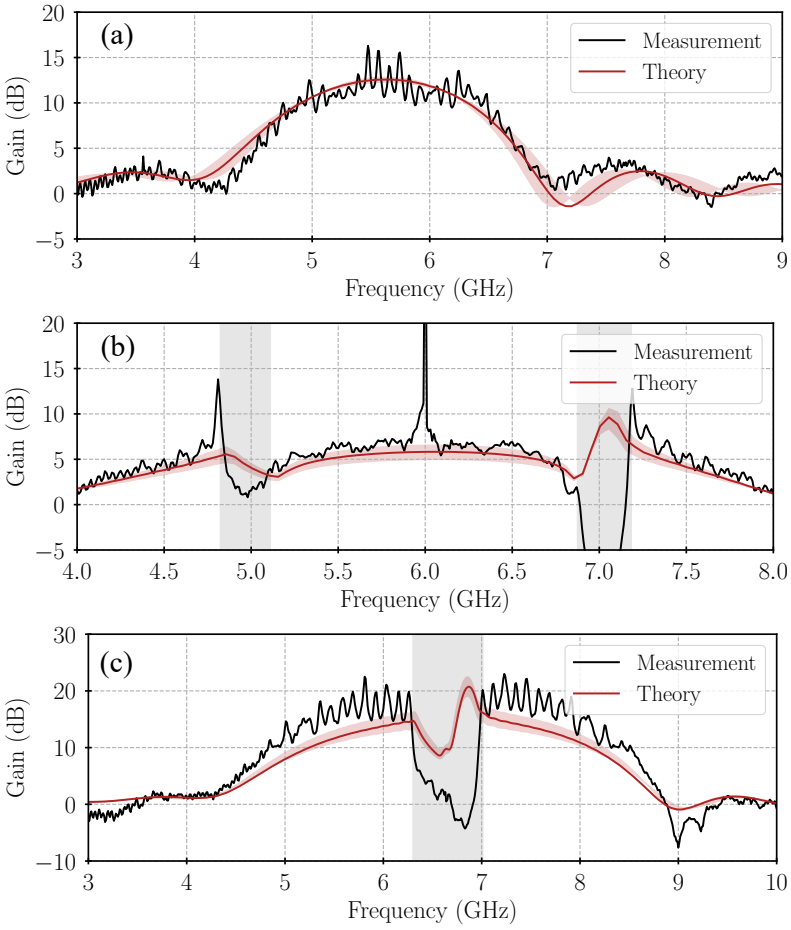

Figure 3.5: Gain profiles measured in [80, 57] compared to the predicted gain simulated using our framework. (a) Non-modulated SQUID array without magnetic flux using $I_\mathrm{p}/I_* = 0.7$ ($P_\mathrm{p,in} \approx -67.6\,\mathrm{dBm}$) for the theoretical calculation. The error margins correspond to a 10% variation of L_0. (b) Modulated SQUID array without magnetic flux using $I_\mathrm{p}/I_* = 0.565$ ($P_\mathrm{p,in} \approx -67.4\,\mathrm{dBm}$) for the theoretical calculation. (c) Non-modulated SQUID array with applied magnetic flux $\Phi/\Phi_0 = 0.2$ using $I_\mathrm{p}/I_* = 0.685$ ($P_\mathrm{p,in} \approx -65.7\,\mathrm{dBm}$) for the theoretical calculation. The shaded area shows the stop-band regions where our calculation are not accurate due to non-physical solutions. The error margins correspond to a 2% variation of L_0.

SQUID array with (without) applied magnetic flux $\Phi/\Phi_0 = 0.2$. In [80, 57], the authors observed a frequency shift on the measured stop-band of the modulated SQUID arrays when using high pump powers; I relate this effect to the increase of the SQUID inductance with the pump power, resulting in an increase on the phase constant. Therefore, modifying the unit cell's inductance using Eq. 2.21, I estimate the amplitude of the pump by matching the stop-band in the cascaded S_{21} profile with the stop-band from the measured gain profile. This results in $I_\mathrm{p}/I_* = 0.565$ ($P_\mathrm{p,in} \approx -67.4\,\mathrm{dBm}$) and 0.685 ($P_\mathrm{p,in} \approx -65.7\,\mathrm{dBm}$) for the case with and without applied magnetic flux respectively[3]. These values are lower than the pump power at the input of the device ($P_\mathrm{p,in}$) calculated by the authors in [80, 57] using their CME framework, i.e., $P_\mathrm{p,in} = -70.3\,\mathrm{dBm}$ and $-70.2\,\mathrm{dBm}$ for the case with and without applied magnetic flux respectively. Further analysis would be needed to understand the origin of the discrepancy between these two techniques and their accuracy, which is out of the scope of this exercise. Nevertheless, the calculated $P_\mathrm{p,in}$ are on the same order of magnitude. After fitting the stop-band, I obtain the pumped S_{21} data that I subsequently use to calculate the wavevector. Before solving the CMEs, the wavevector needs to be corrected so the phase-velocity matches the unpumped case (further discussed in Sec. 3.5.2). The result obtained from the CME without applying magnetic flux, pumping the device at $f_\mathrm{p} = 6\,\mathrm{GHz}$, is plotted in Fig. 3.5 (b). The error margins correspond to a 2% uncertainty in the measured SQUID inductance as indicated by the authors in [80, 57]. Apart from the stop-band regions, the generalised CME framework manages to predict the general behaviour of the experimental gain curve.

Finally, I replicate the curve for the same device when pumped at $f_\mathrm{p} = 6.635\,\mathrm{GHz}$ with a magnetic flux $\Phi/\Phi_0 = 0.2$, plotted in Fig. 3.5 (c). We observe a good resemblance with the experimental gain profile. Despite a perfect match with the measured data is hard to achieve using the circuit parameters presented in [57], using our framework we can still find a set of L_0 and R_shunt that resulted in a perfect match. Note that, the ripple effect originated by an impedance mismatch of the device can be simulated easily with a Fabry-Pérot cavity model as described in [80]. Given the good agreement between these calculations and the experimental data, despite the

[3]To estimate the pump power at the input of the device $P_\mathrm{p,in}$, I calculate I_c from the L_0 provided by the authors, i.e., $I_\mathrm{c} = 5.45\,\mu\mathrm{A}$. Then, I multiply by I_p/I_* to obtain I_p, and calculate the power $P = Z_0 I_\mathrm{p}^2/2$, where Z_0 is the characteristic impedance of the unpumped JTWPA. The factor of 2 in the denominator is included since I_p is defined as the peak amplitude value rather than the root mean square (RMS) in our CME framework.

uncertainties in the calculation of the unit cell parameters reported in [80, 57], I believe our generalised CME framework constitutes a powerful tool for the design and exploration of SQUID-based TWPAs.

3.3 Circuit parameters analysis

Now that I have demonstrated the validity of the generalised CME framework to simulate JTWPAs, we can use it to explore the impact of the unit cell circuit parameters to the main figures of merits of the amplifier. Notice that the junction's L_j and C_j depend on the thickness of the insulator layer and the area of the junction A_jj. The thickness of the insulator layer determines the critical current density (J_c), which can be controlled with the oxidation parameters during the fabrication process, as I shall discuss in Sec. 4.1. The relation between L_j and J_c is given by Eq. 2.7, where $I_\mathrm{c} = J_\mathrm{c} A_\mathrm{jj}$. In the case of C_j, for Nb/Al-AlO_x/Nb junctions (as the ones used for all the devices in this thesis), it relates to J_c through the following empirical expression[4]:

$$C_\mathrm{j}[\mathrm{fF/\mu m^2}] = 72.518 e^{0.0107 J_\mathrm{c}[\mathrm{A/cm^2}]}. \tag{3.7}$$

Therefore, to have a more insightful perspective into the junction fabrication, I used J_c and A_jj instead of L_j and C_j for the analysis.

All the results presented in this section were obtained using the analytical solution of the generalised CMEs for a lossless DP4WM JTWPA as presented in Chapter 2, unless otherwise indicated. I assume a perfect phase-match between the different propagating tones, i.e., $\Delta_\phi = 0$, and suppression of the pump harmonics. Furthermore, I fixed the following values across the calculations: $a = 10\,\mu\mathrm{m}$ and $f_\mathrm{p} = 8\,\mathrm{GHz}$, $I_\mathrm{p}/I_* = 0.5$, unless otherwise indicated.

Gain and bandwidth with number of junctions

The signal gain and bandwidth are among the most critical figures of merit for an amplifier. Ideally, an amplifier should have a gain and bandwidth as large as possible, broadening its practical applications. Fig. 3.6 shows the calculated gain as a function of the number of junctions N_jj in the JTWPA, for different A_jj (columns), C_s (rows), and J_c (colours). The grey areas indicate the parameters region of interest for practical applications.

[4]This expression was experimentally determined by our collaborators at the Observatoire de Paris.

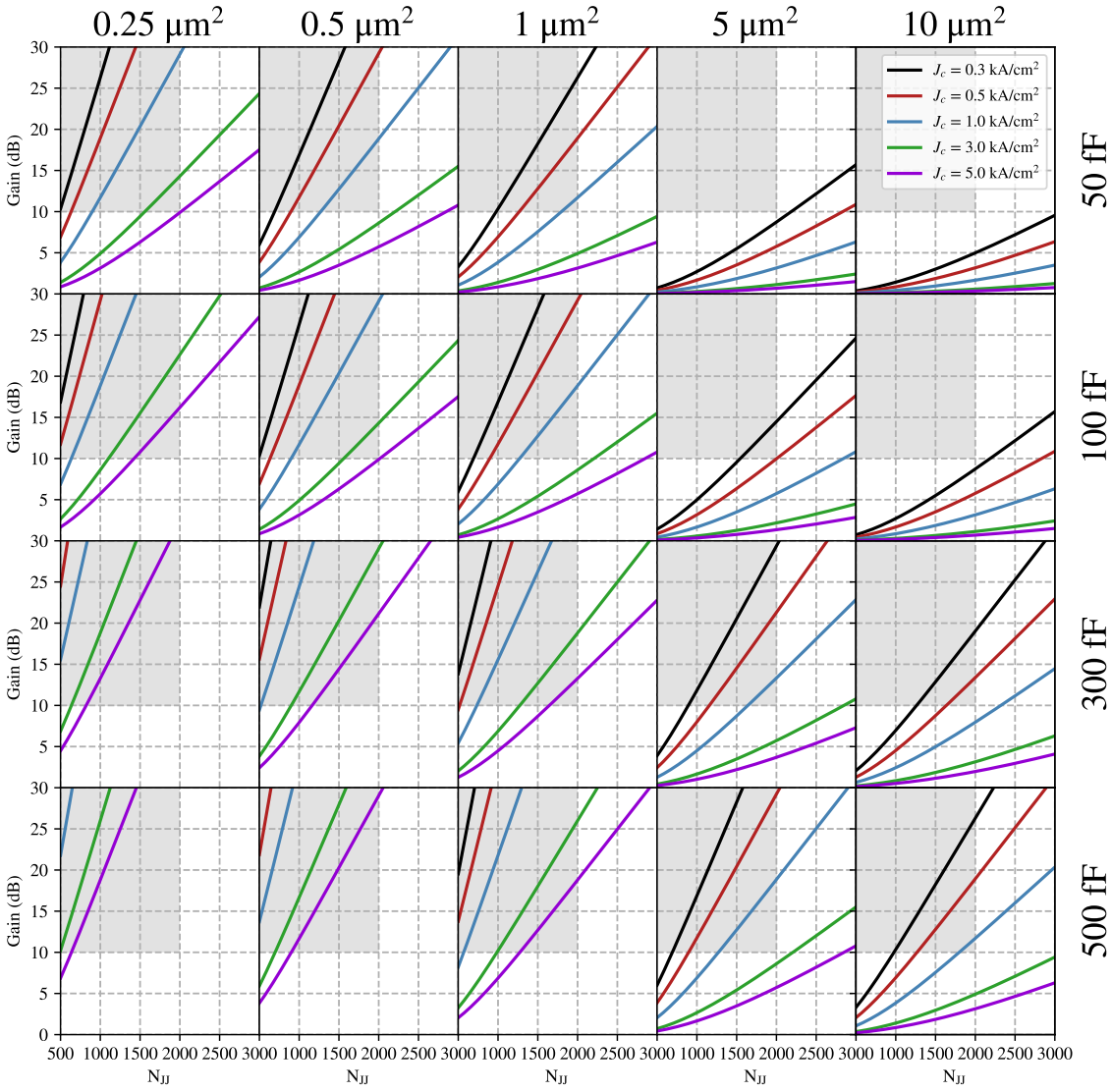

Figure 3.6: DP4WM JTWPA gain at $f_s = f_p = 8\,\text{GHz}$ as a function of N_{jj} for different A_{jj} (columns), C_s (rows) and J_c (colours). The shaded area indicates the $N_{jj} < 2,000$ and $> 10\,\text{dB}$ gain case.

We notice that the gain increases exponentially[5] with the number of junctions as expected for $\Delta_\phi = 0$. The presented results suggest three effective methods to increase the gain and/or reduce the number of junctions required for high gain: (a) reduce A_{jj}, (b) reduce J_c and (c) increase C_s. While (a) and (b) result from an increase in the L_j at the origin of the parametric gain, (c) originates from a larger electrical length of the STL, which increases the interaction time between the propagating tones and hence the energy tranfer processes resulting in signal gain.

We conclude that for moderate C_s values, i.e., $C_\text{s} < 100\,\text{fF}$, junctions of $1\,\mu\text{m}^2$ and smaller, with a critical current density $J_\text{c} < 1\,\text{kA/cm}^2$ are required to achieve over 10 dB gain with less than 2,000 junctions. Nevertheless, increasing the shunt capacitance $C_\text{s} \geq 100\,\text{fF}$ further allows us to relax the J_c and A_{jj} requirement, achieving the target gain with values up to $J_\text{c} = 5\,\text{kA/cm}^2$. However, this larger values of C_s could be challenging to physically implement in an STL, and could result in higher losses, due to potential dielectric loss in the capacitor.

Figure 3.7 presents a similar analysis of the bandwidth. In this case, I do not impose $\Delta_\phi = 0$, since the bandwidth is critically dependent on the values of Δ_ϕ over frequency. We notice that the bandwidth decreases as the number of junctions increases, regardless of other parameters, due to the corresponding increase in amplifier gain. Conversely, fewer junctions result in lower gain but larger bandwidths. Therefore, in the upper-right region of the plots in Fig. 3.7, the curves are sparse due to the low gains (typically less than 3 dB), which require a substantial number of junctions to achieve enough gain for inclusion in the analysis.

While Fig. 3.7 does not provide a clear strategy to increase bandwidth without reducing gain, an interesting parameter region emerges. Here, the designs achieve over 8 GHz bandwidth with fewer than 2,000 junctions, particularly in cases where junction areas are $1\,\mu\text{m}^2$ or smaller and the shunt capacitance is less than 300 fF. Additionally, comparing Fig. 3.6 and Fig. 3.7, we observe that the gain-bandwidth product increases with larger C_s and smaller A_{jj}.

The results presented in Fig. 3.6 and Fig. 3.7 provide the JTWPA designers with a preliminary idea of the amplifier's gain and bandwidth performance, where functional cases complying with their fabrication limitations can be obtained. Nevertheless, the analysis suggests small junctions (under $1\,\mu\text{m}^2$) with relatively low critical current densities (under $3\,\text{kA/cm}^2$) and substantial high shunt capacitance ($50\,\text{fF} < C_\text{s} <$

[5]Notice that the presented gain results are in a logarithmic scale, since they are given in dB units.

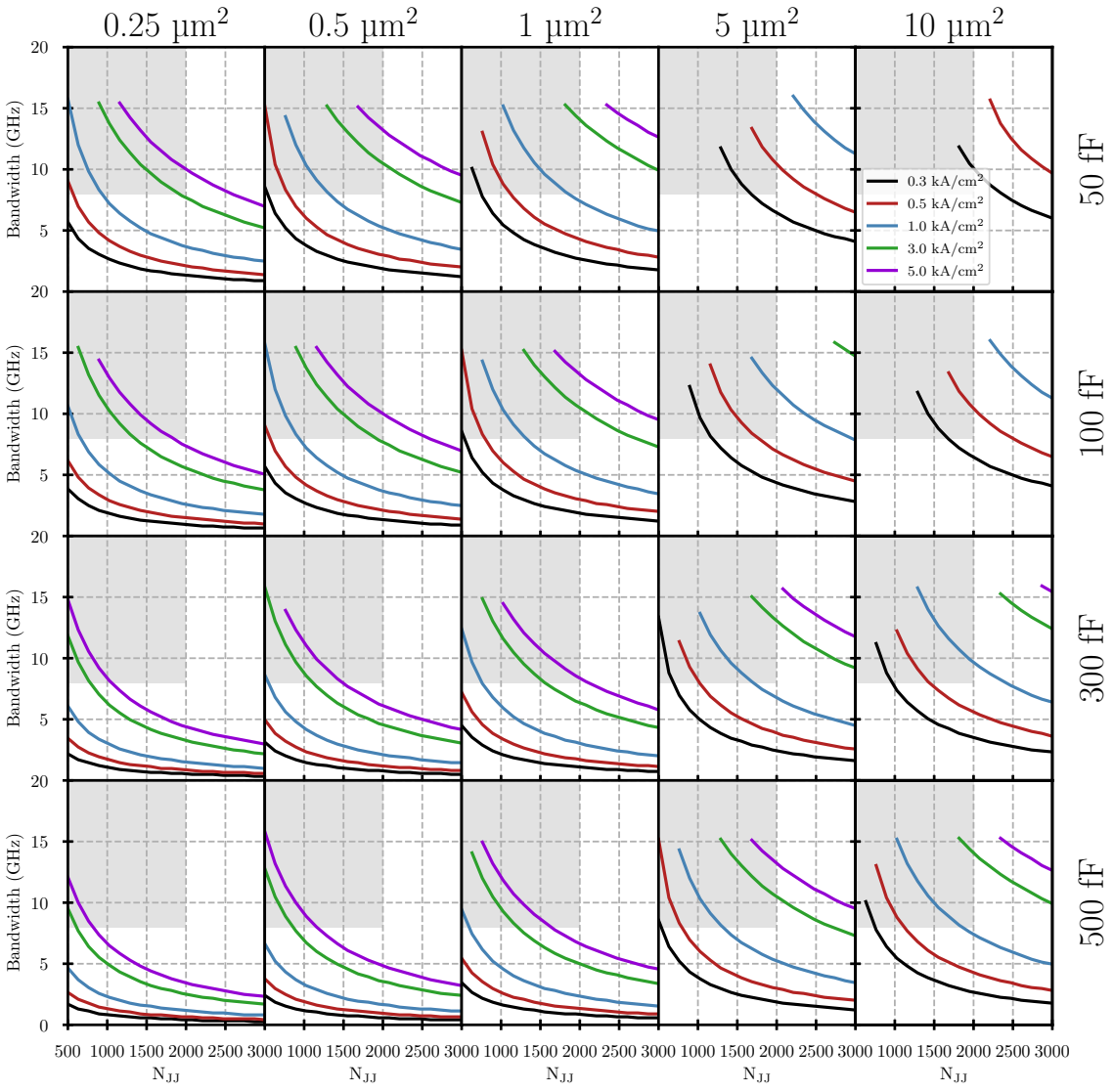

Figure 3.7: DP4WM JTWPA bandwidth at $f_s = f_p = 8\,\text{GHz}$ as a function of N_{jj} for different A_{jj} (columns), C_s (rows) and J_c (colours). The shaded area indicates the $N_{jj} < 2{,}000$ and $> 8\,\text{GHz}$ bandwidth.

300 fF) to be the optimal fabrication parameters to aim for high gain and large bandwidth JTWPAs.

Characteristic impedance and compression point

The characteristic impedance Z_0 of the JTWPA is an important property for practical designs. Often, the electronic environment around the JTWPA carrying the propagating tones, e.g., cables and connectors, has a $Z_0 = 50\,\Omega$. Therefore, to avoid an impedance mismatch that could result in reflection and deteriorating the JTWPA performance, the JTWPA STL is often matched to the $Z_0 = 50\,\Omega$ environment. Furthermore, an ideal amplifier would have a large dynamic range, permitting the amplification of signals within a wide range of power levels. The dynamic range of an amplifier is indicated by the compression point P_{1dB} value.

Fig. 3.8 plots Z_0 (red) and P_{1dB} (blue) as a function of J_{c} for different A_{jj} (columns) and C_{s} (rows) values. The P_{1dB} results are calculated by numerically solving the CMEs. Since P_{1dB} largely depends on the gain value, we change N_{jj} for each point in the curves to ensure a constant gain of 23 dB. From the obtained results, we notice that the P_{1dB} increases with J_{c} and A_{jj}. This is due to a decrease of L_{j}, i.e., an increase of I_{c}; therefore, the junctions can handle larger current amplitudes before switching to the normal state. This translates to a weaker nonlinear STL, which comes at the price of requiring a larger number of junctions to achieve 23 dB. We also notice that C_{s} has a limited impact on the P_{1dB}.

The grey areas in Fig. 3.8 indicate the region where $Z_0 = 50 \pm 2\,\Omega$. The characteristic impedance can be approximated as $Z_0 \approx \sqrt{L_{\mathrm{j}}/C_{\mathrm{s}}}$. We notice that Z_0 exponentially decreases with J_{c} due to a decrease in L_{j}. Similarly, an increase in C_{s} results in a decrease in Z_0. The results presented in Fig. 3.8 suggest that only small junction $A_{\mathrm{jj}} < 1\,\mu\mathrm{m}^2$ with low critical current density $J_{\mathrm{c}} < 1\,\mathrm{kA/cm}^2$ and moderate shunt capacitance $C_{\mathrm{s}} < 100\,\mathrm{fF}$ can successfully meet the target of $Z_0 = 50 \pm 2\,\Omega$.

Junction distribution density and cutoff frequency

JTWPAs operate under the assumption that $\lambda \gg a$, where λ is the wavelength of the signal propagating in the STL, i.e., a distributed system, where the effect of the junctions can be analysed collectively. However, by reducing λ, we can enter a regime where the discrete effect of the junctions alters the transmission line behaviour. Although there is not a precise switching point between these two regimes, a good

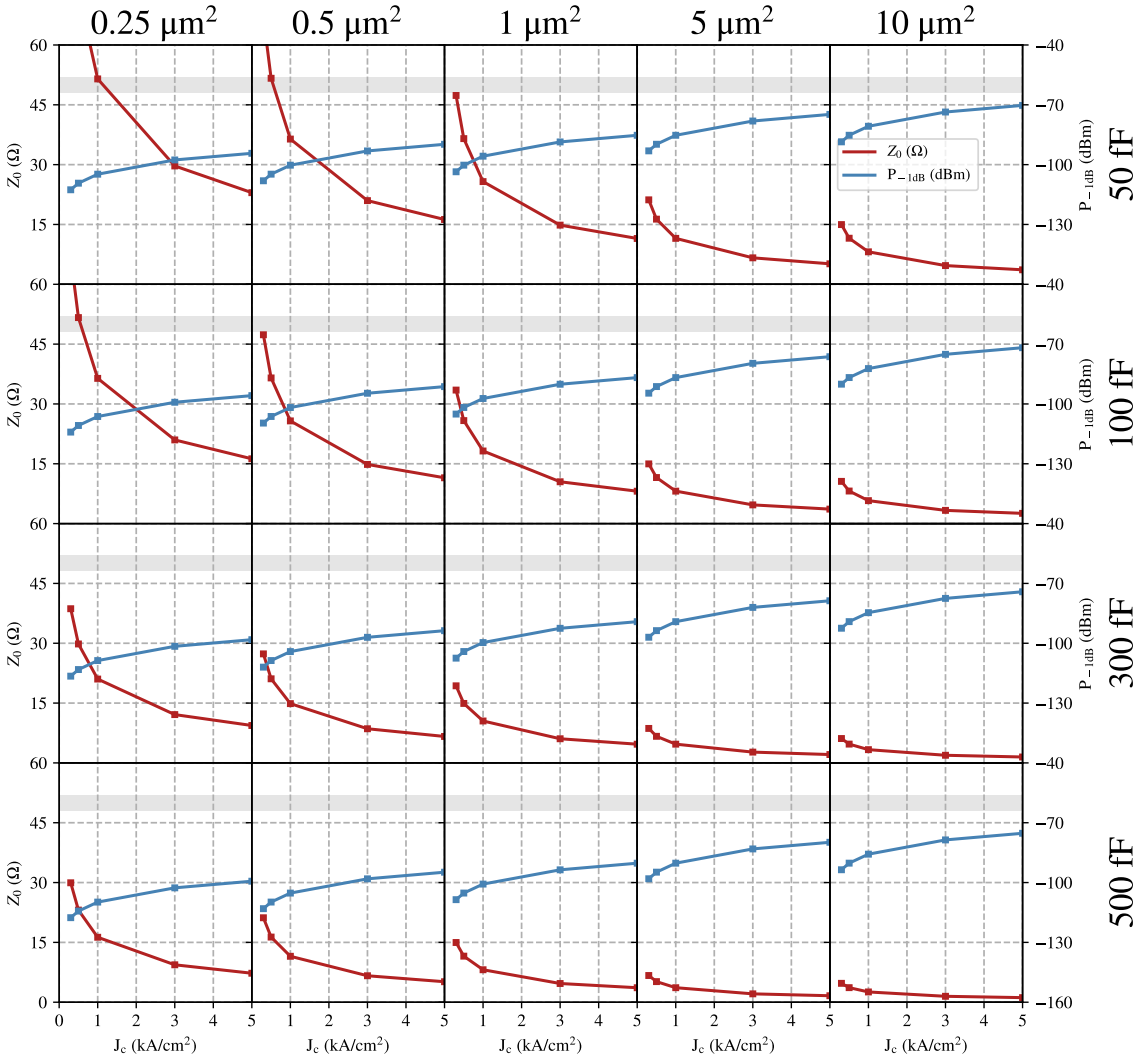

Figure 3.8: DP4WM JTWPA Z_0 (red) and $P_{1\mathrm{dB}}$ (blue) as a function of J_c for different A_jj (columns) and C_s (rows). All the data points in the curves result from different N_jj values ensuring a peak gain of 23 dB. The grey area indicates the region where $Z_0 = 50 \pm 2\,\Omega$.

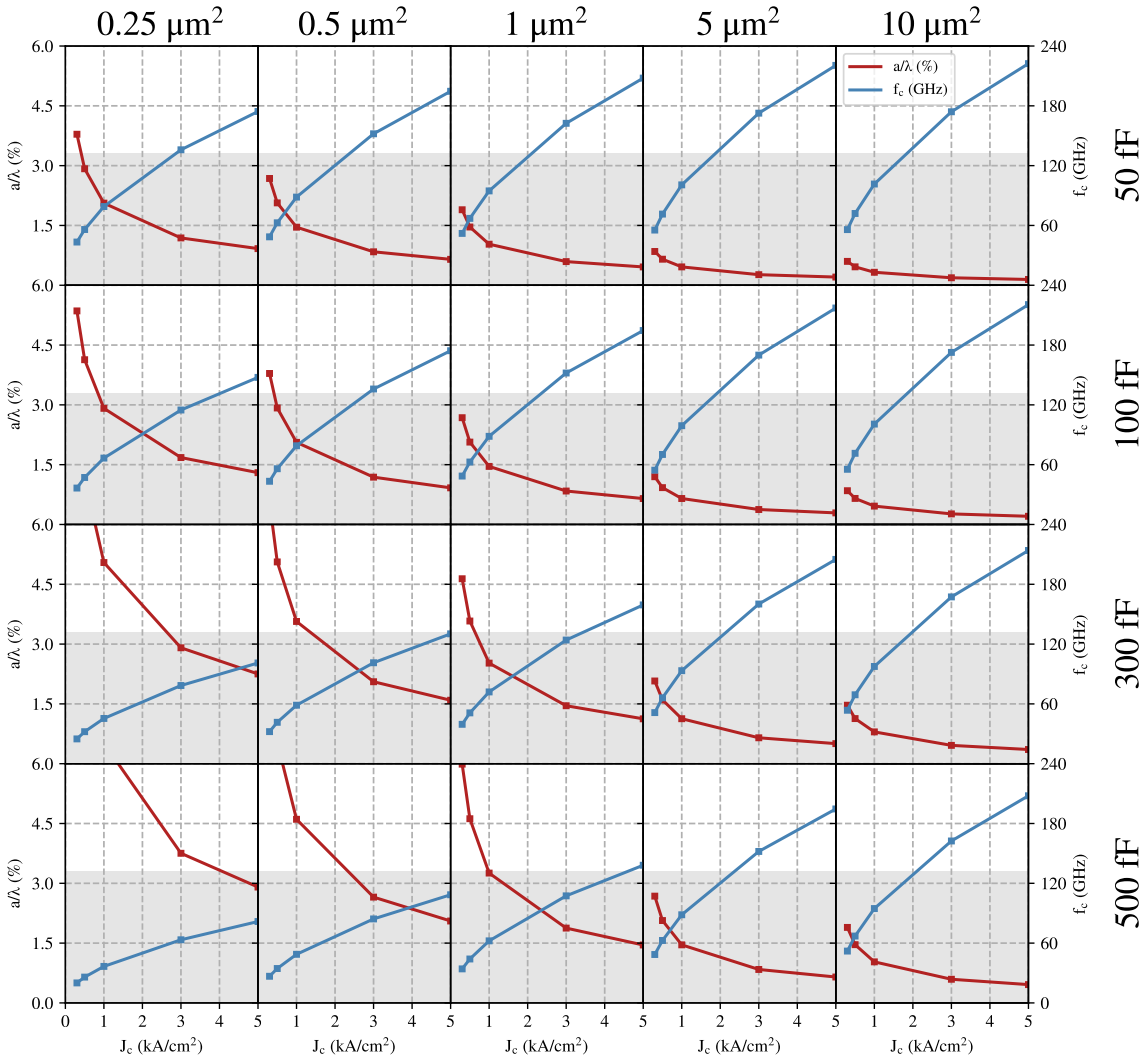

Figure 3.9: DP4WM JTWPA a/λ (red) and f_c (blue) as a function of J_c fixing $f_p = 8\,\text{GHz}$ for different A_{jj} (columns) and C_s (rows). The gray area indicates the region where $a/\lambda < 3.3\,\%$.

rule of thumb to ensure that we operate in the distributed regime is $a < 0.1\lambda$, where λ is the wavelength at the operational frequency. To analyse this effect, we refer to a/λ as the junction distribution density parameter. Assuming that the highest frequency of interest propagating in the JTWPA is $3f_\mathrm{p}$, the previous rule of thumb imposes that $a/\lambda < 3.3\,\%$[6]

As discussed in Sec. 2.2.4, the cutoff frequency f_c of the JTWPA plays an important role in suppressing the generation of higher harmonics of the pump that could deteriorate the gain. Furthermore, f_c is one of the main limiting factors for the operation of JTWPAs at high frequencies, as shall be discussed in Chapter 9. The cutoff frequency in a JTWPA is given by the following expression:

$$f_\mathrm{c} = \frac{2\omega_0}{2\pi\sqrt{1+4\frac{\omega_0^2}{\omega_\mathrm{j}^2}}}, \tag{3.8}$$

where $\omega_0 = 1/\sqrt{L_\mathrm{j}C_\mathrm{s}}$ is the cutoff frequency of the STL and $\omega_\mathrm{j} = 1/\sqrt{L_\mathrm{j}C_\mathrm{j}}$ is the plasma frequency of the junctions.

Fig. 3.9 plots a/λ (red) and f_c (blue) as a function of J_c for different A_jj (columns) and C_s (rows). The grey areas indicate the region where $a/\lambda < 3.3\,\%$. The a/λ decreases with J_c since[7] $\lambda \propto L_\mathrm{j}$, and L_j decreases with J_c. We notice that for the majority of the explored cases, the $a/\lambda < 3.3\,\%$ condition is satisfied. Only the bottom left corner of the table results in high values of a/λ due to the large L_j and C_s resulting in a slow phase velocity, i.e., large λ.

From Fig. 3.9, the f_c increases with J_c, since it pushes the ω_j to higher frequencies. Furthermore, the effect of C_s is negligible for large junctions since $\omega_0 \ll \omega_\mathrm{j}$, and therefore Eq. 3.8 simplifies to $\omega_\mathrm{c} \approx \omega_\mathrm{j}$. Contrary, for small junctions, C_s has a larger impact in reducing f_c. From these plots, we can conclude that big junctions with large J_c are necessary for high f_c.

[6]For any f_p, which sits at the centre frequency of the JTWPA, assuming a linear dispersion $\lambda(3f_\mathrm{p}) = 3\lambda(f_\mathrm{p})$, therefore $a/\lambda_{3f_\mathrm{p}} < 0.1 \Leftrightarrow a/3\lambda_{f_\mathrm{p}} < 0.1 \Leftrightarrow a/\lambda_{f_\mathrm{p}} < 0.033$.

[7]Remember that $\lambda = \omega/v$ and $v \approx \frac{1}{\sqrt{L_\mathrm{j}C_\mathrm{s}}}$.

ω_c derivation

Since the equivalent circuit of the unit cell in a JTWPA can be expressed as a series inductance Z_1 (Josephson junction) and a shunt capacitance Z_2, Eq. 3.2 can be rewritten as

$$ka = \cos^{-1}\left(1 + \frac{Z_1}{2Z_2}\right). \tag{3.9}$$

Given that $Z_1 = \frac{i\omega L_j}{1-\omega^2 L_j C_j}$ and $Z_2 = \frac{1}{i\omega C_s}$,

$$\begin{aligned} 1 + \frac{Z_1}{2Z_2} &= 1 + \frac{i\omega L_j}{2(1-\omega^2 L_j C_j)/(i\omega C_s)} = 1 - \frac{\omega^2 L_j C_s}{2(1-\omega^2 L_j C_j)} \\ &= 1 - \frac{\omega^2/\omega_0^2}{2\left(1-\omega^2/\omega_j^2\right)} = 1 - \frac{\omega^2}{2\omega_0^2\left(1-\frac{\omega^2}{\omega_j^2}\right)}. \end{aligned} \tag{3.10}$$

Therefore, we can rewrite Eq. 3.9 as:

$$ka = \cos^{-1}\left(1 - \frac{\omega^2}{2\omega_0^2\left(1-\frac{\omega^2}{\omega_j^2}\right)}\right). \tag{3.11}$$

From this expression, we notice the wavevector has an imaginary, hence non-physical, solution when $1 - \frac{\omega^2}{2\omega_0^2\left(1-\frac{\omega^2}{\omega_j^2}\right)} > 2$. We can define the cutoff frequency of the JTWPA as:

$$\begin{aligned} 2 &= 1 - \frac{\omega_c^2}{2\omega_0^2\left(1-\frac{\omega_c^2}{\omega_j^2}\right)} \\ \iff \omega_c^2 &= 4\omega_0^2\left(1-\frac{\omega_c^2}{\omega_j^2}\right) = 4\omega_0^2 - \frac{4\omega_0^2}{\omega_j^2}\omega_c^2 \\ \iff \omega_c^2\left(1+\frac{4\omega_0}{\omega_j^2}\right) &= 4\omega_0^2 \\ \iff \omega_c &= \frac{2\omega_0}{\sqrt{1+4\frac{\omega_0^2}{\omega_j^2}}}. \end{aligned} \tag{3.12}$$

Discussion on JTWPA design optimisation

I have presented the circuit parameters' impact on the main figures of merit of a JTWPA. These tables can be used to find optimising approaches to design JTWPAs for specific applications. For example, let us assume that we aim to build a JTWPA operated around 8 GHz with high gain > 20 dB and bandwidth (> 8 GHz) and $N_{jj} <$

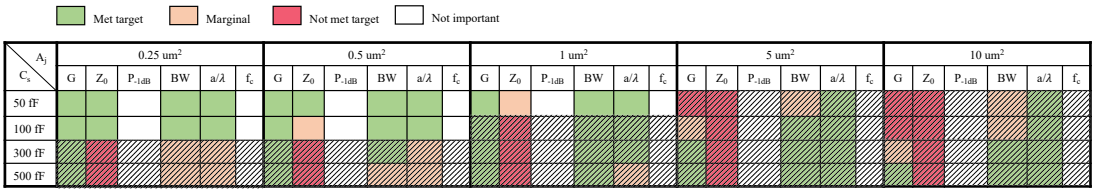

(a) 50 Ω

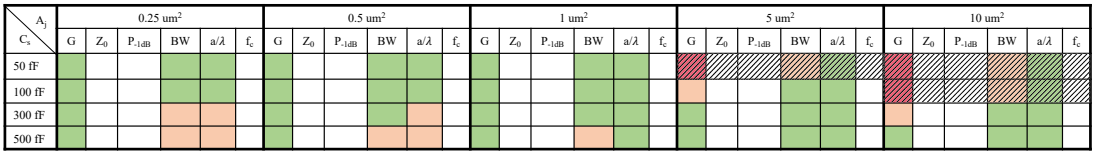

(b) Non-50 Ω

Figure 3.10: Summary of the design configurations resulting in a DP4WM JTWPA operated around 8 GHz with the following requirements: high gain > 20 dB, large bandwidth (> 8 GHz), and $N_{\mathrm{jj}} < 2{,}000$. Each box indicates a parameter configuration and the colours indicate whether the figures of merit requirements are met. The crossed boxes represent the configurations that do not meet the requirements. (a) JTWPA design with $Z_0 = 50\,\Omega$ and (b) $Z_0 \neq 50\,\Omega$.

2,000. Using the results presented in the previous analysis, we can construct the tables presented in Fig. 3.10 for the different A_{jj} and C_{s} cases that meet the targeted requirements of the design. Since for our case, no specific value of the P_{1dB} and f_{c} is required, we leave those columns empty. Fig. 3.10(a) shows the case where we further include the requirement of $Z_0 = 50\,\Omega$ for the design, while in Fig. 3.10(b) we relaxes it. The crossed boxes represent the configurations that do not meet the requirements. While a $Z_0 = 50\,\Omega$ design would entail junction sizes smaller than $1\,\mu\mathrm{m}^2$, $C_{\mathrm{s}} \leqslant 100\,\mathrm{fF}$ and $J_{\mathrm{c}} \leqslant 1\,\mathrm{kA/cm}^2$; by relaxing $Z_0 = 50\,\Omega$, numerous other parameters' combinations are allowed. This would therefore facilitate the fabrication of the device, permitting further optimisation like reducing the number of junctions. This idea of using a $Z_0 \neq 50\,\Omega$ line to reduce N_{jj} has been recently demonstrated experimentally [113], resulting in a JTWPA with a $1.1\,\mathrm{mm}^2$ footprint.

3.4 JTWPA design methodology

Up to this point, we have focused on the design and modelling of JTWPAs based on their circuit parameters. However, the key challenge in JTWPA design lies in translating these circuit parameters into a physical structure that can be fabricated

realistically. While the junction circuit parameters are directly connected to the physical properties of the junction, such as J_c and A_{jj}, as discussed in the previous section, the design of the C_s depends on the STL design and requires more careful consideration. To bridge the gap between the circuit model and the physical implementation of the JTWPA, we developed a technique that leverages the capabilities of electromagnetic (EM) simulation tools like Sonnet®. In this section, I shall use the example of an RPM JTWPA design operated in the DP4WM regime to introduce the design methodology. Although I use Sonnet® for this particular example, the method applies to any other EM simulation software, such as Ansys HFSS® which has been extensively used in the context of KTWPAs in [111, 101].

We start by simulating the unit cell geometry in Sonnet®. The layer distribution used for the simulation is given in Fig. 3.11(a). Although Sonnet® comes with numerous predefined materials that can be used in the simulations, superconductivity is not a built-in feature. To simulate superconducting material in Sonnet, we calculate the real and imaginary surface impedance of the superconductor using the Mattis-Bardeen equations [95] in the intended operational frequency range and temperature of the JTWPA. Then, we fit a polynomial expression to the surface impedance components over frequency, and we add the polynomial expression to a 'General' conductor model in Sonnet®, as shown in Fig. 3.11(b), to simulate the superconductor (niobium in our case).

The geometry of a coplanar waveguide (CPW) unit cell with parallel plate capacitors (PPCs) is illustrated in Fig. 3.11(c), where two niobium layers are used to model the device. The geometry of the PPCs is defined by the top niobium layer, where we add a dimension parameter for the length of the PPCs to allow a parametric sweep later. The two niobium layers are connected through a via as shown in the zoom-in image of Fig. 3.11(c). The junctions are modelled by cutting the transmission line and adding a lumped-element capacitor and inductor in series, as shown in the zoom-in image of Fig. 3.11(c). We use the ideal component feature in Sonnet®, choosing C_j and L_0 as the values for the capacitance and inductance respectively.

In this example, we try to design a JTWPA with $Z_0 = 50\,\Omega$. Therefore, we optimise the PPCs length to ensure $Z_0 = 50\,\Omega$ in the unit cell. We fix the impedance of the ports to $Z_0 = 50\,\Omega$ and we run a single frequency point simulation at a frequency where the JTWPA is intended to operate. This simulation is performed for a linear sweep of the dimension's parameter associated with the PPCs length. Although the

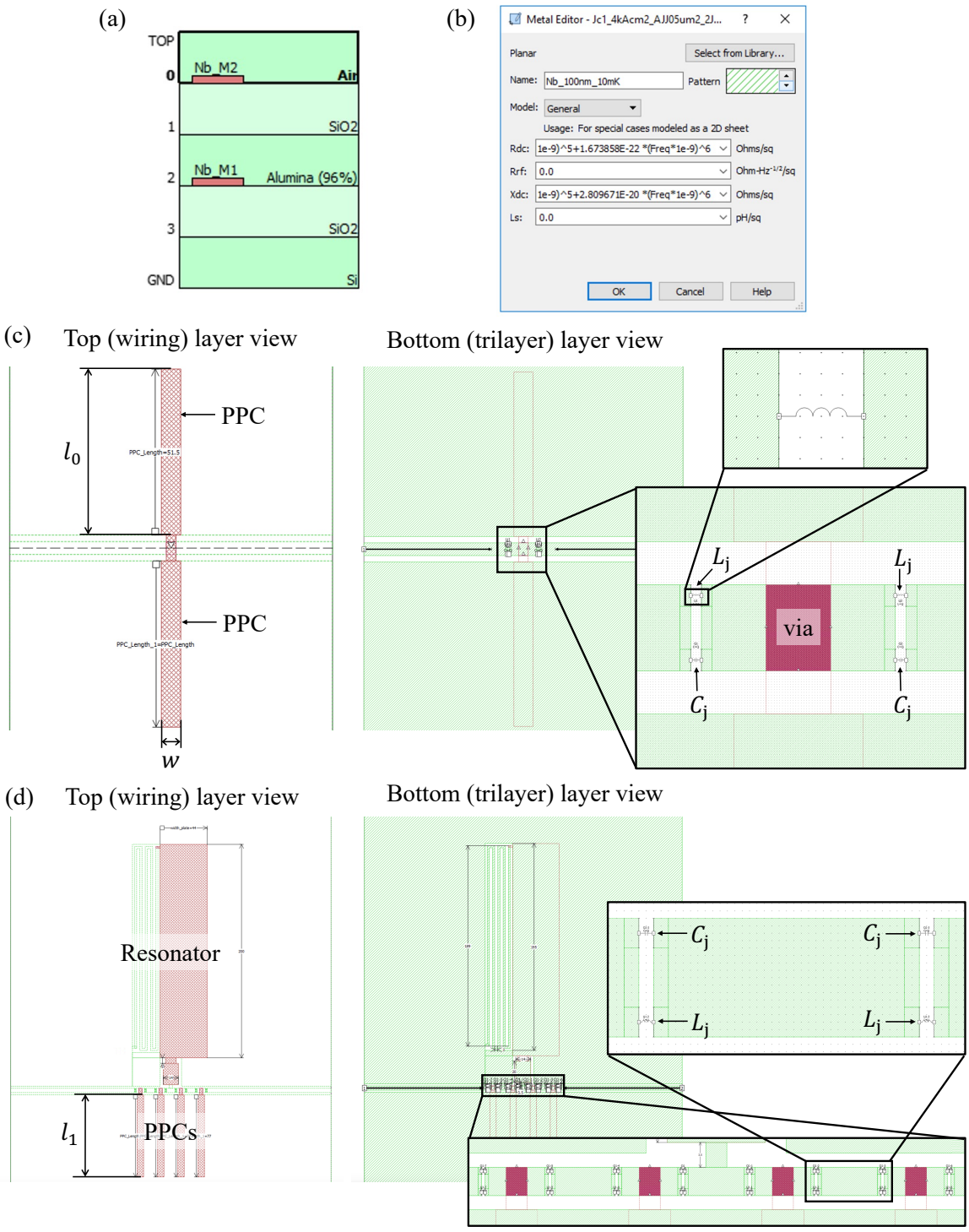

Figure 3.11: Design methodology for an RPM JTWPA using Sonnet®. (a) Schematics of the simulation layers. (b) Metal editor with the parameters used to simulate superconducting niobium. (c) Geometry of the JTWPA unit cell using PPCs to match $Z_0 = 50\,\Omega$. The zoom-in images show the model used for the junctions. (d) Geometry of the JTWPA resonator cell using PPCs to match $Z_0 = 50\,\Omega$. The zoom-in images show the model used for the junctions.

simulation time is closely tied to the simulation parameters, using a cell dimension[8] of 0.125 µm and 10 PPC length values for the sweep, the simulation runs in $\sim$ 20 minutes. Then, by plotting the S_{11} resulting from the simulation against the values of the parameter sweep, we find the optimised PPCs length resulting in the lowest S_{11}, i.e., PPCs length where $Z_0 = 50\,\Omega$. Once the length of the PPCs is fixed, we run the frequency sweep simulation from 10 MHz to 20 GHz[9] to check their behaviour at a wide frequency range.

To implement the RPM technique in the JTWPA design, I further model a resonator cell, illustrated in Fig. 3.11(d). The resonator is composed of a resonator capacitor C_r and inductor L_r, and a coupling capacitor C_c. I optimise the dimensions of C_r and C_c to obtain a resonance with high-quality factor at the intended frequency. For that, we run an Adaptative Band Synthesis (ABS) frequency sweep verifying that f_r is the only resonance frequency in the frequency range of the ABS sweep. Once we fix the geometry of the resonator, similarly to the standard unit cell, we make a single frequency point simulation for a frequency close to but outside the resonance frequency f_r of the resonator, and sweep the PPCs length to match $Z_0 = 50\,\Omega$ to find the required PPCs length for the resonator. As shown in the zoom-in image of Fig. 3.11(d), the resonator cell is composed of 8 junctions modelled as previously described. Finally, I ran a frequency sweep simulation from 10 MHz to 20 GHz to check the broadband behaviour.

From these simulations, we obtain the S-parameters of the unit cell and the resonator cell, that can be transformed into `ABCD` matrices using the conversion equations presented in [100]. From the `ABCD` matrix, we can cascade and combine the unit cell and resonator cell to form the JTWPA model. Therefore, following the techniques introduced in Sec. 3.1.1, we obtain the γ_m of the entire device. However, the calculated wavevector includes the effect of the geometrical inductance L_geo. To remove the effect of L_geo, we follow the techniques introduced in [111, 101]. The corrected γ_m can be used to solve the generalised CME equations to obtain the signal gain of the JTWPA design.

[8]Dimension of the grid used by Sonnet® to solve the electromagnetic field equations in the user-defined geometry.

[9]Starting the sweep at the lowest possible frequency and stopping around $2f_\mathrm{p}$ for 4WM and $1.5f_\mathrm{p}$ for 3WM is a good practice. However, the sweep depends on the range where we aim to solve the CME later. For a fine sweep, such as 20,000 frequency points, the simulation takes several hours.

3.5 JTWPA designs

In this section, I describe the optimised designs of the microwave JTWPAs that are subsequently fabricated and characterised in this thesis. All the designs presented in this section used the same methodology described in the previous sections.

3.5.1 JTWPAs with parallel plates capacitors (PPCs)

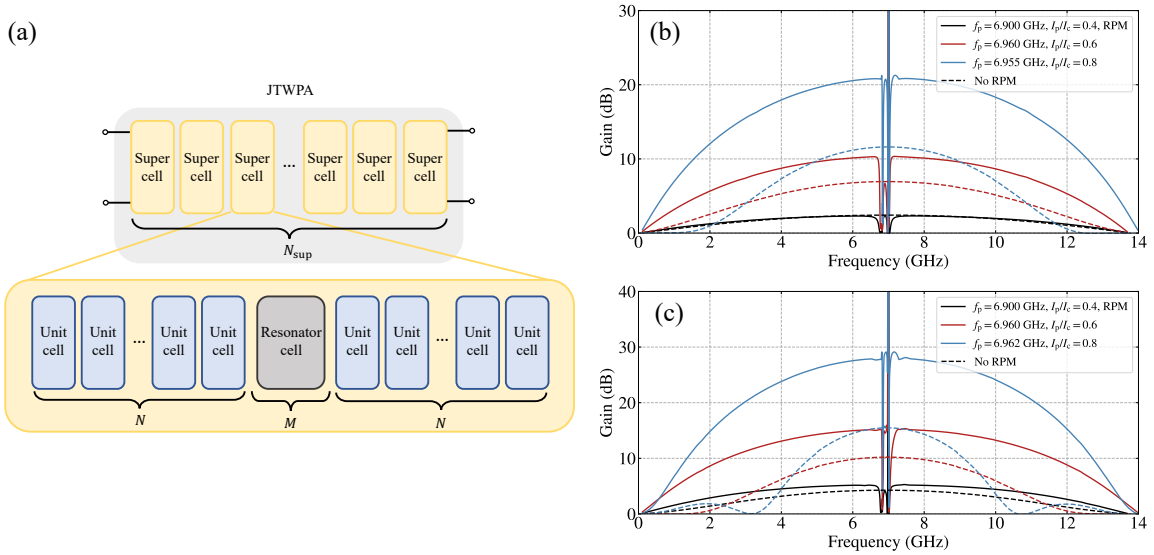

Figure 3.12: (a) Representation of the JTWPA model implementation by cascading the `ABCD` matrices calculated from the Sonnet® simulation of the unit cell and resonator cell. (b) Theoretical gain curve calculated using the generalised CME in the DP4WM pumping at frequencies close to $f_r = 7\,\text{GHz}$ with $I_p/I_c = 0.4$ (black), $I_p/I_c = 0.6$ (red) and $I_p/I_c = 0.8$ (blue) for Design A ($J_c = 1.4\,\text{kA/cm}^2$) and (c) Design B ($J_c = 0.9\,\text{kA/cm}^2$). The dotted line shows the equivalent design without resonators.

First, I aimed to design an RPM JTWPA operating in the DP4WM achieving $> 20\,\text{dB}$ gain in the 4–12 GHz frequency range[10], using PPCs to ensure $Z_0 = 50\,\Omega$. I used a CPW geometry for the STL, motivated by its simplicity to integrate the PPCs with the trilayer junction fabrication process used in this thesis, where the deposition of a dielectric layer (called spacer) is required for the junctions (see Chapter 4).

The Sonnet® model of the unit cell and resonator all were identical to the example provided in the previous section. The resonator's geometry was optimised for $f_r =$

[10]Most of the presented designs aimed to operate in this regime, which is the transmission bandwidth of the circulators used in the experimental setups (see Chapter 4).

7 GHz, and the PPCs length was chosen to match $Z_0 = 50\,\Omega$. I implemented two designs: Design A, using junctions with $A_{\rm jj} = 0.5\,\mu{\rm m}^2$ and $J_{\rm c} = 1.4\,{\rm kA/cm}^2$, and Design B, using junctions with $A_{\rm jj} = 0.5\,\mu{\rm m}^2$ and $J_{\rm c} = 0.9\,{\rm kA/cm}^2$. The choice of these $A_{\rm jj}$ and $J_{\rm c}$ values was intended to reach the highest $L_{\rm j}$ achievable with the fabrication facilities accessed during my DPhil (further discussion in Chapter 5).

I built a supercell in both designs by cascading N unit cells and M resonator cells. Then, the supercell is cascaded $N_{\rm sup}$ times to form the JTWPA, as illustrated in Fig. 3.12(a). Since each unit cell has 2 junctions and each resonator cell has 8 junctions, the number of junctions in the JTWPA is given by $N_{\rm jj} = (2N + 8M)N_{\rm sup}$. The parameter values of both designs are summarised in Tab. 3.1. Numerically solving the generalised CME equations[11] for Design A, I obtained the gain curves plotted in Fig. 3.12(b) for different values of $I_{\rm p}/I_{\rm c}$. We need to tune the $f_{\rm p}$ at each pump power to achieve optimal gain. The dotted line shows the case without RPM, demonstrating the substantial gain and bandwidth enhancement resulting from adding the dispersion-engineering components. Fig. 3.12(c) shows the gain curves for Design B using different $I_{\rm p}/I_{\rm c}$ values, tuning $f_{\rm p}$ to optimise the gain. We observe that both designs can achieve gain values over 20 dB with a large bandwidth. As expected, Design B reaches higher gain values owing to the larger $L_{\rm j}$.

3.5.2 JTWPAs with interdigitated capacitors (IDCs)

As will be discussed in Chapter 5 and Chapter 6, using PPCs in the design resulted in a low fabrication yield due to the high density of pin-holes in the dielectric layer. To circumvent this issue, I designed another microwave JTWPA using interdigitated capacitors (IDCs), which do not require any dielectric layer. This design choice imposes a CPW geometry for the transmission line. The design was also intended to match Z_0, using $A_{\rm jj} = 0.5\,\mu{\rm m}^2$ junctions with $J_{\rm c} = 1.4\,{\rm kA/cm}^2$. Contrary to the previous design, here, I used a periodic loading structure for dispersion engineering instead of coupled resonators. This design choice was motivated by the challenging implementation of microwave resonators without a dielectric layer with the IDCs in the line, as well as the spread in $f_{\rm r}$ that I measured later in Chapter 6. Periodic loading can be easily implemented in the STL by periodically changing the length of the IDCs.

[11] Here, I used numerical methods to solve the CME, rather than the analytical solution in Chapter 2, to include effects such as the pump depletion for a more accurate solution.

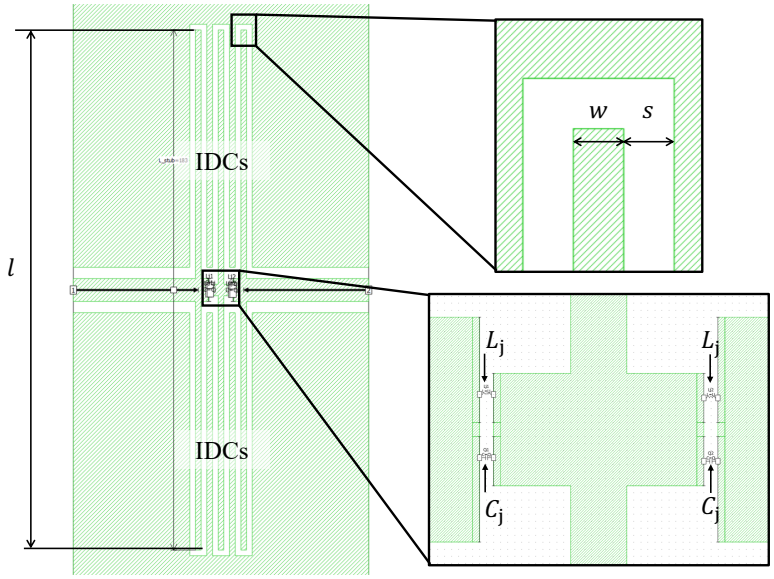

Figure 3.13: Sonnet® model of the JTWPA with IDCs unit cell.

I implemented two designs: Design C, operating in the DP4WM regime, and Design D, operating in the DC3WM regime. Both designs intended to achieve $> 20\,\mathrm{dB}$ in the 4–12 GHz range. I used Sonnet® to model the unloaded ($Z_0 = 50\,\Omega$) and loaded ($Z_0 \neq 50\,\Omega$) unit cells of the design. Fig. 3.13 shows an example of the designs' unit cell model in Sonnet®, where the junctions were implemented as described in Sec. 3.4. I optimised the IDCs length to match the required impedance of the loaded and unloaded unit cell using the same technique as described in Sec. 3.4.

Similar to the PPCs design, I created a supercell with N unloaded unit cells and M loaded unit cells, which I cascaded N_{sup} times to create the JTWPA model. N determines the center frequency of the first stopband[12] f_{per}, which can be calculated as $N = \pi/k_{\mathrm{cell}}(f_{\mathrm{per}})$, where k_{cell} is the wavevector of the unloaded unit cell. Since N can only be an integer, the calculated results need to be approximated to the closest integer value. The k_{cell} is calculated from the simulation's S-parameters results as presented in Sec. 3.1.1.

[12]Remember that stopbands generate at multiples of f_{per}.

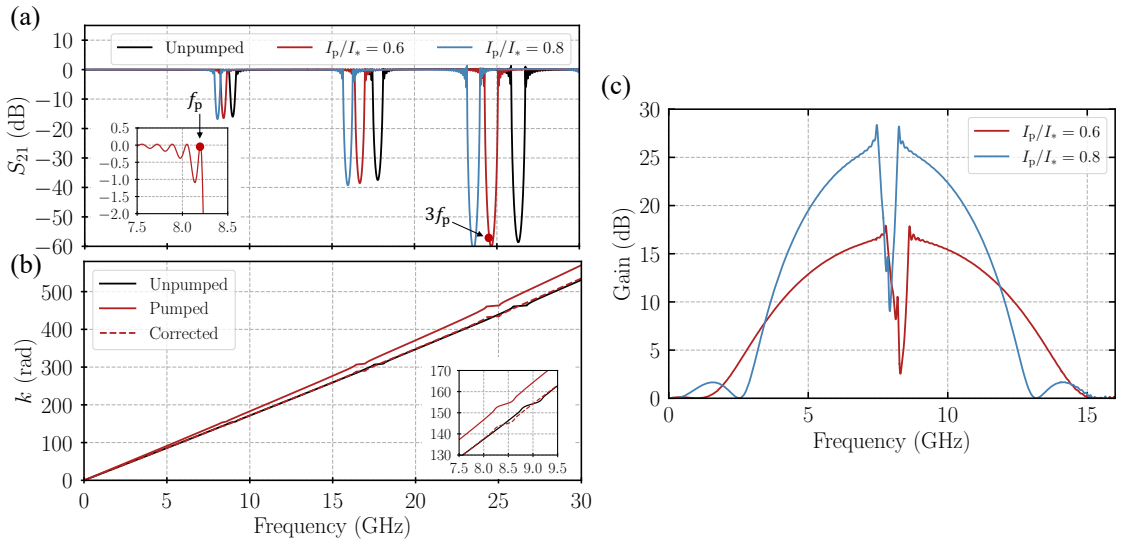

Figure 3.14: Simulation results of JTWPA with IDCs Design A. (a) S_{21} profile for the cascaded model using different I_p/I_* values. The f_p used for $I_p/I_* = 0.6$ to generate the gain in (c) is indicated on the plot, as well as $3f_p$. (b) Total k of the device when unpumped (black) and pumped with $I_p/I_* = 0.6$ (solid red). The corrected k (dashed red) and unpumped k have the same phase velocity. All the curves include the effect of the geometrical inductance. (c) Calculated gain curve using the CME for $I_p/I_* = 0.6$ with $f_p = 8.2\,\text{GHz}$ (red) and $I_p/I_* = 0.8$ with $f_p = 7.85\,\text{GHz}$ (blue).

Since N depend on k_{cell}, which changes when the device is pumped due to the nonlinear inductance, pumping the device results in a frequency shift of the stopbands. This effect can be accounted for by running the simulations using the $L_j(I_p/I_*)$ instead of L_0 for the junction's inductance. Therefore, every I_p/I_* that we want to investigate requires separate simulations. Fig. 3.14(a) shows the S_{21} profile of Device C, calculated from simulations with $I_p/I_* = 0$, 0.6 and 0.8. We clearly notice the shift to lower frequencies of the stopbans due to the increased inductance of the line with pump power. Since the wavevector k in the generalised CME is defined as $k_m = \omega_m/v_0 = \omega_m\sqrt{L_0C_s}$, where $v_0 = 1/\sqrt{L_0C_s}$ is the unpumped phase velocity, when using the S_{21} data to calculate γ_m, we need to correct k to maintain v_0 while accounting for the shift of the stopbands. An example of this process is given in Fig. 3.14(b), where the k obtained from the simulation using $I_p/I_* = 0.6$ (solid red line) is corrected to match the slope, i.e., the phase velocity of the unpumped case (black). Finally, using the corrected γ_m, we can solve the generalised CME equations obtaining the gain curves plotted in Fig. 3.14(c) for Device C. This design successfully achieves $> 20\,\text{dB}$ gain in the intended frequency range, while successfully suppressing the generation of harmonics of the pump.

Following the same process, in Design D, I calculated N for a resulting stopband around 12 GHz when the device is pumped[13]. Fig. 3.15(a) shows the calculated S_{21} for Device D obtained from cascading the results of the simulations in Sonnet®. The depth of the stopband is increased by using larger loading sections, i.e., $M = 2$. Calculating γ_m from the S_{21} results and correcting the wavevector, I numerically solved the generalised CME to calculate the gain curve. Fig. 3.15(b) shows the gain for Design D with $I_{dc}/I_* = I_p/I_* = 0.35$, where values close to 20 dB are achieved. The gain can be further increased by using larger I_{dc} or I_p. Furthermore, this design provides a larger bandwidth than the 4WM counterpart, while still efficiently suppressing the generation of pump harmonics. The design parameters of both designs are summarised in Tab. 3.1.

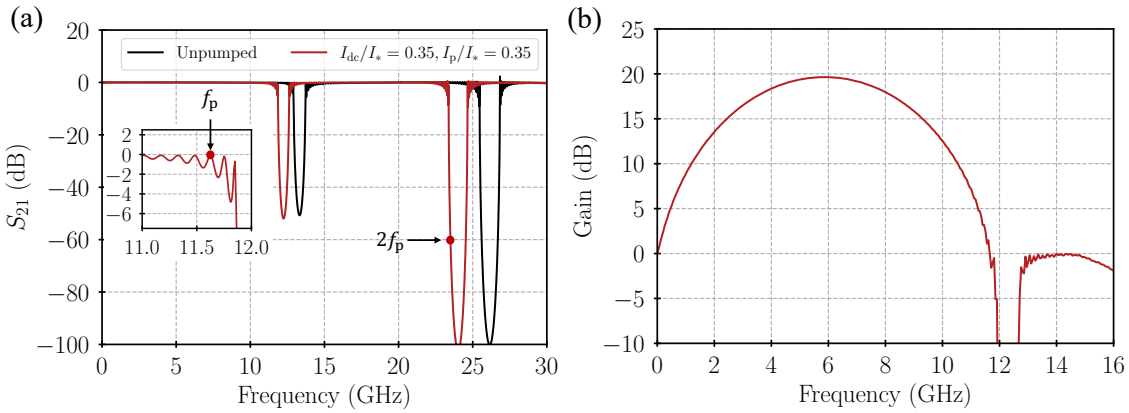

Figure 3.15: Simulation results of JTWPA with IDCs Design B. (a) S_{21} profile for the cascaded model for the unpumped (black) and pumped ($I_{dc}/I_* = I_p/I_* = 0.35$) (red) case. The f_p used to calculate the gain curve in (b) is indicated on the plot, as well as $2f_p$. (b) Calculated gain curve using the CME for $I_{dc}/I_* = I_p/I_* = 0.35$ with $f_p = 11.75$ GHz.

[13]I designed the stopband to be as high as possible in the transmission frequency range of the circulators we had in our laboratory.

Design	C_s tech	J_c $\left(\frac{kA}{cm^2}\right)$	A_{jj} (μm^2)	L_0 (pH)	C_j (fF)	l_0[1] (μm)	l_1[2] (μm)	w[3] (μm)	s (μm)	N	M	N_{sup}	N_{jj}	a (μm)
A	PPC	1.4	0.5	47.0	36.8	51.5	77.0	6	N/A	40	1	23	2,024	10
B	PPC	0.9	0.5	73.2	36.6	81.0	147.0	6	N/A	60	1	15	2,024[4]	10
C	IDC	1.4	0.5	47.0	36.8	183.0	40.0	2.0	2.0	20	1	49	2,058	8[5]
D	IDC	1.4	0.5	47.0	36.8	190.0	107.0	2.0	2.0	12	2	72	2,016	8[5]

[1] Length of the PPCs (IDCs) in the (unloaded) unit cell.
[2] Length of the PPCs (IDCs) in the resonator (loaded) unit cell.
[3] Width of the PPCs (IDCs).
[4] For this design we added 26 unit cells at the beginning and the end of the device to match the aimed dimensions of the chip when implemented in the photolithography mask. These extra unit cells are not accounted in N.
[5] a alternate between 10 µm and 6 µm, therefore, I indicate the average value on the table.

Table 3.1: Design parameters of the microwave JTWPA with IDCs designs.

3.6 Conclusion

In this chapter, I have discussed different approaches I used for simulating JTWPAs, such as harmonic balance simulations and CME-based techniques. I validated the CME framework presented in the previous chapter by comparing it with the standard CME framework and reproducing measurement results. The results were satisfactory, demonstrating the capabilities of this generalised framework, which only requires the γ_m information of the TWPA design. Using this framework, I then explored the JTWPA circuit parameters space and their impact on the figures of merit of the device. This analysis provided better insights into the behaviour of JTWPAs and highlighted possible optimisation approaches to tailor specific applications.

Finally, I introduced a novel design methodology that successfully combines the EM simulators and the generalised CME framework to predict the gain performance of the device from the actual physical layout of the unit cells. This powerful approach was applied to model four JTWPA designs: two using PPCs and RPM, and the other two using IDCs with periodic loading. All designs achieved > 20 dB gain in the 4–12 GHz range, with geometries compatible with the fabrication facilities available during my DPhil. As discussed later, these designs were fabricated and tested, with the experimental results detailed in Chapter 6 and Chapter 7.

Chapter 4

Fabrication techniques and experimental setups

The invention of JTWPAs was only possible through the impressive progress in superconducting micro-fabrication, cryogenics and microwave engineering in the past 50 years. In this chapter, I give an overview of the Josephson junction fabrication techniques, including the trilayer fabrication process used for the devices presented in this thesis. I also discuss the packaging techniques, essential to improve the performance of JTWPAs. Finally, I explain the main cryogenic technologies and the systems used to characterise all the microwave devices presented in this thesis, as well as the different experimental setups for carrying out different types of measurement.

4.1 Devices' fabrication

Our fabrication collaborators from the Institut de Radioastronomie Millimétrique (IRAM) in France, have over 30 years of experience in fabricating superconducting astronomical detectors, continuously delivering devices for the Northern Extended Millimetre Array (NOEMA) and the IRAM-30m telescopes, as well as other major international projects such as ALMA[1] and Herschel space telescope [115]. Some of the superconducting devices fabricated at IRAM include MKID arrays and SIS mixer detectors. The latter requires niobium Josephson junctions for their operation in the mm-wave range; hence, IRAM has developed and optimised niobium junctions trilayer fabrication recipes. With this collaboration between the two groups, I had the opportunity to access their class-100 clean-room facilities to fabricate all the devices presented in this thesis, supported by the members of the superconducting devices group at IRAM. The devices were fabricated over 4 visits from 2022 to 2024.

[1]IRAM fabricated the SIS mixers for band 7 of ALMA [114].

4.1.1 Josephson junction fabrication techniques

Since the first observation of the Josephson tunnelling effect in thin tin oxide (SnO_2) barriers between superconducting tin (Sn) and lead (Pb) [116], numerous techniques and processes have been developed to fabricate Josephson junction with different materials. Nevertheless, junctions fabricated using aluminium (Al) or niobium (Nb) are the most popular choice for applications below 700 GHz. This material choice relies on the their good agreement with the BCS theory of superconductivity and their high-quality fabrication — and high-quality oxide growth in the case of Al — using standard micro-fabrication processes.

Aluminium is currently the preferred choice for microwave applications, driven by the advances in superconducting quantum computing foundries. Aluminium junctions are commonly fabricated using double-angle evaporation techniques [117], achieving junction areas as small as $0.008\,\mu m^2$, with remarkable size and critical current homogeneity over areas of hundred of mm^2 [118, 119]. On the other hand, the higher T_c of niobium is preferred for applications at higher operational temperatures and frequencies. However, early attempts to fabricate junctions using the natural oxide of the Nb as the dielectric layer yielded poor electrical properties mainly due to the affinity of oxygen for niobium, and the absence of a single stoichiometric oxide in the dielectric layer [120, 121, 122]; therefore, making Nb incompatible with double-angle evaporation techniques. Instead, Nb junctions are fabricated using trilayer processes [123], where a 'sandwich' of Nb/Al-AlO_x/Nb is deposited and then patterned to form the junctions. The Al layer (~ 1 nm thick), provides the means for a controlled oxide growth, necessary for a high-quality junction. Trilayer junctions provide more design flexibility over double-angle evaporated junctions due to the availability of crossovers and the ability to define the junction of any shape. This allows to 'stack' different junction layers on top of each other for very large scale integrated (VLSI) circuits, with 8 to 10 superconducting layers, yielding up to $\sim 1.5 \times 10^7$ junctions per cm^2 [124, 125]. However, unlike double-angle evaporation techniques, junctions smaller than $\sim 250\,nm^2$ are challenging to fabricate using trilayer techniques. To circumvent this issue, trilayer-based processes to fabricate Nb/Al-AlO_x/Nb cross-type junctions have equally been developed, further reducing the size and parasitic capacitance of the junctions [126, 127].

The maturity of the junction fabrication techniques over the past 20 years has played a key role in the development of JTWPAs. The large number of junctions required to form a JTWPA imposes a strict control of the junction parameters spread during fabrication, which otherwise could substantially deteriorate the performance.

Foundry	Year	Junction	Fabrication technique	N_{jj}	I_c (µA)	C_s technique	Dielectric material (technique)
MIT Lincoln Laboratory [79]	2015	Nb/Al-AlO_x/Nb	Standard trilayer	2,037	4.6	PPC	SiO_2 (PECVD)[a]
UC Santa Barbara [132]	2015	Al/Al_2O_3/Al	Double-angle evaporation	1,326	5	PPC	a-Si:H
Rigetti computing [128]	2020	Al/Al_2O_3/Al[b]	Double-angle evaporation	Unknown	3.3-8.2	PPC	Unknown
Néel Institut[c][80]	2020	Al/Al_2O_3/Al	Double-angle evaporation	4,320	2.7	Microstrip	AlO_x (ALD)[d]
VTT [133]	2021	Nb/Al-AlO_x/Nb	Cross-type trilayer	4,064	4.4	PPC	AlO_x (ALD)
MIT Lincoln Laboratory [112]	2022	Nb/Al-AlO_x/Nb	Standard trilayer	3,141	3.14	PPC	SiO_2
Néel Institut[e][81]	2022	Al/Al_2O_3/Al	Double-angle evaporation	2,800	2.19 / 0.15	Microstrip	AlO_x (ALD)
Chalmers University [82] of Technology[f]	2023	Al/Al_2O_3/Al	Double-angle evaporation	1,760	Unknown	PPC	a-AlN

[a] Plasma Enhanced Chemical Vapor Deposition (PECVD).
[b] Inferred, not specified on the manuscript.
[c] SQUID-array JTWPA. The number of SQUIDs is $N_{jj}/2$ and I_c refers to the individual junctions in the SQUID.
[d] Atomic Layer Deposition (ALD).
[e] SNAIL-array JTWPA. The number of SNAILs is $N_{jj}/4$ and $I_c = 2.19\,\mu A$ corresponds to the three junctions in one branch and $I_c = 0.15\,\mu A$ to the single junction in the other branch.
[f] SNAIL-array JTWPA. The number of SNAILs is $N_{jj}/4$.

Table 4.1: Summary of the different fabrication aspects of successful JTWPAs reported in the literature.

The study of the junctions' fabrication tolerance impact on the JTWPA performance has been the focus of many studies [103, 128, 129, 130, 131]. Despite numerous efforts to fabricate these devices, in the past 10 years only a handful of institutions have reported high ($> 15\,dB$) broadband gain. The main fabrication aspects of these successful implementations are summarised in Tab. 4.1. Although each implementation has a different design, uses different material combinations and junction technologies, all the JTWPAs share two characteristics: large number of junctions (over 1,000), and low critical current ($I_c < 5\,\mu A$).

4.1.2 Fabrication recipe

All the devices fabricated over the course of my DPhil used a trilayer junctions recipe originally developed for the fabrication of SIS mixers with high critical current. This recipe was adapted for the fabrication of JTWPAs, which requiring much lower critical current junctions, as well as other structures such as parallel plate capacitors (PPCs). In this section, I present in details the final recipe used for the fabrication of all the devices discussed in this thesis.

The devices were fabricated using intrinsic silicon wafers with a resistivity $R >$

20 kΩcm to limit the losses in the substrate. The thickness of the substrate was 280 µm and 500 µm, depending on designs, with a diameter of 2 inches. The wafers were double-side polished, with a <100> crystal growth orientation. The fabrication recipe is divided in three main steps.

SiO_2 protective layer and trilayer deposition

The first step in the fabrication recipe consists of depositing an SiO_2 protective layer to avoid etching the silicon substrate at later stages of the fabrication (Fig 4.1(a)&(b)). The SiO_2 protective layer is deposited using a sputtering machine (PLASSYS MP300), where the ions from an argon plasma bombard an SiO_2 target which ejects SiO_2 particles in a high vacuum environment (10^{-7} mbar) in the machine's chamber, resulting in a thin layer deposition on the surface of the wafer. The main parameters controlling the deposition are the argon input rate in the chamber, controlling the density of plasma ions, and the power applied to the target that accelerates the plasma ion. Using the parameters presented in Appendix A (Tab. A.1), I obtain an SiO_2 layer of ~ 70 nm.

Once the SiO_2 protective layer is deposited, I spin a photosensitive resist on top of the wafer creating a resist layer of 1.2 µm (Fig 4.1(c)). Then, I use a mask made of glass, where the trilayer structures that need to be patterned on the resist are covered with chrome. Using a mask aligner machine, the wafer and the mask are held in contact and ultra-violet (UV) light is shined through the mask, changing the physical properties of the areas of the resist exposed to it. In this recipe, I apply the resist AZ5214 JP which can be used as a positive or a negative resist. In this step, I use it as a negative resist by baking the wafer and performing a second exposure without the mask (flood). Since using a negative resist, the areas exposed to the light remain after the development of the resist. This process is called UV photolithography[2].

After the development of the resist (Fig 4.1(d)), the trilayer is deposited using a sputtering machine with a niobium and an aluminium target (Alcatel SCM 450) (Fig 4.1(e)). The trilayer deposition requires three steps; a first niobium layer of 120 nm is deposited, followed by a very thin aluminium layer. Then oxygen is added to the machine's chamber where the deposition takes place to oxidise the aluminium,

[2]Note that although this step involves a negative photoresist, photolithography can be implemented with both negavite and positive resist.

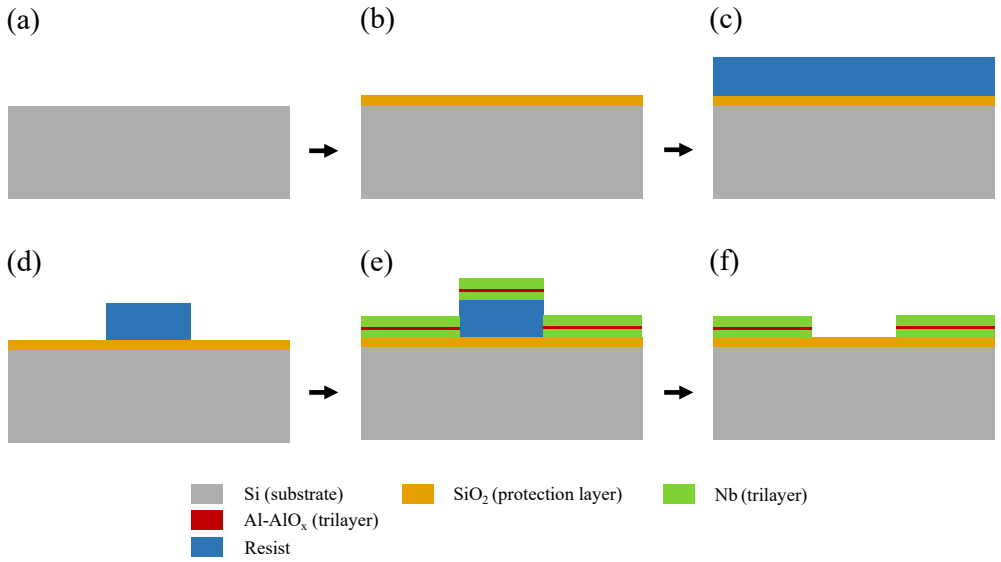

Figure 4.1: Fabrication steps, figures not to scale. (a) Silicon wafer at the beginning of the process. (b) Deposition of the SiO_2 protective layer. (c) Deposition of the resist. (d) View of the wafer after the photolithography, the trilayer structures are patterned on the resist. (e) Trilayer deposition. (f) View after the liftoff step.

creating an AlO_x layer[3]. The thickness of this dielectric layer determines the critical current density of the junction, which is controlled by the O_2 pressure in the chamber and the oxidation time. For the fabrication of my devices, I explored different oxidation parameters, summarised in Appendix A (Tab. A.1). Finally, another niobium layer of 140 nm is deposited on top of the AlO_x, concluding the trilayer structure. Subsequently, I perform a liftoff step to remove the trilayer from the unwanted areas on the wafer (Fig 4.1(f)). This step basically defines the 'ground' and part of the trace of all my devices.

Junctions definition and dielectric growth

Once the trilayer is successfully patterned, the next step consists of defining the junctions using electron beam (ebeam) lithography. Compared with the UV photolithography used in the previous step to define the trilayer structures, the ebeam lithography uses an electron beam to pattern the resist. Since electron beams have a smaller wavelength than UV light, smaller structures can be patterned with a higher

[3]The formation of the fully stoichiometric form of aluminium-oxide (Al_2O_3) requires a more thorough oxidation process or higher oxygen pressures. The partial oxidation often employed in trilayer processes results in non-stoichiometric oxides, referred as AlO_x

precision[4]. UV photolithography usually struggles to achieve structures smaller than 1 µm. Because my designs require junctions smaller than 1 µm^2, an ebeam lithography step is required in the recipe. Similarly to the previous lithography step, I start by spinning the resist Ma-N 2405, a negative resist sensitive to electron beams and UV light (Fig 4.2(a)). Then, I pattern the junctions in a Raith eLine scanning electrons microscope (SEM). To make sure the junctions are aligned, I add alignment crosses at the corners of each chip, which is used by the machine's software to locate the structures to write.

Following the junctions' patterning, a dielectric window around the junctions needs to be created to isolate the two metallisation layers used to contact the two electrodes of the junction. In a conventional trilayer fabrication process of an SIS mixer, the dielectric window is patterned at the same time as the junction using UV lithography [135]. In my case, defining the dielectric windows using ebeam lithography would be an extremely slow process, since the whole chip but the areas of the dielectric windows would need to be patterned with the electron beam[5]. Therefore, once the junctions are patterned, I perform an UV photolithography exposure of the wafer, patterning the dielectric windows around the junctions and creating the dielectric structures of the capacitors (when it applies). Finally, I develop the resist to expose the surfaces were the dielectric needs to be deposited (Fig 4.2(b)).

After the development of the resist, the second niobium layer of the trilayer needs to be etched away around the junction (Fig 4.2(c)). I use an Alcatel 601E Inductively Coupled Plasma - Reactive Ion Etching (ICP-RIE) machine, where the ions of a plasma of SF6 and C4F8 are accelerated against the surface of our wafer, etching the niobium at a speed of $\sim$ 100 nm/min. While the plasma has a much lower etching rate for the AlO_x and SiO_2, the etching rate for the silicon is $\sim$ 3-5 µm/min, i.e., much faster than the niobium. Therefore, the need of an SiO_2 protective layer on top of the bare silicon wafer deposited at the beginning of this recipe, to avoid an over-etching that could result in open-circuited structures in our devices.

From the characterisation of the JTWPA test devices presented in Chapter 5, I observed that using a dielectric layer made of $\sim$ 20 nm Al_2O_3 and 200 nm SiO_2 helped

[4]The photolithography resolution is ultimately limited by the wavelength of the UV light used in the process. Although using $\lambda \sim 250 - 350$ nm in this process, reaching such a small resolution requires high-quality optics that were not available in the mask aligner machine used for this recipe. Nevertheless, the semiconductor industry has pushed the boundaries of photolithography to the extremes, regularly using UV light with $\lambda \sim 13.5$ nm for the most demanding electronic chips [134].

[5]Remember that I am using a negative resist in this step. Given the small size of the electron beam, insulation of large areas is very time consuming.

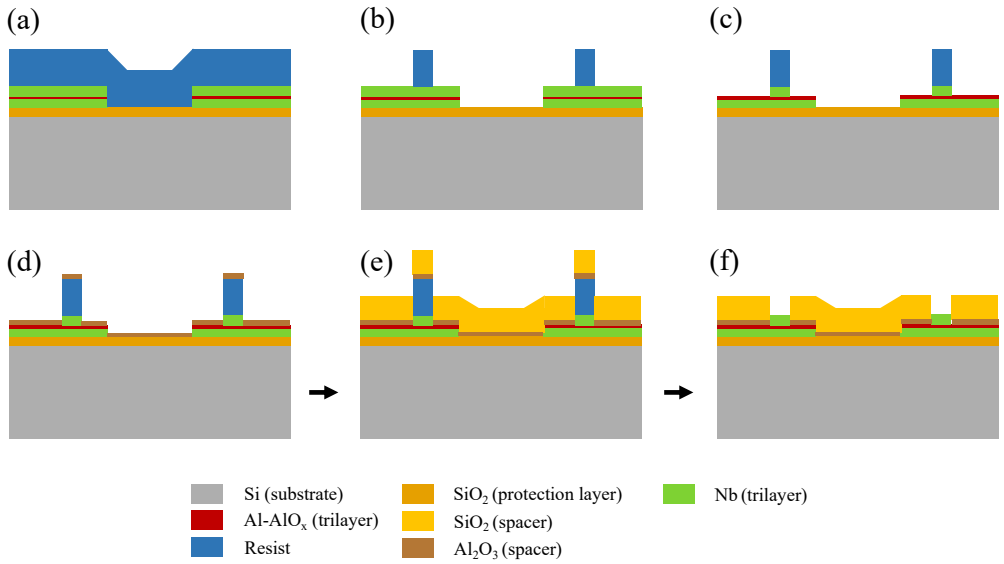

Figure 4.2: Fabrication steps, figures not to scale. (a) Spining of the resist. (b) View of the wafer after the ebeam lithography and photolithography steps. The resist on top of the trilayer at the centre of the figure represents the resist patterned with the ebeam lithography, which will form the junction. The resist on the edges of the substrate represent the resist patterned with the UV lithography, which helps to create a window around the junctions where the dielectric will be deposited. (c) Etching of the top niobium layer of the trilayer. (d) Al_2O_3 evaporation. (e) SiO_2 sputtering deposition. (f) View after liftoff step.

to reduce the pin-holes causing short-circuits in the devices (see Sec. 5.4). Therefore, following the etching, I deposit a thin layer of Al_2O_3 using a Plassys MP500S evaporation machine (Fig 4.2(d)). The deposition is performed in a high vacuum chamber, where a target containing the material to deposit is heated, by the mean of an electron-beam, until evaporation resulting in a deposition on the wafer's surface. In my case, I use an aluminium target in an atmosphere filled with O_2, therefore, the aluminum particles react with the oxygen creating a thin Al_2O_3 layer. The parameters used to deposit an Al_2O_3 layer of ~ 20 nm are shown in Appendix A (Tab. A.2). Next, I deposit a $\sim$200 nm SiO_2 layer (Fig 4.2(e)) using the same sputtering machine used for the deposition of the protective layer and I complete this step with a liftoff in acetone (Fig 4.2(f)). Note that given the small sub-micron size of the junctions, the wafer needs to be left for a long time (about 10 hours) in acetone to make sure that the resist below the junctions is fully dissolved, avoiding open-circuited junctions in our devices.

Second metallisation layer and bonding contacts deposition

Following the growth of the dielectric layer, I deposit the second metallisation layer, connecting the wiring layer to the junctions to form the trace of the coplanar waveguide (CPW) and also to form the PPC. First, I pattern the negative resist using UV photolithography (Fig 4.3(a)&(b)), which requires a fine alignment ($< 1.5\,\mu m$) with respect to the existing structures on the wafer in this step. Next, I deposit a 420 nm thick niobium layer (Fig 4.3(c)) using the same sputtering machine used for the trilayer deposition. The deposition parameters for this are summarised in Appendix A (Tab. A.3). Finally, I perform a liftoff to remove the niobium from the unwanted areas (Fig 4.3(d)).

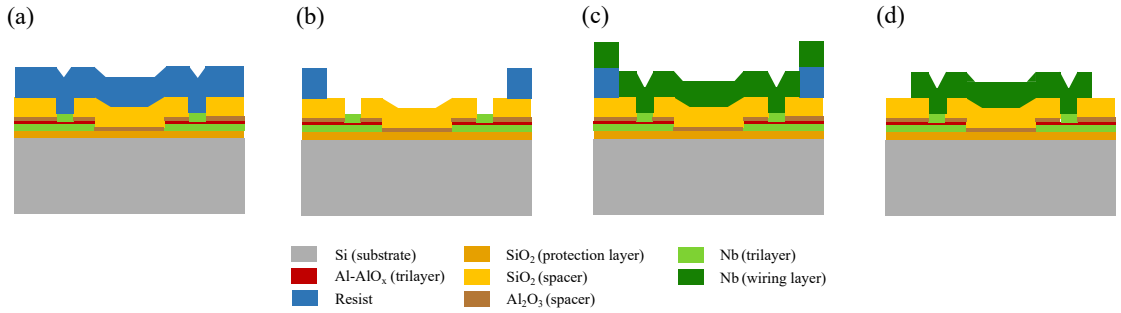

Figure 4.3: Fabrication steps, figures not to scale. (a) Spinning of the resist. (b) View of the wafer after the photolithography. (c) Sputtering deposition of the niobium layer. (d) Liftoff.

It is well known that the niobium is a difficult material to connect with bondwires, which are essential to electrically connect the chip with the external circuitry. A common practice, implemented in my designs as well, consists of covering bondwires connection areas with gold. However, due to the poor chemical affinity between the gold and the niobium, a titanium layers needs to be used as an adhesion layer. Therefore, the final step in the fabrication recipe consists of growing in some dedicated areas of the wafer a very thin ($\sim$5-7 nm) titanium layer before the deposition of a $\sim$ 120 nm thick gold layer. For this process, I use a positive resist[6] patterned using UV photolithography, followed by the titanium and gold deposition using a Plassys MP500 sputtering machine. The deposition of both metals take place in the machine's chamber without breaking the vacuum to avoid the interaction of the titanium with

[6]In this recipe, the fabrication parameters of the negative resist are optimised for a liftoff process, contrary to the positive resist. However, the positive resist requires less steps. Since the gold structures do not require a precise definition, we chose a positive resist to speed up the process.

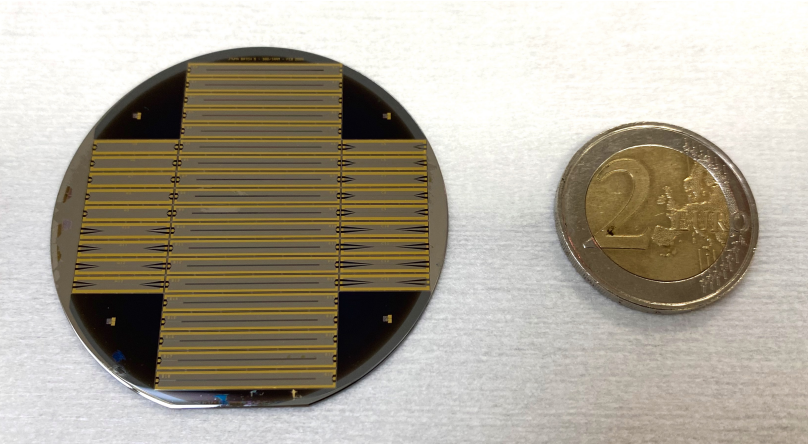

Figure 4.4: Image of a fabricated wafer before dicing. A 2 € coin is placed next to it for scale comparison.

oxygen that could form an oxide layer. The parameters used for the deposition are shown in Appendix A (Tab. A.4). After carrying out the liftoff step, the entire fabrication process is completed. An example of the completed wafer is shown in Fig 4.4. The final step consists of separating the individual devices using a dicing machine.

4.2 Mounting techniques and sample-holders

Interconnecting microwave planar nonlinear circuits with the passive 50 Ω coaxial cables without creating an impedance mismatch is a challenging task. The mounting techniques require precise engineering to optimise the devices' performance. In this section, I give an overview of the approaches used for the devices presented in this thesis. An image of a device assembly is shown in Fig. 4.5. There are four main parts of the sample holder:

RF connectors

Numerous connector technology exist varying in shape and operational frequency, e.g., SMK, SMA or SMB. In all the devices presented in this thesis, we used SMA (SubMiniature version A) connectors, which have a 50 Ω impedance and operate in the DC to $\sim$ 18 GHz regime[7].

[7]The frequency limit results from the dielectric used to separate the center pin and the ground. Other solutions like the SMK connectors get rid of this dielectric material extending the operational frequency to 40 GHz.

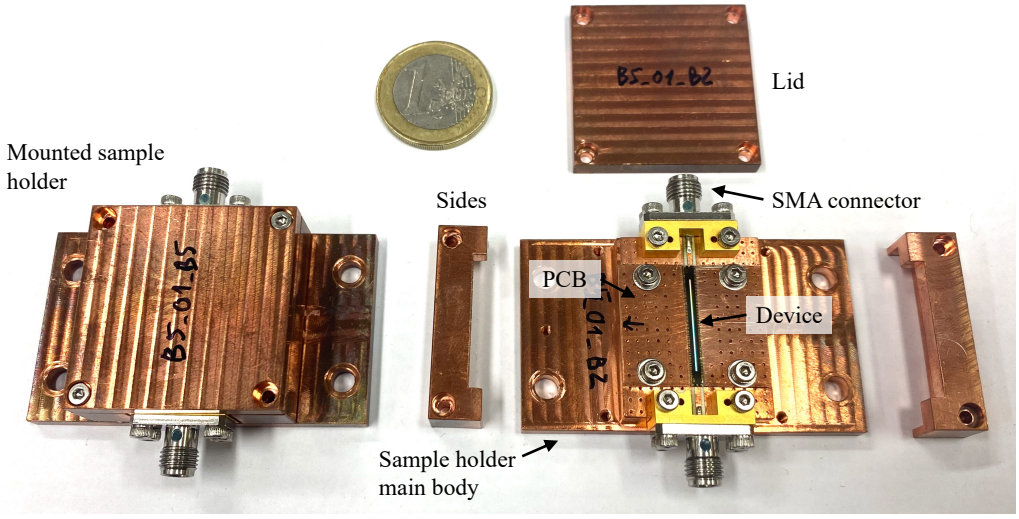

Figure 4.5: Sample-holder A assembly. The sample holder on the left is assembled, while the sample holder on the right is dismounted showing the different parts. A 1 € coin is included for scale comparison.

Printed circuit board (PCB)

Normally, a printed circuit board (PCB) is used to connect the TWPA chip with the RF connectors. I designed all the connecting PCBs used in all the devices presented in this thesis. They were fabricated by Mr. Rik Elliot using the in-house PCB fabrication facility.

All the PCB designs consisted of a 50 Ω copper CPW. The centre pins of the RF connectors were soldered at each end to the CPW trace. The dielectric material used for the PCBs was a 0.508 mm thick Roger Duroid® RO4350b, which has a dielectric constant $\epsilon \approx 3.66$ and loss tangent $\tan\delta \approx 3.7 \times 10^{-3}$. The two ground planes of the CPW were populated with vias-holes to ensure the electrical continuity of these ground planes to the body of the sample holder, as well as to disrupt possible resonant modes originating in the PCB. Two different techniques were used for the devices presented in this thesis. The first technique, used PCBs with the cooper layer etched where the chip was located at the centre of the PCB, illustrated in Fig. 4.6(a). Since the cooper below the chip was removed, chips with different dimensions needed different PCB designs. Furthermore, the dielectric constant from the PCB material was accounted in the design of the chips' bondpads, restricting the chips to that specific PCB material and design. Also, since the device was sitting on top of the PCB, long bondwires were needed to connect to the trace and ground of the PCB due

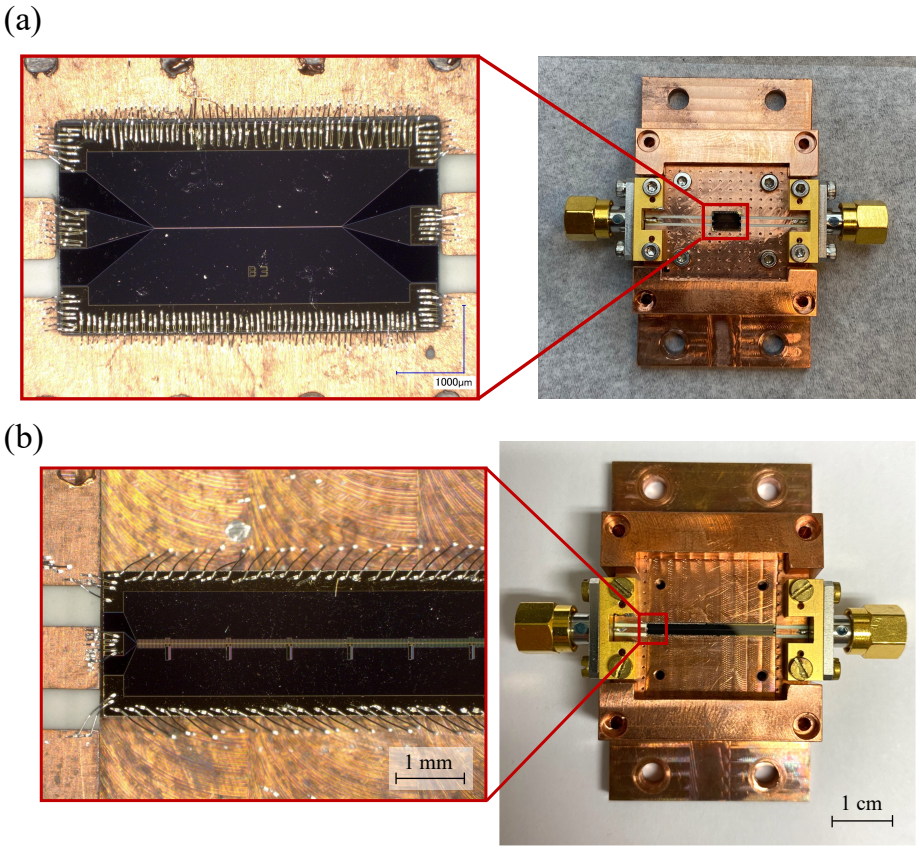

Figure 4.6: (a) The device is mounted on top of the PCB, and connected to the PCB trace and ground using bondwires. (b) The PCB is cut and the device sit on top of the sample holder main body. The device's ground plane is directly connected to the sample holder using bondwires.

to the height difference, which could contribute to an impedance mismatch[8]. This technique was only used for the devices presented in Chapter 5. To alleviate some of these issues, for the rest of the devices presented in this thesis, I used the second technique illustrated in Fig. 4.6(b). In this technique, the device sits on top of the sample holder body, glued using crystalbond™ adhesive, and only small PCBs are used at the extremes to connect with the RF connectors. Since the thickness of the PCB and chip are similar, much shorter bondwires are needed to interconnect them. The ground of the chip is directly bonded to the ground of the sample holder.

[8]The bondwires have an intrinsic inductance proportional to their length. This could generate impedance mismatches at the input/output of the device, resulting in unwanted reflections affecting the performance of the device. Often, several short bondwires in parallel are used to connect the PCB trace with the chip, as shown in Fig. 4.6, to minimise this effect.

Bondwires

To electrically connect the planar superconducting circuit chip with the PCB board, we used aluminium bondwires (99% aluminium and 1% silicon), as shown in Fig. 4.6. During my DPhil, I also investigated the effect of replacing the Al bondwires with gold bondwires, which did not show any improvement in the RF characteristics of the tested devices, but requiring a more complicated bonding technique[9]. Therefore, all the devices presented in this thesis used wedge Al bondwires with a 25 µm^2 cross-section area. We observed a better RF performance of the devices with higher number of bondwires connecting the ground plane of the device and the PCB board. Hence, all the devices that I tested incorporated a high density of bondwires ($\sim$ 5/mm), which made the bonding process time-consuming and tedious, often taking over one hour per chip. I wire-bonded all the tested devices presented in this thesis using the in-house wedge-bonding machine Kulicke & Soffa® Model 4523.

Sample-holder

The sample holder is the enclosure that host the DUT and the PCB, with the RF connectors installed in its interfaces. The sample holder is generally affixed to the cold-plate of a cryostat and connected with coaxial cables for interaction with the experimental setup. To ensure a good thermal contact with the cold plate, we used oxygen-free copper as the material for all the sample holders[10].

During my DPhil programme, I mainly used two different sample holder designs. Sample-holder A, shown in Fig. 4.6, was designed by Dr. Boon-Kok Tan. This modular design opts for flexibility in hosting a large number of different TWPA designs, including KTWPAs. It uses Gigalane® PSF-S05-000 SMA connectors, which allow for ease connecting and disconnecting the RF connectors, hence facilitating the use of different PCB designs. However, its constrained dimensions complicated the bonding process for long devices, since the connectors would block the bonding wedge. To alleviate this issue, and to optimise the sample holder specifically designed for the JTWPA devices presented in this thesis, I designed sample-holder B using the computer-aided design (CAD) sofware Autodesk® Inventor. This sample holder, as shown in Fig. 4.7, extended the distance between the RF connectors to the edge of

[9]The chip needed to be warmed up to $\sim 80\,^{\circ}$C during the bonding process for the gold bondwires to successfully bond with the chip and the PCB.

[10]Some of the sample-holders were gold-plated to avoid oxidation and improve the thermal contact.

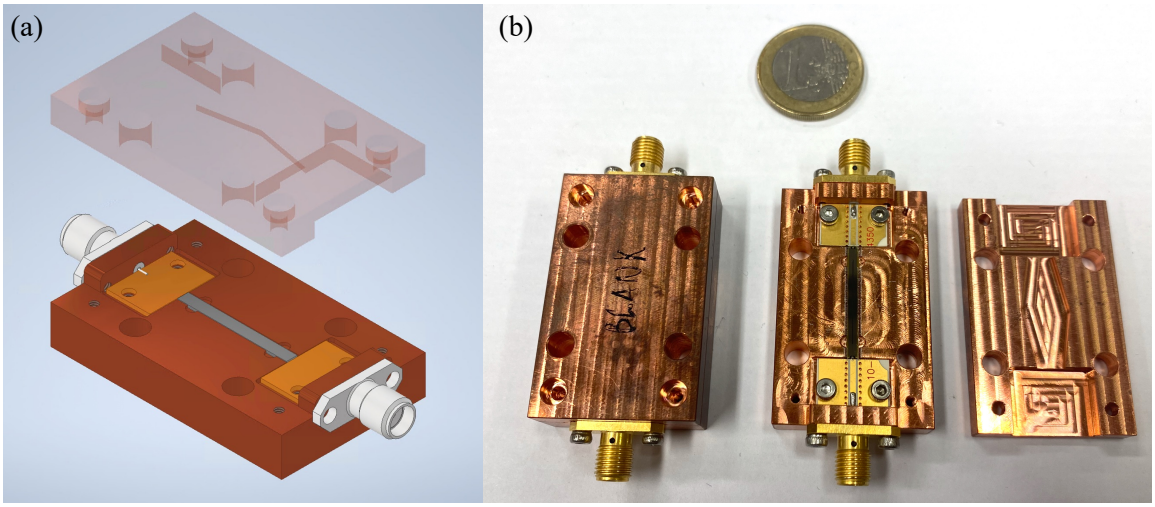

Figure 4.7: (a) CAD model of sample-holder B assembly. (b) Fabricated sample-holder B assembly with a JTWPA chip installed.

the chip to facilitate the bonding process, while keeping the PCB and RF connectors fixed. The DUT sits in a groove of the sample-holder bottom split block, and the ground plane of the DUT is directly bonded to the sample holder instead of the PCB. The lid has a diamond-shaped cavity on top of the device to leave room for the arching bondwires while avoiding the formation of cavity modes below 14 GHz. Sample-holder B was designed with two different length to accommodate two different device's design. The sample-holder were fabricated with the in-house mechanical workshop.

4.3 Cryogenic test systems and experimental setups

In this section, I will introduce the different cryogenic systems that I have worked with to test my devices, as well as the different setups used for the experiments presented in the following chapters.

4.3.1 Cryogenic systems

The research field of superconductivity is impossible without the advancement of cryogenics systems. The first liquefaction of Helium-4 (He-4) in 1908 by H. Kamerlingh Onnes [136], permitted the investigation of materials' properties at $\sim$ 4 K, demonstrating the first evidences of superconductivity in Mercury in 1911 [89]. Ever since, numerous cryogenic technologies have been developed achieving a wide range

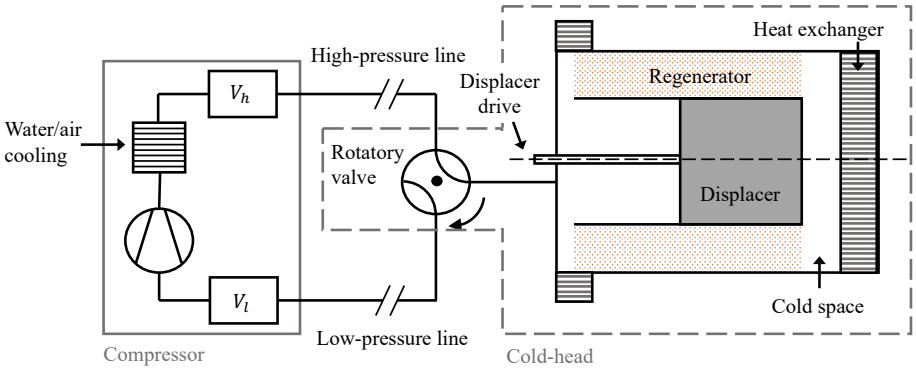

Figure 4.8: Schematics of a Gifford-McMahon (GM) cryocoolers.

of low-temperatures, down to 10 mK. Here, I present the cryogenic systems used to characterise all the superconducting devices relevant to this thesis.

4.3.1.1 Gifford-McMahon (GM) cryocoolers

Gifford-McMahon (GM) cryocoolers are an affordable choice for cryogenic system requiring temperatures ~ 4 K without reduced mechanical vibrations. GM coolers use a closed cycle of helium-4 (^{4}He) gas, which is periodically compressed and expanded to produce a cooling cycle. As shown in Fig. 4.8, the main parts of a GM cryocooler are the compressor unit and the cold-head. The compressor takes the ^{4}He gas from a volume v_l, decreasing the pressure in this volume, and injects it in a separate volume v_h where the ^{4}He pressure is therefore higher. These two ^{4}He volumes with different pressures are connected to the system through two separate lines. The cold-head contains a compression and expansion space, a displacer and a regenerator. A rotatory valve periodically connects the inside space of the cold-head with the high and low-pressure volumes which, synchronised with the movement of the displacer, produces the Gifford-McMahon cooling cycle. The regenerator acts as a thermal reservoir, storing heat during the high-pressure compression phase and releasing it during the low-pressure expansion phase. For a detailed explanation of the Gifford-McMahon cooling cycle, I refer the reader to [137].

4.3.1.2 Sub-Kelvin sorption cooler: OX300

At temperatures below 3 K, the regenerator heat capacity and the cooling cycle efficiency drop significantly in GM cryocoolers. Therefore, alternative solutions such as sorption coolers are required to achieve sub-Kelvin temperatures. The main parts of

a 300 mK sorption cooler system are illustrated in Fig. 4.9, clearly showing the two sorption cooler modules, using helium-3 (^{3}He) and and helium-4 (^{4}He) as the refrigerant respectively. Each module is composed of a sorption pump, a pump tube, an evaporator, a heater and two heat switches connecting the sorption pump and evaporator to the heat sink. The heat sink is cooled at $T \sim 4$ K, which is often achieved using a GM cryocooler, or another type of cryocooler such as pulse-tube (PT). The sorption coolers use evaporative cooling to remove heat from the cold-plate. First, both sorption pumps, made of a porous material, are heated to release helium into the system (Fig. 4.9(a)). At this stage, both evaporators are connected to the heat sink. The ^{4}He moves through the pump tube, cooling down to 4 K and condensing in the evaporator. Once the ^{4}He is condensed, to further decrease the temperature of the system below 4 K, both evaporators are disconnected from the heat sink while the ^{4}He sorption pump is connected to the heat sink (Fig. 4.9(b)). The ^{4}He in the evaporator absorbs heat from the cold-plate, and the cooled-down sorption pump decreases the evaporated ^{4}He pressure, resulting in $T \sim 800$ mK at the evaporator. Since the ^{4}He evaporator is connected to the ^{3}He pump tube, it cools-down the pump tube to $T \sim 800$ mK ensuring the condensation of ^{3}He (Fig. 4.9(b)). Finally, once the ^{3}He is condensed, the ^{3}He sorption pump is connected to the heat sink, decreasing the evaporated ^{3}He pressure, resulting in $T \sim 300$ mK at the ^{3}He evaporator. The system therefore stays at $T \sim 300$ mK until all the ^{3}He evaporates. For a detailed description of sorption coolers, I refer the reader to [138].

During my DPhil programme, I have extensively operated the cryogenic system OX300 (Fig. 4.10(a)&(b)), to carry out many experiments discussed in this thesis. OX300 uses a Sumitomo® RDK-408D GM cryocooler and a GL7 sorption cooler acquired from Chase Research Cryogenic® (Fig. 4.10(c)) to reach $T \sim 300$ mK. The system is composed of 4 temperature stages at 40 K, 4 K, 1 K and 300 mK respectively. The mechanical design, fabrication, assembly and electrical wiring of OX300 — except the cold head and the sorption cooler system — was done in-house by members of the Superconducting Quantum Detectors group with in-house mechanical workshop support.

4.3.1.3 Dilution refrigerator: LD250

At low enough temperature, often below 800 mK, the mixture of ^{3}He and ^{4}He separates in two phases: a phase rich in ^{3}He (concentrated phase) and a phase poor in ^{3}He (dilute phase), as shown in Fig. 4.11. At temperatures approaching absolute zero, the concentrated phase becomes pure ^{3}He, while the dilute phase maintains about 6.4%

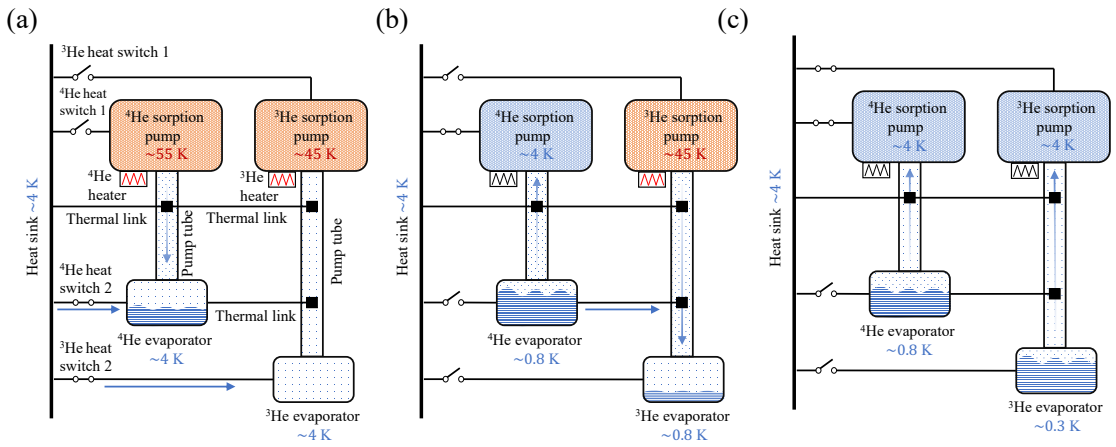

Figure 4.9: The operation of a generic sub-Kelvin sorption cooler system. (a) Both sorption pumps are heated, realeasing the helium in the system. The ^{4}He condenses in the evaporator. (b) The ^{4}He sorption pump is cooled by connecting it to the heat sink. The evaporative cooling of the ^{4}He brings the temperature in the ^{4}He evaporator to 0.8 K condensing the ^{3}He. (c) The ^{3}He sorption pump is cooled down, and the evaporative cooling reduces the temperature in the ^{3}He evaporator to 0.3 K.

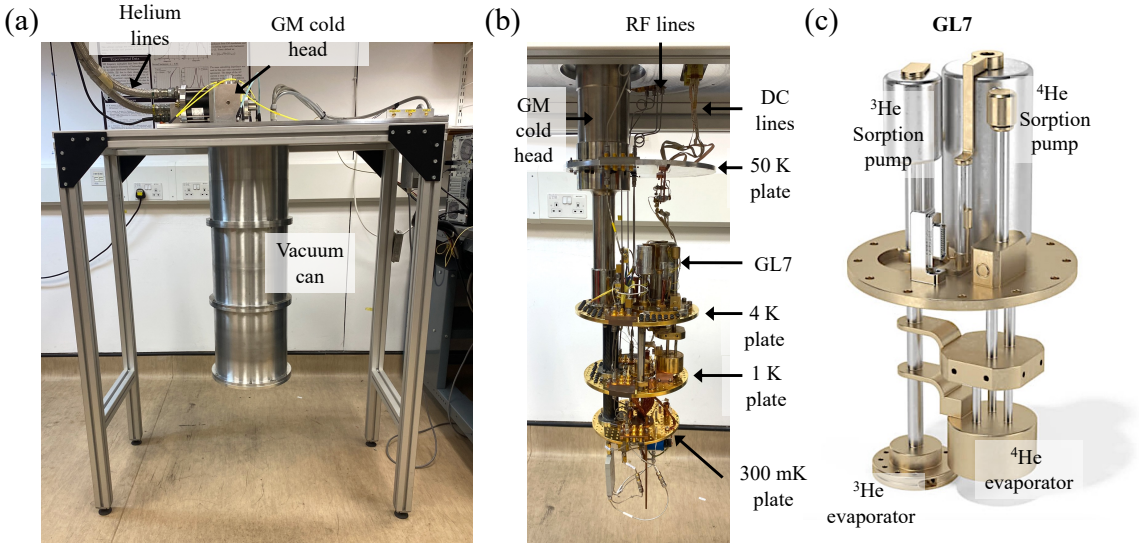

Figure 4.10: OX300 cryogenic system. (a) Photograph of the system under operation. (b) Photograph with the system open. The GM coldhead cools the system to 4 K, where the sorption cooler (GL7) further reduce the temperature to 300 mK. (c) Image of the Chase Research Cryogenic® GL7 sorption cooler, reproduced from Chase Research Cryogenics website [139].

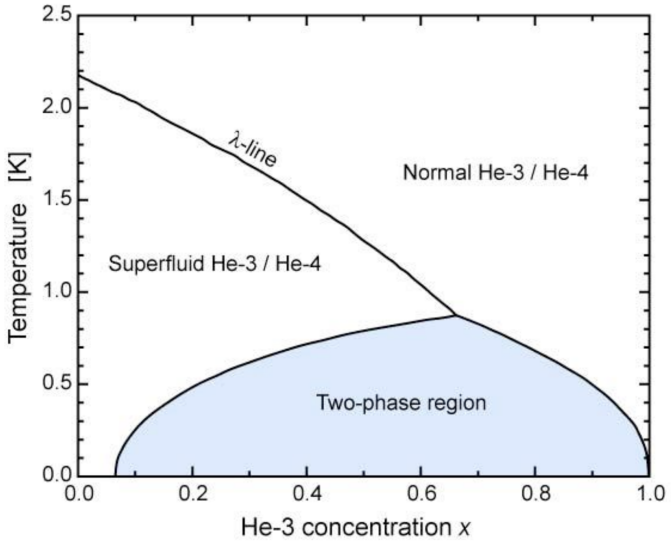

Figure 4.11: ^{3}He/^{4}He phase diagram reproduced from the Blufors® LD250 User Manual [140].

of ^{3}He. To move ^{3}He atoms from the concentrated phase to the diluted phase requires some energy; in a dilution refrigerator (DR) this energy is provided from the cold-plate, to reach temperatures below $T < 10\,\mathrm{mK}$.

The main parts of a DR are shown in Fig 4.12(a). Before starting the cooling cycle, the DR needs to be cooled to $T \sim 4\,\mathrm{K}$, which can be achieve with a conventional GM or PT crycooler[11]. A compressor increases the pressure of the ^{3}He/^{4}He mixture to $P = 2\,\mathrm{Pa}$, which is injected through the condensing line, cooling down and liquefying inside the DR. The liquid mixture fills the condensing line, the mixing chamber (MXC) and the still stages. Then the cooling cycle is started by pumping the mixture from the still pumping line, resulting in evaporative cooling the MXC and still to $T < 700\,\mathrm{mK}$. At this temperature, the two-phase transition occurs, and given the larger mass of ^{4}He, the diluted phase sediments on the bottom of the mixing chamber Fig 4.12(b). Given the larger vapor pressure of ^{3}He compared with ^{4}He, the evaporated helium in the still is almost pure ^{3}He, which is pumped from the still pumping line and reinjected in the DR through the condensing line. While propagating in the condensing line, the ^{3}He cools down with a counter-flow heat exchanger. Once in the mixing chamber, the ^{3}He dilutes in the diluted phase by taking energy from the MXC cold-plate, cooling it down. The diluted ^{3}He moves towards the still by an osmotic pressure due to the lack of ^{3}He in the still as a consequence of pumping, and the cycle repeats. Intuitively, the cooling power will be determined by the number of ^{3}He atoms crossing the phase

[11]In the case of LD250, a Cryomech PT 410 RM®

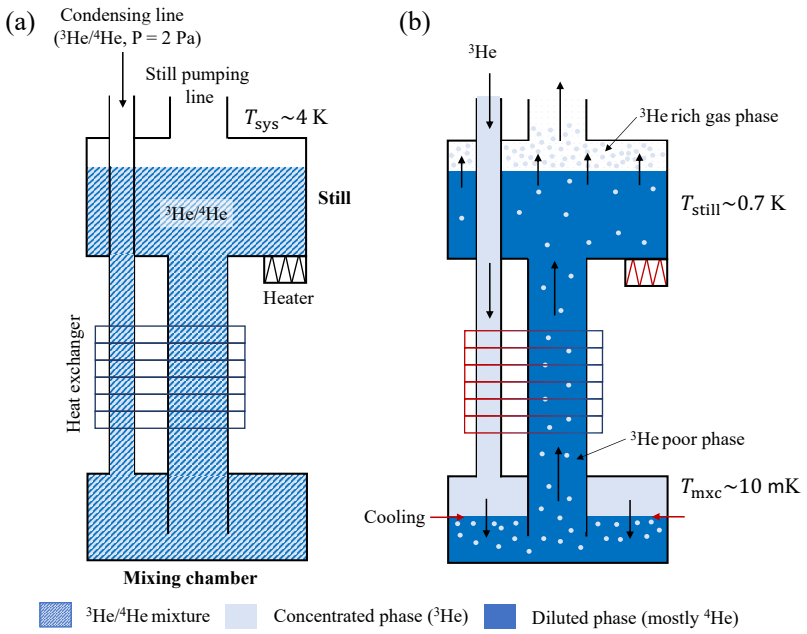

Figure 4.12: Operating procedure of a dilution refrigerator. (a) State of the DR at $T \sim 4\,\mathrm{K}$ before starting the cooling cycle. (b) Cooling-cycle of a DR. The transition of the ^{3}He in the diluted phase generates the cooling power of the system.

boundary, which can be increased by applying heat to the still to increase the vapor pressure, and hence the flow rate of diluted ^{3}He. For a further discussion on the operation of dilution refrigerators, I refer the reader to [137].

In my research, I have extensively operated an LD250 DR system from Blufors®. As shown in Fig. 4.13, the system is composed of 5 temperature stages at 50 K, 4 K, 700 mK (still), 100 mK and 10 mK (MXC). The system was commissioned in August 2021. It was originally populated with 3×12 DC lines and 12 SMA RF lines, including 4 superconducting RF lines; and in September 2023, we further included 6 SMK RF lines to increase the frequency operation range to 40 GHz. Often, the devices under test (DUTs) are mounted at the 10 mK stage, as shown in Fig. 4.13(b).

4.3.2 DC characterisation setups

The DC characterisation of junction-based devices can provide valuable information, from possible open or short-circuits in the device, to junction fundamental characteristics such as the critical current. Here, I describe the two main experimental setups that I used for the DC-characterised devices presented in this thesis.

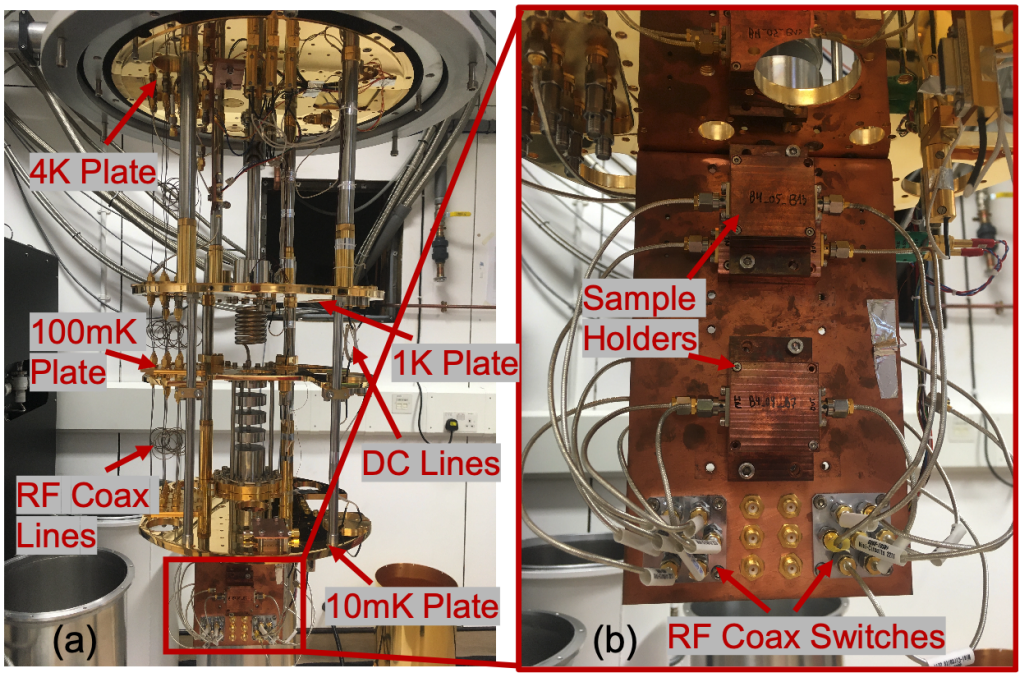

Figure 4.13: LD250 cryogenic system[12]. (a) Generic internal setup of the system. (b) Zoom-in photo at the 10 mK stage, showing a generic JTWPA DC/RF measurement setup.

4.3.2.1 Screening procedure via dipstick

Dipstick measurements allow for quick characterisation of DUTs at $T = 4\,\mathrm{K}$ by dipping them in liquid helium. As shown in Fig. 4.14, the main parts are the sample holder, sample block, dipstick, helium dewar and electronics box. The test device is mounted in the sample holder, which is connected to the sample block via the 'pogo' pins that provide the electrical connection with the test device. The sample block is affixed to the bottom end of the dipstick, which is dipped in a helium (^{4}He) dewar, to cool down the device to $T = 4\,\mathrm{K}$. The electronics box controlled via a computer, DC-bias the DUTs mounted at different channels. During my DPhil, I used two dipstick setups, one setup at Oxford and another setup at IRAM. Both were conceptually identical, but differed in the mechanical and electrical design. Nevertheless, both dipsticks setups were designed for the DC-characterisation of SIS mixers with up to 3 high I_c junctions in series. Therefore, the output impedance of the current source is in the order of hundreds of kΩ, which is sufficient for the SIS mixers case, but will result in some limitations for the DC-screening of JTWPAs as discussed in Sec. 9.3.

[12]Credits of the images: Joseph C. Longden [101]

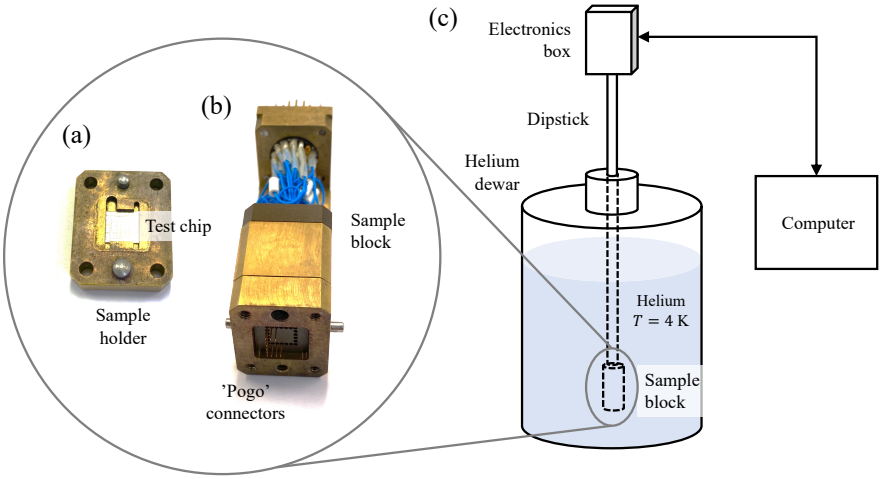

Figure 4.14: Schematics of the dipstick system at IRAM. (a) Image of the sample holder containing the test chip. (b) Image of the sample block. (c) Drawing of the dipstick setup.

4.3.2.2 DC-screening in LD250

Despite the rapid measurement allowed by the dipstick setups, the sample holder and block originally designed for other experiments constraints the DUTs to a specific size, which may not always be compatible with the design of my JTWPA devices. Furthermore, it requires the use of large amount of liquid helium, which is expensive and challenging to get[13]. To alleviate these inconveniences, we modified the internal setup of LD250 to provide a platform for fast DC-screening of DUTs with different sizes. As shown in Fig. 4.15, the setup consists of two PCB boards with 5 CPW traces each; the two ends of the trace are disconnected. Each chip is glued in the center of the trace, and connected to the trace and the ground using bond-wires. The DC twisted-pair lines in the fridge are connected with the PCB through the connectors, as shown in Fig. 4.15(a). The DC measurements were done with a Keithley® 6221 current source and a Keithley® 2182A nanovoltmeter. A total of 10 devices, can be measured per cooldown.

4.3.3 RF characterisation setups

Although most DC measurements were done with a generic setup, for RF characterisation the setups often need to be altered depending on the objective of the experiment.

[13]During my time at Oxford, we faced severe issues in the supply of liquid helium due to numerous technical and logistics problems.

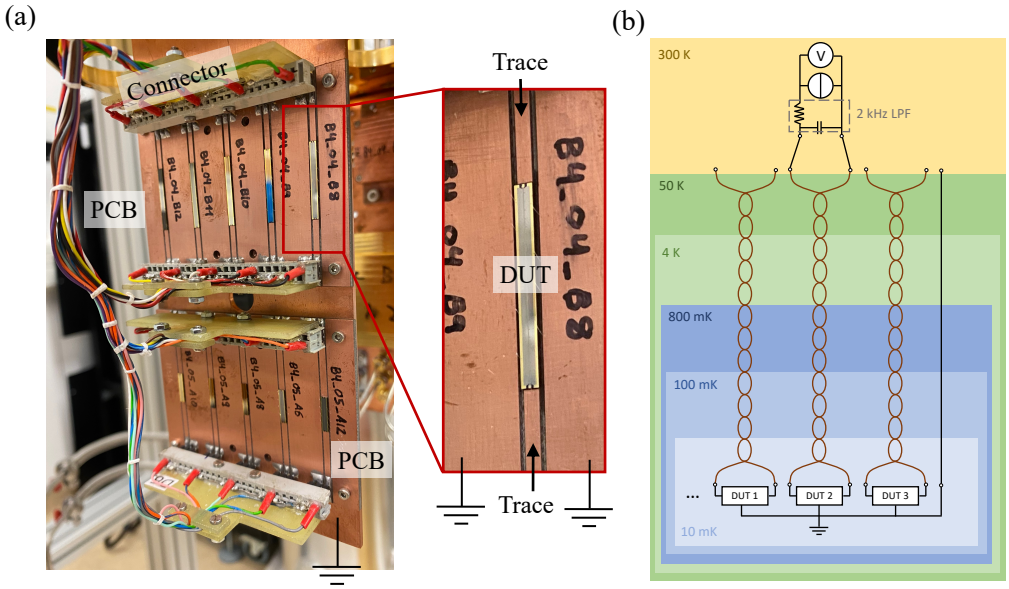

Figure 4.15: DC-screening setup in LD250. (a) Bracket holding the 2 PCBs and wiring of the setup inside the cryostat. The zoom-in shows where the device is located on the PCB. (b) circuit diagram of the experimental setup.

Here, I summarise the three main RF setups that I used. In all these setups I used the Vector Network Analyser (VNA) Anritsu® MS4644B, the signal generator Hittite® HMC-T2100 or the Anritsu® MG36241A, the spectrum analyser Anritsu® MS2665C, the current source Keithley® 6221 and the voltmeter Keithley® 2182A.

4.3.3.1 Setup-A

Setup-A, shown in Fig. 4.16, was implemented in OX300 without running the GL7 sorption cooler, therefore, the base temperature was at 4 K[14] instead of 300 mK. The setup allows for the characterisation of 3 devices and a blank (for calibration purposes) simultaneously using a 4-way splitter and a 4-way RF switch. A 20 dB attenuator installed in front of the DUTs is used to isolate each branch from possible reflections from other branches coupled through the 4-way splitter. Both the RF and DC characteristics of the devices can be measured with the addition of a pair of bias-tee before the splitter and after the switch.

This setup was the first iteration of the experimental setups used for the characterisation of the devices in this thesis. No efforts were made in minimising the noise at the input of the devices. Nevertheless, the setup is sufficient for measuring the RF

[14]All the devices presented in this thesis are based on Niobium, with $T_c \sim 9.2\,\mathrm{K}$. Therefore, they can be operated in the superconducting state at $T = 4\,\mathrm{K}$.

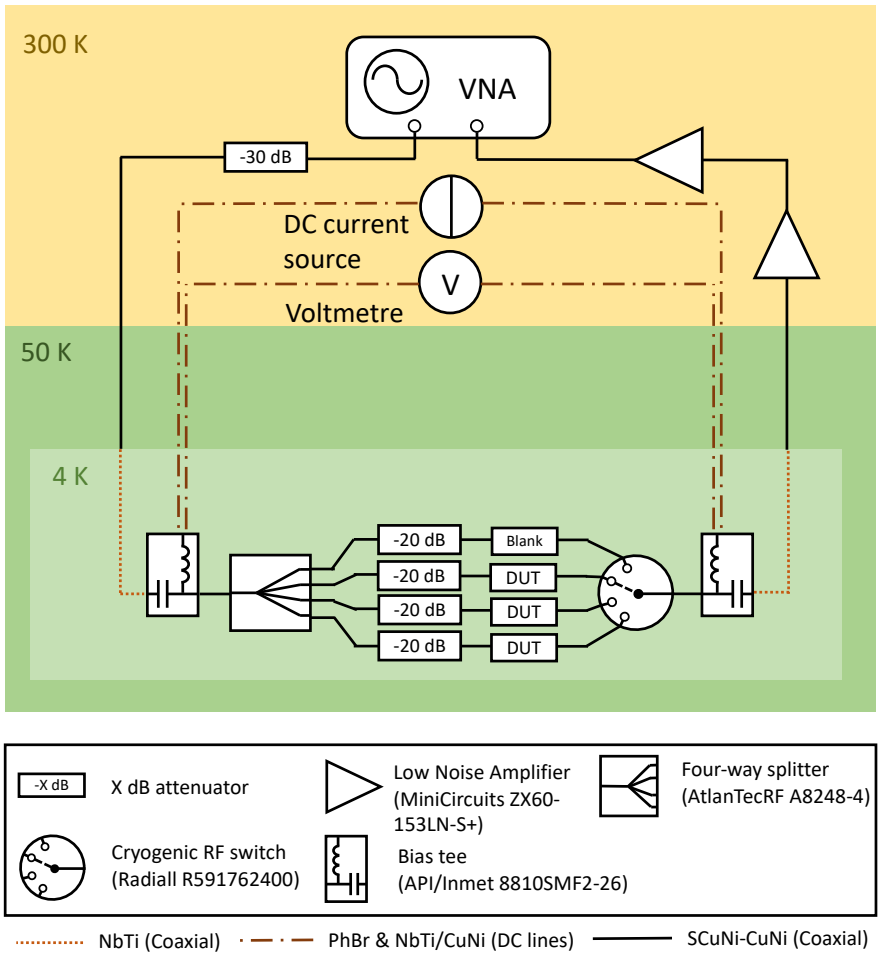

Figure 4.16: Experimental Setup-A, used for S_{21} and IV-curve measurements.

transmission profiles and IV characterisation of the devices, and was extensively used for the characterisation of test devices (See Chapter 5).

4.3.3.2 Setup-B

Setup-B, shown in Fig. 4.17, was implemented in OX300 for the gain characterisation of the JTWPA devices. Depending on the experiment, the system was run at 4 K with only the GM cryocooler, or at 300 mK by further running the GL7 sorption cooler. The signal tone is generated with the VNA, and combined at the cryogenic stage with the pump tone generated from the signal generator, using a 10 dB coupler. Similar to Setup-A, I used a 4-way splitter and a 4-way RF switch, which allows to measure 3 devices and a blank per cooldown with a single RF switch (which are often bulky, require DC wiring and can warm-up the MXC stage when used). However, when measuring one of the DUTs, part of the signal injected in the splitter

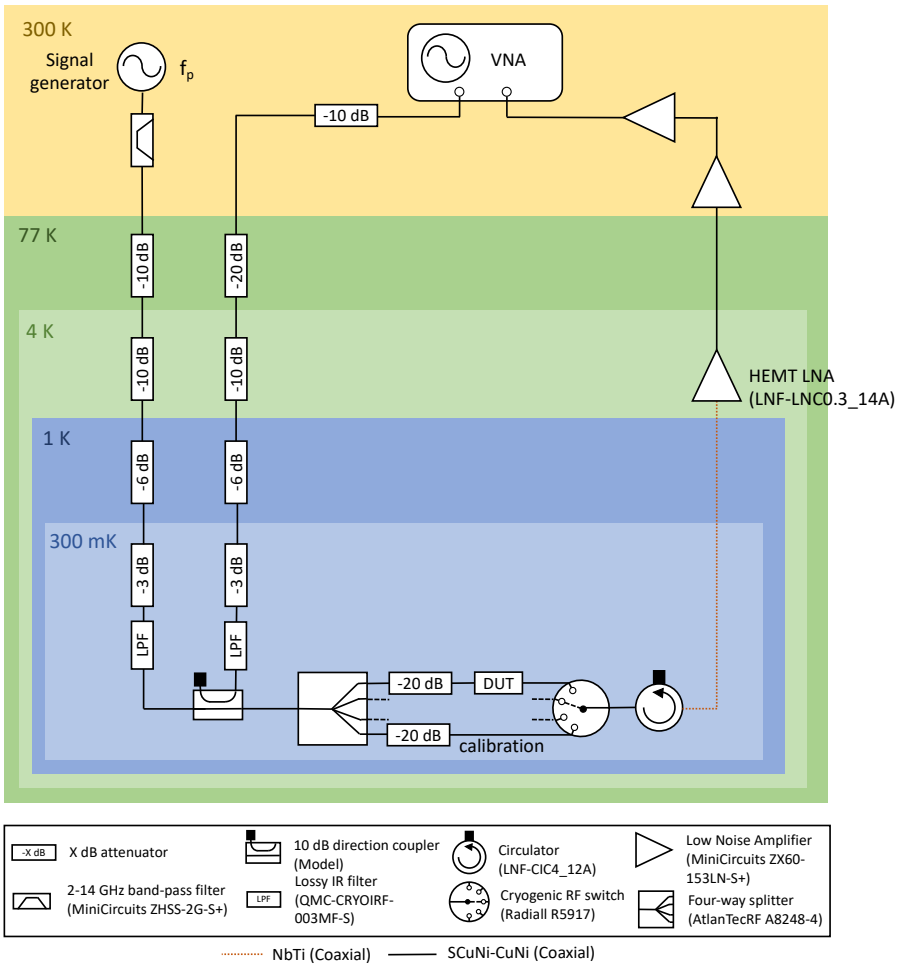

Figure 4.17: Experimental Setup-B, used for JTWPA gain characterisation.

can propagate through the other DUTs and get reflected back at the switch leaking through the splitter to the DUT under measurement. To limit this effect, which could deteriorate the measurement, we added 20 dB attenuators in front of every DUT. The output signal from the DUTs is readout via several low noise amplifiers, including a cryogenic HEMT LNA and one or two room-temperature amplifiers.

It is well known that the JTWPA gain deteriorates with input noise; a main source of noise is the room temperature thermal noise coupled through the coaxial lines. Assuming a 16 GHz bandwidth (B) of the coaxial lines, we can calculate the noise power of the thermal noise ($T = 300\,\mathrm{K}$) as $P = k_\mathrm{B}TB \approx -70.8\,\mathrm{dBm}$. If the VNA's signal power at room temperature is below the thermal noise, the VNA will not be able to resolve the signal. Since JTWPA operation requires signal powers in the order of –120 dBm, we need to keep the thermal noise well below this value

at the input of the device. This is achieved by adding attenuators at each stage of the cryostat, ensuring the thermal noise originated at each temperature stage is conveniently attenuated before reaching the device. To further attenuate other sources of noise outside the operational bandwidth of our device, a standard technique consists of incorporating lossy IR filters in the 300 mK stage. These filters are made of Eccosorb® CR 110, which uses the thermal dissipation above the cutoff frequency to attenuate signals higher than 10 GHz. Note that this type of filters are different from the lumped-element filters, where the out-of-band signals are reflected. IR filters, using thermal dissipation rather than reflection to block signals above the cutoff, help to limit unwanted signal reflections potentially deteriorating the performance of the JTWPA. I also used a combination of room temperature band-pass filters to avoid low frequency noise and signal harmonics — generated from the signal generator — from coupling in the DUTs. Finally, to avoid reflections from the HEMT LNA, I further added a ciculator at the output of the cryogenic switch, where one of the circulator's ports is terminated, hence behaving as an isolator.

4.3.3.3 Setup-C

Setup-C, shown in Fig. 4.18, was a versatile experimental setup, allowing the measurement of gain, as well as the effects of applied DC-current in the RF-spectrum of the devices. The setup was implemented in LD250, and operated at the base temperature of 10 mK. Apart from the noise and reflection reduction techniques explained in Setup-B, here, I further reduce the noise coupling through the DC-lines by using a room-temperature low-pass filter in the setup at LD250. A pair of 6-way RF switches allows for characterising 5 devices and a blank in a single cooldown. Furthermore, two readout setup options were implemented. Option-1, hereafter Setup-C1, only permits to readout the output signal using the VNA, while Option 2, hereafter Setup-C2, the output signal is split for readout between the VNA and the spectrum analyser simultaneously. The majority of the gain results presented in this thesis were observed with this setup, or slightly modified versions.

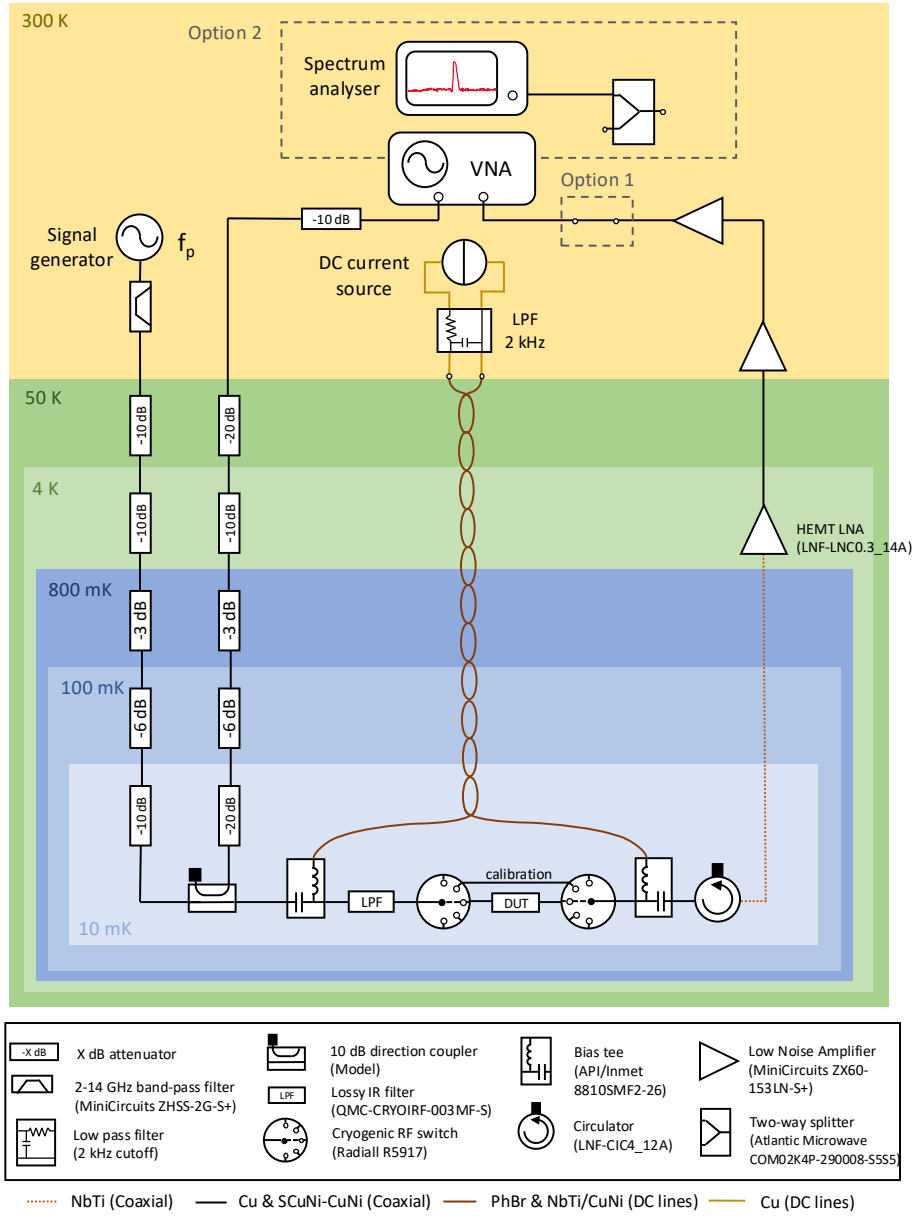

Figure 4.18: Experimental Setup-C used to characterise the gain and the S_{21} changes with applied DC current to the DUTs.

Chapter 5

Study of the fabrication process limitations

In this chapter, I investigate the possible limitations in the JTWPA fabrication process, to optimise the fabrication recipe for our devices. In particular, the critical current density of the junctions as a function of the fabrication parameters, aiming to reach the low values required for JTWPAs, and the fabrication yield of components such as parallel plate capacitors (PPCs) and resonators — often required in JTWPA designs. These efforts led to the identification of the pin-holes in the dielectric, which we subsequently tried to mitigate using two techniques presented in this chapter.

5.1 Introduction

JTWPAs are complex devices to fabricate, requiring over 1,000 junctions with low critical current, as well as other structures such as PPCs and resonators. The fabrication recipe used for the devices presented in this thesis was originally developed for high-frequency SIS mixers, which have different requirements than JTWPAs. Therefore, before venture directly in fabricating the JTWPA devices, I first investigated the limitations of the fabrication process using the facilities available at IRAM, and adapted the recipe for my JTWPA devices. With this exercise, I aimed to answer the following questions about the fabrication recipe:

A. Can the recipe be modified to reach a low enough critical current density (J_c) required for the junctions?

B. Can we fabricate over 1,000 functioning junctions in a single chip using this recipe?

C. Can we fabricate resonators and PPCs using this recipe?

Question	Device design ID	Deviece description	devices on wafer
A	A.1	Single junctions $A_{jj} = 0.25, 1, 2.25, 4, 6.25, 9, 12.25, 16, 20.5, 25\,\mu m^2$ (IRAM design[a])	3
	A.2	Single junctions $5 \times A_{jj} = 1\,\mu m^2$ and $5 \times A_{jj} = 0.25\,\mu m^2$ (Oxford design[b])	1
	A.3	Single junctions $5 \times A_{jj} = 1\,\mu m^2$ and $5 \times A_{jj} = 0.5\,\mu m^2$ (Oxford design[b])	1
	A.4	Single junctions $5 \times A_{jj} = 0.25\,\mu m^2$ and $5 \times A_{jj} = 0.5\,\mu m^2$ (Oxford design[b])	1
B	B.1-X[c]	CPW line with $N_{jj} = 50, 100, 500$ and $A_{jj} = 0.25\,\mu m^2$	3
	B.2-X[c]	CPW line with $N_{jj} = 1, 10, 50, 100, 500, 1000$ and $A_{jj} = 0.5\,\mu m^2$	6
	B.3-X[c]	CPW line with $N_{jj} = 50, 100, 500$ and $A_{jj} = 1\,\mu m^2$	3
C	C.1	CPW with 1,000 PPCs shunted to ground ($780\,\mu m^2$ per PPC)	1
	C.2	CPW with 10 resonators shunted to ground	1

[a] Chip designed at IRAM, including 10 Josephson junctions with different sizes for J_c measurement using their dipstick setup.
[b] Chip designed by members of the Superconducting Quantum Detectors (SQD) group at Oxford. It includes 10 Josephson junctions with identical or different sizes for J_c measurement using our dipstick setup.
[c] X indicated the N_{jj} of each particular device e.g., B.1-50 is the CPW line with $N_{jj} = 50$ and $A_{jj} = 0.25\,\mu m^2$.

Table 5.1: Summary of the fabricated test devices.

I have designed and fabricated a series of test devices. Tab. 5.1 shows the main test device designs, and which of the above questions they targeted to address. Apart from the devices presented in Tab. 5.1, other devices combining junctions, PPCs and resonators were also included on the wafer, to investigate the fabrication yield when these structures were combined together. A complete description of the test device designs and the layout of the mask is given in Appendix. B.

The fabrication of these devices took place during the two visits to IRAM from the 22nd of June to the 14th of July 2022, and from the 24th of April to the 5th of May 2023 respectively. On the first visit, I fabricated 3 wafers, each using different oxidation parameters. The devices from that fabrication round were extensively tested at IRAM and Oxford. The second visit simply aimed to explore further oxidation parameters to reduce the critical current of the junctions. I fabricated two wafers on that fabrication round, and the devices were only DC tested at IRAM to provide the required information about the J_c.

5.2 Junction's critical current density

As discussed previously, low critical current density junctions translate to a higher nonlinear inductance, a key parameter to obtain high gain in JTWPA designs. All the working JTWPAs presented in the literature to date use J_c values of 0.3-0.5 kA/cm^2 [79, 132, 80, 112], over an order of magnitude smaller than the SIS mixers devices that

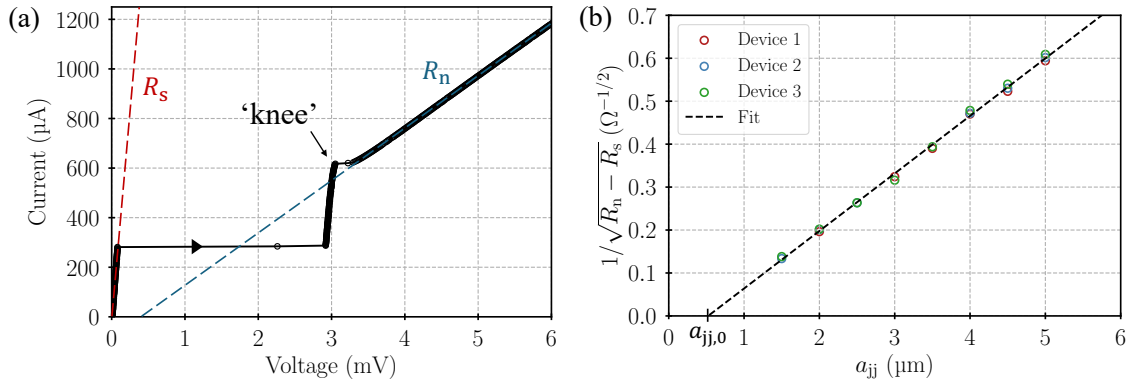

Figure 5.1: J_c calculation using the devices A.1 from the wafer with $t_{ox} = 120$ min and $P_{ox} = 1.6$ Pa. (a) Measurement of the IV curve of a junction with $a_{jj} = 4$ µm in the A.1 test device, when sweeping the voltage from 0 V to 6 mV. From the curve, we extract $R_n = 4.72\,\Omega$, $R_s = 0.25\ \Omega$ and $V_{gap} = 2.97 \pm 0.06$ mV. (b) $1/\sqrt{R_n - R_s}$ as a function of a_{jj} for the three A.1 devices from the same wafer. From the fit, we extract $a_{jj,0} = 0.52$ µm and $R_{nc} = 55.8\,\Omega$.

our fabrication recipe was originally conceived for. The J_c relates to the oxide barrier of the junction and can be controlled by changing the oxidation parameters during the trilayer deposition. Therefore, I investigated the effect of different oxidation times (t_{ox}) and pressures (P_{ox}) on the junctions' J_c.

This study was performed using the layout A.1, which was designed by IRAM and included 10 squared-junctions with sides' length of $a_{jj} = 0.5$ µm to 5 µm, at 0.5 µm steps. Unlike in the rest of the test devices, the junctions were defined using photolithography. Utilising the dipstick setup introduced in Sec. 4.3.2.1, we measured the current-voltage (IV) curve of the individual junctions in the devices. Fig. 5.1(a) shows an example of the measured IV curve of a junction with $a_{jj} = 4$ µm. We recognise the characteristics traces of an underdamped Josephson junction IV curve, as introduced in Sec. 2.1.2. For each junction, we recorded the normal resistance (R_n), and the series resistance originating from the wires used for the measurement (R_s). Then, for each of the three A.1 devices on the wafer, we plot $y = 1/\sqrt{R_n - R_s}$ as a function of a_{jj} as shown in Fig. 5.1(b). These devices should have the same J_c, since they were fabricated on the same wafer simultaneously[1], and therefore y should linearly increase with the junction size. We fit a linear regression $y(a_{jj}) = c_0 + c_1 a_{jj}$ to the data; the a_{jj} value at which the linear regression intersects the x-axis, i.e., $a_{jj,0} = -c_0/c_1$, is the systematic junction size error potentially originating from over-etching and/or unaccounted extra oxidation of the junctions side-walls. We calculate

[1]Assuming a homogeneous oxidation process across the entire wafer.

t_{ox} (min)	P_{ox} (Pa)	J_c (kA/cm^2)
120	1.6	4 ± 0.15
180	1.6	3.4 ± 0.15
180	2	2.5 ± 0.15
300	4	1.4 ± 0.15

Table 5.2: Summary of J_c values obtained with different oxidation parameters during the trilayer deposition.

an average $a_{jj,0} = 0.54 \pm 0.07\,\mu m$ from all the measured wafers. Furthermore, from c_1, we can calculate the normal resistance for a $1\,\mu m^2$ junction $R_{nc} = 1/c_1^2$. Using the measured R_{nc}, we estimate the J_c of the wafer using Ambegaokar-Baratoff formula for tunnel junctions [95]:

$$I_c R_n = \left(\frac{\pi\Delta}{2e}\right) \tanh\left(\frac{\Delta}{2k_B T}\right) \tag{5.1}$$

where Δ is the superconducting gap energy, k_B is the Boltzmann constant, e is the electron charge and T is the physical temperature of the junction. Since $\Delta = eV_{gap}/2$, we can rewrite the above equation as:

$$I_c R_n = \left(\frac{\pi V_{gap}}{4}\right) \tanh\left(\frac{eV_{gap}}{4k_B T}\right) \tag{5.2}$$

hence we can estimate J_c through I_c via the measured R_n. The calculated values of J_c for the different fabrication parameters are summarised in Tab. 5.2.

Apart from the test devices described in this section, at the beginning of my DPhil programme, I have also measured the DC characteristics of numerous Nb/Al-AlO_x/Nb junctions fabricated by our collaborators at Observatoire de Paris Laboratoire Galaxies, Etoiles, Physique et Instrumentation (GEPI) using different fabrication parameters. I used the dipstick setup at Oxford, and I estimated the J_c using the current values at the 'knee' (see Fig. 5.1(a) for the definition of 'knee') of the IV-curve and the designed area of the junctions. The results from the devices fabricated at GEPI and IRAM are plotted in Fig. 5.2, as a function of the oxygen exposure $E = P_{ox} \cdot t_{ox}$. As expected, J_c exponentially decreases with E. We fit the data to the function $f(E) = \alpha E^{-\beta}$, obtaining $\alpha = 37.3$ and $\beta = 0.4$, comparable with results reported from other fabrication facilities [141, 142].

Numerous studies have demonstrated an efficient reduction of the junctions' I_c with thermal annealing processes, as a result of increasing the AlO_x barrier thickness due to reacting oxygen [143, 144, 145]. Thermal annihilation was explored at

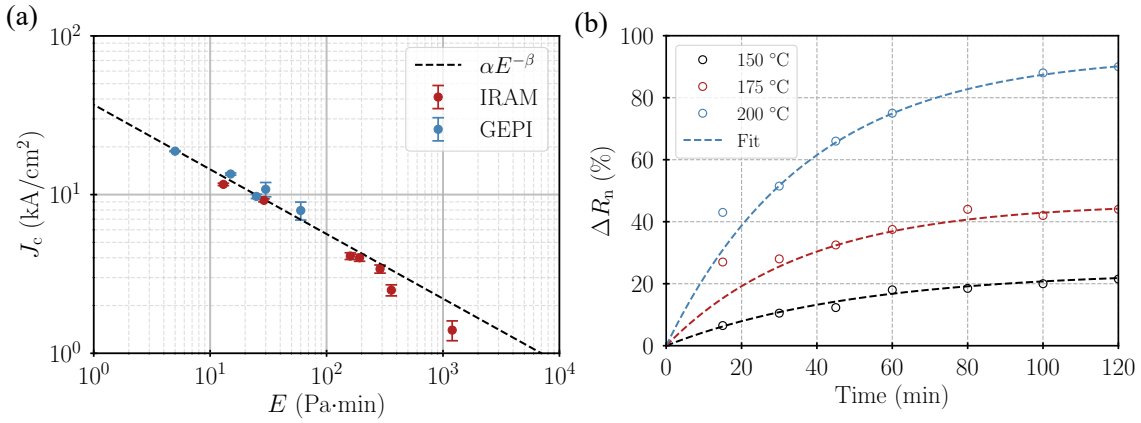

Figure 5.2: (a) J_c calculated from the measured IV curve of the junctions fabricated at IRAM[2](red) and GEPI (blue) as a function of E. The dotted line shows the fitted equation $\alpha E^{-\beta}$, where $\alpha = 37.3$ and $\beta = 0.4$. (b) Variation of the normal resistance with time of baking at different temperatures. The fitting curves are $\Delta R_n = 24 - 24e^{-0.02t}$, $\Delta R_n = 46 - 46e^{-0.027t}$ and $\Delta R_n = 94 - 94e^{-0.02656t}$ for 150 °C, 175 °C and 200 °C respectively, where t is the baking time. Credits: IRAM.

IRAM in 2004; the study measured the normal resistance of Nb/Al-AlO_x/Nb junction before and after undergoing a baking process for different times and at different temperatures. The resulting normal resistance variation (ΔR_n) is plotted in Fig. 5.2. Based on these results, we baked two of our A.1 devices originally measured with $J_c = 1.4\,\mathrm{kA/cm^2}$ for 2 hours at 120 °C. From the measurement of the junctions' IV-curve after baking, we obtained a $J_c = 0.9\,\mathrm{kA/cm^2}$, i.e., a 64 % of reduction in J_c.

5.3 Josephson junction arrays and resonators

To investigate the fabrication yield of large number of junctions, we used designs B.1, B.2 and B.3, consisting of Josephson arrays with different numbers of junctions embedded in a CPW line, which included junctions sizes of $0.25\,\mu\mathrm{m}^2$, $0.5\,\mu\mathrm{m}^2$ and $1\,\mu\mathrm{m}^2$. Using Setup-A, I measured the DC and RF properties of these arrays. A detailed investigation of the DC and RF characteristics of some of these devices is given in Chapter 8, therefore, here I just focus on the statistical analysis.

The liftoff of the SiO_2 (spacer) layer is a critical step during the fabrication process of these devices. The unsuccessful liftoff of a single junction in the array could result in a resist layer remaining on top of the junction, creating an open-circuit in the

[2]The three data points with the highest J_c were measured at IRAM before the start of my project, and added here for completeness.

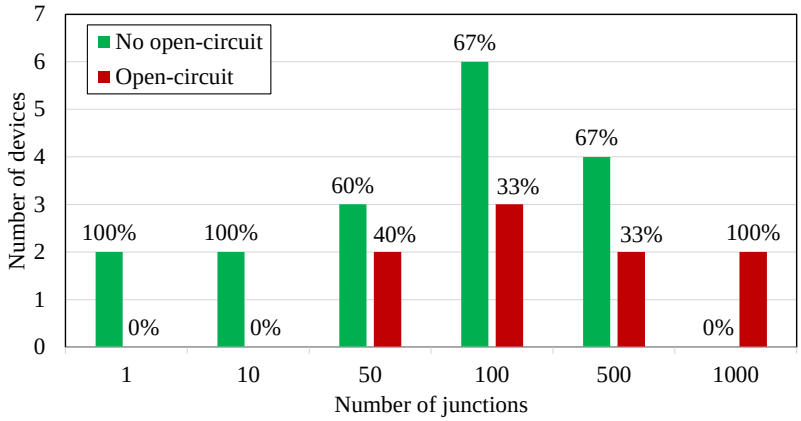

Figure 5.3: Results of the measured B.1, B.2, B.3 design devices, showing the number of open-circuits as a function of number of junction in the device. Devices with different A_{jj} are combined together under the same number of junctions.

device. These malfunctioning devices can be identified at cryogenic temperatures under RF characterisation, if they show no transmission through the device ($S_{21} < -30\,\mathrm{dB}$), or via DC characterisation, if they show very large resistance ($R > 1\,\mathrm{M\Omega}$). Fig. 5.3 presents the results obtained for all the tested devices with different number of junctions. Although the number of tested devices is not large enough for an accurate statistical analysis, it is clear that the number of open-circuited devices increases with the larger number of junctions, as expected. Using the 500-junctions case, where I measured 2/3 of working devices, the probability of a single working junction (p_{j}) is given by $p_{\mathrm{j}}^{500} = 2/3 \Leftrightarrow p_{\mathrm{j}} = (2/3)^{1/500} \approx 0.99919$. Assuming a JTWPA with 2,000 junctions, the probability of no open-circuited junction in the device is then $p_{\mathrm{j},2000} = p_{\mathrm{j}}^{2000} = 19.8\,\%$. This estimation includes devices with different junctions' sizes; however, smaller junctions naturally have a lower fabrication yield[3]. In the 500-junctions case, the two open-circuited devices indicated in Fig. 5.3 correspond to a $0.25\,\mu\mathrm{m}^2$-junctions device, and a $1\,\mu\mathrm{m}^2$-junctions device. Excluding the $0.25\,\mu\mathrm{m}^2$ case from the analysis, we can re-estimate $p_{\mathrm{j},2000} = p_{\mathrm{j}}^{2000} \approx 41\,\%$. Although this result should be more accurate for junctions with $A_{\mathrm{jj}} > 0.5\,\mu\mathrm{m}^2$, the accuracy of the estimation is still limited due to the small number of samples. However, assuming a 41 % fabrication yield for devices with 2,000 junctions, given the small footprint of JTWPAs — over 20 of them fitting in a single 2-inch wafer — we believed that the fabrication yield of $A_{\mathrm{jj}} > 0.5\,\mu\mathrm{m}^2$ junctions could be sufficient for JTWPA fabrication.

[3]The smaller the junction, the harder it is to solve the resist in the acetone during the liftoff process of the spacer layer.

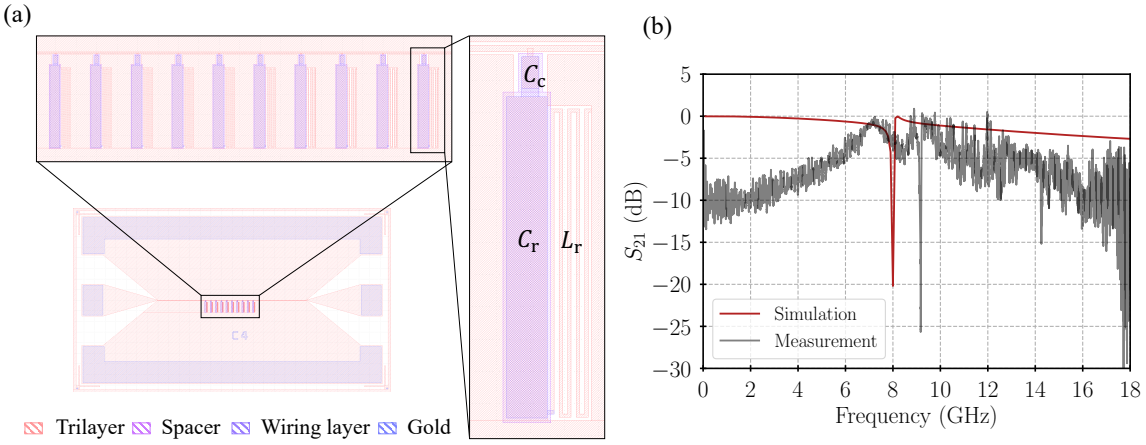

Figure 5.4: (a) Layout of the test device design C.2. The Zoom-in image shows the arrangement of 10 resonators coupled to the CPW line and the different parts forming the resonator. (b) Measured (grey) and simulated (red) S_{21} of the device. There is a 14 % discrepancy between the simulated and measured resonant frequency.

As presented in Sec. 2.2.4, the RPM technique requires a number of LC resonators shunted to the ground. We investigated the fabrication of just the LC resonators without junctions using design C.2. The layout of the device is illustrated in Fig. 5.4(a), showing 10 identical resonators coupled to a CPW line. The zoom-in image shows the coupling capacitance C_c, the resonator capacitance C_r and inductance L_r. I optimised the resonator's geometry for a resonant frequency $f_r = 8\,\text{GHz}$ using Sonnet®. Then, I cascaded ten times the `.s2p`[4] resulting from the Sonnet simulation using Keysight ADS® to recreate the behaviour of the device. The S_{21} resulting from the ADS simulation is shown in red in Fig. 5.4(b), together with the experimental result measured from a C.2 device (grey). The measured resonance $f_r = 9.17\,\text{GHz}$ is $\sim 14\,\%$ higher than expected, which could originate from a 24 % increase in the dielectric thickness compared to the targeted value of 200 nm. In posterior fabrication rounds, we measured $\sim 10\,\%$ increase in the dielectric thickness when targeting the $\sim 200\,\text{nm}$ SiO_2 deposition. Therefore, we believe the shift in the resonant frequency mainly originated from an unexpectedly thicker dielectric layer, alongside other possible factors such as a poor definition of the meandered inductor line or a limited accuracy on the EM simulation. A systematic $\sim 14\,\%$ shift in the resonant frequency of the resonators, as the one that we observed, is not critical in our JTWPA designs. Furthermore, the

[4]File format used as a standard for the output of 2-port circuits simulations from electromagnetic simulation softwares such as HFSS®, Sonnet® or ADS®. The file contains, among other information, the Scattering parameters resulting from the simulation.

thicker dielectric layer can be taken into account in subsequent resonators designs to improve the accuracy of the simulation. Therefore, we validated the resonator design for our applications. Finally, we notice a poor transmission at low and high frequencies. We associate the deterioration of the transmission above 10 GHz partly to the PCB, sample holder designs, and mounting technique, which were not optimised for those frequencies. On the other hand, we believe the pin-holes in the dielectric layer act as an inductive short to the ground, deteriorating the transmission below 8 GHz. At low frequencies, the low impedance of the pin-holes results in the signal leaking to the ground, however, at high frequencies the impedance is large enough that the main propagation path for the signal remains the transmission line. This could create the high-pass effect that we observe in Fig. 5.4(b).

5.4 Pin-hole issues in parallel plate capacitors (PPCs)

As mentioned earlier, apart from the designs presented in Tab. 5.1, other devices combining different numbers of junctions, PPCs and resonators were also fabricated. After DC and/or RF characterisation, I found indications of short-circuits to the ground in all the devices that incorporated any amount of PPCs. This included design C.1, consisting on a CPW with 1,000 PPCs and no other components. We believe this effect originates from pin-holes in the spacer layer used as the dielectric for the PPCs and the junctions. As illustrated in Fig. 5.5(a)&(b), pin-holes form due to imperfections when depositing the spacer layer, leading to short-circuits between the wiring layer and the trilayer. The recipe I used for RF-sputtered SiO_2 layers, for most of my devices, appeared to be particularly sensitive to the formation of pin-holes. There are numerous factors that contribute to their formation e.g., the substrate surface conditions, substrate's temperature during sputtering and pressure fluctuations in the chamber. Other deposition techniques, such as plasma-enhanced chemical vapor deposition (PECVD) or atomic layer deposition (ALD), could potentially help to reduce the pin-holes density [146], but unfortunately, we did not have access to the required facilities to perform such deposition.

To limit the short-circuits to the ground in our devices, we investigated two possible pin-holes mitigation strategies for RF-sputtered SiO_2. The pin-holes density is inherently related to the deposition technique and the material choice e.g., evaporated Al_2O_3 has shown to have a lower pin-hole density, which could be used as a mitigation technique. Furthermore, it is well known that the density of pin-holes decreases exponentially with the dielectric thickness [147]. Therefore, a thick dielectric

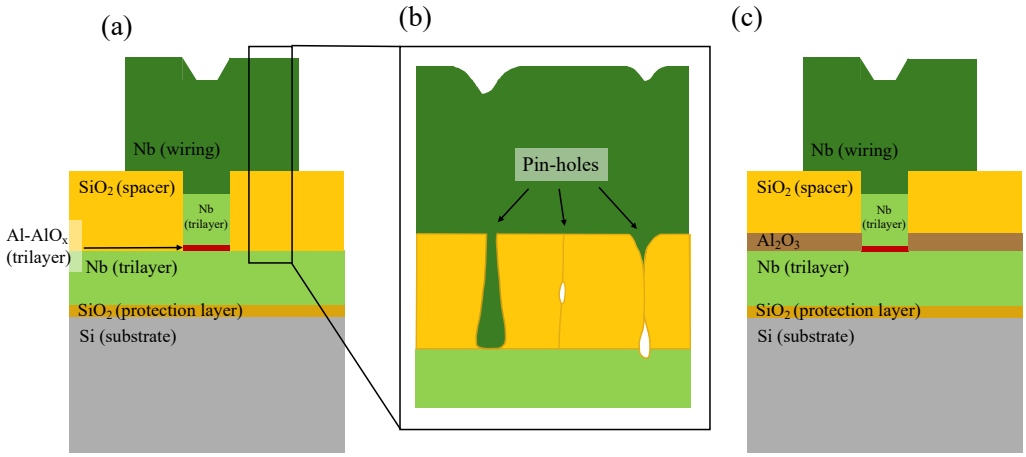

Figure 5.5: (a) Expected layer distribution in the trilayer junctions. (b) Zoom-in image of the spacer (dielectric) layer, showing the formation of the pin-holes. (c) A 20 nm of Al_2O_3 added to the spacer layer acting as an additional protection layer.

layer is another viable mitigation strategy. We explored both strategies: (a) adding a protective layer of 20 nm evaporated Al_2O_3 underneath the 200 nm RF-sputtered SiO_2, as shown in Fig. 5.5(c), and (b) increasing the RF-sputtered SiO_2 spacer layer from 200 nm to 400 nm. We compare the performance of these two approaches by fabricating a suite of test devices composed of a niobium CPW embedded with 100, 500 and 1,000 PPCs coupled to the transmission line. To ease the fabrication and reduce the complexity, the trilayer of these test devices was substituted with simply a bottom niobium layer, and no junctions are added to the line. Mitigation technique (a) and (b) are implemented in two different wafers, denoted Wafer 1 and Wafer 2 respectively. We use a 280-um thick high resistivity silicon wafers for the substrate.

I DC-screened these devices at cryogenic temperatures using the DC-screening setup from Sec. 4.3.2.2. At temperatures well below 9 K, the device's resistance is negligible, and I measured an average resistance $R_{\text{throu}} = 31.1\,\Omega$ which is originated from the cooper wires used to connect the current source and voltmeter. When measuring the resistance from the trace of the device to the ground, I found an average value of $R_{\text{gnd}} = 19.4\,\Omega$ for short-circuited test devices and 2.22 kΩ for non-faulty devices. The two orders of magnitude difference in the resistance allows us to easily identify devices with pin-holes issues that result in electrical shorts to ground.

To further confirm the validity of the measurements, I measured the RF transmission of two non-faulty devices with 100 and 1,000 PPCs, plotted in Fig. 5.6(a) and (b) respectively. Note that the devices' characteristic impedance $Z_0 \neq 50\,\Omega$ (due to the absent of the tunnel junctions) results in a Fabry-Perot-like effect in the transmission

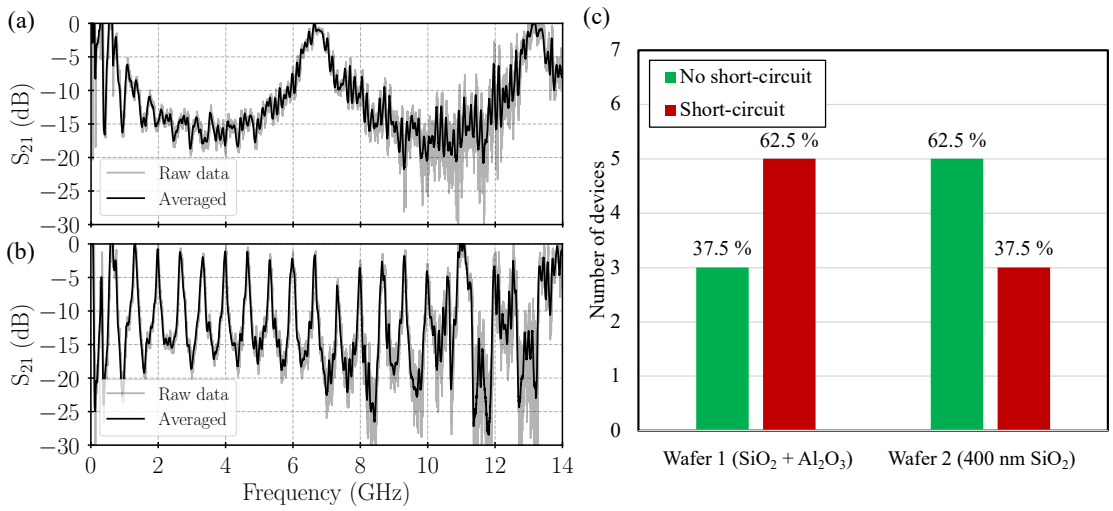

Figure 5.6: RF transmission of test-devices from Wafer 1 with (a) 100 PPCs and (b) 1,000 PPCs. The grey curve is the raw data and the black curve is the averaged data using a average window of 4.32 MHz. (c) Histogram of the number of test-devices from Wafer 1 and Wafer 2 with (red) and without (green) a measured short-circuit to the ground.

profile. The periodicity of this transmission variation is inversely proportional to the length of the lines, hence the ten times more rapid periodicity for the 1,000 PPCs sample compared to the 100 PPCs sample.

I tested a total of 16 PPCs test-structure devices, 12 at cryogenic temperatures and 4 at room temperature, where the effect of the pin-holes can equally be observed through the DC screening process. The results from these measurements are summarised in Fig. 5.6(c). Despite the limited number of fabricated test devices, the larger number of 'good' test devices in Wafer 2 indicates that increasing the dielectric thickness is the preferred pin-holes mitigation strategy. However, the capacitance of the PPCs decreases linearly with the thickness of the dielectric layer, therefore, to achieve the same shunt capacitance values, the PPCs will need to have a much larger area than originally intended. The larger PPC area required not only increases the footprint of the JTWPA device, but will equally increase the chances of having a pin-hole, hence potentially limiting the yield. On the other hand, the addition of a 20 nm evaporated Al_2O_3 will barely modify the size of the required PPCs in our design, while showing promising improvements in the reduction of pin-holes.

From the measured PPCs test-structure devices, 2 out of 4 devices with 1,000

PPCs worked in Wafer 1. Using this value[5], we can calculate the probability of a single capacitor to work as $p_c \approx 0.999307$, i.e., the probability of 2,000 working PPCs is $p_{c,2000} = p_c^{2000} \approx 36.7\,\%$. Therefore, assuming a JTWPA requires 2,000 junctions and 2,000 PPCs, using the previous estimation on the junctions yield (for $A_{jj} \geq 0.5\,\mu m^2$), we can estimate the yield for a JTWPA as $p_{JTWPA} = p_{j,2000} \times p_{c,2000} \approx 15.0\,\%$. Although small, this yield should be sufficient to result in several functioning JTWPA devices per fabricated wafer using IRAM fabrication facilities.

5.5 Conclusion on the fabrication limits

The results from this study partially answer the questions about the fabrication process I presented earlier in this chapter:

A. Can the recipe be modified to reach a low enough critical current density (J_c) required for the junctions?

Yes. Using optimised fabrication parameters, we managed to reach $J_c = 1.4\,kA/cm^2$, which combined with $0.5\,\mu m^2$ junctions results in $I_c = 7\,\mu A$, in line with current JTWPA implementations [79, 80, 81, 82]. Furthermore, we demonstrated that the J_c can be further reduced to $0.9\,kA/cm^2$ by baking the device at 200 °C for 2 hours. Nevertheless, we measured a systematic size error in the junctions of $a_{jj,0} = 0.54 \pm 0.07\,\mu m$, which could complicate the fabrication of small junctions.

B. Can we fabricate over 1,000 functioning junctions in a single chip using this recipe?

Yes. Although the risk of open-circuited junctions start to be noticeable for arrays with $N_{jj} > 50$, the results from $N_{jj} = 500$ devices with $A_{jj} \geq 0.5\,\mu m^2$ allows to estimated a 40.1 % fabrication yield for the $N_{jj} = 2,000$ arrays needed for a JTWPA. This yield is sufficient to obtain several working devices in a single 2-inch wafer compatible with our fabrication process.

C. Can we fabricate resonators and PPCs using this recipe?

[5] We neglect the devices with lower number of PPCs since the sample (number of devices) is too small to have any meaningful statistical implication.

Resonators can be fabricated using this recipe, although we measured a $\sim 14\,\%$ shift in f_r. This inaccuracy partly originates from a thicker dielectric layer fabricated than originally designed for, which can be corrected in future designs. Nevertheless, both the resonators and PPCs samples exposed an issue with pin-holes in the dielectric layer. We investigated two pin-holes mitigation techniques for the RF-sputtered SiO_2 forming the spacer layer, and we concluded that using a 20 nm Al_2O_3 protective layer is a more suitable technique since it barely changes the dimensions of the PPCs required for our JTWPA designs. Furthermore, using the 20 nm Al_2O_3 fabricated PPCs test-devices, we estimated the fabrication yield of 2,000 PPCs to 36.7 %. Therefore, assuming a JTWPA with 2,000 junctions and PPCs, we estimate the fabrication yield to 15.0 % which is sufficient to obtain several working devices per wafer with our fabrication process. Nevertheless, the fabrication yield could be substantially improved by avoiding using PPCs in our JTWPA designs.

Chapter 6

Microwave JTWPAs with PPCs

The exploratory work presented in the previous chapter resulted in a better understanding of the fabrication limitations and techniques required to fabricate JTWPAs. Following that analysis, I embark in the fabrication and characterisation of a microwave JTWPA design with parallel plate capacitors (PPCs). In this chapter, I present the experimental results from this design, including novel characterisation techniques. I analyse and discuss the results to give a better understanding of the limitations in the design, and conclude with possible improvements to the design.

6.1 Design and fabrication overview

Design A and Design B, presented in Sec. 3.5.1, were fabricated during my visit to our collaborators' facilities at IRAM from the 18$^{\text{th}}$ of June to the 8$^{\text{th}}$ of July 2023. The three first wafers (wafer 1-3) failed at some crucial step during fabrication. The more successful runs for the subsequent three wafers (wafer 4-6) resulted in a total of 57 JTWPA devices. A detailed layout of the photolithography masks used during the fabrication is presented in Appendix C. Both designs consisted of JTWPAs formed by an array of 2,024 Nb/Al-AlO_x/Nb junctions, with resonators coupled to the transmission line for resonant phase matching (RPM) and PPCs ensuring a $Z_0 = 50\,\Omega$. The main difference between the two designs was the I_c of the junctions (7 µA for Design A and 4.5 µA for Design B), resulting in different sizes of the PPCs. They were intended to operate in the DP4WM regime around ~ 7 GHz.

These devices were fabricated using the recipe from Chapter 4. I used 2-inch 500 µm thick high resistive ($R > 20,000\,\Omega$cm) silicon as the substrate. The spacer layer, which acted as the dielectric layer of the PPCs, was formed with 20 nm Al_2O_3 and 200 nm SiO_2 to attempt mitigating the pin-holes issue discussed in Sec.5.4. The trilayer was deposited using an oxidation time and pressure of $t_{ox} = 5$ h and $P_{ox} = 4$ Pa

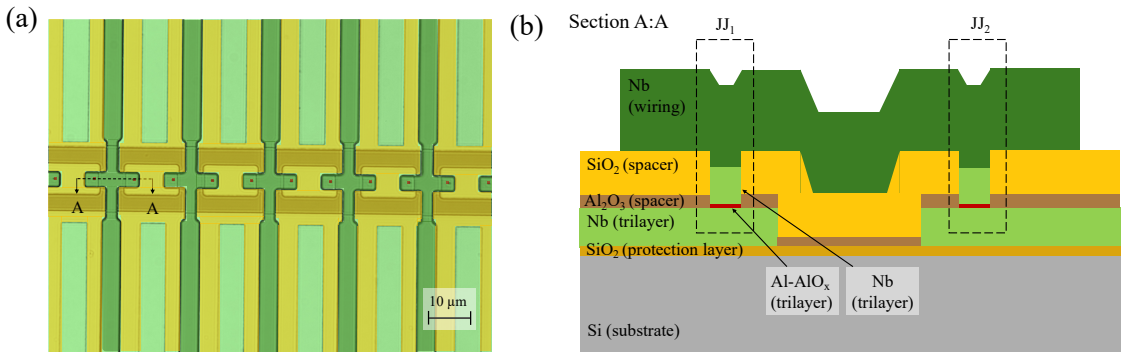

Figure 6.1: (a) Microscope image of the JTWPA with PPCs design. The fake colours in the zoom-in image shows the trilayer (light green), SiO_2 from the spacer (yellow), wiring layer (dark green) and junctions (red). (b) Cross-section of the JTWPA (not to scale).

respectively, for the targeted $J_c = 1.4\,\mathrm{kA/cm^2}$ (Design A). After dicing, some devices were baked at 120 °C for 2 hours to further reduce the critical current density to $J_c = 0.9\,\mathrm{kA/cm^2}$ (Design B). Fig. 6.1 shows a microscope image of the final device, as well as its layer stack-up topology.

Before the experimental characterisation, a careful observation under a high-magnification optical microscope allowed me to identify the devices with potential critical issues arising from the fabrication. Tab. 6.1, summarises the observed results. I identified a total of 28 devices without a major appreciable fabrication issue, such as missing junctions, critically damaged/deformed transmission line, etc.

Wafer ID	Major issue[1](# devices)	Minor issue[2](# devices)	No issue (# devices)
4	7	5	7
5	8	4	7
6	14	0	5

[1] Issues that will render the device unusable, such as missing junctions, broken CPW line, etc.
[2] Issues that can potentially compromise the performance of the device, but do not render it unusable, such as slightly deformed wiring layer plate of the capacitor, junctions shifted, etc.

Table 6.1: Yield statistics for the JTWPAs with PPCs examined using an optical microscope. A total of 57 devices were inspected, where 28 showed minor or no issue.

6.2 DC-screening

To identify other potential issues difficult to observe under the microscope, such as open-circuits due to junctions with unsuccessful liftoff or short-circuits to the

ground due to pin-holes in the dielectric layer, I DC-screened 15 out of the 28 devices that had minor or no issues. For these measurements, I used the DC-screening setup introduced in Sec. 4.3.2.2, which measures the current-voltage (IV) curve at $T = 10\,\mathrm{mK}$ of the DUTs. Fig. 6.2(a)&(b) plot the IV curves of device B9 (wafer 4, $J_c = 1.4\,\mathrm{kA/cm^2}$) through the trace and from the trace to the ground respectively. Similarly, Fig. 6.2(c)&(d) plot the IV curves of device B12 (wafer 4, $J_c = 0.9\,\mathrm{kA/cm^2}$) through the trace and from the trace to the ground respectively. The black curves indicate an upward sweep from –10 µA to 10 µA, whereas the red curves represent the downward sweep in the same range.

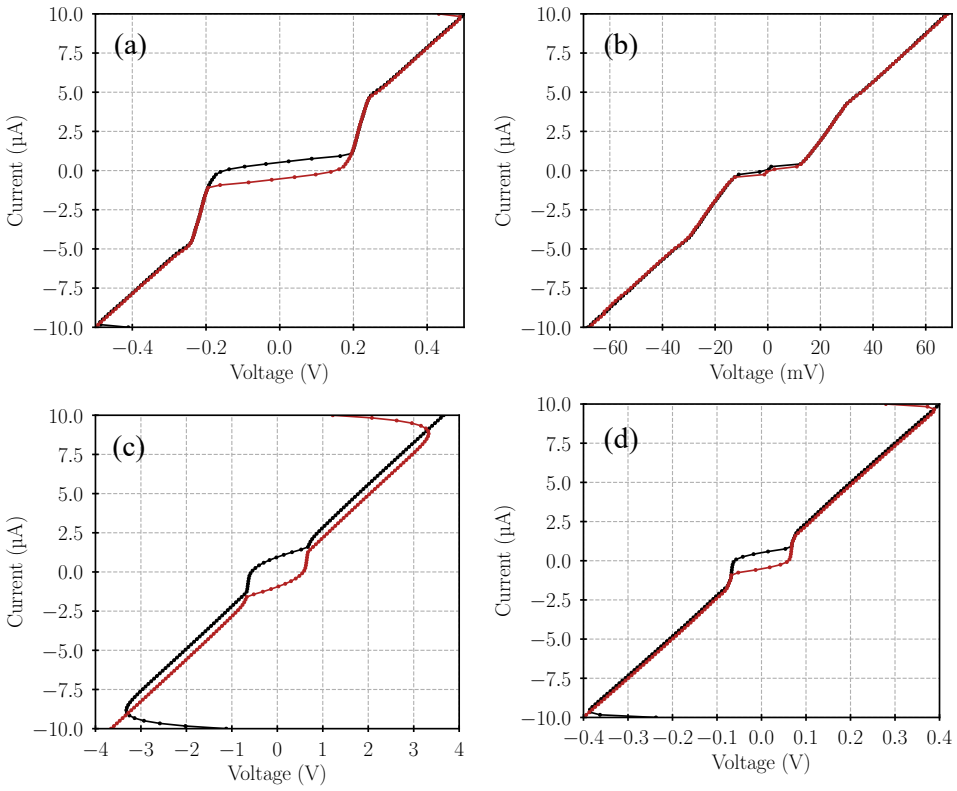

Figure 6.2: IV curves of the JTWPA devices measured at $T = 10\,\mathrm{mK}$ for Device B9 (a) through the device and (b) from the device trace to the ground, and for Device B12 (c) through the device and (d) from the device trace to the ground. The current is swept from –10 µA to 10 µA (black) and from 10 µA to –10 µA (red). The artifact noticed at the start of the sweep in (c) results from the raising time of the current source larger than the acquisition time of the measurement, due to the high resistance of the device. The indication of a gap voltage in panels (b) and (d) indicates a possible short-circuit in the line.

IV curve measurement considerations

Dielectric break-down voltage
When measuring the IV curve to the ground in the JTWPA, the voltage generated by the current source (Keythley 6221) needs to be kept below the break-down voltage of the dielectric layer of the PPCs to avoid permanent damage of the device. Assuming $\sim 200\,\mathrm{nm}$ of SiO_2, I estimate the breakdown voltage to $\sim 270\,\mathrm{V}$. During all the experiments, the compliance voltage of the current source is set to 6-8 V.

Current source output impedance
The large number of junctions in series forming the JTWPA results in an approximated normal resistance of the device $R_\mathrm{n} \sim 1\,\mathrm{M\Omega}$. For a satisfactory IV measurement, the output impedance of the current source needs to be substantially larger than R_n, otherwise, it will result in a lower measured current than expected through the device. For the current source used in this experiments (Keythley 6221), the output impedance is $10^{14}\,\Omega$, 8 orders of magnitudes larger than the expected R_n to measure, hence ensuring the accuracy of the measurement.

Assuming no short-circuits to the ground in the DUT, we would expect an IV characteristic similar to a bare single Josephson junction, but with a gap voltage 2,024 times higher than the $V_{\mathrm{gap,1JJ}}$ of a single junction, since the junctions are connected in series. However, from Fig. 6.2(a)&(c), we observe that the transition to normal state occurred at a value smaller than the expected $V_{\mathrm{gap,JTWPA}} \approx 6.4\,\mathrm{V}$. We suspect that this is due to the presence of several short-circuits in the transmission line as illustrated in Fig. 6.3(a), where the current partly flows through the ground plane, bypassing several junctions. When measuring the IV curve to the ground (Fig. 6.2(b) and (d)), we notice the same effect for a lower value of $V_{\mathrm{gap,JTWPA}}$. This is consistent with our theory, since in this case the current only flows through the junctions before the first short-circuit in the device, without returning to the trace, as shown in Fig. 6.3(b).

Despite the existence of short-circuits in the line, the data in Fig. 6.2 can be used to estimate the I_c of the junctions. From the $V_{\mathrm{gap,JTWPA}}$, we estimate the number of junctions through which the DC-current flows through to $N_\mathrm{jj} = 74 \pm 7$, 218 ± 10 and 23 ± 2 for Fig. 6.2(a), (c) and (d) respectively (we exclude Fig. 6.2(b) due to the large uncertainty in the $V_{\mathrm{gap,JTWPA}}$ transition). Measuring the normal resistance value and dividing by the estimated number of junctions, we can make use of the Ambegaokar-Baratoff formula to estimate the average I_c of the junction arrays, which results in $I_\mathrm{c} = 3.65 \pm 0.34\,\mu\mathrm{A}$ and $I_\mathrm{c} = 1.37 \pm 0.06\,\mu\mathrm{A}$ for device B9 and B12 respectively. These results are substantially lower than the targeted value of $I_\mathrm{c} = 7\,\mu\mathrm{A}$ and $4.5\,\mu\mathrm{A}$ for

devices B9 and B12 respectively. The rest of the DC-screened devices showed similar results, hence suggesting a persisting pin-holes issue in the dielectric layer.

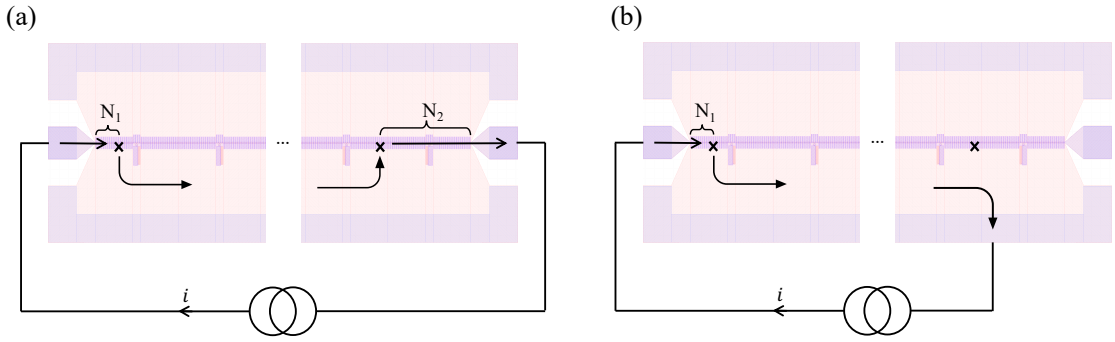

Figure 6.3: Schematic representation of the current flowing in the JTWPA when several short-circuits to the ground (crosses) are presented in the line, (a) when the current is applied through the trace, and (b) from the trace to the ground.

6.3 Transmission profile and losses

Following the DC-screening of the devices, I performed the RF characterisation of 13 devices. I measured devices that were, and were not, DC-screened since at that stage we were concerned that the DC-screening setup may be faulty causing permanent short-circuit damage to the DUTs. In this attempt, I accidentally used an experimental setup without any cryogenic RF attenuation or filtering, therefore, limiting the performance of the devices[1]. This filtering issue is corrected in Setup-B (Sec. 4.3.3.2) and Setup-C (Sec. 4.3.3.3), which I used to further characterise another 17 devices, including repeating some of the 13 devices previously RF characterised. I performed over 23 cooldowns using both LD250 and OX300 in parallel from July 2023 to January 2024, and found a single device (device B7, wafer 5) with promising results. In the rest of this section, I shall focus on this particular device. The device was mounted using the sample holder and techniques presented in Sec. 4.2, and the

[1]Input lines without attenuation were initially used to characterise KTWPAs in a separate project and were carried over as a first approach in my project. The high compression point $P_{1\mathrm{dB}} \sim -60\,\mathrm{dBm}$ of KTWPAs, i.e, larger than the thermal noise in the SMA coaxial lines $P_{\mathrm{n}} \sim -70.8\,\mathrm{dBm}$, make them operational without input attenuation. However, for the JTWPA devices in this chapter, the targeted $I_{\mathrm{c}} = 7\,\mu\mathrm{A}$ translates to a device's input power of $P_{I_{\mathrm{c}}} \sim -59.1\,\mathrm{dBm}$. Since P_{n} is just an order of magnitude smaller, it resulted in extra losses in our JTWPA devices. Furthermore, JTWPAs have a $P_{1\mathrm{dB}} \sim -110\,\mathrm{dBm}$, hence P_{n} will substantially saturate the JTWPA gain, preventing the measurement of gain without attenuated input lines.

performances were measured at $T = 10\,\mathrm{mK}$ in LD250 using Setup-C, unless otherwise stated.

6.3.1 Low signal power transmission

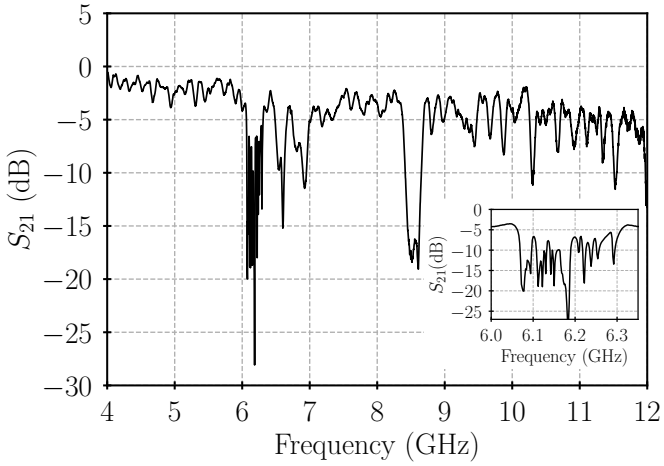

Figure 6.4: Measured transmission for JTWPA device B7 with $P_{\mathrm{vna}} = -10\,\mathrm{dBm}$. The inset shows the area around $\sim 6.15\,\mathrm{GHz}$, where the high-Q resonances are believed to be induced by the resonators. The dip around $\sim 8.5\,\mathrm{GHz}$ is suspected to be originated from the loading effect of the resonators in the STL.

I started by analysing the transmission profile of the device. Fig. 6.4 shows the measured S_{21} profile using a VNA power of $P_{\mathrm{vna}} = -10\,\mathrm{dBm}$[2]. It is clear from the plot that the transmission loss increases with frequency, as expected for the dielectric losses in the STL. Furthermore, the measured ripples in the transmission, especially noticeable at frequencies above 9 GHz, suggest that $Z_0 \neq 50\,\Omega$ for the device, resulting in an unintended impedance mismatch. This effect could originate from the smaller I_{c} of the junctions, as measured in the DC-screened devices. Furthermore, after a careful inspection following the fabrication of the devices, I noticed an error in the wiring layer photolithography mask where the capacitor plates area was 23.6% smaller than originally designed, further contributing to the impedance mismatch. The non-optimal mounting technique of the device could equally contribute generating these ripples. We also notice a spread of high-Q resonances above 6 GHz (inset Fig. 6.4). As I shall present later, these resonances barely shift in frequency with applied DC or RF power, therefore, we attribute them to the resonators, originally designed to resonate at $f_{\mathrm{r}} \sim 7\,\mathrm{GHz}$. These resonance frequencies were spreading over 300 MHz, centred

[2]The VNA power P_{vna} indicates the output power of the VNA at room temperature.

at a lower value than expected, which could be originated from the limitations in the fabrication accuracy of the photolithography steps used to define the LC circuits. On the other hand, the observed stopband around 8.5 GHz experiences a consistent frequency and amplitude shift with input power, hence we associate it to the periodic loading effect induced by the resonators' position along the transmission line.

6.3.2 Dispersion relation

The dispersion relation of the device can be calculated as $k_{\text{tot}} = -\angle S_{21}$. The measured phase is calibrated with the calibration line using Setup-B (SMA feedthough). To obtain an accurate estimation of $\angle S_{21}$ through the device, we further corrected for the additional phase between the SMA feedthrough and the identical sample holder with a blank 50 Ω PCB. Fig. 6.5(a)&(b) plot the measured dispersion for $P_{\text{vna}} = -20$ dBm and 16 dBm respectively. Fitting the experimental results shown in Fig. 6.5(a) with a linear regression, we extract a phase velocity value of $v = 5.82 \times 10^6\,\text{ms}^{-1}$. For $P_{\text{vna}} = -20$ dBm, one notices no major disruption of the dispersion curve around the resonators' resonance frequency, i.e., $f_{\text{r}} \sim 6.2$ GHz (originally targeting $f_{\text{r}} = 7$ GHz). However, when the signal power increases, as shown in Fig. 6.5(b), this effect becomes noticeable. This discontinuity is expected from the stopband generated by the resonators, and the signal power dependence effect could originate from the saturation of dielectric or two-level system (TLS) losses in the resonators, hence improving their Q-factor.

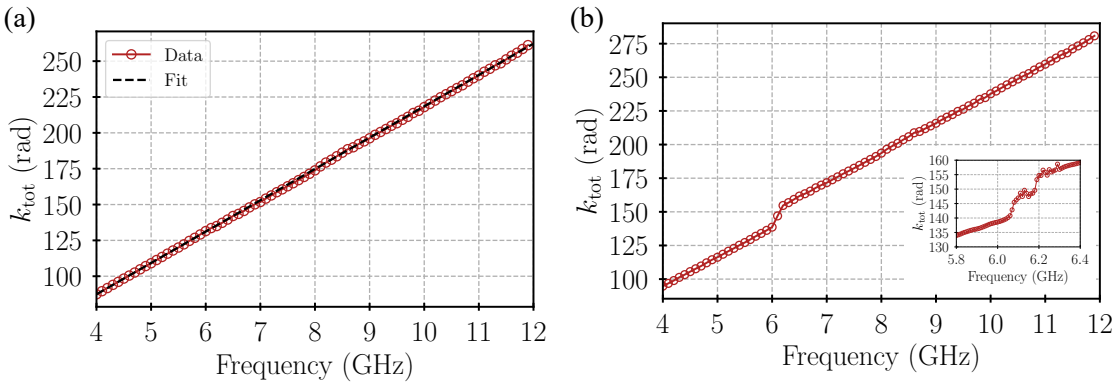

Figure 6.5: Total measured dispersion (red dots) of the JTWPA for (a) $P_{\text{vna}} = -20$ dBm and (b) $P_{\text{vna}} = 16$ dBm. In (a), we extract the phase velocity from the fitted curve (black dashed line), resulting in $v = 5.82 \times 10^6\,\text{ms}^{-1}$. At high signal powers, we notice the expected discontinuity resulting from the stopband created by the resonators in the STL.

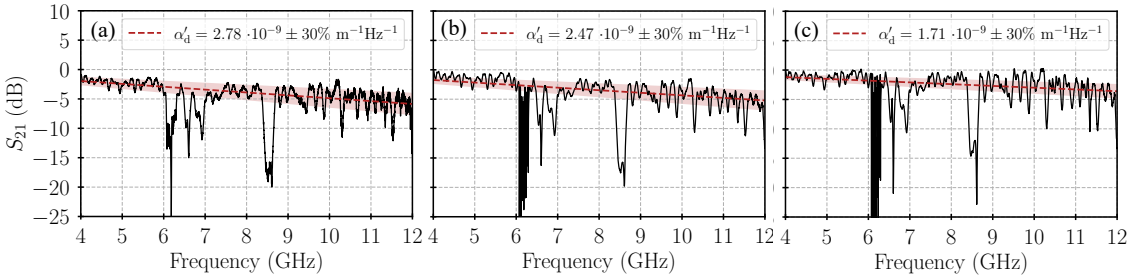

Figure 6.6: Fit of the dielectric attenuation constant $\alpha_d(f) = \alpha'_d f$ from the transmission profile for (a) $P_{vna} = -20\,\text{dBm}$, (b) $P_{vna} = 0\,\text{dBm}$ and (c) $P_{vna} = 16\,\text{dBm}$. The best α'_d fit (red dashed line) includes an arbitrary $\pm 30\%$ uncertainty interval (light red area) to account for the ripples in the transmission profile. We notice an improvement on α'_d with signal power.

6.3.3 Losses analysis

As introduced in Sec. 2.2, a signal propagating through the length (z) of a transmission line at a fixed time can be modelled as:

$$A(z) = A_0 e^{-\gamma z} = A_0 e^{-(\alpha + ik)z} = A_0 e^{-\alpha z} e^{-ikz}, \tag{6.1}$$

where A_0 is the propagating tones' amplitude. From this expression, we can clearly see the effect of the attenuation constant α in attenuating the signal amplitude over the length of the device. The attenuation constant is a cumulative effect from various contributions, and can be written as:

$$\alpha = \alpha_d + \alpha_c + \alpha_g + \alpha_r, \tag{6.2}$$

where $\alpha_d, \alpha_c, \alpha_g, \alpha_r$ are the contribution from the dielectric, conductor, substrate and radiation losses respectively. Since at $T = 10\,\text{mK}$, all the conductors in the JTWPA are superconducting, hence, we can safely neglect the contribution of α_c. Furthermore, α_g can be equally neglected given the choice of high resistive silicon for the substrate, especially at the measurement temperature of the device (10 mK) where the substrate resistance is further increased. Finally, no indication of electric field radiation was noticed from the EM simulations, as the high dielectric constant of the substrate ($\epsilon \approx 11.9$) concentrates the electric field around the trace and the PPCs. Therefore, we also neglect the contribution of α_r. As a result, we only account for the dielectric loss. This loss is frequency dependent $\alpha_d(f) = \alpha'_d f$, and can be written as [100]:

$$\alpha_d(f) = k(f) \tan \delta / 2, \tag{6.3}$$

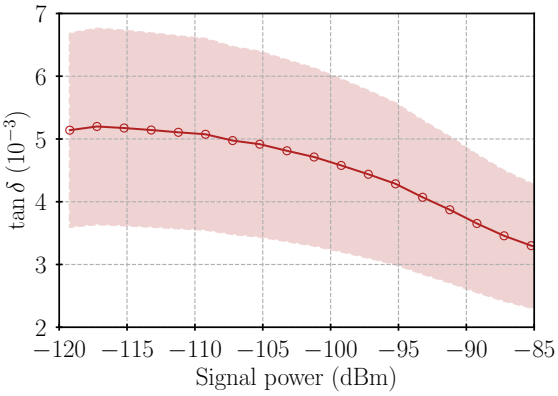

Figure 6.7: $\tan\delta$ as a function of the estimated signal power at the input of the device, showing an average value of $\tan\delta \approx 4.5 \pm 1.35 \times 10^{-3}$, consistent with the expected SiO_2 losses.

where $\tan\delta$ is the loss tangent, and $k(f)$ is the dispersion previously measured. Therefore, we can fit $-\alpha'_{\mathrm{d}} f$ to $\ln|S_{21}(f)|$ to obtain the value of α'_{d}. Fig. 6.6 shows the measured transmission and α'_{d} fit for different VNA input signal powers. We notice a reduction of the losses with increasing VNA power, as well as an improvement of the Q-factor of the resonators. Using the above expression, we can calculate the corresponding $\tan\delta$ as a function of VNA power, plotted in Fig. 6.7. We clearly notice an improvement of the $\tan\delta$ with increasing VNA power, which could originate from the saturation of the TLS or dielectric losses due to the heating effect caused by the high input power. Overall, I measured an average value of $\tan\delta \approx 4.5 \pm 1.35 \times 10^{-3}$, in line with similar JTWPAs using SiO_2 PPCs presented in the literature [148].

6.4 Nonlinear behaviour with applied I_{dc}

In Sec. 2.1.2, the expression of the current-dependent inductance of a JTWPA is shown. If we consider the Taylor expansion to the second order, Eq. 2.7 can be rewritten as:

$$L_{\mathrm{j}}(I) = L_0 \left[1 + \frac{1}{2}\left(\frac{I}{I_*}\right)^2 + \frac{1}{24}\left(\frac{I}{I_*}\right)^4 + O\left(I^6\right)\right], \tag{6.4}$$

where $I_* = I_{\mathrm{c}}$ in the case of a JTWPA. This relation indicates that we could probe the nonlinearity of the device by measuring the phase velocity of the STL $\left(v \propto 1/\sqrt{L_{\mathrm{j}}(I)\, C_{\mathrm{s}}}\right)$ when driving the device with different levels of DC current (I_{dc}); since only the inductance of the STL is modified by the amplitude of the current, not the shunt capacitance.

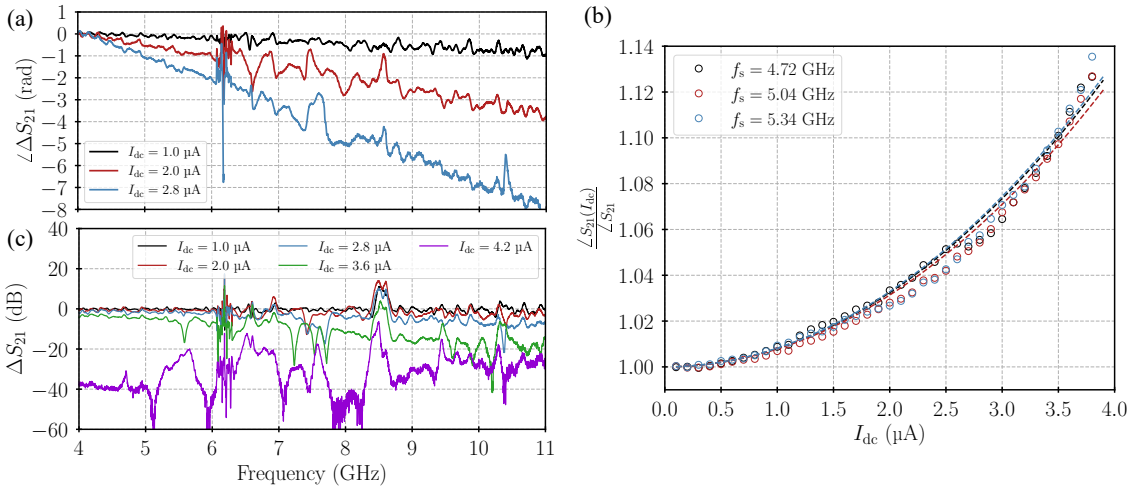

Figure 6.8: (a) Measured phase and (c) transmission amplitude with applied I_{dc} to the DUT, normalised with the transmission profile without applied I_{dc}. The change in the slope in (a) indicates a change in the phase velocity. (b) Measured data (dots) and fitted lines (dashed lines) of the ratio of transmission phase with and without I_{dc} for different signal frequencies. We calculate an average fitted $I_c = 8.25 \pm 0.09\,\mu A$.

Fig. 6.8(a) plots the shift in the phase of the transmitted RF signal measured for the JTWPA device under this condition, which clearly shows that the phase velocity of the STL increases with the amplitude of the driving DC current. These changes in phase are the direct consequence of the terms in the parenthesis of Eq. 6.4, hence we can fit this expression to estimate the value of the critical current I_c of the Josephson junctions. Fig. 6.8(b) shows the phase data (circles) measured for different signal frequencies between 4.4-5.4 GHz with their corresponding fitting curves (dotted lines), where I_c is the only fitting parameter used to match the measured curves. The fitted value of I_c and its standard deviation as a function of the signal frequency is plotted in Fig. 6.9. With this technique, we estimated an average value of $I_c = 8.25 \pm 0.09\,\mu A$, which is close to the designed $I_c = 7\,\mu A$.

Since the inductance change with applied I_{dc} is a purely reactive effect, we expect to measure a phase change without any impact on the transmission amplitude for $I_{dc} < I_c$. But, when the applied DC current exceeds the critical current value of the junctions, the STL will switch to the normal state, dissipating energy and hence resulting in a substantial reduction in the transmission amplitude. Assuming all the junctions in the JTWPA have an identical I_c value of 8.25 µA, we expect no major change in the transmission amplitude until $I_{dc} > 8.25\,\mu A$. However, as shown in Fig. 6.8(c), I measured a progressive increase in transmission losses with I_{dc}, with

the losses accelerating significantly as I_{dc} approached 4.2 µA. Beyond this point, the transmission was dominated by the losses. This effect could indicate a spread in the I_c of the junctions, most likely due to the variation in the junction size. Since we use sub-micron junctions to increase the junction inductance, a small change in the width and/or length of the junction would induce a large spread in area and hence the critical current of individual junction. Therefore, even though the previous measurement estimated an average I_c of 8.25 µA, we believe that a small number of the junctions in the array may have a much lower critical current, hence switching to the normal state at I_{dc} lower than expected. The number of these 'faulty' junctions may not be large enough to fully suppress the power transmission of the device, i.e., turn the entire STL normal. Nevertheless, their resistive state, resulting in a characteristic impedance change, may create unfavourable conditions that give rise to the unwanted effect of resonant cavities inside the STL, therefore affecting the performance of the device.

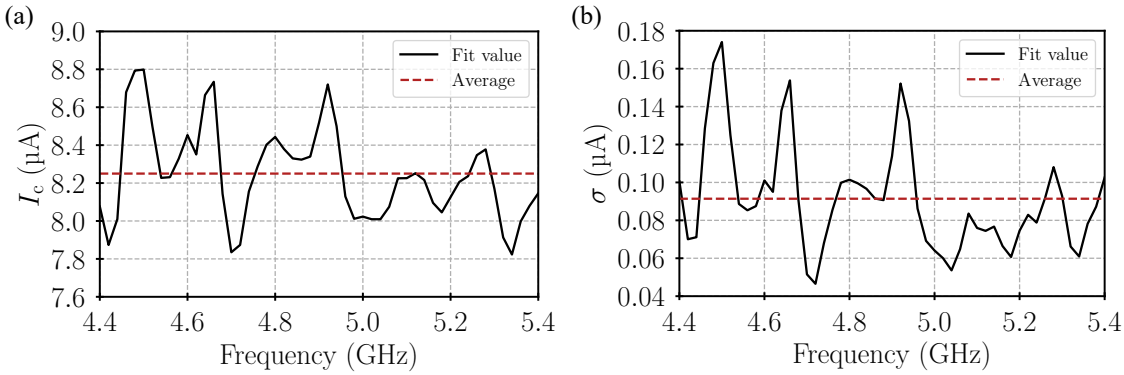

Figure 6.9: (a) I_c values obtained for the fit of the different frequencies 4.4-5.4 GHz, with the average marked in red. (b) Standard deviation error of the fitting parameter I_c, from this we can conclude an estimated fitting value of $I_c = 8.25 \pm 0.09$ µA, close to the design value for our design of $I_c = 7$ µA.

6.5 Harmonics generation

The JTWPA is fundamentally a $\chi^{(3)}$ nonlinear transmission line, therefore when a signal tone at frequency f_p is applied, we expect to observe the generation of the odd harmonic tones, e.g., the third harmonic ($3f_p$), without the even harmonics like the second harmonic ($2f_p$). For this experiment, I used a modified version of Setup-C[3],

[3]The IR filter is placed before the directional coupler, and another IR filter is added after the circulator. A single room temperature amplifier was used in this case for the readout.

where the signal generator inputs a strong pump tone into the DUT, and I measured the output power of the different harmonic tones using the spectrum analyser. The pump frequency in this setup is limited to $f_\mathrm{p} = 4\,\mathrm{GHz}$ due to the bandwidth of the circulator used for the experiment.

Fig. 6.10(a) shows the measured output power of the pump tone ($P_\mathrm{p,meas}$) as a function of the power set on the signal generator ($P_\mathrm{p,in}$). We observed a linear trend as expected, with a sudden drop around $P_\mathrm{p,in} \sim -22\,\mathrm{dBm}$, associated with the deterioration of the transmission through the device. Fig. 6.10(b) plots the measured ratio between the second and the third harmonic's amplitude with respect to the pump's amplitude $A_\mathrm{h}/A_\mathrm{p} = 10^{\left(P_\mathrm{h,meas}[\mathrm{dBm}]+\mathrm{L[dB]}-\mathrm{P_{p,meas}[dBm]}\right)/20}$, where $P_\mathrm{h,meas}$ is the measured power of the harmonics from the spectrum analyser and L is the losses in the device at the harmonic frequency normalised with the losses at the pump frequency. Calibrated with the previously measured transmission profile of the device, I estimate that $L = 4\,\mathrm{dB}$ and $10\,\mathrm{dB}$ for the second and third harmonic respectively. The error bars in the plot account for the uncertainty in the calculated losses at the output line, which I estimate to be $1\,\mathrm{dB}$ and $2\,\mathrm{dB}$ for the second and third harmonic respectively. Note that since I used $P_\mathrm{p,meas}$ to calculate $A_\mathrm{h}/A_\mathrm{p}$, the pump depletion results in a small overestimation of the calculated ratio. For a precise calculation of $A_\mathrm{h}/A_\mathrm{p}$, a proper power calibration of the setup would be required, which was not possible at the time of taking the measurements. Nevertheless, the general trend clearly showed a substantial third harmonic generation and negligible second harmonic generation, as expected for a $\chi^{(3)}$ nonlinear material.

Finally, Fig 6.10(c) shows the $A_\mathrm{h}/A_\mathrm{p}$ predicted through the theoretical calculation using the CME[4] as a function of the input current in the device. I simulate the two potential I_c values suggested from previous measurements. Assuming that the transmission deterioration, marked with a grey area in Fig 6.10(a) & (b), happens at $I \sim 4.2\,\mu\mathrm{A}$ (as measured in Sec. 6.4), the theory and measurement for the $I_\mathrm{c} = 4.2\,\mu\mathrm{A}$ case show different behaviours. However, when simulating $I_\mathrm{c} \sim 8.25\,\mu\mathrm{A}$, we obtain a better match with the measurements. Therefore, these results agree with the measurements presented in Sec. 6.4, suggesting $I_\mathrm{c} \sim 8.25\,\mu\mathrm{A}$, with a transmission drop at $I \sim 4.2\,\mu\mathrm{A}$, probably caused by an spread of the junctions I_c.

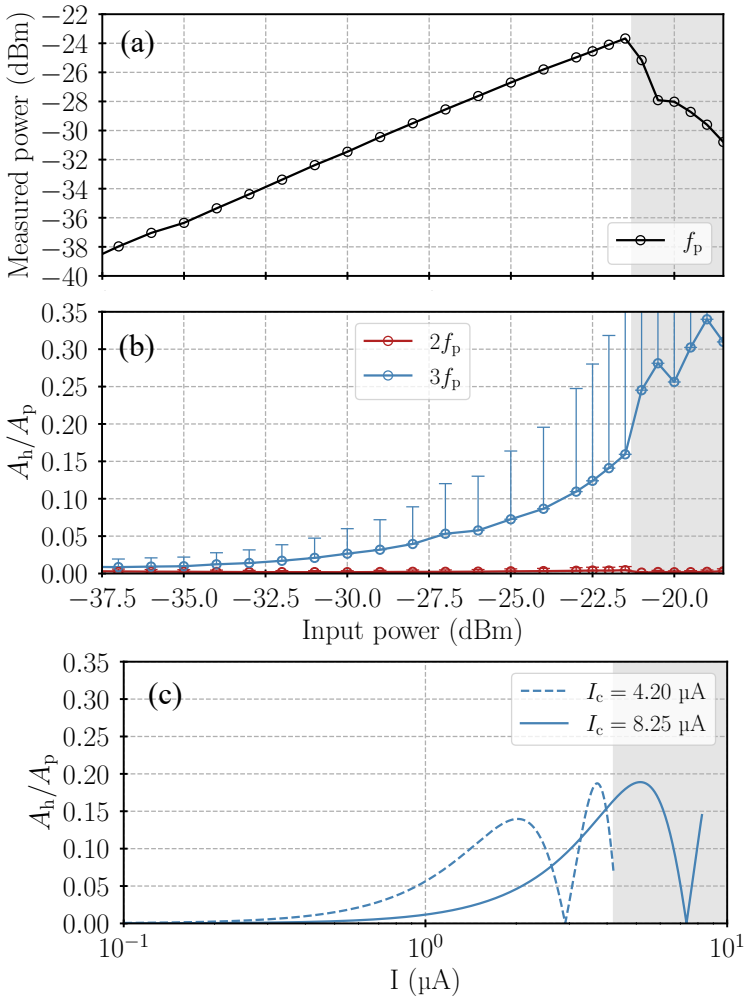

Figure 6.10: Harmonics generation in the JTWPA. (a) Measured output power of a pump tone at $f_p = 4\,\text{GHz}$ as a function of the power set from the signal generator. The drop in the otherwise linear curve around –22 dBm is linked to a deterioration of the transmission through the device at high power. (b) Ratio of the measured amplitude of the second (red) and the third (blue) harmonic and the pump (A_h/A_p) as a function of the pump power set by the signal generator. (c) Theoretical calculation of the third harmonic A_h/A_p as a function of input current in the JTWPA for $I_c = 4.2\,\mu\text{A}$ and $8.25\,\mu\text{A}$. The x-axis is plotted in log scale, and $C_s = 14.36\,\text{fF}$ for this calculation[5].

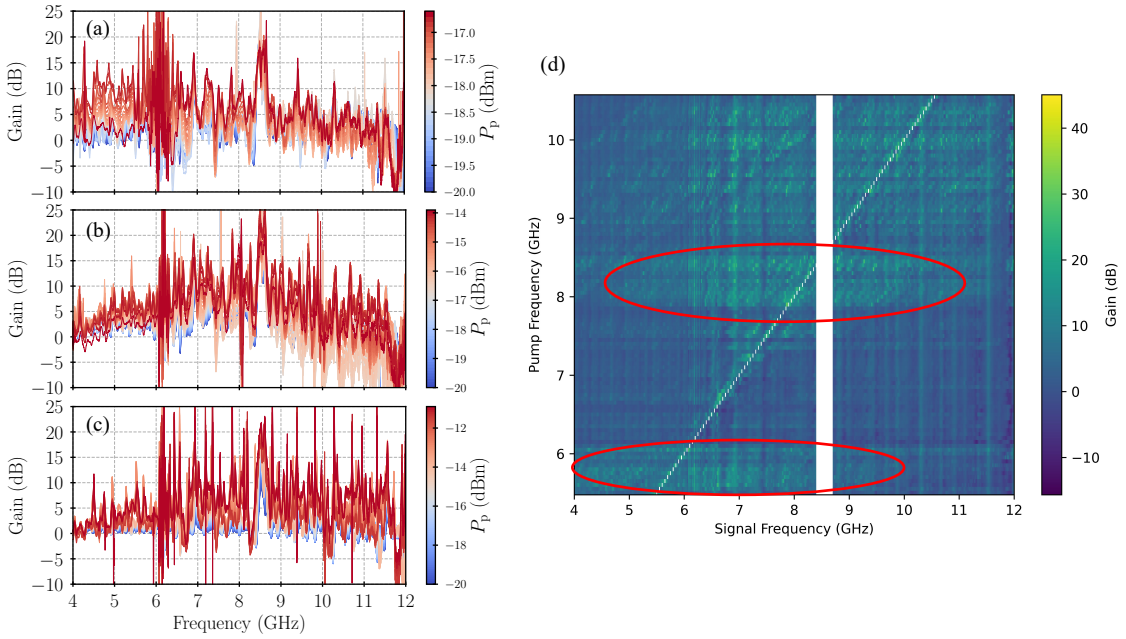

Figure 6.11: Measured pump on/off gain of JTWPA device B7 in using Setup-C[6]at different pump powers and frequencies (a) $f_p = 6.05\,\text{GHz}$, (b) $f_p = 8.05\,\text{GHz}$ and (c) $f_p = 10.2\,\text{GHz}$. The gain reach larger values around the pump frequency as expected. We associate the gain peaks to resonant cavities resulting from the impedance mismatch of the device and 'faulty' junctions with a lower critical current than the average. (d) 2D plot of the maximum gain for different pump frequencies. The circles indicate the regions with larger gain.

6.6 Gain and saturation

From the previous sections, we observe clear indications of the nonlinearity required for parametric amplification in the JTWPA. Therefore, next I explored the changes in the transmission profile of the device when pumping it with a strong pump tone at different frequencies and powers. Fig. 6.11(a), (b) & (c) plot the measured profile when pumping at $f_p = 6.05\,\text{GHz}$, $8.05\,\text{GHz}$ and $10.2\,\text{GHz}$ with different pump power levels. We clearly observe a broadband 4WM gain, with rapid variation, where some of the gain peaks reach values over 25 dB. This gain variation could partly result from the impedance mismatch of the JTWPA, but it could also be a consequence of the large spread of I_c as discussed in Sec. 6.4. In the three cases shown here, we notice a region of maximum gain around the pump frequency. I further measured

[4]For simplicity, I used the undepleted-pump approximation.

[5]The design value was $C_s \sim 18.8\,\text{fF}$, for this simulation we account for the 23.6% reduction of PPCs size.

[6]No room-temperature attenuation was used in the input line for this measurement.

the gain profile from $f_p = 5.5\,\text{GHz}$ to $10.5\,\text{GHz}$ using OPAL python library [149], increasing the pump power from $P_p = -20\,\text{dBm}$ until reaching the I_c of the junctions; Fig. 6.11(d) plots the maximum gain curve measured within the scanning range. We remove the pump frequency points (diagonal dotted line) and the stopband resulting from the resonators' periodic loading (white vertical band) for clarity. This plot shows two distinguishable regions with broadband gain, below 6 GHz and 8.5 GHz (circled regions), that we associate with a partial phase-match due to the stopbands of the resonators' resonance frequency and the resonators' periodic loading effect respectively. Nevertheless, given the fabrication uncertainties, these phasematches are not optimal, hence possibly resulting in an improvement of the gain lower than expected.

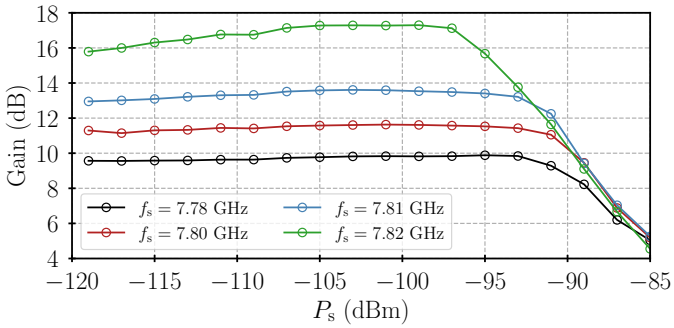

Figure 6.12: Gain value at different signal frequencies as a function of the signal power at the input of the device. We calculated a compression point of $P_{1\text{dB}} = -95.8, -91.4, -90.3$ and $-90\,\text{dBm}$ for a gain value of $17.3, 13.5, 11.6$ and $9.8\,\text{dB}$ respectively.

I further measured the saturation of the device when pumped at $f_p = 8\,\text{GHz}$ with $P_p = -13.7\,\text{dBm}$. In Fig. 6.12, I plot the change in gain relative to the input signal power level, for different signal frequencies. I used the measured transmission of the signal line at room temperature ($-99.17\,\text{dB}$ at $8\,\text{GHz}$) to calibrate the signal power, and estimate the power level at the input of the device. However, this technique may result in an overestimation of the losses in the input line, since the transmission improves at cryogenic temperatures. The 1 dB compression points of $P_{1\text{dB}} = -95.8, -91.4, -90.3$ and $-90\,\text{dBm}$ were obtained for gain values of $17.3, 13.5, 11.6$ and $9.8\,\text{dB}$ respectively. These values are higher than similar JTWPA designs reported in the literature [79, 80], hence resulting in the advantage of an increased dynamic range of the amplifier. Furthermore, note that in this measurement the input losses are overestimated by using the value measured at room temperature,

therefore, underestimating the compression point. We expect the actual P_{1dB} of the device to be close to $\sim 1-2\,$dB larger than measured[7]. The rather high compression point measured in this device results from the modest gain, since low gain naturally increases the compression point of a JTWPA, and the larger I_c of the junctions compared to other JTWPA implementations.

Similar to other JTWPAs presented in the literature [80], we also noticed an improvement on the measured gain for intermediate signal powers, usually between $-115\,$dBm and $-97\,$dBm in our case, as it can be seen in the green curve in Fig. 6.12. This effect is frequency dependent and is more noticeable for signal frequencies that experience high gain, often located inside the gain peaks observed in Fig. 6.11(a)-(c). This effect could result from the improvement in the dielectric losses measured in Sec. 6.3. However, from the measured values, we only expect a $\sim 0.42\,$dB improvement in the transmission at $f_s = 7.8\,$GHz from $P_s = -120\,$dBm to –100 dBm, which is insufficient to explain the measured $\sim 1.4\,$dB gain improvement. Another contributing factor could be the under-pumping of the device [64], i.e., the pump power is lower than required for optimal gain. Increasing the signal power could shift the transmission features, changing the actual pump and signal power transmitted through the line and therefore the generated gain. Although a more sophisticated analysis would need to be carried out to understand this effect, we can discard the saturation of dielectric losses as the only originating factor.

6.7 Discussion on gain stability

Despite the observation of broadband gain in Device B7 using Setup-C, I noticed that the gain behaviour was not reproducible between different cooldowns despite using identical setups. Sometimes, pumping the device with the same pump frequency and amplitude as before only resulted in narrow-band gain. Fig. 6.13(a)&(b) show an example of the gain measured in one of these cooldowns, when pumping the device at $f_p = 7\,$GHz. As we can see, the gain increases with the pump power, before the transmission drops as expected from reaching the critical current of the junctions. We also observed a similar behaviour at different pump frequencies, but the gain shape varied drastically from cooldown to cooldown. Furthermore, the shape, frequency extent, and amplitude of the narrow-band gain changed when waving a magnet outside the cryostat, indicating a high sensitivity to external magnetic fields.

[7]Expected transmission improvement of the input line at cryogenic temperatures.

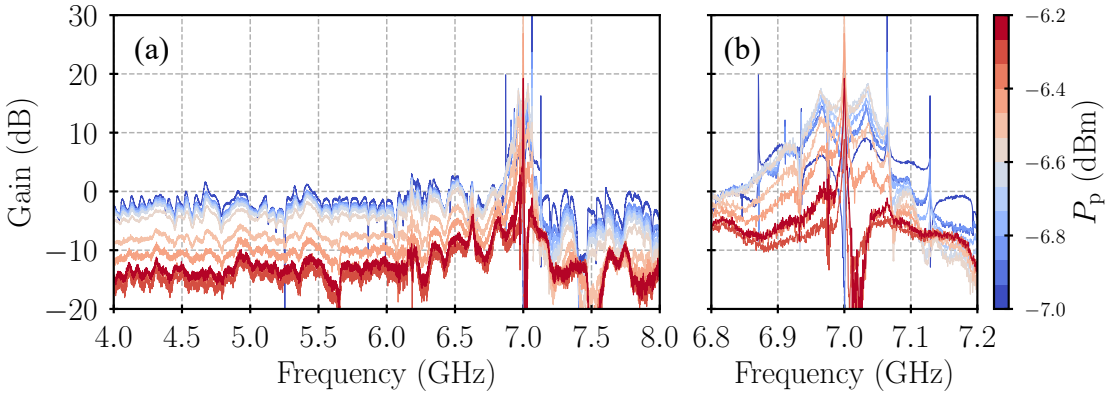

Figure 6.13: JTWPA device B7 measured in a different cooldown using Setup-C. (a) Measured pump on/off gain pumped at $f_\mathrm{p} = 7\,\mathrm{GHz}$, and different pump powers. The pump power values correspond to the power set in the signal generator. (b) Zoom-in around f_p.

The observed effects could originate from trapped magnetic fluxes in the device. Trapped magnetic fluxes may vary from cooldown to cooldown, and they can be removed by warming the device above the critical temperature and cooling down again. Furthermore, they will interact with an external magnetic field as we observed in our experiments. There are techniques to mitigate trapped magnetic fluxes, e.g., using a magnetic shield during the cooldown to protect the device from the external magnetic field or adding holes to the conducting layer forming the ground plane of the CPW to trap the magnetic fluxes far from the trace, however, they were not implemented in the experiments presented in this chapter due to time limitations. We suspect that the conditions during the cooldown where we observed broadband gain were somehow favourable, inducing no (or very little) trapped magnetic fluxes in the device. In further cooldowns, I could reproduce the broadband gain again by using a cryoperm shield to protect the device. Nevertheless, the amplitude of the gain was still largely dependent on the setup used or the conditions of the cooldown. We believe this may have resulted from the reflection induced by the different components and the RF cables used in the experimental setup. For example, I used hand-flex coaxial SMA cables, not specified for cryogenic temperatures, which after several bending and cooldown cycles can quickly deteriorate their performance.

6.8 Conclusion

In this chapter, a thorough investigation into the performance of the JTWPA with PPCs designs was carried out. Despite incorporating a 20 nm Al_2O_3 protective layer during fabrication to address the issue of pin-holes in the PPCs, these defects remain a significant challenge, leaving the majority of the devices unusable. However, one device (B7) showed promising results, particularly in terms of its transmission profile, dispersion, and gain characteristics.

Further analysis of device B7 revealed clear signs of nonlinear inductance in the transmission line, such as changes in the S_{21} phase with applied I_{dc} and harmonics generation. Although these experiments suggested a critical current of $I_{\mathrm{c}} = 8.25$ µA, an unexpected drop in transmission was observed above $I_{\mathrm{dc}} = 4.2$ µA. This anomaly could be due to variability in the I_{c} across the junctions, probably due to a variation of the junctions size. Further investigation will be required to fully understand this effect.

When pumping the device, a broadband gain was observed, though with substantial ripples that are likely caused by an impedance mismatch. In some frequency ranges, the gain exceeded 25 dB. Furthermore, the compression point was measured at $P_{\mathrm{1dB}} = -95.8\,\mathrm{dBm}$ for a gain of 17.3 dB, outperforming other JTWPA implementations. However, the gain varied inconsistently between cooldowns, suggesting possible issues with trapped magnetic fluxes in the device.

In conclusion, while this chapter represents significant progress in understanding and advancing the designs of JTWPAs with PPCs, the identified fabrication challenges and inconsistencies in device behaviour highlight the need for further improvements to achieve a more reliable performance.

Chapter 7

Microwave JTWPA with IDCs

As presented in the previous chapter, pin-holes in the dielectric layer is a persistent issue in the JTWPA with PPCs, resulting in a low fabrication yield. To improve the fabrication yield while maintaining a similar performance, I re-designed the microwave JTWPA, replacing the PPCs with single layered interdigitated capacitors (IDCs). I have fabricated and tested a number of these devices in the final phase of my DPhil programme, due to time limitations resulting in less comprehensive results than the JTWPA with PPCs presented in the previous chapter. In this chapter, I summarise and discuss the experimental results from these microwave JTWPAs with IDCs.

7.1 Design and fabrication overview

Design C and Design D, presented in Sec. 3.5.2, were fabricated during my visit to IRAM from the 4^{th} to the 29^{th} of February 2024. Both designs included IDCs instead of PPCs to increase the shunt capacitance to the ground resulting in $Z_0 = 50\,\Omega$. One design was optimised for a 4WM operation with $f_\text{p} \sim 8\,\text{GHz}$, formed with 2,058 junctions, and the other design was intended to operate in a DC3WM regime with $f_\text{p} \sim 12\,\text{GHz}$, formed with 2,016 junctions. I successfully fabricated two wafers, resulting in 38 JTWPA devices in total. A detailed layout of the photolithography masks used during the fabrication is presented in Appendix D.

Both designs were fabricated on the same wafer following the fabrication recipe presented in Chapter 4. I used 500-µm thick high-resistive silicon substrates, and the trilayer was deposited using an oxidation time and pressure of $t_\text{ox} = 5\,\text{h}$ and $P_\text{ox} = 4\,\text{Pa}$ respectively, to obtain a $J_\text{c} = 1.4\,\text{kA/cm}^2$. As explained in Sec. 3.5.2, for these designs I replaced the LC resonators by a periodic loading scheme for dispersion engineering. Fig. 7.1(a) shows a microscope image of the DC3WM JTWPA design,

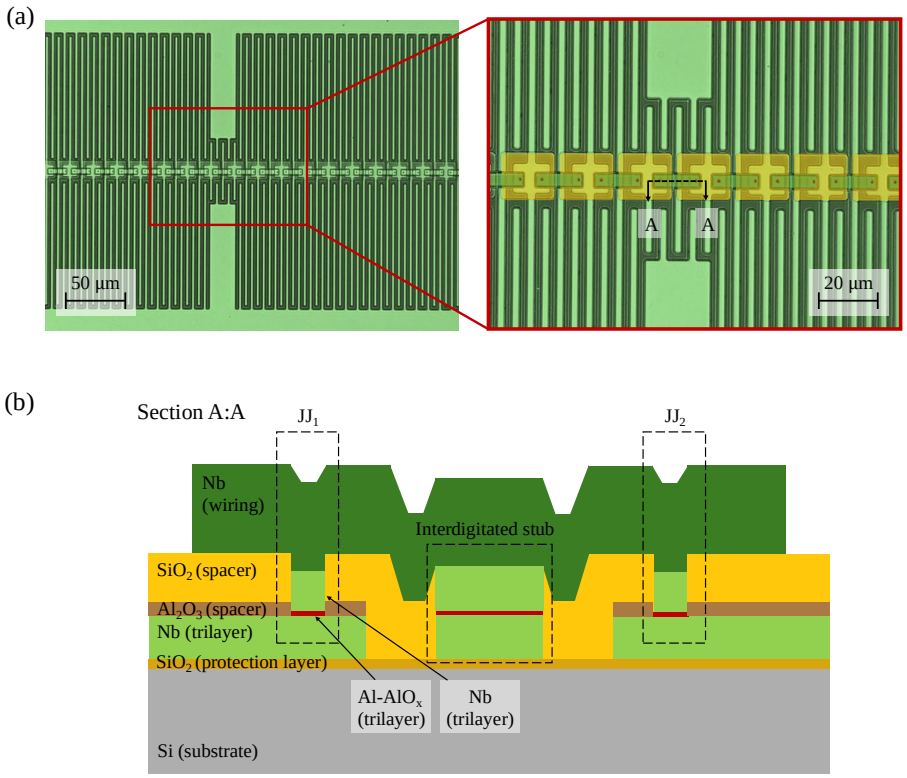

Figure 7.1: (a) Microscope image of the DC3WM JTWPA with IDCs design. The section with shorter stubs is periodically repeated to create a loading effect, replacing the *LC* resonators as dispersion engineering element. The fake colours in the zoom-in image shows the trilayer (light green), SiO_2 from the spacer (yellow), wiring layer (dark green) and junctions (red). Note the small misalignment of the SiO_2 windows, which was observed in numerous devices. (b) Cross-section of the JTWPA (not drawn to scale).

where the loading section is clearly shown. The stack-up topology of the device is presented in Fig. 7.1(b).

Following the fabrication, I inspected the devices using the optical microscope to identify possible fabrication issues. The results from my observations are summarised in Tab. 7.1. For many devices, I noticed a shift in the SiO_2 windows depending on the chip's location on the wafer. This is due to the misalignment during fabrication. Of the 37 devices that I inspected, 27 did not show appreciable defects.

Wafer ID	Major issue (# devices)	Minor issue (# devices)	No issue (# devices)
1	5	5	8
2	5	9	5

Table 7.1: Yield statistic for the fabricated JTWPA with IDCs examined using optical microscope. A total of 37 devices were observed, where 27 showed minor or no issue.

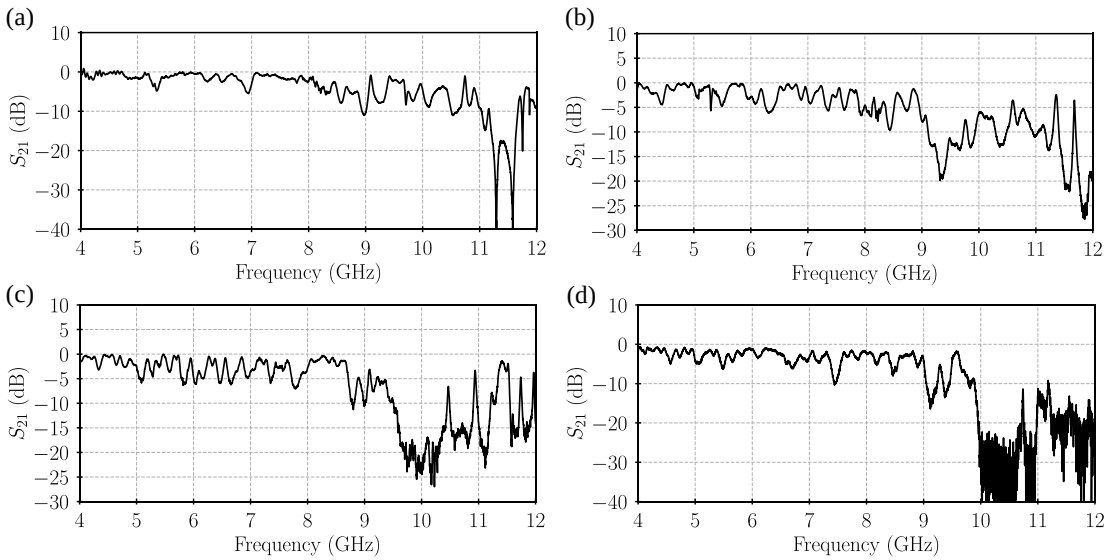

Figure 7.2: RF transmission measured at cryogenic temperature for DC3WM JTWPAs designs with IDCs from Wafer 1 for (a) Device B2, (b) Device B5, (c) Device B4 and (d) Device B3. Device B2, B4 and B5 were measured in OX300, while B3 was measured in LD250.

7.2 RF transmission profiles

Following the inspection under the microscope, I selected 5 devices (B1-B5 from Wafer 2), that do not exhibit major fabrication issues, for DC screening using the setup scheme in Sec. 4.3.2.2. When applying current through the trace of the devices, however, I measured an open-circuit for all of them. This could indicate an unsuccessful liftoff for some of the junctions in the array. Given these results, I decided not to continue DC-screening more devices, considering that the DC-screening setup may be faulty and could be damaging the devices. Therefore, I proceeded straight into RF characterisation using OX300 and LD250 for some of these devices without previous DC screening. From April 2024 until the time of writing, I performed 12 cooldowns, measuring 11 different devices. The devices were mounted in the sample holders using the techniques described in Sec. 4.2.

Out of the 11 tested devices, I measured good transmission in 4 of them. All 4

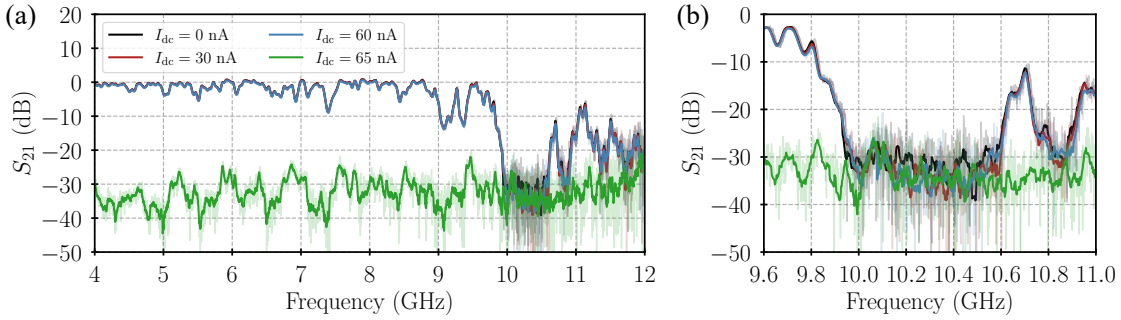

Figure 7.3: (a) Transmission profile of device B3 for different values of applied current I_{dc}. (b) Zoom-in around stopband structure. The light and dark coloured lines represent the raw and averaged data respectively. The signal power in the VNA is set to $P_{vna} = -20\,\text{dBm}$.

devices were the DC3WM design (Design D) from Wafer 1[1]. For the remaining of this chapter, I will focus on these 4 devices. Fig. 7.2 plots the transmission profiles with respect to a feedthrough without DUT, measured at the cryostat's base temperature ($T = 10\,\text{mK}$ in LD250 and $T = 600\,\text{mK}$ in OX300[2]) using slightly modified Setup-B and Setup-C[3]. As expected, we do not observe a linear increase of the losses with frequency anymore, which was originated from the dielectric layer as observed for the JTWPA with PPCs. Nevertheless, the measured transmissions show numerous dips and ripples that differ substantially from device to device. This effect could be potentially originated from a systematic error in the junction size, the non-optimal mounting technique used for the devices, and/or the minor fabrication issues such as the shift of the SiO_2 windows. The designed periodic loading stopband for this design was expected to form around 12 GHz. However, we cannot identify a clear stopband structure in all the 4 devices, but in Fig. 7.2(c)&(d) we notice a dip around 10 GHz that could potentially be originated from the loading effect.

To further characterise the nonlinear effect of these devices, I measured the RF transmission profile when applying a DC-current (I_{dc}) through the device. Fig. 7.3 shows the results obtained for device B3, with a cryoperm shield to protect the device from external magnetic flux. No substantial change in the transmission amplitude or phase is observed until we reach $I_{dc} = 65\,\text{nA}$. This I_{dc} value is well below the

[1]Due to time constrain, I did not have the opportunity to test all of the devices in both Wafer 1 & 2, including most of the DP4WM design (Design C). Therefore, it is possible that there are some functioning devices remaining among the untested ones.

[2]When numerous components are installed in the cold-plate, the system struggles to reach the base temperature of 300 mK, often stabilising at $\sim 600\,\text{mK}$

[3]Device B3 had a 3 dB attenuator at the input and output of the device.

targeted critical current of the device $I_c = 7\,\mu A$, which could indicate the presence of outlier junctions in the line with $I_c \sim 65\,nA$. Furthermore, a closer look around 10 GHz (Fig. 7.3) shows no sign of frequency shift of the stop band as we would expect with increasing I_{dc}. However, this could be due to the small I_{dc} values used, since assuming $I_c = 7\,\mu A$ implies $I_{dc} = 65\,nA = 0.009 I_c$, for which we expect only a 0.004 % increase in L_j, therefore a $\sim 200\,kHz$ shift. As the transmission data was taken with a frequency step of 2 MHz, the expected shift is too small to be observed in our measurements. I found similar results for the remaining three devices.

7.3 Calibrated dispersion

As presented in the previous section, changes in the transmission phase were difficult to be observed with applied DC-current, making it challenging to estimate the JTWPA average I_c using the techniques presented in Sec. 6.4. Nevertheless, I_c can also be estimated from the fit of the dispersion relation of the device. As presented in Sec. 3.1.1, assuming translation symmetry, we can write the total wavevector (k_{tot}) in a JTWPA as a function of the unit cell parameters:

$$k_{tot}(\omega) = N_{jj} \cos^{-1}\left(1 + \frac{Z_1}{2Z_2}\right) \tag{7.1}$$

where $Z_1 = \frac{1}{1/(iL_0\omega)+iC_j\omega} + iL_{geo}\omega$, $Z_2 = \frac{1}{iC_s\omega}$, and N_{jj} is the number of junctions in the JTWPA. Using the design parameters obtained from the simulation of our JTWPA, I set all the parameters to the designated values except those depending on I_c, i.e., just Z_1, hence the only free parameter to fit in k_{tot} is I_c. For that, I measured the phase of the transmission through the device ($\angle S_{21,raw}$) and subtracted it with the phase measured with an SMA feedthrough replacing the device ($\angle S_{21,feedthrough}$). I further corrected the extra phase of the device's sample holder compared to the SMA feedthrough used for the calibration ($\Delta\angle S_{21,blank}$). Hence, we can re-write the total dispersion of the device as $k_{tot}(\omega) = \angle S_{21,raw}(\omega) - \angle S_{21,feedthrough}(\omega) + \Delta\angle S_{21,blank}(\omega)$. Fig. 7.4 plots the results obtained, where the circles represent the measured data and the dotted line correspond to the parameters' fit. The values for the different parameters obtained from the fit for each device are summarised in Tab. 7.2. We obtained an average $I_c = 4.61 \pm 0.56\,\mu A$, lower than the targeted $I_c = 7\,\mu A$. This effect could originate equally from a smaller J_c and/or A_{jj}, compared with the targeted design value. Assuming $J_c = 1.4\,kA/cm^2$ as targeted, the junctions need to be $\sim$ 34.1% smaller than expected to explain the measured I_c. This reduction of A_{jj} might

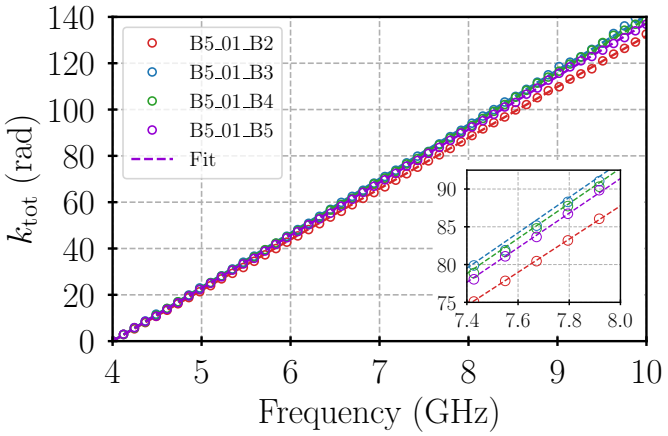

Figure 7.4: Calibrated wavevector of the JTWPA devices. The measured data (circles) are fitted with Eq. 7.1 (dashed lines) fixing the following design parameters: $C_s = 58.4\,\text{fF}$, $L_{geo} = 16.45\,\text{pH}$, $N_{jj} = 2016$ and $A_{jj} = 0.5\,\mu\text{m}^2$. The only free parameter in the equation is I_c. We obtained an average value of $I_c = 4.61 \pm 0.56\,\mu\text{A}$ for the four devices, lower than the targeted $I_c = 7\,\mu\text{A}$. The k_{tot} data is normalised to k_{tot} at 4 GHz.

Device	B2	B3	B4	B5
I_c (µA)	5.11 ± 0.63	4.31 ± 0.52	4.41 ± 0.53	4.59 ± 0.56

Table 7.2: Summary of the calculated I_c from the parameters fit of the wavevector data. We consider a 10% uncertainty in C_s, to reflect possible fabrication inaccuracies.

result from an over-etching or oxidation of the junctions side-walls, as previously noticed in in Chapter 5, which we believe is the most likely scenario.

7.4 Narrow-band 4WM gain

As explained in Sec. 2.2.1, unlike the standard 3WM regime — used in JTWPAs formed with SNAILs and RF-SQUIDs — requiring an external magnetic field, the DC3WM uses a DC-current to break the centrosymmetry of the device at the origin of the 3WM interactions. This technique, originally implemented in KTWPAs [77], has not been yet demonstrated in JTWPAs. The four devices explored in this chapter were designed to operate at the DC3WM regime. However, the results presented in Sec. 7.2 demonstrate the difficulty in DC-biasing them for DC3WM operation. Therefore, I explored the generation of a non-phase-matched 4WM gain. Fig. 7.5 shows the measured pump on/off gain of device B2 measured in OX300 using Setup-B when pumped at $f_p = 6\,\text{GHz}$ (Fig. 7.5(a)&(b)) and 7.6 GHz (Fig. 7.5(c)&(d)). I

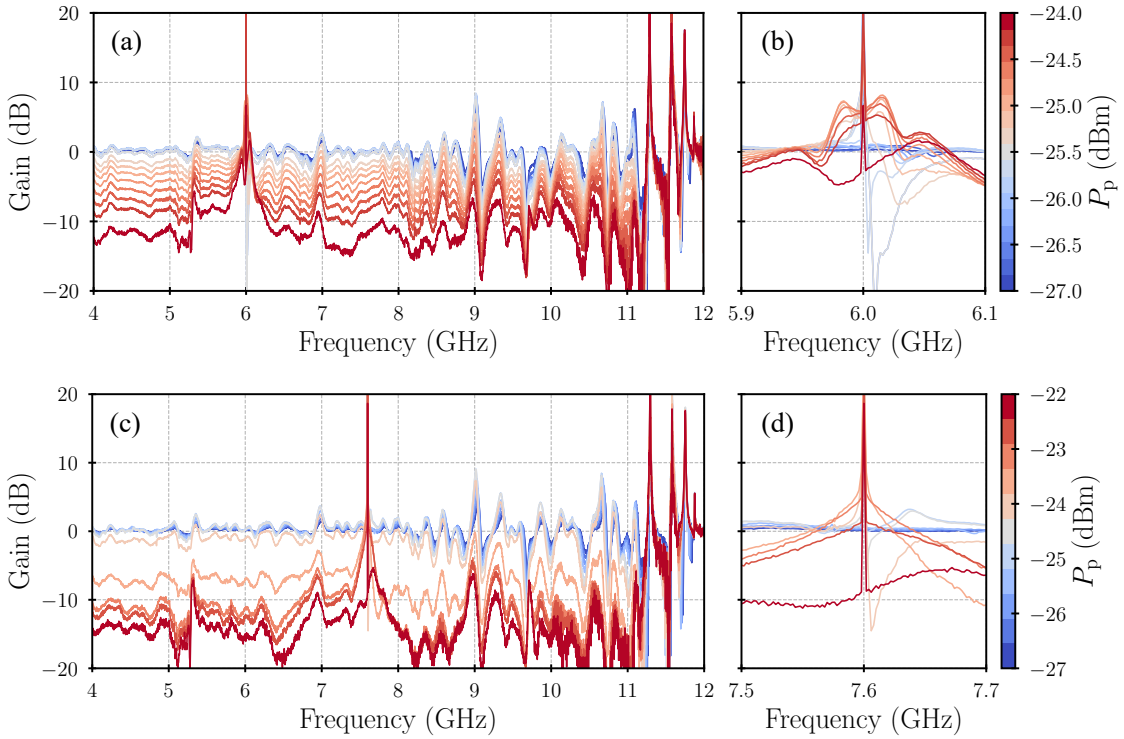

Figure 7.5: Measured 4WM gain in Device B2 when pumping at (a) $f_p = 6\,\text{GHz}$ — (b) zoom-in plot around f_p — and (c) $f_p = 7.6\,\text{GHz}$ — (d) zoom-in plot around f_p. The colours represent different pump powers; the values on the colour bar refer to the output of the signal generator.

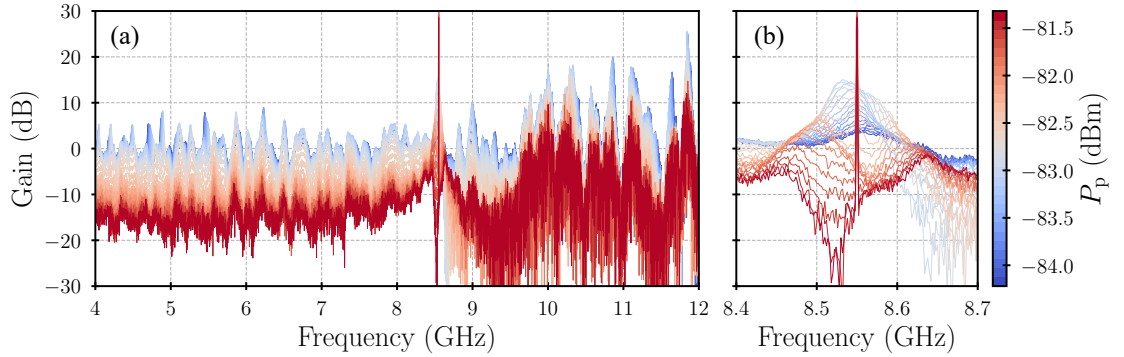

Figure 7.6: Measured 4WM gain in Device B4 when pumping at $f_p = 8.55\,\text{GHz}$. (a) Plot from $f_s = 4\,\text{GHz}$ to $12\,\text{GHz}$. (b) Zoom-in plot around f_p. The colours represent different pump powers; the values on the colour bar refer to the device's input.

observed the rise of narrow-band gain around the pump frequency, reaching values close to $\sim 8\,\mathrm{dB}$ and extending over a couple tens of MHz. These gain profiles are largely dependent on the pump frequency and power. The same device was measured in LD250 using Setup-C with a cryoperm shield to protect the device from external magnetic field, however, interestingly we measured identical results. Using the same setup, I further measured device B4 and the results for pumping the device at $f_\mathrm{p} = 8.55\,\mathrm{GHz}$ are plotted in Fig. 7.6. We achieved narrow-band gain at several frequency points, with the higher gain reaching values of $\sim 15\,\mathrm{dB}$. We observed similar results for the remaining 2 devices.

7.5 Noise analysis

A quick way to check the noise performance of a JTWPA is by measuring the signal-to-noise ratio (SNR) of the system with and without pumping the device [57, 79]. Assuming the JTWPA's noise is much smaller than the HEMT amplifier used for the readout, pumping the JTWPA would result in an improvement of the system SNR (as it can be inferred from Friis equation introduced in Chapter 1, Sec. 1.1). I used device B4 for this experiment, measured in LD250 using Setup-C2. The signal tone at $f_\mathrm{s} = 8.536\,\mathrm{GHz}$ is generated using the continuous wave mode (CWM) of the VNA, with a signal power $P_\mathrm{VNA} = -20\,\mathrm{dBm}$. The pump tone at $f_\mathrm{p} = 8.55\,\mathrm{GHz}$ is generated with the Anritsu® MG36241A signal generator, and the power level is swept during the experiment. I chose the signal and pump frequency range that resulted in the maximum gain observed in device B4 presented in the previous section. I set the spectrum analyser acquisition parameters centered at f_s over 1 MHz window, with a 10 kHz radio bandwidth. Fig. 7.7(a) shows the power spectra density (PSD) of Device B4, referred at the input of the DUT, with and without applying the pump tone. For the pump power $P_\mathrm{p} = -83.34\,\mathrm{dBm}$ at the input of the device, I observed an 8.4 dB SNR improvement, therefore demonstrating the lower added noise of the JTWPA compared with the HEMT. The measured PSD can be expressed in noise temperature as $T = P[\mathrm{W}]/k_\mathrm{B}B$, where $P[\mathrm{W}]$ is the PSD in Watts, and B is the measurement bandwidth. Therefore, the system noise at the input of our device went from 31.5 K to 4.5 K by pumping the JTWPA. The measured noise temperature is about an order of magnitude larger than the standard quantum-limit (SQL) added noise ($\sim 410\,\mathrm{mK}$)[4].

[4]Here we define the SQL as 1 photon, since assuming that our JTWPA is quantum-limited, we would measure $h\nu/2$ noise from the vacuum fluctuations and $h\nu/2$ of added noise by the amplifier. Therefore, the smallest noise measurable in the system is $h\nu$, i.e., one photon.

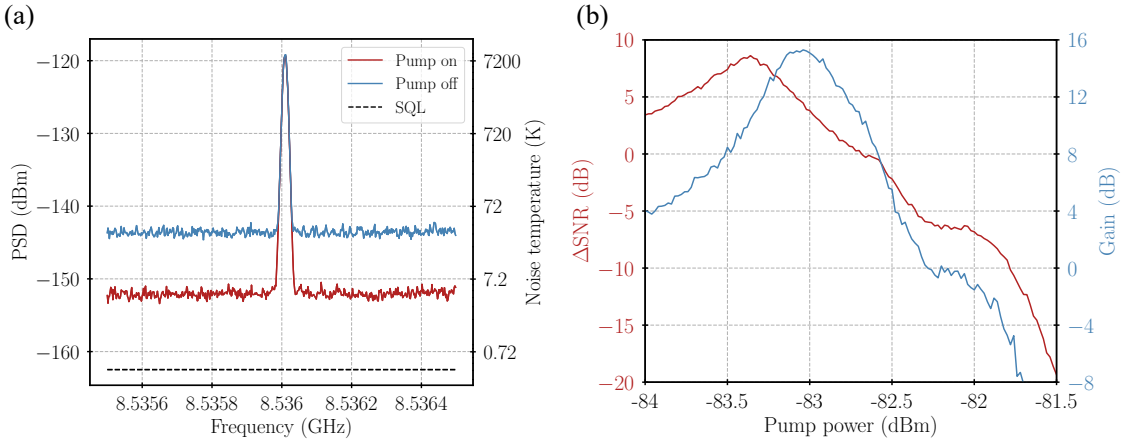

Figure 7.7: (a) PSD measured in 1 MHz window around $f_s = 8.536\,\text{GHz}$, when the pump at $f_p = 8.55\,\text{GHz}$ and $P_p = -24.12\,\text{dBm}$ ($P_{p,in} = -83.34\,\text{dBm}$) is switched on and off, using a radio bandwidth setting $B = 10\,\text{kHz}$. The PSD is expressed in power (dBm) and equivalent noise temperature (K) referenced to the input of the device. The SQL noise $P_{SQL}[W] = h\nu B$, i.e., $T_{SQL} \sim 410\,\text{mK}$, is marked with a dashed line. The average noise floor with pump off versus pump on is 31.5 K and 4.5 K, resulting in an SNR improvement of $\Delta SNR = 8.4\,\text{dBm}$. (b) Gain (pump on/off) and SNR improvement as a function of pump power referenced to the input of the device. The maximum gain 15.2 dB is achieved with $P_{p,in} = -83.04\,\text{dBm}$, which does not coincide $P_{p,in}$ with the maximum $\Delta SNR = 8.4\,\text{dB}$ occurred.

This result is not surprising, since the experimental setup was not optimised to minimise the system noise. A $\sim 4\,\text{dB}$ loss between the device and the HEMT — in line with the insertion loss of the numerous components in the measurement chain — could explain the larger than expected noise temperature at the JTWPA itself. Finally, I investigated the relation between the gain and the SNR improvement (ΔSNR) as a function of the pump power. The measured results are plotted in Fig. 7.7(b). The maximum $\Delta\text{SNR} = 8.4\,\text{dB}$, corresponds to a measured gain of 10.84 dB. Contrary to what one might expect, the maximum ΔSNR and gain is obtained at different pump powers. This effect could originate from the generation of higher-order harmonics and nonlinear mixing products for high pump powers. These frequency tones manifest at higher frequencies than the operational range of the JTWPA, where the amplifier experiences higher losses, hence dissipating and increasing the noise in the system [88]. However, the signal gain can still be efficiently generated despite this increase in the system noise. If the pump power keeps increasing, the higher-order harmonics and nonlinear mixing products can be generated more efficiently than the processes resulting in signal gain, therefore reducing it.

PSD calibration

Setup-C2 can be simplified as shown in Fig. 7.8. To de-embed all the measured PSD in Fig. 7.7(a) to the input of the device, I measured at room temperature the input losses (G_{in}). This is done by generating a signal tone at $f_{\text{s}} = 8.536\,\text{GHz}$ with the VNA, and linearly increasing the signal power while the power at the reference plane 2 (RP_2) is measured with the spectrum analyser. Fitting the measured power as a function of the input power, I concluded that $G_{\text{in}} = -99.17\,\text{dB}$. Furthermore, from the transmission measurements of device B4, we know that $G_{\text{JTWPA,off}} = -3.86\,\text{dB}$. Therefore, with the input power of the signal tone $P_{\text{vna}} = -20\,\text{dBm}$ (at RP_1), and measuring the output PSD P_{out} (at RP_3) without pumping the JTWPA, we can calculate $G_{\text{out}} = P_{\text{vna}} + G_{\text{in}} + G_{\text{JTWPA,off}} - P_{\text{out}} = 52.77\,\text{dB}$. Hence, we can refer any measured PSD measured at RP_3 to RP_2 by subtracting $G_{\text{out}} + G_{\text{JTWPA}}$.

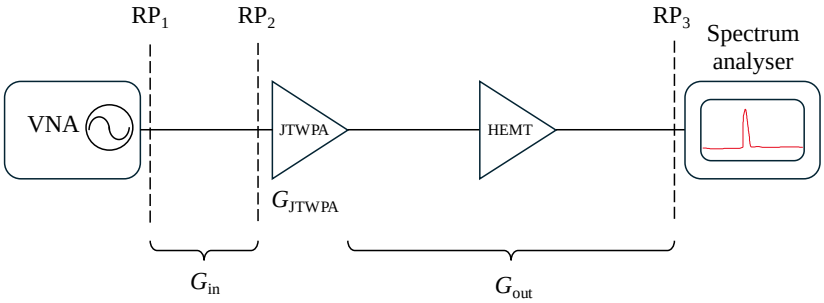

Figure 7.8: Simplified diagram of the JTWPA experimental setup, including the relevant reference planes (RP_n, $n = \{1, 2, 3\}$) and losses/gain (G_n, $n =$\{in, out, JTWPA\}.

7.6 Conclusion

In this chapter, I have presented the experimental results obtained from testing JTWPAs with interdigitated capacitors (IDCs) instead of parallel-plate capacitors (PPCs), which minimises the area requiring a spacer layer. Eleven devices were evaluated in an RF setup, with four demonstrating good transmission. This outcome suggests an improved fabrication yield over JTWPAs with PPCs. As anticipated, these four devices did not exhibit the frequency-dependent loss typically associated with dielectric materials. However, their transmission was quite irregular, with no clear stopband structure observed, except in devices B4 and B5, where a gap emerged around 10 GHz — lower than the expected $f_{\text{per}} \sim 12\,\text{GHz}$.

Moreover, an unexpected drop in RF transmission occurred in these four functional devices when very small DC currents ($I_{\text{dc}} \leq 65\,\text{nA}$) were applied. We suspect

that this may be due to outlier junctions in the line, with critical currents $I_{\mathrm{dc}} \leq 65\,\mathrm{nA}$. Based on calibrated wavevector measurements, I estimated the average critical current of the junctions to be $I_{\mathrm{c}} = 4.61 \pm 0.56\,\mu\mathrm{A}$, which is smaller than the targeted $I_{\mathrm{c}} = 7\,\mu\mathrm{A}$. This discrepancy likely results from a 34.1 % systematic reduction in junction size due to over-etching and/or sidewall oxidation, causing a $\sim 16\,\%$ reduction in the stopband frequency, in line with the measured stopband forming around 10 GHz.

When the devices were pumped, only narrow-band DP4WM gain was observed, typically near the pump frequency, potentially due to the outlier junctions dissipating energy before broadband gain could develop. Regardless, these devices were designed to operate in the DC3WM regime, and therefore we do not expect optimal broadband amplification when operated in the DP4WM. Additionally, the smaller junctions may have contributed to an impedance mismatch of the devices, further degrading the gain. Despite the narrow-band gain, for a particular combination of f_{p} and f_{s} within the gain frequency-band, I observed an 8.4 dB improvement in signal-to-noise ratio (SNR), comparable to values reported in successful JTWPA implementations used in practical applications [150]. Therefore, JTWPAs with IDCs could be a possible platform for quantum-limited amplification provided the fabrication and design issues that impacted their performance are addressed.

Chapter 8

Observation of non-travelling wave parametric effects

In this chapter, I will describe some observations of non-travelling wave parametric effects, particularly measured from some low-Q resonant-based Josephson parametric amplifiers, hereafter referred to as Standing Wave Parametric Amplifier (SWPA). These devices were originally designed and fabricated to characterise the junction fabrication yield of Josephson-array metamaterial lines, as introduced in Chapter 5. Nevertheless, unexpected interesting RF properties observed during measurement motivated a careful investigation of the behaviour of these devices. SWPAs share the characteristics with both the JTWPAs and the JPAs. Due to their much lower Q resonant cavity compared with JPAs, SWPAs demonstrate signal gain up to $\sim$ 20 dB over a moderate operational bandwidth $\sim$ 600 MHz, and $P_{\mathrm{1dB}} \sim -106.2$ dB. Furthermore, we found indications of efficient phase-sensitive amplification in the SWPA, unlocking their potential applications as a squeezer. The full characterisation of these devices and the full understanding of their behaviour are still a work in progress at the time of writing. Nevertheless, in this chapter, I present our preliminary observations.

8.1 Concept, topology and fabrication

As presented in Sec. 1.3.1, Josephson Parametric Amplifiers (JPA) use high-Q cavities, in the order of $Q \sim 10^2$-10^3 [151], to enhance the parametric gain. Therefore, they achieve a signal gain > 20 dB at the expense of the frequency bandwidth, often limited to ~ 10 MHz. The bandwidth of a JPA is inversely proportional to the quality factor of the resonant cavity ($B \propto 1/Q$). One could naturally think of lowering the Q-factor

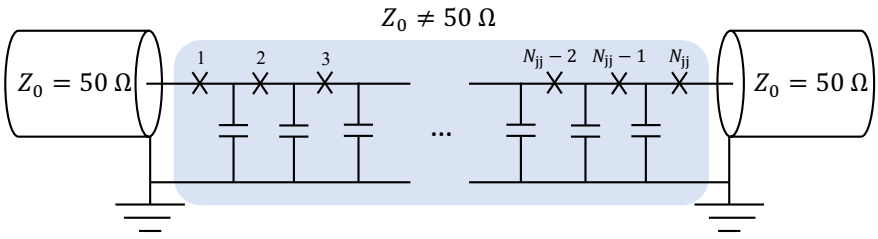

Figure 8.1: Circuit diagram of a SWPA. A $Z_0 \neq 50\,\Omega$ line is formed by embedding a large number of junctions ($N_{jj} \sim 500$) in a transmission line, creating a Fabry-Pérot cavity. The shunt capacitance to the ground results from the natural capacitance of the transmission line, no PPC or IDC structures are needed.

to further increase the bandwidth. However, in conventional JPAs, this comes at the cost of reducing the gain (G) due to the gain-bandwidth product:

$$B\sqrt{G} \propto \frac{1}{Q}. \tag{8.1}$$

This relation can intuitively be understood as the longer the interaction time of the microwave photons with the junction in the cavity (the higher the Q-factor), the higher the gain. Nevertheless, to increase the interaction time by increasing the Q-factor, we unavoidably reduce the bandwidth.

Our Standing Wave Parametric Amplifier (SWPA), on the other hand, consists of a large array of approximately 500 Josephson junctions, with moderate critical current, embedded in series in a superconducting CPW. Unlike JTWPAs, no additional shunt capacitance structures, such as parallel-plate capacitors (PPCs) or interdigitated capacitors (IDCs), are used. Consequently, the junction's inductance causes a characteristic impedance $Z_0 \neq 50\,\Omega$, forming a Fabry-Pérot cavity. Similar nonlinear Fabry-Pérot cavities formed with SQUIDs have been investigated, demonstrating the generation of parametric narrow-band gain [152].

As illustrated in Fig. 8.1, the impedance mismatch at both ends of the line creates the cavity, which, due to its low Q-factor, helps broaden the bandwidth. Frequency tones partially reflect at each end, bouncing within the cavity and interacting with the nonlinearity of the Josephson junctions, potentially leading to parametric gain. A larger array allows signals to propagate longer within the nonlinear medium, thereby increasing the gain. Additionally, the moderate critical current of the Josephson junctions helps to improve the compression point of SWPAs compared to traditional JPAs, due to the reduced Kerr nonlinearity [153, 154]. SWPAs can be seen as a middle ground between JPAs and JTWPAs. While the array is not large enough to

achieve high gain through travelling waves, the low-Q resonant cavity compensates by extending the interaction time. Unlike conventional JPAs, SWPAs are two-port devices, allowing pump injection from either side, simplifying the experimental setups.

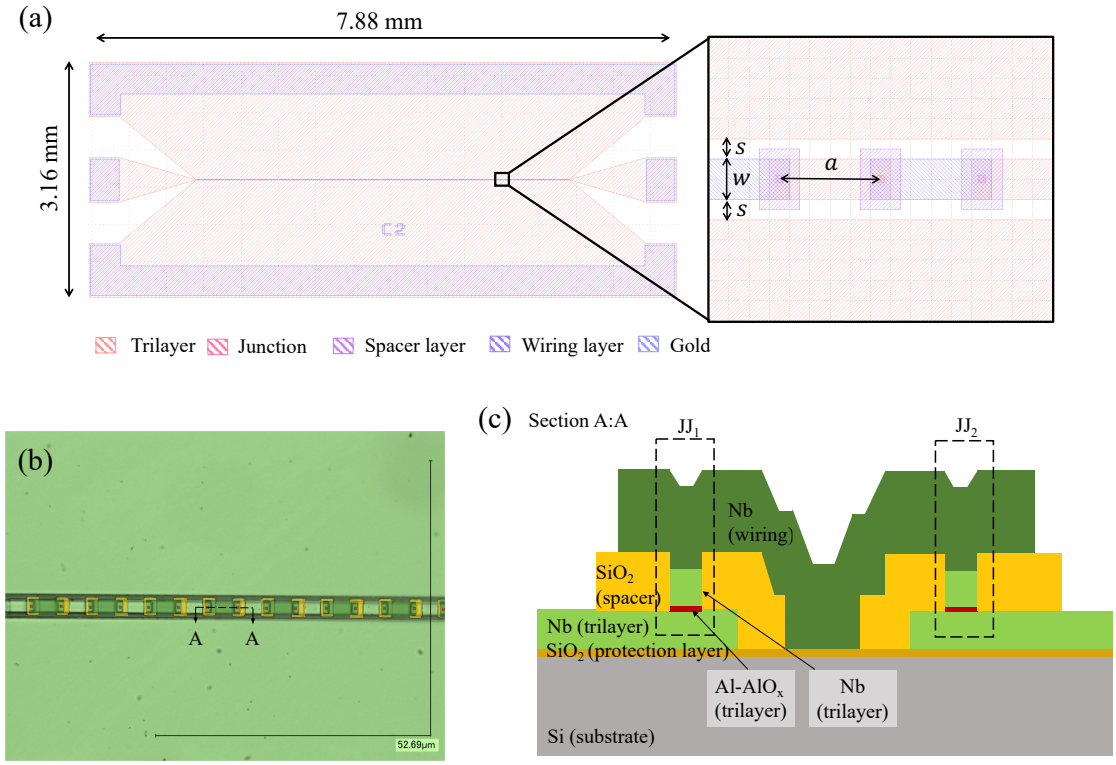

Figure 8.2: (a) Chip layout of SWPA device C2 (wafer 7), where $s = 2\,\mu\text{m}$, $w = 4\,\mu\text{m}$ and $a = 10\,\mu\text{m}$. (b) Microscope image of SWPA device with fake colours to represent the different layers. (c) Cross-section layer distribution in a SWPA.

Another advantage of developing SWPAs lies in their higher fabrication yield compared to JTWPAs. They typically require $\sim 75\,\%$ fewer junctions without the need for PPCs or IDCs, which can suffer from fabrication defects like pin-holes (discussed in Sec. 5.4). SWPAs can potentially operate with higher critical current junctions than both JTWPAs and JPAs. In fabrication processes where high-pressure oxidation is not possible, longer oxidation times (e.g., $>$ 5 hours at 4 Pa) are needed to achieve low critical current densities ($J_c < 1.5\,\text{kA/cm}^2$). However, the higher I_c used for SWPAs — such as the $I_c = 8.67\,\mu\text{A}$ used in the device discussed later — can be achieved with shorter oxidation times ($\sim$ 1.5 hours at 4 Pa), making SWPAs faster to fabricate in some scenarios.

As described in Chapter 5, during my first visit to IRAM, I fabricated several Josephson arrays to asses the junction's fabrication yield. The fabricated arrays

varied in the total number of junctions ($N_{jj} = 100, 500$ and 1,000), junction area ($A_{jj} = 0.25, 0.5$ and $1\,\mu m^2$), and critical current density ($J_c = 2.5, 3.4$ and $4\,kA/cm^2$). All these devices could potentially operate as SWPAs, however, in the rest of this section I focus on a particular device (C2, wafer 7), consisting of an array of 500 junctions with $J_c = 2.5\,kA/cm^2$ and $A_{jj} = 0.5\,\mu m^2$. Fig. 8.2 shows the layout, a microscope image and the cross-section of the device.

8.2 Experimental setups

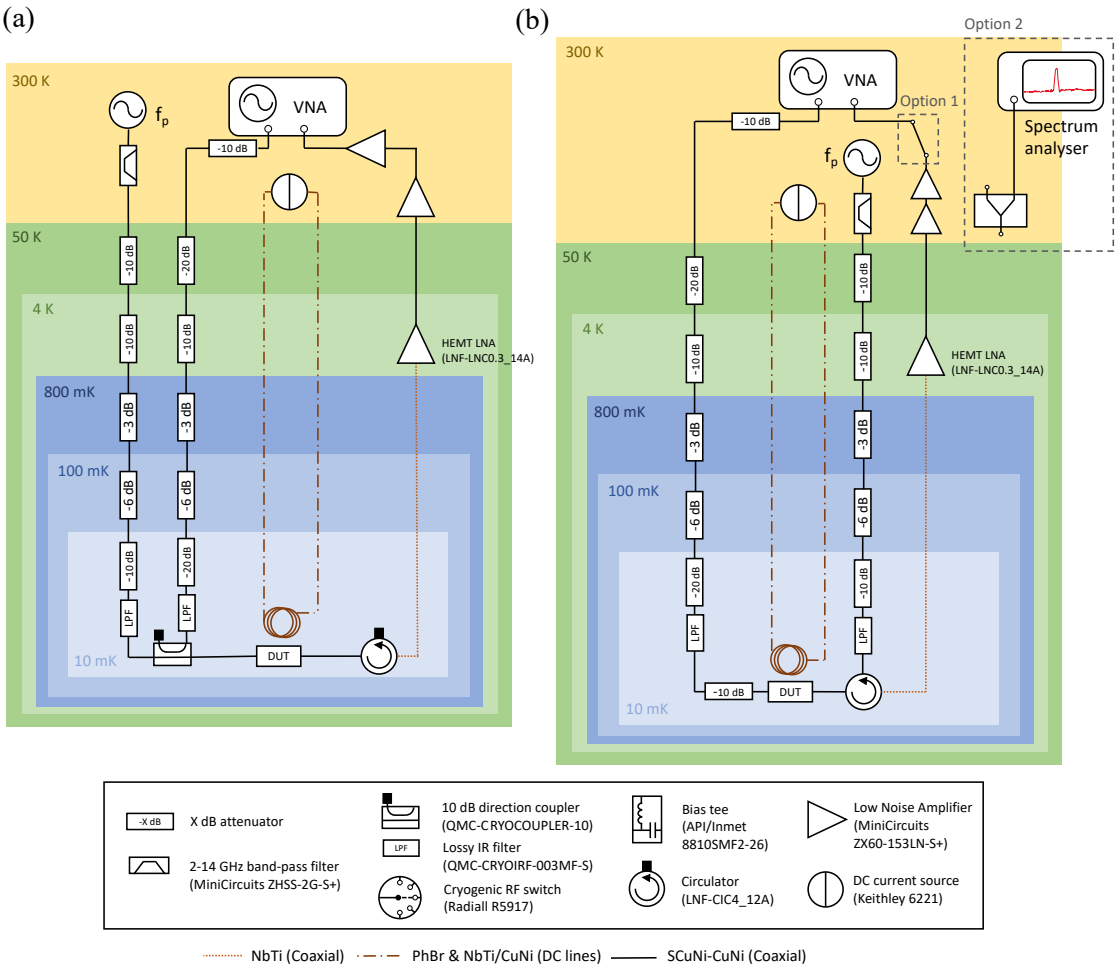

Figure 8.3: Addition experimental setups used to characterise the SWPAs. (a) Setup-D and (b) Setup-E.

Apart from the experimental setups presented in Sec. 4.3.3, I also used the two setups illustrated in Fig. 8.3 to characterise the device presented in this chapter.

- Setup-D (Fig. 8.3(a)): implemented in LD250. The pump and signal are combined inside the cryostat, and applied to the device through the same port. The setup also included a magnetic coil to apply a magnetic field to the device.
- Setup-E (Fig. 8.3(b)): implemented in LD250. The pump and signal are injected to the device from different ports. It included two options for the readout: (1) directly connected to the VNA and (2) splitting the output signal for readout with the VNA and the spectrum analyser. I will refer to these options as Setup-E1 and Setup-E2 respectively.

8.3 Characterisation

In this section, I present the experimental results obtained for the SWPA device across various experiments. While these findings offer valuable insights into the device's operation, the full characterisation and understanding of the SWPA remains an ongoing process at the time of writing.

8.3.1 DC characteristics and RF transmission

Using Setup-A (described in Sec. 4.3.3.1), operated at $T = 4\,\mathrm{K}$, I measured the current-voltage (IV) characteristics of the SWPA. The results, shown in Fig. 8.4(a), reveal a gap voltage $V_{\mathrm{gap}} = V_{\mathrm{gap,1JJ}} \times 500 = 1.42\,\mathrm{V}$, as expected for a 500-junctions array. Using Ambegaokar-Baratoff equation for tunnel junctions, I calculated an average $I_{\mathrm{c}} = 8.67 \pm 0.58\,\mu\mathrm{A}$, substantially lower than the expected $I_{\mathrm{c}} = 12.5\,\mu\mathrm{A}$. In Chapter 5, we conducted a detailed characterisation of the wafer, determining a $J_{\mathrm{c}} = 2.5\,\mathrm{kA/cm^2}$ for Wafer 7, from which the device discussed here was fabricated. Therefore, assuming J_{c} uniformity across the wafer, the reduced I_{c} suggests a $\sim 30.6\,\%$ smaller size of the junctions. This discrepancy is likely due to over-etching or oxidation of the junctions' side-walls.

Furthermore, using the same setup, I measured the RF transmission profile of the SWPA with $P_{\mathrm{vna}} = -20\,\mathrm{dBm}$, plotted in Fig. 8.4(b). The transmission oscillates in frequency between 0 dB and approximatelly $-5.42\,\mathrm{dB}$, with a period of $\sim 3\,\mathrm{GHz}$. This is a clear indication of the Fabry-Pérot cavity effect, where the first, second and third resonant mode correspond approximately to 3.1, 6.2 and 9.3 GHz. Using the previously measured I_{c} value and assuming a 36 % reduction in junction area, I calculate $L_0 \approx 38\,\mathrm{pH}$ and $C_{\mathrm{j}} = 26\,\mathrm{fF}$. To calculate the rest of the circuit parameters of the unit cell (contribution of the geometrical inductance L_{geo} and C_{s} assuming a

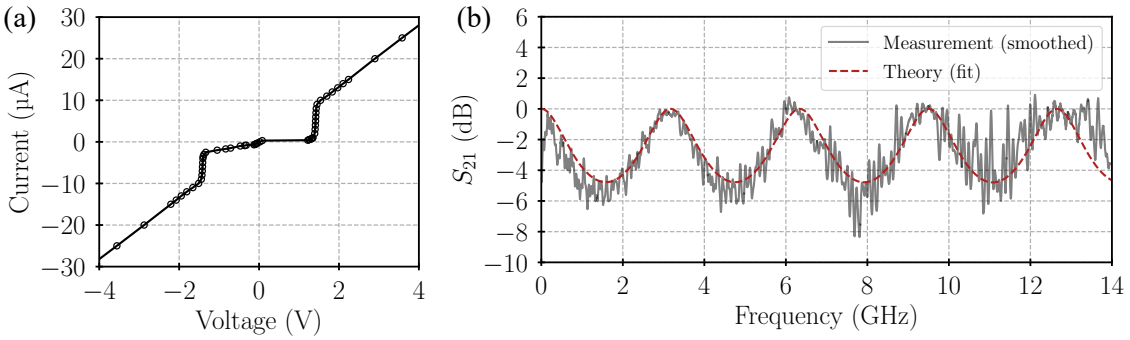

Figure 8.4: (a) SWPA IV curve. $V_{\text{gap}} = 1.42\,\text{V}$ as expected, and we calculate $I_{\text{c}} = 8.67 \pm 0.58\,\mu\text{A}$, substantially smaller than the expected value of $I_{\text{c}} = 12.5\,\mu\text{A}$. (b) Measured SWPA calibrated S_{21} (solid grey line) with $P_{\text{vna}} = -20\,\text{dBm}$ using Setup-A, and theoretical profile (dotted red line) obtained from the circuit model of the SWPA's unit cell with: $L_0 = 38\,\text{pH}$, $C_{\text{j}} = 26\,\text{fF}$, $L_{\text{geo}} = 11.5\,\text{pH}$ and $C_{\text{s}} = 2\,\text{fF}$. The oscillations originate from the Fabry-Pérot cavity, where the frequency of the resonant modes is $f_{\text{n}} \approx n \times 3.1\,\text{GHz}$, $n \in \mathbb{N}$.

lossless STL), I numerically fit the measured S_{21} data with the theoretical S_{21} of the SWPA. The theoretical S_{21} is calculated in Python by constructing the `ABCD` matrix of the SWPA's unit cell circuit model, then cascaded 500 times to simulate the entire device. The final `ABCD` matrix is then used to extract the device's S_{21}. Using standard Python optimisation functions, I fit the calculated S_{21} to the measured data, obtaining an optimal fit for $L_{\text{geo}} = 11.5\,\text{pH}$ and $C_{\text{s}} = 2\,\text{fF}$. From these results, I can estimate the characteristic impedance of the line to $Z_0 = 195\,\Omega$.

8.3.2 Signal gain and saturation

Next, I attempt to measure the generation of parametric gain in the SWPA. The measurements were taken in LD250 at $T = 10\,\text{mK}$, unless otherwise stated. In the rest of this chapter, the gain is defined as the value of the transmission with the pump on, calibrated with the transmission without the pump.

Signal gain

Using setup-D, where both the signal and the pump are injected into the SWPA from the same port, I measured the signal gain for different pump frequencies f_{p} and powers in the range from 4 GHz to 12 GHz. Fig. 8.5(a) plots the gain curves with maximum gain for each pump frequency. While most of the explored f_{p} values yielded no gain, when pumping at $f_{\text{p}} \sim 6.2\,\text{GHz}$ and $9.3\,\text{GHz}$ — corresponding with the 2^{nd} and 3^{rd}

resonant mode of the Fabry-Pérot cavity — we measured gain generation around $f_s = f_p$. These two gain regions, circled in Fig. 8.5(a), extend over 2 GHz around f_p, reaching values as high as ~ 30 dB. Fig. 8.5(b)&(c) plot the measured gain for $f_p = 6.15$ GHz and 9 GHz respectively. We observe rapid changes of the gain with P_p (an increase of 0.05 dBm would lead to > 5 dB gain increase at certain signal frequencies). This gain sensitivity to the pump power is comparable with conventional JPAs when operated for high gain [57]. Furthermore, the gain profile displays ripples with a frequency separation of $\Delta f \sim 103$ MHz and 84 MHz for $f_p = 6.15$ GHz and 9 GHz respectively, which we suspect may originate from reflections in the experimental setup[1].

Since the SWPA exploits the standing-wave mode of a Fabry-Pérot cavity to enhance the gain, it should in principle operate independently of the port used to inject the pump. Using Setup-E1, I investigated the different gain profiles when injecting the signal and the pump from the input and output ports of the device respectively. Fig. 8.6(a)&(b) plot the maximum gain when sweeping f_p in the $5-7$ GHz and $8-10$ GHz range respectively. I obtained similar results as with Setup-D, with the two main gain regions corresponding to the 2^{nd} and the 3^{rd} resonant mode of the Fabry-Pérot cavity. Unlike using Setup-D, with this setup, I measured larger gain values around 6.2 GHz instead of 9.3 GHz. This could originate from the experimental setups, where signal reflections deteriorating the gain may differ in frequency from one setup to another, or it could indicate a weak asymmetry in the device. Furthermore, in Fig. 8.6(b) we can notice the generation of the second harmonic of the pump (circled region). Even harmonics are typically suppressed in a perfectly symmetric line. However, variations in I_c across the line can break this symmetry, leading to their generation. Additionally, even harmonics could also arise from DC leakage currents, though this is unlikely in our case as the RF lines are filtered and no DC lines are connected to the device. Fig. 8.6(c)&(d) plot the gain measured for $f_p = 5.85$ GHz and 8.9 GHz respectively. As previously observed, the gain shows a large sensitivity to the pump power, and displays amplitude ripples.

[1]Deteriorated cables or imperfect connections in the setup can lead to reflections, potentially forming a standing wave around the SWPA. Since these reflections may occur over long cable distances, the standing wave oscillations can be rapid. Despite its small amplitude, a highly sensitive amplifier like the SWPA can significantly amplify this effect.

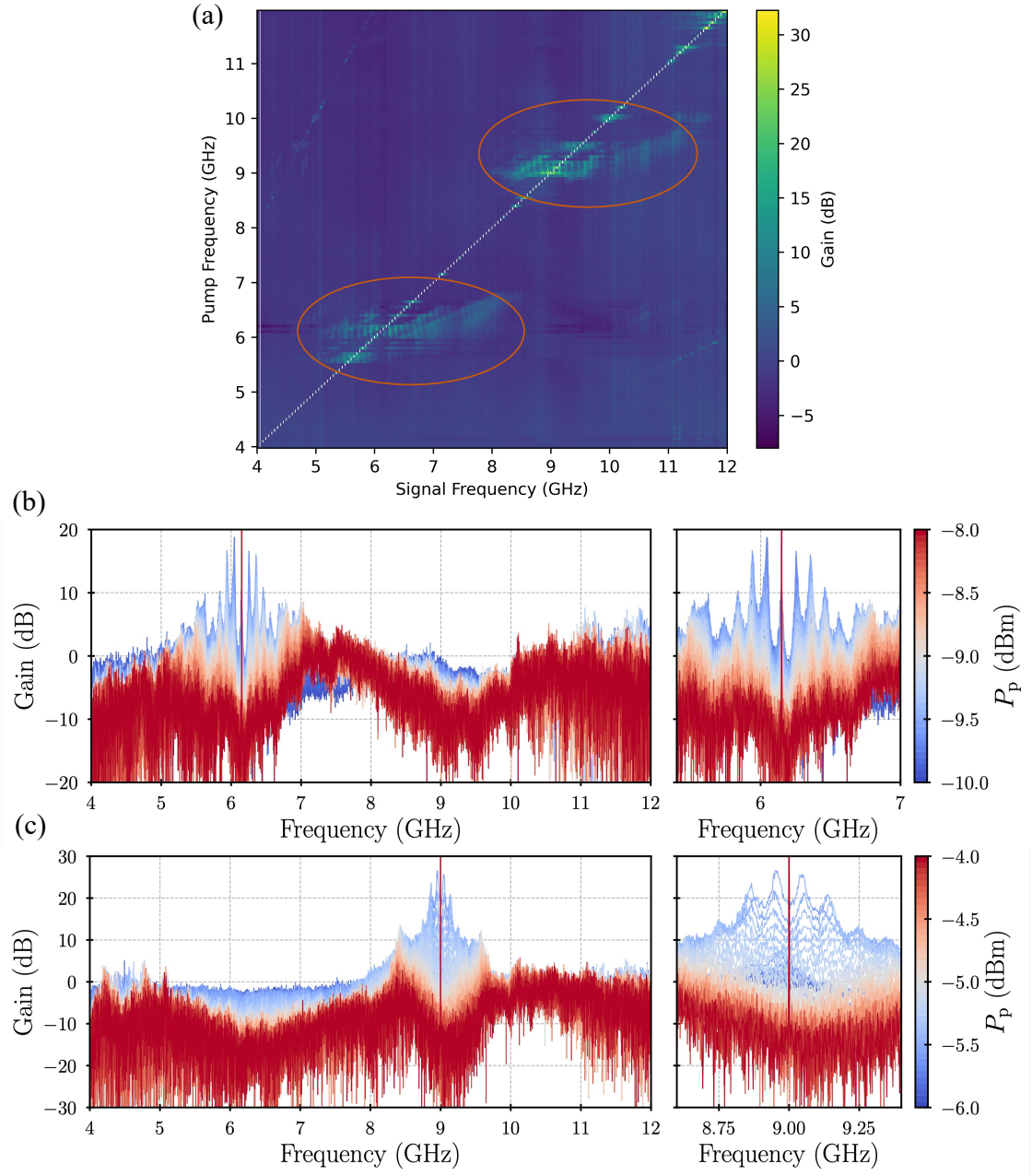

Figure 8.5: SWPA gain measurements using Setup-D, the pump and signal are injected from the same port. (a) 2D colormap of the maximum gain profiles obtained for each f_p. The gain at f_p is removed from the plot (diagonal white line). We observe two regions of gain around 6.2 GHz and 9.3 GHz (orange circles), coinciding with the 2^{nd} and 3^{rd} resonant modes of the SWPA. The data was averaged using a 6 MHz average window. (b) Measured gain for $f_p = 6.15$ GHz with powers ranging from -10 dBm to -8 dBm (left plot) and zoom-in around f_p (right plot). (c) Measured gain for $f_p = 9$ GHz with power ranging from -6 dBm to -4 dBm (left plot) and zoom-in around f_p right plot.

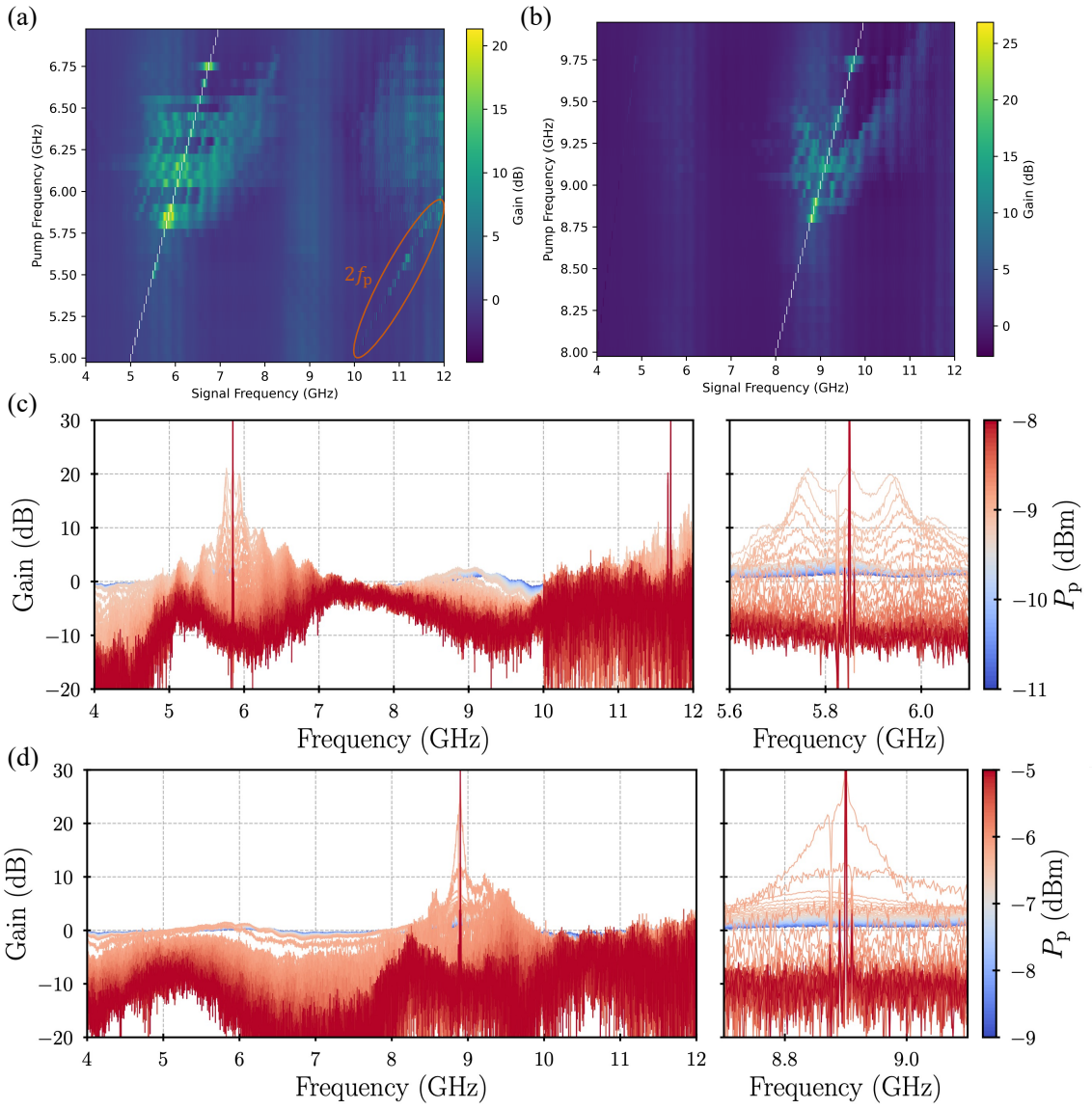

Figure 8.6: SWPA gain measurements using Setup-E1, the pump and signal are injected from different ports. (a) 2D colormap of the maximum gain profiles obtained for f_p from 5 GHz to 7 GHz and (b) 8 GHz to 10 GHz. The data was averaged using a 6 MHz average window. (c) Gain for $f_p = 5.85$ GHz, for values of P_p from -11 dBm to -8 dBm at the output of the signal generator (left plot) and zoom-in around f_p (right plot). (d) Gain for $f_p = 8.9$ GHz, for values of P_p from -9 dBm to -5 dBm at the output of the signal generator (left plot) and zoom-in around f_p (right plot).

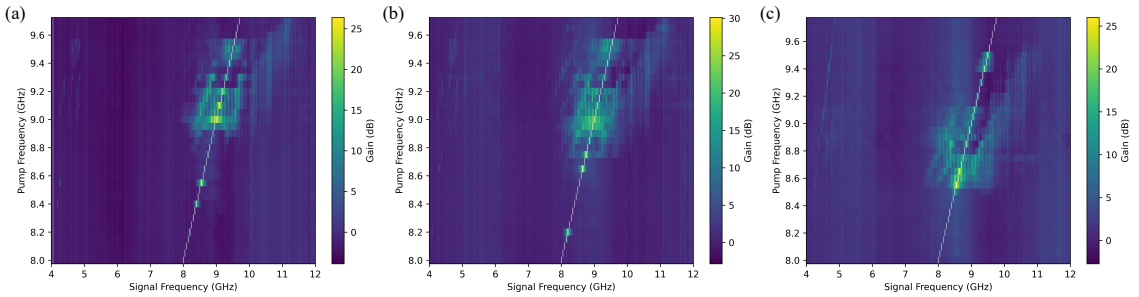

Figure 8.7: Effect of external magnetic field on SWPA gain, using Setup-D. Measured gain map for (a) No magnetic field, (b) $I_\mathrm{b} = 22\,\mathrm{mA}$ and (c) $I_\mathrm{b} = 45\,\mathrm{mA}$.

Magnetic field effect

Using Setup-D, I explored the effect of an external magnetic field on the gain of the SWPA. For that, I installed a coil on the lid of the sample holder containing the SWPA. The position and orientation of the coil were not optimised to maximise the magnetic field coupled to the device. The coil, made of NbTi wire, was superconducting at the measurements' temperature, and it could drive a current $I_\mathrm{b} \leqslant 45\,\mathrm{mA}$ before breaking superconductivity. Fig. 8.7(a), (b) & (c) shows the measured maximum gain in the SWPA with $I_\mathrm{b} = 0$, 22 and 45 mA respectively. We see a clear shift (Δf) of the gain towards lower frequencies with increasing magnetic field, reaching $\Delta f \sim 300\,\mathrm{MHz}$ for $I_\mathrm{b} = 45\,\mathrm{mA}$. Similarly, without applied pump, the transmission peaks from the Fabry-Pérot cavity also shift to lower frequency. This effect most certainly results from altering the Josephson current in the junction due to the magnetic field presence [95]. Although noticeable, the gain frequency shift is relatively small compared with JPAs implemented using SQUIDs [57], which suggests a larger resilience of this SWPA design to an external magnetic field, as expected.

Gain saturation

Using Setup-E2, I explored the compression point P_1dB of the SWPA. Fig. 8.8 shows the change of the signal gain when pumping the device at $f_\mathrm{p} = 5.85\,\mathrm{GHz}$ and $P_\mathrm{p} = 9.17\,\mathrm{dBm}$ (at the output of the signal generator), as a function of the signal power P_s at the input of the device. I calibrated the power at the input of the device using the measured losses of the input line at room temperature. The different curves represent different signal frequencies, resulting in various values of the peak gain. We obtained $P_\mathrm{1dB} = -106.2$, -103.6, -101.1 and $-99.5\,\mathrm{dBm}$ for values of the gain of

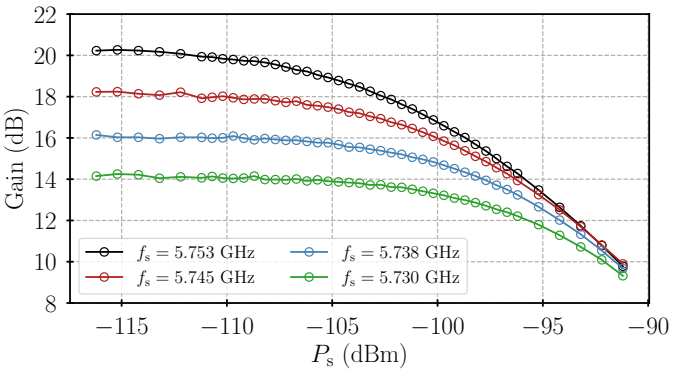

Figure 8.8: SWPA's signal gain change as a function of P_s at the input of the device for different f_s values. The measurements were taken with $f_p = 5.85\,\text{GHz}$ and $P_p = 9.17\,\text{dBm}$ (at the output of the signal generator).

20.2, 18.2, 16.0 and 14.2 dB respectively. Since the losses of the input line decrease at cryogenic temperatures, we expect that our calculation probably underestimates the actual $P_{1\text{dB}}$ of the device by 1 or 2 dB. Nevertheless, the SWPA gain saturation is clearly improved compared with conventional JPAs, where the highest reported $P_{1\text{dB}}$ when operated at 20 dB gain ranges between $-120\,\text{dBm}$ and $-110\,\text{dBm}$ [153, 155, 154].

8.3.3 Signal-to-noise ratio (SNR)

In this section, I investigate the improvement of the SWPA's SNR using Setup-E2. The SNR improvement (ΔSNR) is defined as $\Delta\text{SNR} = \text{SNR}_{\text{p,on}} - \text{SNR}_{\text{p,off}}$, where $\text{SNR}_{\text{p,on/off}}$ is the measured SNR with the pump on/off. I followed the same measurement techniques presented in Sec. 7.5, using identical settings of the spectrum analyser. Fig. 8.9 shows four different pump frequencies cases (a) $f_p = 5.85\,\text{GHz}$, (b) 6.75 GHz, (c) 8.8 GHz and (d) 8.9 GHz. For each pump frequency, I measured 500 signal frequency points around f_p in the span of 1 GHz, therefore, each frequency point is separated by 2 MHz. Fig. 8.9 plots the ΔSNR (solid lines) and the gain (dotted lines) as the pump power increases for all the signal frequency points. Focusing on the solid lines, we notice that the maximum ΔSNR ($\Delta\text{SNR}_{\text{max}}$) highly depends on f_p; for example, at $f_p = 6.75\,\text{GHz}$ $\Delta\text{SNR}_{\text{max}} \sim 0\,\text{dB}$, while at $f_p = 8.9\,\text{GHz}$, $\Delta\text{SNR}_{\text{max}} \sim 6.5\,\text{dB}$. A larger $\Delta\text{SNR}_{\text{max}}$ could be potentially found for this device, although it would require a very time-consuming sweep of all the pump frequencies. For the cases where we observed an SNR improvement (Fig. 8.9(a),(c)&(d)), we notice that the improvement of the ΔSNR follows the gain profile, until just before the

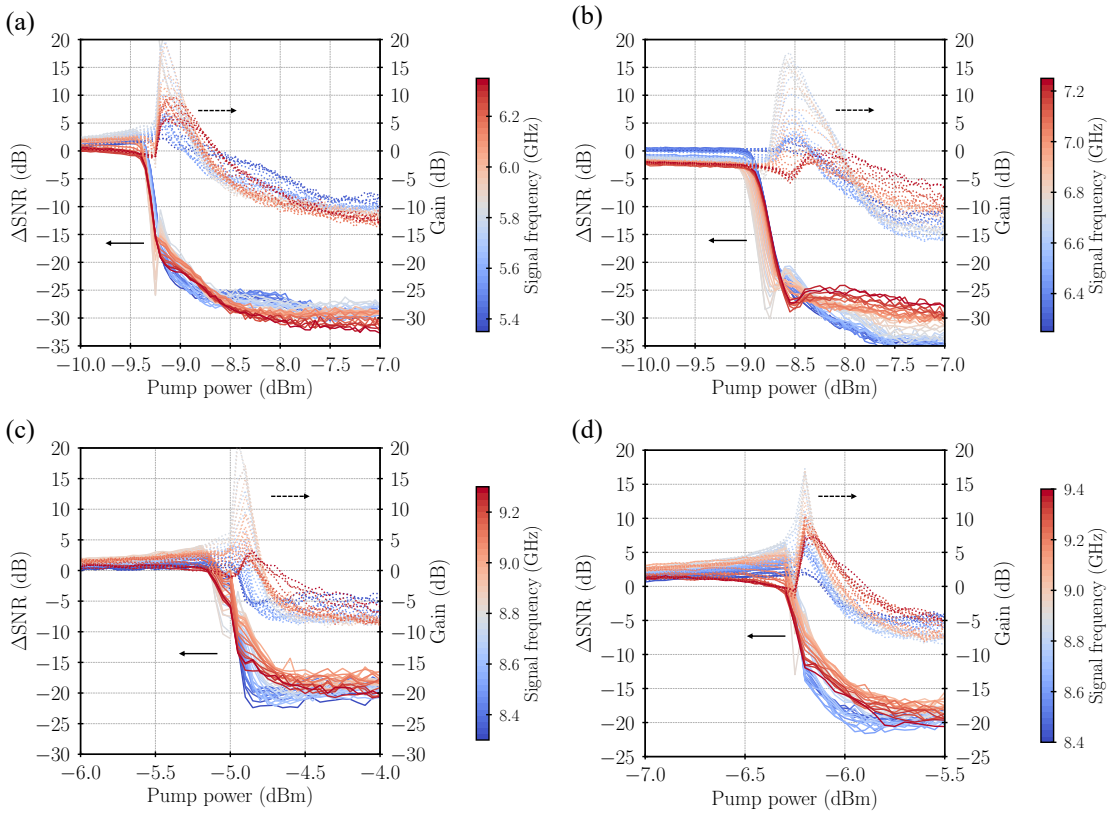

Figure 8.9: SWPA measured evolution of ΔSNR (solid lines) and signal gain (dotted lines) with pump power using Setup-D2 for (a) $f_p = 5.85\,\text{GHz}$, (b) 6.75 GHz, (c) 8.8 GHz and (d) 8.9 GHz. The different colours indicate different signal frequencies 1 GHz around f_p at 2 MHz separation. The pump power values are referred at the output of the signal generator. We observe the best SNR improvement $\Delta\text{SNR}_{\text{max}} \sim 6.5\,\text{dB}$ at $f_p = 8.9\,\text{GHz}$.

gain exponentially increases with pump power, but unexpectedly resulting in a drop of the ΔSNR. The high sensitivity of the signal gain to the pump power is obvious in these plots, with a very sharp rise and drop of the gain; in some cases with less than 0.25 dBm change of pump power. We believe the observed high gain is due to the strong nonlinearity of the line induced by the large pump power, which inevitably generates higher harmonics and mixing products at higher frequencies, leading to the SNR degradation. However, further analysis is needed to fully understand this SNR deterioration, which currently limits the device's practical applications.

8.3.4 Phase-sensitive amplification

As discussed in Sec. 1.2.2.2, phase-sensitive amplification in JPAs and JTWPAs can be used to generate squeezed microwave light states. In this section, I describe the observation of phase-sensitive amplification in the SWPA without requiring the coherent detection system conventionally used in phase-sensitive amplification experiments [54, 112, 156]. All the measurements were taken in LD250 at $T = 160\,\mathrm{mK}$.

Fundamentally, a VNA performs a coherent detection to measure the S-parameters of the DUT. The input signal to the VNA port (f_s) is mixed with a local oscillator (LO) at frequency f_LO to generate an intermediate frequency (IF) at f_IF. The IF is then filtered with a band-pass filter, where the bandwidth (IF bandwidth, B_IF) is set by the user. The output is then amplified and further treated before being sampled by an Analog-to-Digital converter (ADC). To facilitate the signal readout, VNAs such as the one used in these experiments have a fixed IF frequency, i.e., $f_\mathrm{IF} = 10\,\mathrm{MHz}$, and the LO frequency changes with f_s to ensure that f_IF stays fixed. Furthermore, the mixers are dual-band mixers, where both $f_\mathrm{LO} + f_\mathrm{IF}$ and $f_\mathrm{LO} - f_\mathrm{IF}$ bands are down-converted to the same IF frequency.

With Setup-E2, I operated the VNA in the continuous-wave mode (CWM) to generate a single signal tone f_s, while the signal generator provided the pump f_p. I fixed the signal sweep to 1 s, and the number of frequency points to 4,001 (which is limited by the IF bandwidth, in this case $B_\mathrm{IF} = 5\,\mathrm{kHz}$). Therefore, the VNA samples the signal at $\sim 4\,\mathrm{kHz}$, measuring the S_{21} amplitude and phase. Under this setup, if $f_\mathrm{p} = f_\mathrm{LO}$ and $f_\mathrm{s} = f_\mathrm{IF} \pm f_\mathrm{IF}$, both the signal and idler generated at the SWPA would be mapped into the same IF frequency, resulting in phase-sensitive amplification. This homodyne detection scheme is identical to the experimental setups presented in early works on microwave squeezing-state generation with JPAs, except for our limited ability to alter the signal-pump frequency offset due to the fixed f_LO of the VNA [51, 157]. Fig. 8.10(a) shows the measured profile of the signal when $f_\mathrm{p} = 8.90\,\mathrm{GHz}$ and $f_\mathrm{s} = 8.91\,\mathrm{GHz}$. When the pump is off (red); as expected, we observe a constant value of the S_{21} over the acquisition time. However, when the pump is turned on (black), the amplitude of the S_{21} oscillates at $\sim 23\,\mathrm{Hz}$ around the pump off S_{21} value. These oscillations shift in time, but they maintain the same amplitude and periodicity. Furthermore, when using the signal generator 10 MHz output source as the reference source of the VNA (blue), to ensure phase stability in both instruments, the oscillations disappear.

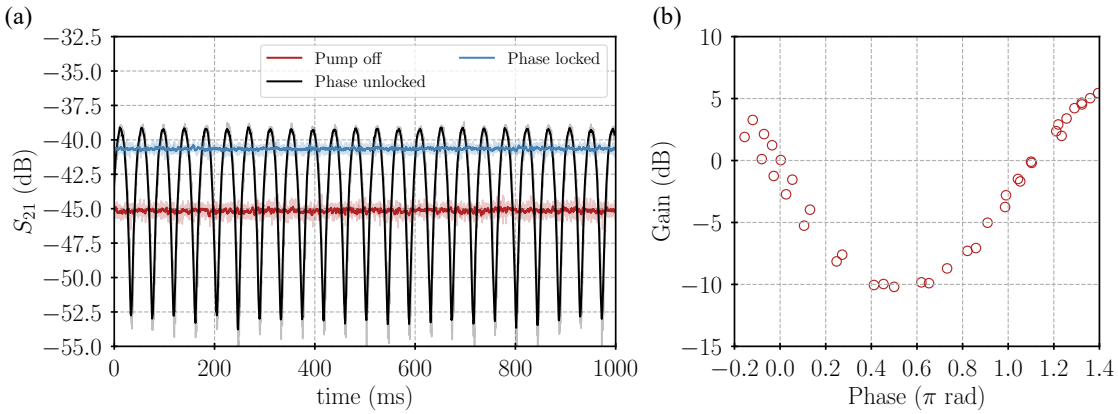

Figure 8.10: SWPA phase-sensitive gain. Measurements were taken with $f_p = 8.90\,\text{GHz}$, $P_p = -8\,\text{dBm}$, $f_s = 8.91\,\text{GHz}$, $B_{IF} = 5\,\text{kHz}$ and 4,001 points over 1 s sweep. (a) S_{21} at f_s with pump-off (red), pump-on with (blue) and without (black) sharing the same 10 MHz signal reference for the signal generator and the VNA. (b) Measured signal gain (pump on/off at f_s) as a function of the measured S_{21} phase when changing the input signal phase using a phase-shifter.

For the rest of this section, I focus on the case where the VNA and the signal generator share the same 10 MHz reference signal (phase locked). Adding a phase-shifter in the signal input path at room temperature, I manually control the phase of the signal at the input of the device, and measure the S_{21} amplitude and phase. Fig. 8.10(b) plots the signal gain (measured S_{21} calibrated with the pump-off case) as a function of the measured signal phase. We notice a consistent change in the measured gain when changing the input signal phase, suggesting phase-sensitive amplification in the device under this configuration.

Next, we explored the phase-sensitive amplification when shifting the pump frequency of Δf, so $f_p = f_{p,0} + \Delta f$, where $f_{p,0} = 8.9\,\text{GHz}$. This frequency shift is equivalent to a time-dependent phase shift of the pump tone $\phi(t) = \Delta f \cdot t$. Fig. 8.11 plots the measured S_{21} for different Δf values with fixed $f_s = 8.91\,\text{GHz}$. As expected, detuning f_p results in S_{21} oscillations at a frequency $f = \Delta f$. The amplitude of the oscillations is independent of Δf, however, the oscillations increase with Δf until it becomes larger than the IF bandwidth ($\Delta f > B_{IF}$), where the gain oscillates too fast for the VNA to sample it, resulting in a continuous S_{21} value.

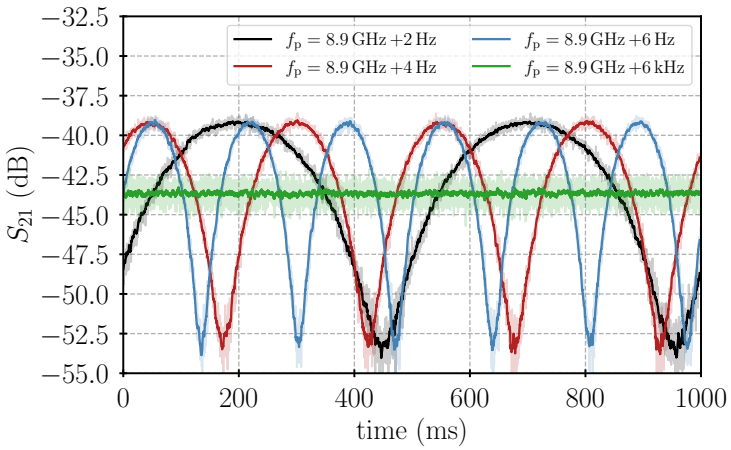

Figure 8.11: S_{21} oscillations for a fixed $f_s = 9.1\,\text{GHz}$ and different $f_p = f_{p,0} + \Delta f$, where $f_{p,0} = 8.9\,\text{GHz}$. S_{21} oscillates at Δf for values below $B_{IF} = 5\,\text{KHz}$, $P_p = -8\,\text{dBm}$ and $P_{vna} = -20\,\text{dBm}$.

During these measurements, we not only captured the changes in the S_{21} but we also measured the transmitted signal phase time evolution. Using a detuning frequency of $\Delta f = 6\,\text{Hz}$, and optimising the pump and signal power, I measured the data plotted in Fig. 8.12(a). In the bottom plot, we see that the measured phase of the signal increases linearly, except when the values reach $-\pi$ or π. The increased phase noise at these regions results from the deterioration of the SNR due to the low signal power, a consequence of the de-amplification. Therefore, in order to plot the measured signal gain as a function of the measured phase, I performed a linear fit of the phase shown by the red dotted line in Fig. 8.12(a). Fig. 8.12(b) shows the gain change with phase (from the fitted curve), which can be related to the phase difference between the signal and the pump, and the acquisition frequency of the IF in the VNA. We see a periodicity of π as expected, where the measured signal oscillates between the in-phase component/quadrature (I) — resulting in amplification — and the quadrature-phase component/quadrature (Q) — resulting in de-amplification — over a $\pi/2$ phase difference. Therefore, as illustrated in Fig. 8.12(b), the local maxima and minima of the plot correspond to the gain values of the I and Q quadrature respectively.

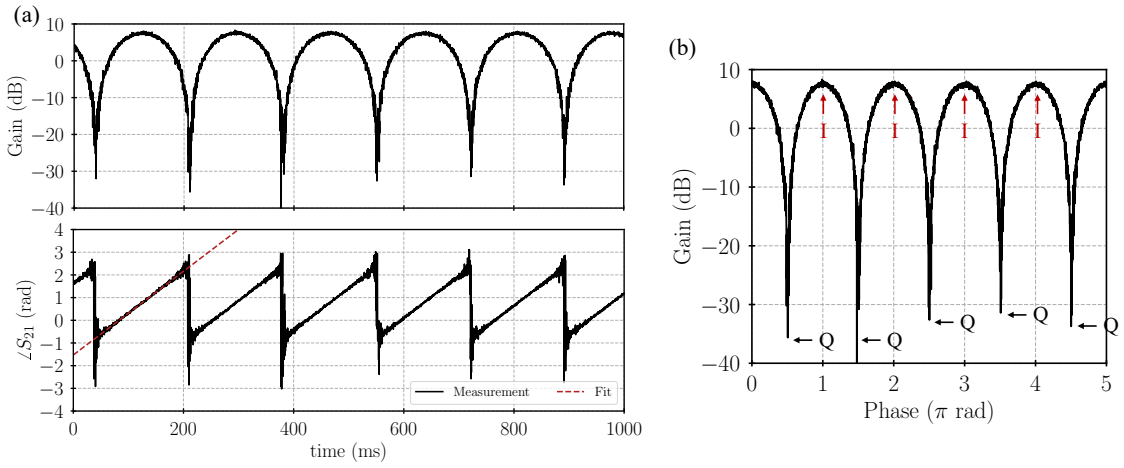

Figure 8.12: (a) Measured gain and phase of the transmitted signal at f_s. (b) Measured gain as a function of the measured S_{21} phase. The local maxima and minima correspond to the in-phase (I) and quadrature-phase (Q) components or quadratures. The measurements were taken with $\Delta f = 6\,\text{Hz}$, $P_{\text{vna}} = -13.5\,\text{dBm}$, $P_{\text{p}} = -8\,\text{dBm}$.

Finally, I investigated the changes in the gain values at each quadrature with applied pump power (P_{p}). For that, I repeat the previous experiment, fixing $\Delta f = 6\,\text{Hz}$, $P_{\text{vna}} = -13.5\,\text{dBm}$, for different values of P_{p}. Then, I extract the average gain value at the dips (Q) and peaks (I) and their uncertainty. Fig. 8.13(a) shows the gain amplitude of both quadratures when sweeping the pump power in the signal generator from $-20\,\text{dBm}$ to approximately $-6\,\text{dBm}$, where we reach the I_{c} of the junctions. We notice an asymmetry between both quadratures, where the de-amplification increases at a faster pace than the amplification. This asymmetrical behaviour with pump power could partially originate from losses in the transmission line. Furthermore, we notice that the de-amplification quickly deteriorates for pump powers close to the critical current of the junctions. Similarly, I measured the change in gain amplitude for both quadratures with signal power. In Fig. 8.13(b), I fixed the pump power to $P_{\text{p}} = 8\,\text{dBm}$ and swept the signal frequency. While the I quadrature gain progressively decreases with signal power, suggesting gain saturation, the Q quadrature gain suddenly decreases from $P_{\text{s}} = -20\,\text{dBm}$ to $P_{\text{s}} = -13\,\text{dBm}$, and then raises to get to $0\,\text{dB}$ at $P_{\text{s}} = 0\,\text{dBm}$. However, at $P_{\text{s}} \sim -14\,\text{dbm}$, we observe a sweet-spot where the phase-sensitive extinction ratio (PSER) — defined as the difference between the maximum phase-sensitive amplification and de-amplification — reaches a value of $42.30 \pm 2.81\,\text{dB}$. This result is similar to the largest PSER reported in JPAs [158, 159]. The mechanisms leading to the observed behaviour of the de-amplification value with signal power are unknown at the time of writing.

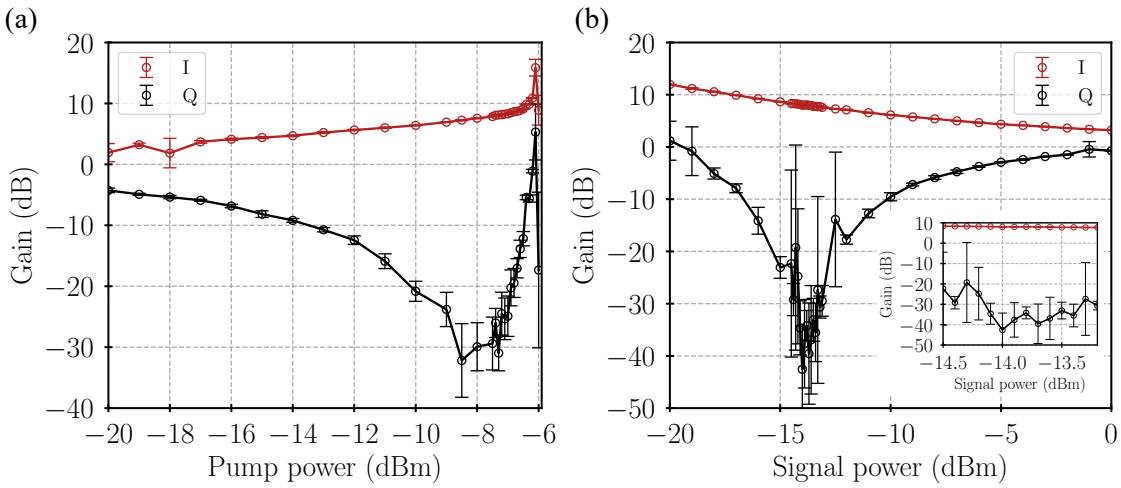

Figure 8.13: Measured de-amplification (black) and amplification (red) states as a function of the (a) pump power level in the signal generator ($P_{\mathrm{vna}} = -13\,\mathrm{dBm}$), and (b) signal power in the VNA ($P_{\mathrm{p}} = -8\,\mathrm{dBm}$).

8.4 Conclusion

In this chapter, I investigated a 500-junction Josephson array, which forms a Fabry-Pérot cavity and exhibits unique RF properties. The IV curve and RF transmission of this device — named the Standing Wave Parametric Amplifier (SWPA) — revealed a $\sim 30.6\,\%$ reduction in junction size, consistent with measurement of other devices using the same fabrication techniques. This supports the hypothesis that the junctions experienced over-etching or oxidation of their side-walls. Without applying a pump tone to the device, I measured a characteristic impedance of $Z_{0,\mathrm{cav}} = 195\,\Omega$, with cavity modes appearing at multiples of 3.1 GHz.

When the SWPA was pumped, it achieved approximately 20 dB of gain over a moderate operational bandwidth of 600 MHz centred around the cavity modes, independent of the pump injection port. The gain demonstrated a high sensitivity to pump power, where a 0.05 dBm increase resulted in more than 5 dB gain at specific signal frequencies. Additionally, we observed a 300 MHz shift towards lower frequencies when applying an external magnetic field. The SWPA also exhibited a $P_{\mathrm{1dB}} \sim -106.2\,\mathrm{dBm}$ at 20 dB gain, which is an improvement over the standard JPAs, which typically saturate between $-120\,\mathrm{dBm}$ and $-110\,\mathrm{dBm}$. However, we noticed continuous SNR degradation at high gain levels, that we suspect could originate from higher harmonics and mixing products caused by strong nonlinearities.

In this chapter, I also introduce a novel method for performing phase-sensitive

amplification only requiring a VNA and signal generator, which demonstrated efficient phase-dependent signal amplification and de-amplification of the SWPA. The phase-sensitive extinction ratio (PSER) reached $42.30 \pm 2.81\,\mathrm{dB}$, comparable to the highest values reported for JPAs. However, the complex behaviour of the I and Q quadratures' gain as a function of pump and signal power requires further investigation.

In conclusion, while further analysis is needed to fully understand the origins of the observed effects, such as the gain sensitivity, the SNR degradation at high gain, and the phase-sensitive amplification dynamics, SWPAs present several advantages. Their performance metrics, such as gain, bandwidth, and compression point, are on par with or exceed those of current JPAs. Additionally, SWPAs are easier to fabricate compared to JTWPAs. Therefore, with a deeper understanding of their behaviour, SWPAs have the potential for application as quantum-limited amplifiers and beyond.

Chapter 9

Preliminary design and characterisations of W-band JTWPA

In the previous chapters, I have presented our efforts on developing microwave Josephson junction parametric amplifiers. Although TWPAs were originally demonstrated in the microwave regime, they hold the potential to operate at higher frequencies. In this chapter, I describe our effort to — using the know-how from the mm astronomical instrumentation field — extend the operational frequency range of JTWPAs to the W-band (75-110 GHz). First, I present the design considerations for the W-band device, resulting in two separate designs — with and without dispersion engineering, which I fabricated using our collaborators facilities at IRAM. Then, I present the preliminary DC and RF characterisation of the devices. The chapter is concluded with discussions of the measured results and possible improvements envisioned.

9.1 Motivation for high frequency operation

In addition to their applications in the microwave regime, TWPAs could find a broad range of applications at higher frequencies. As discussed in Chapter 1, mm and sub-millimetre wave astronomy would largely benefit from the development of quantum-limited amplifiers used at the front-end of the detection chain. For example, replacing the current ALMA band 3 (84-116 GHz) receivers' technology with a quantum-limited amplifier operated at those frequencies, would lead to doubling the system sensitivity, and a four times increase in the observation speed [160]. The potential improvements are even larger at frequencies > 400 GHz, were superconductor-insulator-superconductor (SIS) mixers have higher conversion losses.

Beyond astronomy, at frequencies higher than microwaves, superconducting qubits could operate at temperatures above 1 K. At these temperatures, cryogenic systems based on Helium-4 (^{4}He) can be used to cooldown the devices, resulting in up to four orders of magnitude larger cooling power than standard dilution refrigerators using ^{3}He/^{4}He mixtures to achieve 10 mK. This could potentially solve the cryogenic bottleneck for the scalability of superconducting quantum computers. Furthermore, use of mm-wave qubits eases the frequency conversion to optical frequencies, hence facilitating the implementation of efficient superconducting-photonic links for qubit control and operation [161]. This could pace the way to replace the numerous RF cable lines inside the cryostats with a single broadband optical fibre permitting signal multiplexing. Due to these advantages, novel approaches have been suggested to operate qubits at the W-band range using high kinetic inductance nano-wires [162], and recently been demonstrated using Nb/Al-AlO_x/Nb junctions [163]. All these efforts would require high frequency quantum-limited amplifiers to read out the qubits, hence the need for high frequency TWPAs.

KTWPAs have been demonstrated for operation at frequencies higher than microwaves [164, 165]. However, there is a lack of exploration for JTWPA operation at high frequencies, which in principle could leverage the optimised niobium-based SIS tunnel junction fabrication infrastructures developed for mm-wave astronomical instrumentation, making this technology more accessible to the scientific community. This could open up the possibility for on-chip integration of JTWPAs with SIS-mixers, and/or other niobium-based detectors, in the future.

9.2 JTWPA designs

9.2.1 Design considerations for W-band operation

I started the design process by identifying factors that may limit the operation of a JTWPA in the W-band, which firstly related to the superconducting gap frequency (f_Δ) of the tunnel junction, since photons with frequency $f > f_\Delta$ will break the Cooper pairs, and hence the superconducting state. Most of the recent JTWPAs use aluminium junctions [80, 81, 82], leveraging the maturity of this technology for qubit applications. However, the low gap frequency of aluminium ($f_\Delta \approx 90$ GHz) limits its application to the microwave regimes. For operation in the W-band, we opt to use Nb/Al-AlO_x/Nb junctions, where $f_\Delta \approx 680$ GHz and their trilayer fabrication technique has been largely matured in the past decades.

Most microwave JTWPAs make use of silicon dioxide (SiO_2) parallel plate capacitors [79, 112] or inverted microstrip with an aluminium oxide (Al_2O_3) dielectric layer [80, 81] to increase C_s, and thus match the device to the 50 Ω environment. The loss of these dielectric materials increases with frequency, and can reach loss tangent values of $\tan\delta \sim 4.5 \cdot 10^{-3}$, i.e., > 6 dB losses at 8 GHz, as measured in Chapter 6. Therefore, I opt for a coplanar waveguide (CPW) geometry as the choice of transmission line forming the W-band JTWPA, to minimise the need for lossy dielectric materials. Furthermore, operating the device in the W-band means that we are not confined to a 50 Ω environment, since the device will be mounted in a waveguide environment with waveguide-to-CPW transitions that generally have higher characteristic impedance around 100 Ω. This reduces the required C_s value, allowing the use of interdigitated capacitors (IDCs), which do not need any dielectric layer.

As introduced in Sec. 3.3, the cutoff frequency (f_c) of the transmission line forming the JTWPA will also determine the upper-frequency limit:

$$f_c = \frac{2\omega_0}{2\pi\sqrt{1 + 4\frac{\omega_0^2}{\omega_j^2}}}, \tag{9.1}$$

where $\omega_0 = 1/\sqrt{L_j C_s}$ is the cutoff frequency of the STL and $\omega_j = 1/\sqrt{L_j C_j}$ is the plasma frequency of the junctions. Both L_j and C_j are correlated and depend on the critical current density (J_c) and the size (A_{jj}) of the junction. In Fig. 9.1(a), I plot f_c as a function of J_c for different values of A_{jj}, with C_s fixed at 0.3 fF to account for the shunt capacitance of a CPW with approximately 2 µm gap (value obtained from Sonnet

As I aim to pump the JTWPA at $f_p \approx 90$ GHz, I set $f_c = 2f_p = 180$ GHz to suppress higher pump harmonics and other parasitic parametric effects, without compromising the operational bandwidth. From Fig. 9.1(a), we could reach this value with $J_c \approx 3.16\,\mathrm{kA/cm^2}$. However, assuming $A_{jj} = 0.5\,\mu\mathrm{m}^2$, the small C_s value results in $Z_0 \approx 300\,\Omega$, complicating the design of a waveguide-to-CPW transition[1]. As shown in Fig. 9.1(b), a small increase in the shunt capacitance to $C_s = 6.5$ fF, would allow us to reduce the characteristic impedance to $Z_0 = 70\,\Omega$ for the same A_{jj} with $J_c \approx 3.4\,\mathrm{kA/cm^2}$, while still maintaining $f_c = 180$ GHz. This not only eases the design of the waveguide-to-CPW transition, but also increases the phase velocity of the JTWPA, further reducing the number of junctions required for high gain. Therefore,

[1]Larger junctions result in smaller L_j and therefore would also require a larger number of junctions to reach the same gain.

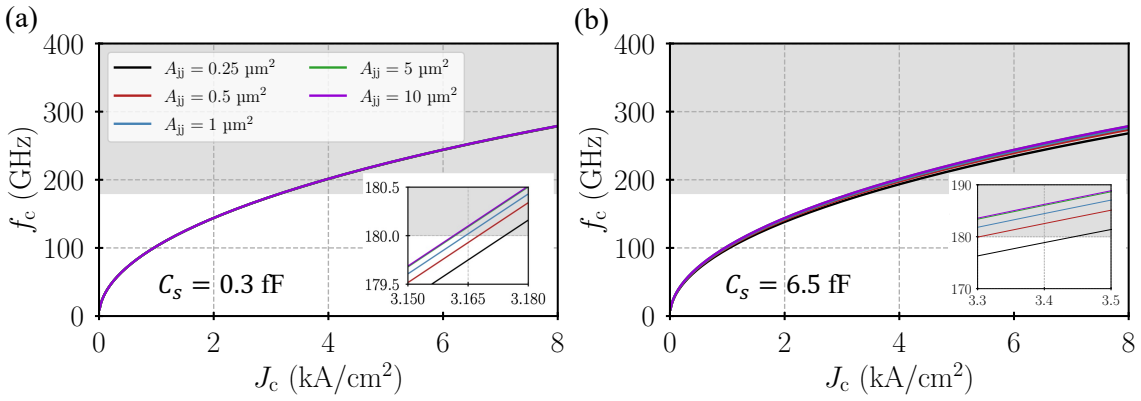

Figure 9.1: JTWPA cutoff frequency f_c plotted against the J_c of the junctions for different junction's area, with a shunt capacitance value of (a) $C_s = 0.3\,\text{fF}$ and (b) $C_s = 6.5\,\text{fF}$. A cutoff frequency higher than twice the operation frequency of our device, i.e., $f_c > 180\,\text{GHz}$, is shaded in grey. Insets show the zoom-in plots focusing on the range near 180 GHz.

I fixed the junctions parameters for the design to $J_c \approx 3.4\,\text{kA/cm}^2$, $A_{jj} = 0.5\,\mu\text{m}^2$, and $C_s = 6.5\,\text{fF}$.

9.2.2 Gain simulation and coupling strategy

To convert the electrical parameters of the design into physical dimensions, I use 3D electromagnetic simulator HFSS® [166] to ensure an accurate representation of the electromagnetic behaviour of the STL. The unit cell model of the device is shown in Fig. 9.2(a). The length of the IDC stubs of the CPW is optimised to reach $Z_0 = 70\,\Omega$, with $C_s \approx 6.5\,\text{fF}$. We further added equipotential ground bridges to suppress the potential generation of slotline mode at high frequencies. As shown in Fig. 9.2(a), the topology of the device combines a 400 nm Nb bottom layer, with a 200 nm SiO_2 spacer layer separating the bottom and the top Nb layer (400 nm). Both Nb layers are connected through a pair of $0.5\,\mu\text{m}^2$ junctions with $L_j = 19.4\,\text{pH}$ and $C_j = 37.6\,\text{fF}$. The S-parameter of the simulated unit cell is cascaded 352 times (704 junctions in total) to form the entire JTWPA. Extracting the propagation constant and solving the coupled-mode equations following the technique presented in Chapter 3, I simulated the gain profile of the device as shown in Fig. 9.2(b) for different values of pump power $(I_p)^2$. With this design, hereafter the unloaded design, we expect to reach a decent gain of $\sim 15\,\text{dB}$ with $I_p/I_* = 0.6$ and a bandwidth of $\sim 10\,\text{GHz}$ around 90 GHz.

[2]Due to time constraints, only the $I_p/I_* = 0.6$ case was fully simulated in HFSS®. The $I_p/I_* = 0.4$ and 0.6 were calculated from the corrected propagation constant obtained from the $I_p/I_* = 0.6$ simulations — which should give a fairly precise estimation of the gain and bandwidth.

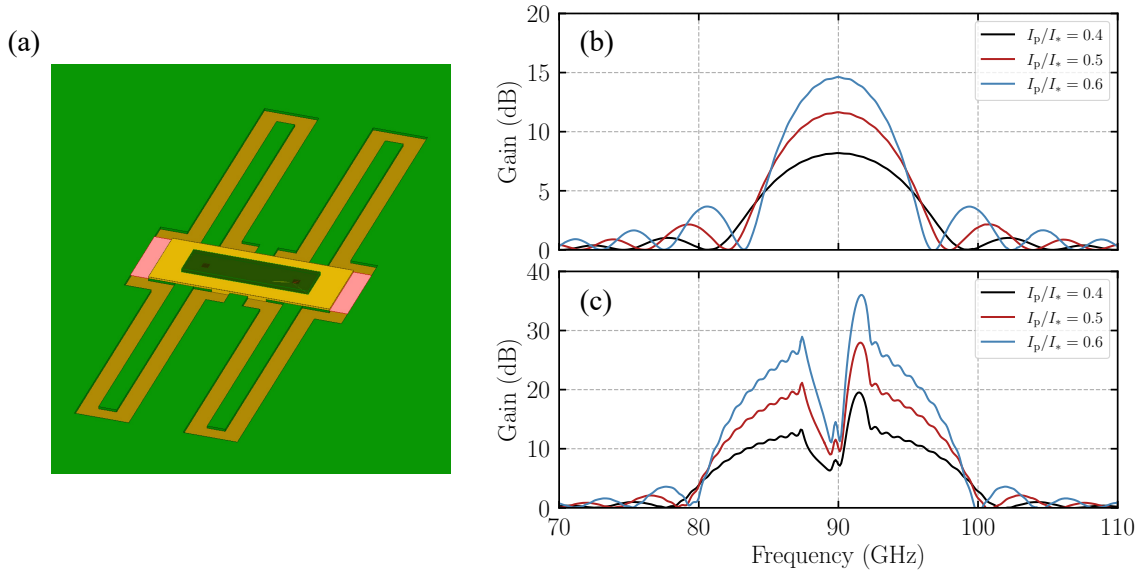

Figure 9.2: (a) Layout of our JTWPA unit cell modelled in HFSS®, showing the bottom layer (light green), spacer (yellow), top layer (dark green) and the junctions (red). The pink 2-D structures represent the input and output port in the HFSS® model. (b) Simulated gain curve for a 704 junctions JTWPA when pumped at three I_p/I_* values.

In a separate design, hereafter the loaded design, I further improve the gain-bandwidth product by incorporating phase-matching elements, namely periodic loading structures, along the transmission line. This results in a transmission line where the length of the stubs is periodically altered, with a modulation period of $\lambda_{per}/2$, where λ_{per} is the wavelength at $f_{per} \approx 92\,\text{GHz}$. As explained in Sec. 2.2.4, this modulation creates a stopband around f_{per}, locally distorting the dispersion relation of the device, allowing for phase mismatch correction, hence facilitating exponential gain. The predicted gain profile for this design when pumped at $f_p = 89.9\,\text{GHz}$ is presented in Fig. 9.2(c) showcasing a significant enhancement in the gain-bandwidth product.

For operation in the W-band, the device needs to be mounted in a WR-10 waveguide environment, instead of interfacing with the commonly used microwave connectors. To achieve this, we need to couple the TE_{10} mode propagating in the waveguide into the CPW chip. This transition can be realised using a probe antenna. Using HFSS®, I simulate the Nb probe antenna on a 100 µm thick high-resistive silicon substrate, and I optimise the geometry (Fig. 9.3(a)) to maximise the power coupling in the W-band range while matching the output impedance of the probe antenna to $Z_0 = 70\,\Omega$. Fig. 9.3(b)&(c) show the simulated S_{21} and S_{11} of the probe antenna for

the unloaded and loaded design respectively[3], and Tab. 9.1 summarises the design parameters for both antenna designs. The simulations predict a return loss less than –15 dB from 70 GHz to 100 GHz the unloaded design and below –20 dB for the loaded design. The better performance of the loaded design is due to the smaller substrate width compared to the unloaded design. The smaller width translates in a smaller groove, and therefore a smaller gap above the chip, which lets part of the energy from the waveguide escape without coupling to the probe antenna. An identical pair of these antennas are then connected to the input and output port of the JTWPA to couple the energy from the waveguide to the chip and back to the waveguide (see Fig. 9.4).

Design	l_{bs} (µm)	l_{pr} (µm)	θ (°)	Width[1](µm)	Thickness[1](µm)
Unloaded	829.1	610	56	1000	100
Loaded	842.8	642.8	51.8	600	100

[1] Width and thickness of the substrate.

Table 9.1: Probe antenna design parameters.

Design	J_{c} (kA/cm^2)	A_{jj} (µm^2)	N_{jj}	l_1 (µm)	l_2 (µm)	w (µm)	s (µm)	a (µm)
Unloaded	3.4	0.5	704	60	NA	1.75	2	10
Loaded	3.4	0.5	704	60	37	2	2	10

Table 9.2: Design parameters for unloaded and loaded W-band JTWPA.

9.3 Device fabrication and screening

The layouts of the JTWPA chips with the probe antennas are presented in Fig. 9.4. The unloaded design (Fig. 9.4(a)) has a meandered transmission line geometry to reduce the chip length, making it compatible with DC-screening setup as I will present later. This design choice comes at the price of a potential larger signal leakage[4]. On the other hand, the loaded design (Fig. 9.4(b)) has a straight-line geometry, resulting in a larger but narrower chip compared to the unloaded design, potentially reducing signal leakage in the sample holder. The main design parameters from both designs are summarised in Tab. 9.2.

[3]Different geometries for the probe antenna are required due to the different chip's width of the two designs.

[4]The chip sits inside the split-block on a groove, with a 100 µm empty space on top of the chip. The wider the chip, the larger the empty volume on top of it, potentially increasing the leakage.

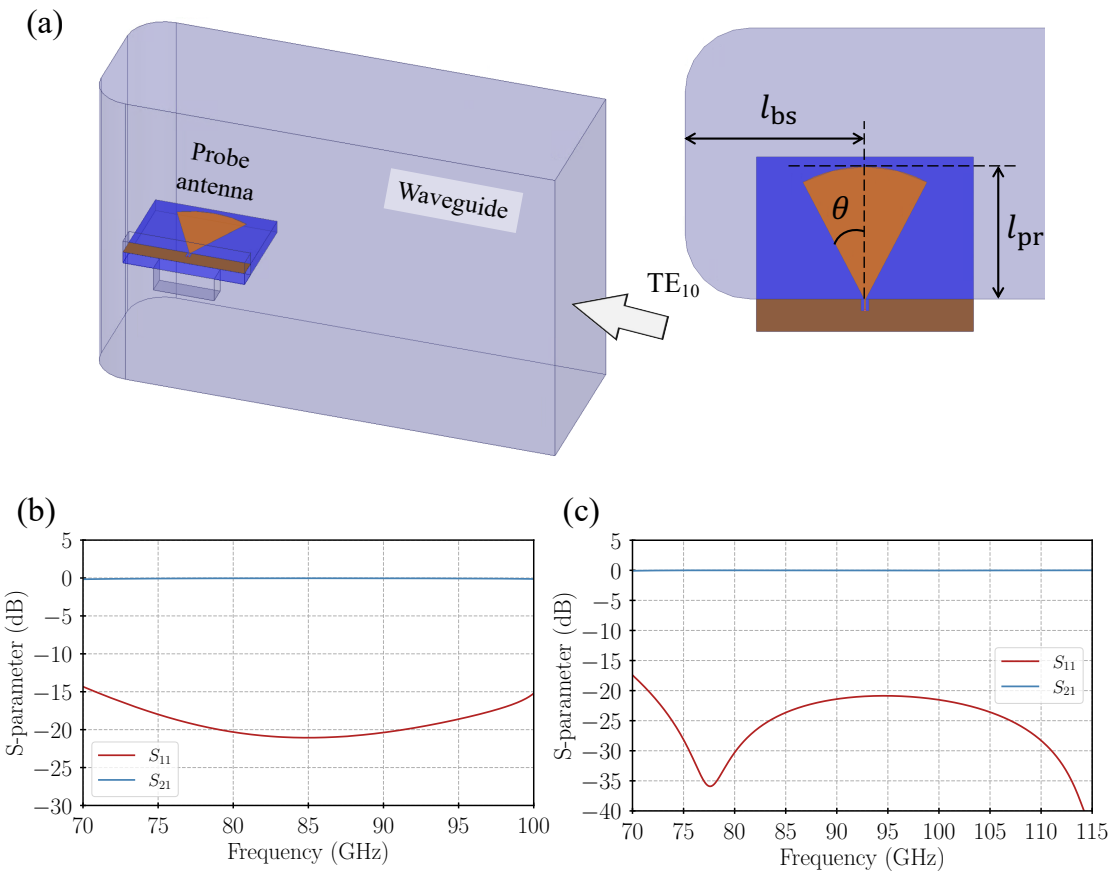

Figure 9.3: (a) The probe antenna of the unloaded design modelled in HFSS® including the WR-10 rectangular waveguide and the backshort. The geometry is optimised to maximise the coupling in the W-band. Simulation results of the transmission (blue) and return loss (red) for the probe antenna of (b) the unloaded design and (c) the loaded design. Both antenna designs are matched to a $Z_0 = 70\,\Omega$ CPW.

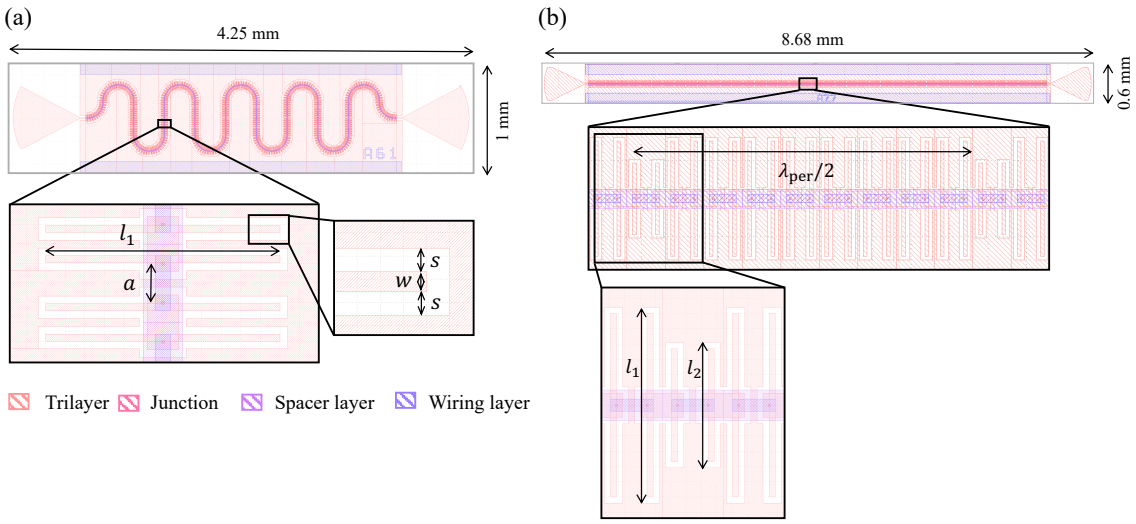

Figure 9.4: Final layout of the JTWPA for (a) the unloaded design and (b) the loaded design. The different dimension parameters are indicated on the layout.

Both designs were fabricated on the same wafer, using the photolithography masks layout shown in Appendix E. I successfully fabricated a single wafer, following the recipe presented in Chapter 4, during my visit to IRAM from the 4$^{\text{th}}$ to the 29$^{\text{th}}$ of February 2024. For these devices, I used a 280 µm high-resistance (R >20,000 Ω·cm) 2-inch silicon wafer as the substrate. After fabrication, I mechanically polished the substrate down to the required thickness of $\sim$ 100 µm. The trilayer was deposited using an oxidation time and pressure of $t_{ox} = 3$ h and $P_{ox} = 1.6$ Pa respectively, for the targeted $J_c = 3.4\,\text{kA/cm}^2$. Fig. 9.5 shows the microscope images of a small section of the fabricated devices, with a schematics of the cross-section.

To DC-screen the fabricated devices, I adopted a pre-designed frame[5] structure in the mask that would allow me to check for open- or short-circuit (to the ground) defects in individual devices using the dipstick setup described in Sec.4.3.2.1. Nevertheless, only the unloaded design was compatible with the size of this frame, hence I only performed the DC-screening on this design. The dicing of the devices from the wafer happened in two steps; first, I diced the framed chips (3 chips in a single frame), and after DC-screening, I performed a second dicing process to separate the individual devices. Despite fabricating 42 unloaded devices, a mechanical fracture on the wafer as a consequence of the thinning process damaged 24 of them. From the remaining 18 devices, 6 were open-circuited (33%) after DC-screening, probably due to unsuccessful liftoff of one or multiple junctions in the device.

[5]Designed by IRAM for other projects.

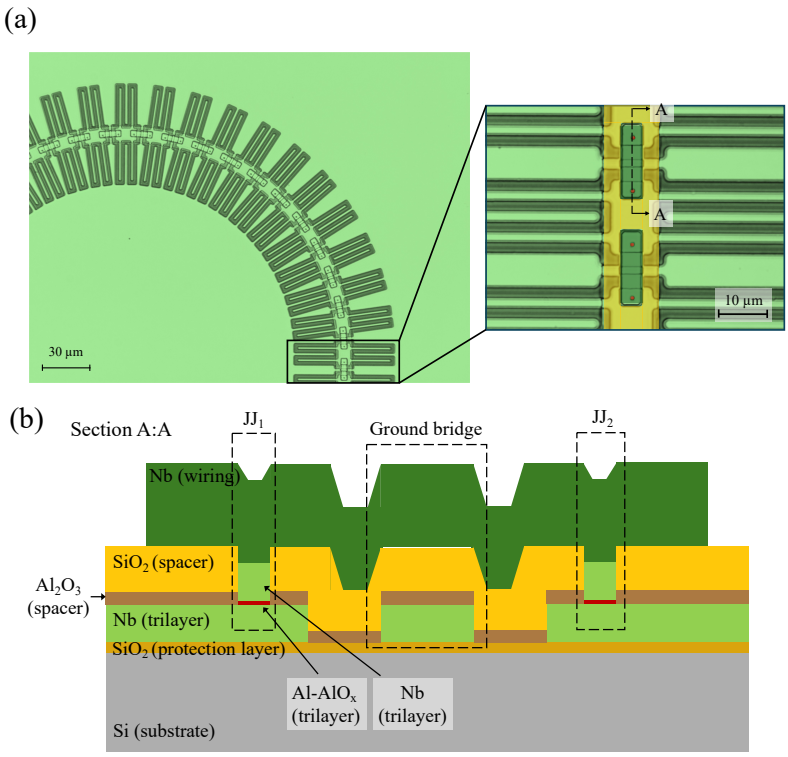

Figure 9.5: (a) Microscope image of a small section of one of the fabricated JTWPA devices. The zoom-in image shows the main structures of the unit cell. (b) Cross-section representation of the unit cell, the materials and identifiers of the different layer are stated on the figure. The representation is not drawn to scale.

Fig. 9.6 plots the measured IV curves for the unloaded JTWPAs, which resembles the standard IV curve for a Josephson junction, with a larger gap voltage proportional to the number of junctions in the device $V_{\mathrm{gap,704JJ}} = 704 \times V_{\mathrm{gap,1JJ}} = 704 \times 2.85\,\mathrm{mV} \approx 2\,\mathrm{V}$. Three of the 12 devices show a slightly lower V_{gap} by about 0.2 V, probably due to a number of short-circuited tunnel junctions in the array. Note that the negative slope below the gap is an artefact originated from the systematic error in the measurement setup for very high resistance values in the order of several MΩ. This is because the electronic setup of the dipstick was designed originally for the IV curve measurement of SIS mixers with only one or a few junctions rather than a large array of junctions with much higher normal resistance, hence the accuracy deteriorate above 1 MΩ. But the measurement below this limit is reliable as we calibrated the system with a known resistor value.

To estimate the critical current of our device, I measured an average normal resistance value of $R_{\mathrm{n}} = 180 \pm 7\,\mathrm{k\Omega}$. Using the Ambegaokar-Baratoff formula for

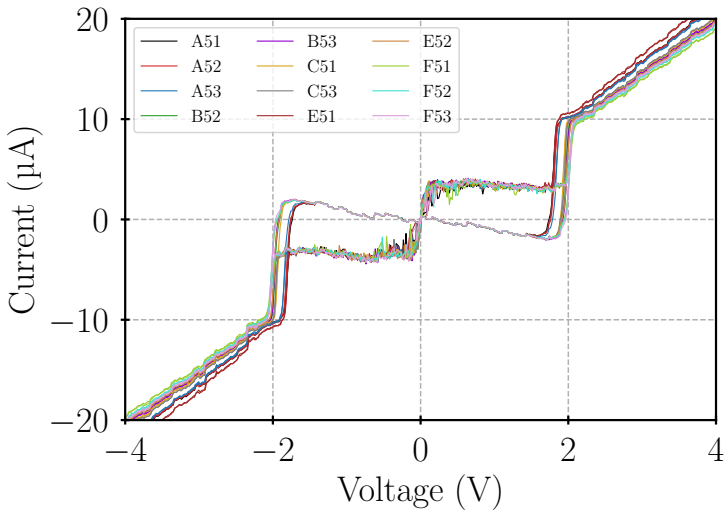

Figure 9.6: Measured IV curve of the unloaded JTWPAs. The voltage is swept from –4 V to 4 V upwards and downwards, resulting in the observed hysteresis effect. The results clearly show a $V_{\mathrm{gap}} \sim 2\,\mathrm{V}$ as expected for 704 junctions in series. The average normal resistance value is measured at $R_{\mathrm{n}} = 180 \pm 7\,\mathrm{k\Omega}$

tunnel junctions, we infer an average critical current value of $I_{\mathrm{c}} = 8.43 \pm 0.2\,\mu\mathrm{A}$, substantially smaller than the targeted $I_{\mathrm{c}} = 17\,\mu\mathrm{A}$. This could originate from an unexpected J_{c} and/or A_{jj} reduction. Assuming $J_{\mathrm{c}} = 3.4\,\mathrm{kA/cm^2}$ as targeted, the measured I_{c} value would result from a $\sim 50.4\,\%$ reduction of the junction size, possibly due to an over-etching and/or the oxidation of the side-walls. This value is in line with previous measurements performed in Chapter 5 and Chapter 7. Assuming $\sim 50.4\,\%$ smaller junctions and $I_{\mathrm{c}} = 8.43 \pm 0.2\,\mu\mathrm{A}$, using Eq. 9.1, we re-estimate the cutoff frequency of the device $f \approx 122\,\mathrm{GHz}$. Therefore, despite the large reduction in f_{c}, the device should remain capable of operating in the W-band.

DC-screening frame design

Each DC-screening frame includes 3 unloaded JTWPAs, as shown in Fig. 9.7. The dipstick setup allows to measure the IV curve between the three connection pads in the upper left of the frame (C_1, C_2 and C_3) and the 'ground' pad (C_{g1}). The connections pads C_1, C_2 and C_3 are connected to the left antenna of device 1, 2 and 3 respectively. Similarly, the connection pads C_4, C_5 and C_6 are connected to the right antenna of device 1, 2 and 3 respectively. Note that an 'interconnection line' made of aluminium, connects C_4, C_5 and C_6 to C_g. The DC-screening is performed in two steps. First, the device is mounted on the sample holder following the orientation in Fig. 9.7, hence measuring the IV curve through device 1, 2 and 3. Next, I dip the chip in SVC-14 for about $\sim 30\,\text{min}$ to dissolve the interconnection line. Once the interconnection line is dissolved, I rotate the chip $180\,^\circ$ to mount it in the sample holder. Therefore, when we perform a second IV measurement, we measure the current from C_4, C_5 and C_6 to C_{g2}, which is connected to the ground plane of the three JTWPA devices. This measurement allows to check for short-circuits to the ground.

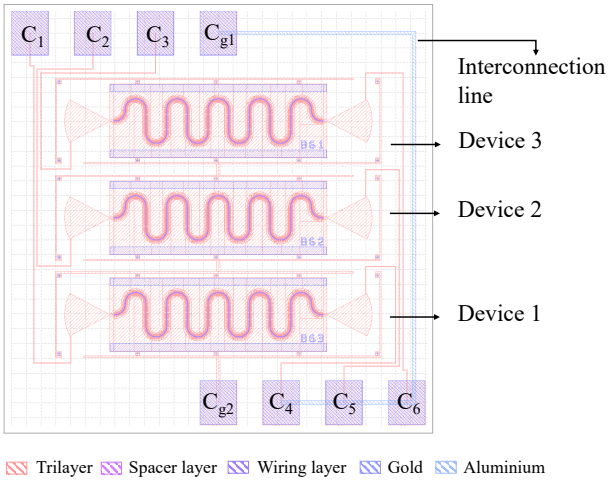

Figure 9.7: Layout of the DC-Screening frame. C_n, where $n = \{1, 2, 3, 4, 5, 6, g1, g2\}$, are the different connection pads that provide an electrical connection with the pins of the sample holder. The interconnection line allows for transition from measuring the IV curve through the device and from the device to the ground.

9.4 RF characterisation

Subsequently, I performed the RF characterisation of the devices using the setup at the Jet Propulsion Laboratory (Pasadena, CA, USA), during my visit there from the 11^{th} of March to the 5^{th} of April 2024. During this time, I performed 4 cooldowns,

testing 4 of the previously DC-screened unloaded JTWPAs and 1 loaded JTWPA. All the devices except one (device E52) resulted in no, or very poor, measurable transmission. Therefore, in the rest of this section, I will focus on the device E52. All the measurements were taken at $T = 1\,\mathrm{K}$, unless otherwise stated.

9.4.1 Cryogenic system and mounting technique

The RF characterisations were performed using the cryogenic platform depicted in Fig. 9.8(a), where a cryocooler is used to cool the system down to 4 K and a helium-4 sorption cooler (GL4 from Chase Research Cryogenics®) further decreases the temperature of the cold-plate to 1 K. The system is equipped with four WR-10 waveguide lines, allowing for the measurement of two devices per cooldown. The JTWPA is mounted in a WR-10 waveguide copper split-block interfacing the waveguide channels of the system. The split-block consisted of two curved WR-10 waveguides, interconnected with a groove to accommodate the JTWPA chip (Fig. 9.8(b)). The groove has a 300 µm wide and 200 µm deep channel underneath the chip to suppress possible resonant modes in the substrate. As shown in Fig. 9.8(b), the device is manually aligned to the groove slot and silver dust-arrester-ground (DAG) paint is applied at the edges of the chip to ground the device.

9.4.2 Transmission measurement

I measured the transmission profile of the device using the experimental setup presented in Fig.9.9. The signal from the Vector Network Analyser (VNA) and the pump tone from a signal generator are up-converted with frequency multipliers to the W-band, and combined at room temperature before injecting to the device under test (DUT). Fixed attenuation inside the cryostat reduces the estimated $\sim -68\,\mathrm{dBm}$ room temperature thermal noise to $\sim -98\,\mathrm{dBm}$, well below the critical current limit of the device $P_{I_\mathrm{c}} = -52\,\mathrm{dBm}$[6]. Additional variable attenuators outside the cryostat were used to adjust the signal and pump power reaching the DUT. A pair of isolators were connected to the DUT to protect the device from possible power reflections. The output spectrum of the DUT was then amplified using a room temperature amplifier before being down-converted and readout with the VNA.

Fig. 9.10(a) shows the measured transmission profiles, calibrated with the room temperature transmission data measured through a feedthrough line replacing the

[6]Considering the measured $I_\mathrm{c} = 8.43\,\mu\mathrm{A}$, instead of the targeted value.

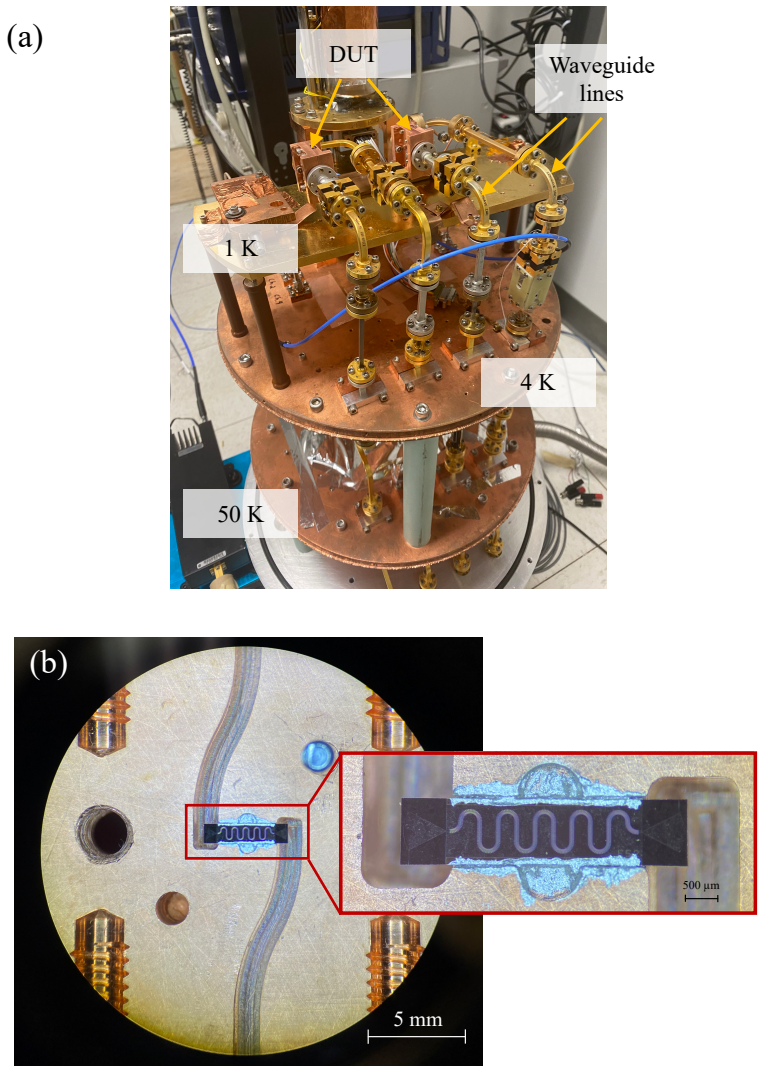

Figure 9.8: (a) Cryogenic platform used for the RF measurement of our W-band devices. The DUTs are mounted at the 1 K stage equipped with waveguide lines. (b) Microscope image of our JTWPA device mounted in the WR-10 waveguide split-block. The RF signal is coupled in and out of the JTWPA chip through curved waveguide structures. Zoom-in image: The chip is manually mounted on a groove connecting both waveguides, using silver DAG to connect the CPW ground to the cooper block and to hold the device.

DUT, for different values of the variable attenuator in the signal path (α_s). I estimate the power at the input of our device of $P_{in} = -62$, -52 and -42 dBm for α_s values of 40, 30 and 20 dB respectively. Assuming an ideal signal coupling into our device, we would expect to observe a flat 0 dB transmission for P_{in} less than -52 dBm, and a sudden drop in transmission for $\alpha_s = 20$ dB when the input power exceeds P_{I_c}.

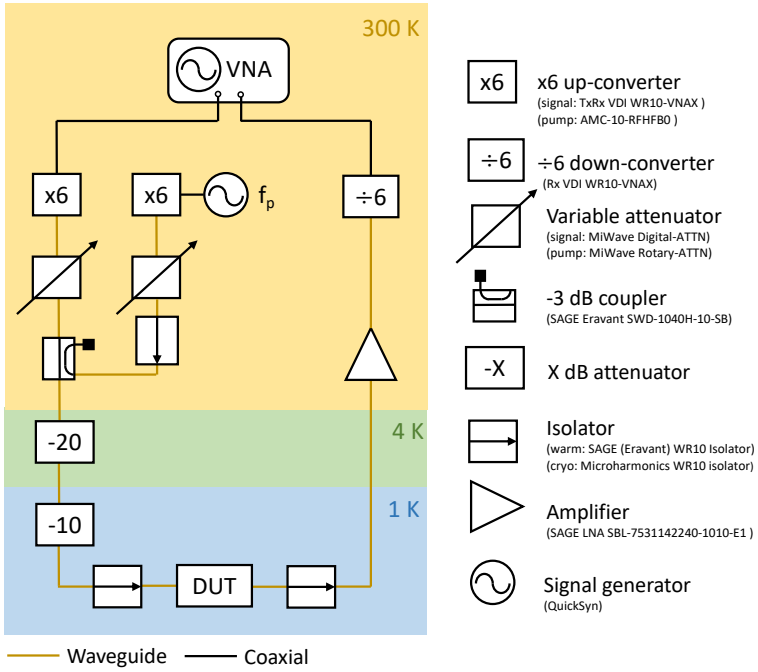

Figure 9.9: Experimental setup for the W-band RF transmission measurements.

However, for all the α_s settings, we observed over 30 dB losses with periodic features that cleared up with lower attenuation. This suggests a $\sim$30 dB loss in the antenna coupling and/or power propagation in the block, limiting the amount of power entering and exiting the JTWPA. This further indicates that the actual power coupled to the device for an attenuation of 40 dB may be at –92 dBm (if all loss is due to the input antenna and the waveguide before the antenna), close to the room temperature noise level, resulting in a poor SNR. Therefore, when we increase P_{in} by decreasing the attenuation, more energy is coupled into the device and the SNR improves as shown in Fig. 9.10(a). However, due to the quasi-fixed setting of the system, I was unable to further reduce the attenuation beyond 30 dB, hence I could not observe the breaking of superconductivity by exceeding the critical current of the device. We suspect the losses could also be originated from the poor grounding of the device. I further discuss the potential sources of this losses in Sec. 9.5.

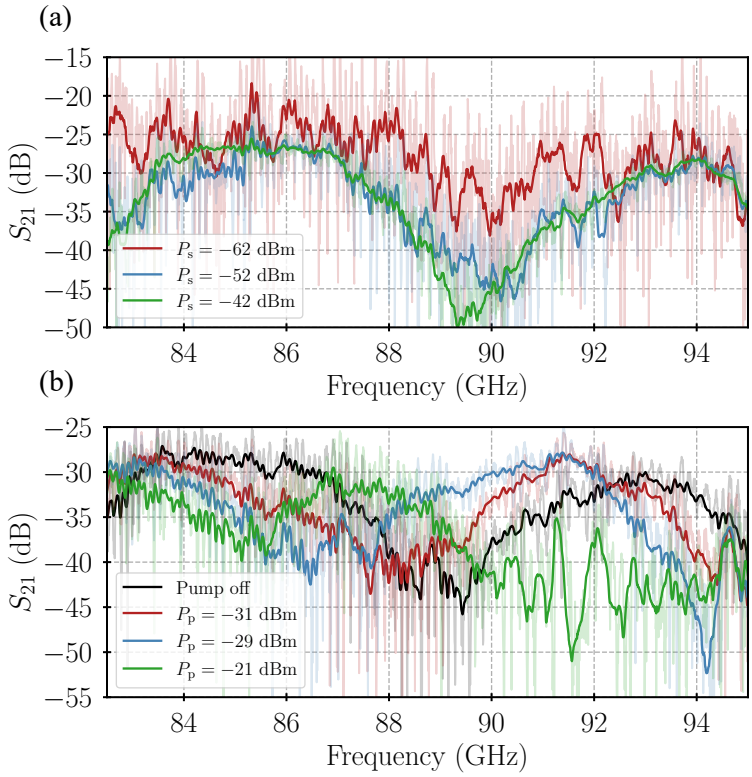

Figure 9.10: (a) Transmission profile of the JTWPA with different applied signal power P_s levels. (b) RF transmission when pumped at $f_p = 92\,\text{GHz}$ with different pump power P_p levels when P_s is set at $-42\,\text{dBm}$. The values in the legends indicate the estimated power at the input of the device, without considering the coupling losses. The raw data is shown in light colours, and the dark colours represent the averaged data.

Based on the previous results, I fixed $\alpha_s = 20\,\text{dB}$, i.e., $P_s \sim -72\,\text{dBm}$ at the input of the device after taking into account the 30 dB coupling loss, and apply a pump tone at $f_p = 92\,\text{GHz}$. I measured the transmission profiles for different values of the variable attenuator in the pump path resulting in a pump power $P_p = -61, -59$ and $-51\,\text{dBm}$ at the input of the device (after coupling loss)[7]. The results are plotted in Fig. 9.10(b), which clearly show that the periodic features in the transmission profile shift in frequency with increasing pump power. This indicates a change in the phase velocity of the transmission line with pump power, an evidence of the nonlinear inductance of the junctions forming the W-band JTWPA. Focusing on the regime between 90–94 GHz, we further observed a sudden drop in transmission power for $P_p = -51\,\text{dBm}$ (after coupling loss), suggesting that some of the junction may

[7]The total power coupled into the device is dominated by the pump power in this case, since the signal power is marginal at –72 dBm, hence I quote only the pump power in the text.

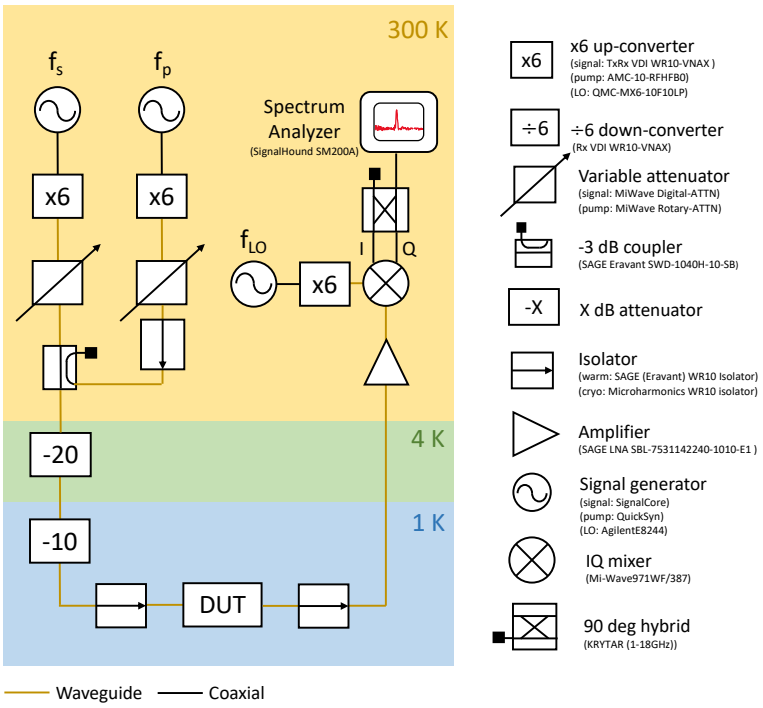

Figure 9.11: Experimental setup for the measurement of the 4WM idler. The output signal from the DUT is down-converted to the microwave regime using an IQ-mixer instead of a down-converter. A one-port terminated 90-degrees hybrid is used to reject the image band of the mixer, and the down-converted signal is read using a spectrum analyser.

have transitioned to their normal state, as the input pump power is just above $P_{I_c} = -52\,\mathrm{dBm}$. Note that the coupling losses are hard to estimate from the measurements, and could be frequency-dependent, which may explain why a sudden transmission drop is not observed across all the frequencies.

9.4.3 Parametric wave-mixing processes

Despite the unexpected loss, the transmission measurements showed promising indications of the nonlinear behaviour of the W-band JTWPA. As presented in Chapter 2, this nonlinearity — akin to the Kerr nonlinearity in optics — should give rise to four-wave mixing (4WM) parametric processes. As a result, when a pump ω_p and signal tone ω_s are applied to the STL, an idler tone at $\omega_\mathrm{i} = 2\omega_\mathrm{p} - \omega_\mathrm{s}$ should be generated. I explored the idler generation in the device using the experimental setup shown in Fig. 9.11, where two tones (ω_p and ω_s) are injected into the DUT and subsequently down-converted to the microwave regime using an IQ-mixer and a quadrature hybrid

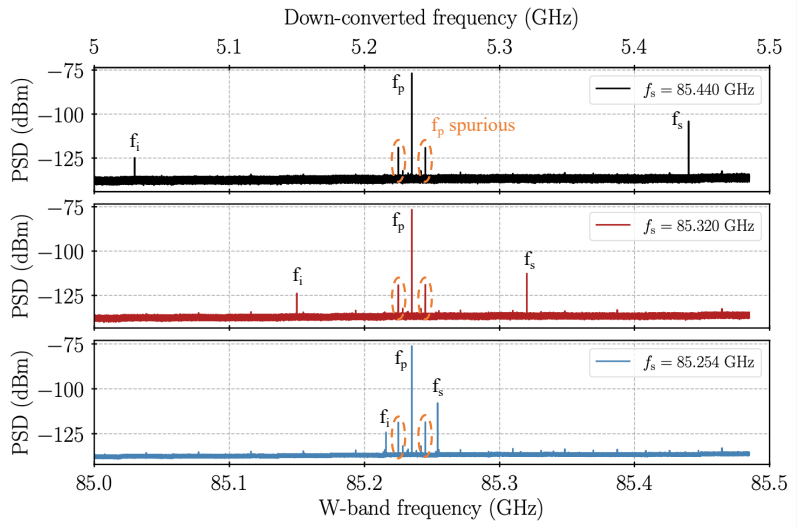

Figure 9.12: Power spectrum density (PSD) measured using the setup shown in Fig. 9.11 with the setting $\alpha_s = 50\,\text{dB}$, $\alpha_p = 0\,\text{dB}$, $f_p = 85.235\,\text{GHz}$ and $f_{LO} = 80\,\text{GHz}$, when applying a signal tone at (top panel) $f_s = 85.44\,\text{GHz}$, (middle panel) $f_s = 85.32\,\text{GHz}$ and (bottom panel) $f_s = 85.254\,\text{GHz}$. The two tones around the pump is associated the frequency synthesiser generating the pump and LO tones. An idler tone at $\omega_i = 2\omega_p - \omega_s$ appears for all the measured signal frequencies.

with one of the output port terminated to reject the image band of the mixer. The other output port is then readout using a spectrum analyser.

I searched for the idler generation in the 85 – 85.5 GHz range where the transmission is less lossy. I fixed the pump frequency at $f_p = 85.235\,\text{GHz}$ and the local oscillator (LO) frequency for the mixer at $f_{LO} = 80\,\text{GHz}$. The results measured for different signal frequencies, when $\alpha_s = 50\,\text{dB}$ and $\alpha_p = 0\,\text{dB}$, are plotted in Fig. 9.12(a)-(c). In addition to the signal and pump, we noticed two spurious tones from the pump that are fixed in frequency around the pump, which we suspected are originated from the synthesiser used to generate the pump and the LO tones. Apart from this, we can clearly see that an idler tone is always generated at $\omega_i = 2\omega_p - \omega_s$, demonstrating that a 4WM mixing process is occurring in the JTWPA and the STL is highly nonlinear in the W-band, as intended.

To further confirm that the observed idler tone is indeed generated from the device, I re-ran the experiment by connecting the output of the $-3\,\text{dB}$ coupler to the input of the readout amplifier (bypassing the cryogenic stages including the DUT), via an extra 30 dB room temperature attenuator to replicate the attenuation setting inside the fridge. Using the same f_p, f_s and f_{LO} values as before, we adjust the pump and signal powers, i.e., $50 < \alpha_s < 70\,\text{dB}$ and $10 < \alpha_p < 28\,\text{dB}$, and no idler tone was

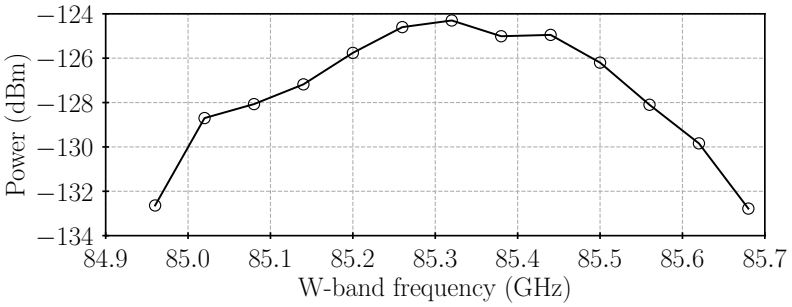

Figure 9.13: Measured power of the idler tone for $\alpha_\mathrm{p} = 0\,\mathrm{dB}$ $\alpha_\mathrm{s} = 50\,\mathrm{dB}$ and $f_\mathrm{p} = 85.235\,\mathrm{GHz}$ when sweeping the signal frequency. The x-axis corresponds to the W-band frequency of the idler.

observed.

Finally, in Fig. 9.13, I fixed $\alpha_\mathrm{s} = 50\,\mathrm{dB}$, $\alpha_\mathrm{p} = 0\,\mathrm{dB}$, and $f_\mathrm{p} = 85.235\,\mathrm{GHz}$, then I swept the signal frequency and record the idler frequency and amplitude read from the spectrum analyser. From the plot, we see that the maximum amplitude of the idler is located near the pump frequency, in which the parametric process is most efficient. Although I did not observe significant high gain in the device, most probably due to the unexpected high loss caused by the poor grounding issue, these measurements clearly show the promising prospects of developing highly nonlinear meta-material lines required for operating JTWPAs at high frequency in the mm-wave range.

9.5 Discussion

In this chapter, we have observed unexpected transmission losses in our W-band JTWPA, the cause of which remains under investigation at the time of writing. It is natural to speculate that the losses originate from the measured junction's $I_\mathrm{c} = 8.43 \pm 0.2\,\mu\mathrm{A}$, which is significantly lower than the targeted value. While this lower junction's I_c can indeed reduce the cutoff of the JTWPA to $\sim 122\,\mathrm{GHz}$, it is still higher than the intended operational frequency range of the device. However, the reduced junction's I_c could also lead to a characteristic impedance $Z_0 \neq 70\,\mathrm{Ohms}$ of the JTWPA, potentially contributing to an impedance mismatch with the probes antennas, hence limiting the energy coupling into the device. Assuming the lower I_c results from a reduction of the junction's size, I calculated the new Z_0 value of the line (without applied pump) using HFSS®, resulting in $Z_0 = 88\,\Omega$. Next, I re-ran the HFSS® simulation for the unloaded design probe antenna, using the updated port impedance $Z_0 = 88\,\Omega$, instead of the $Z_0 = 70\,\Omega$ previously used. The results,

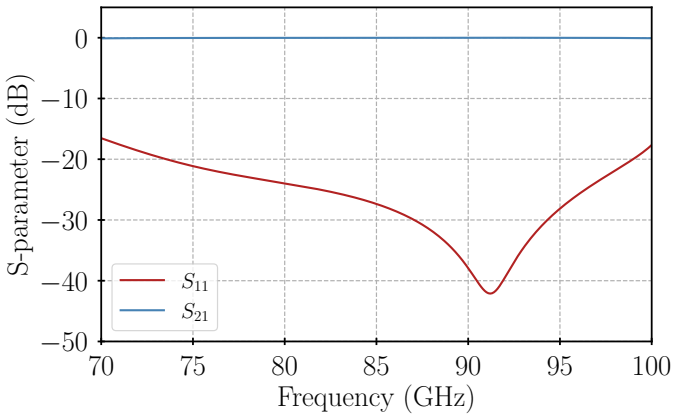

Figure 9.14: Results from the HFSS® simulation of the unloaded design probe antenna, with port impedance $Z_0 = 88\,\Omega$ to simulate the expected characteristic impedance of the JTWPA line with $I_c = 8.43\,\mu A$.

shown in Fig. 9.14, indicate $S_{11} < -20\,dB$ from 70 GHz to 100 GHz, suggesting a better coupling than the original design. Therefore, we can rule out the impedance mismatch as the main cause of the observed losses. Additionally, the re-simulation shows optimal coupling around 92 GHz, which might explain the transmission drop at increasing pump power observed only around that frequency, as discussed in Sec. 9.4.2.

We suspect the losses could be caused by the poor electrical grounding of the DUTs and the misalignment of the chip. The signal coupled through the probe antennas is largely dependent on their position in the waveguide; therefore, a small misalignment of the device, as it can be noticed in Fig. 9.8(b) will deteriorate the antennas coupling. Furthermore, as shown in Fig. 9.8(b), the silver DAG requires manual application on the chip to connect the ground planes of the CPW with the sample holder that is electrically grounded to the system. The amount of silver DAG used and the points of application require accurate manual precision, since any exceeding paint touching the CPW trace would result in a short-circuit to the ground, rendering the device unusable. Furthermore, widening the groove section where the devices sits, to facilitate the DAG paint application, would result in substantial signal leaking and additional resonant modes, hence it is not a practical solution. Similar reasons limit the use of bondwires for the grounding of our devices. Therefore, we believe an insufficient amount of DAG paint combined with the presented challenges during its application could have resulted in a poor ground connection, affecting the actual coupling efficiency of the probe antennas. This could affect the transmission mode of the CPW as well, as the propagating tones may not be transversing in the pure CPW

mode anymore, with some energy being dissipated in different transmission modes such as slotline modes.

The losses could also originate from two-level system (TLS) losses due to the spacer layer in our device. However, TLS losses would only appear at low temperature and we see no substantial difference in the behaviour of our device from 4 K to 1 K. The dielectric layer protecting the ground bridges could also contribute to the losses in the device, however, from EM simulations, the small size of the bridges make this contribution negligible. Furthermore, dielectric losses linearly increase with frequency, unlike the measured results. Finally, trapped magnetic fluxes could also induce high losses in our devices, although these are likely to change the transmission behaviour of the devices in each cooldown, which we have not observed.

Imperfections or misalignment in the split-block used to hold the device could also contribute to the losses. To have a better understanding of the origin of these losses, a calibration chip could be fabricated. This device would consist of a $Z_0 = 70\,\Omega$ CPW, with identical probe antennas as used in the JTWPA design. If using the same mounting techniques we observe a much better transmission, this would contradict our hypothesis of a poor grounding. Unfortunately, no calibration chip was included in the mask design used for the fabrication due to the short window available for me to travel to IRAM and JPL to conduct all these experiments. Assuming the losses originate from a poor grounding, a possible solution consist of using beam-leads [167, 168] to facilitate the ground plane connection with the sample holder. Another, but more complicated solution, consists of using an inverted microstrip geometry, provided a low-loss dielectric material such as amorphous silicon [165]. Finally, to further improve the performance of the device, we should include a hole pattern in the ground plane for magnetic flux trapping, and protect the device with a magnetic shield during the experiment.

9.6 Conclusion

In summary, this chapter presents the design, fabrication, and characterisation of W-band JTWPAs. Although the measured performance demonstrated unexpected transmission losses, the results provide valuable insights into possible causes. DC-screening measurements revealed a lower-than-expected critical current of the junctions ($I_c = 8.43\,\mu A$) probably due to a $\sim 50.4\,\%$ reduction of the junction's size due to over-etching and/or oxidation of the side-walls. This lower I_c may have contributed to impedance mismatches, although re-simulations ruled this out as the main source

of the issue. Instead, we believe possible imperfections in the split-block holding the device, as well as grounding challenges and potential misalignment of the device during mounting, could have contributed to the observed losses.

Despite the limitations, key characteristics were observed, such as the broadband nonlinear response of the device to an applied pump tone and the idler generation in the four-wave mixing process. These findings indicate the promising nonlinear behaviour required for high-frequency operation in the mm-wave range. With further design optimisations, especially addressing grounding and alignment issues, the W-band JTWPA could achieve the desired performance, paving the way for future quantum-limited amplifiers at higher frequencies.

Chapter 10

Conclusion and future work

This thesis presents the development of Josephson Traveling Wave Parametric Amplifiers (JTWPAs) for operation in the microwave and W-band (70-115 GHz) range. This is the first attempt of our research group to develop these devices. My work spanned from theoretical design, cleanroom fabrication, to detailed cryogenic characterisation to provide a comprehensive understanding of their behaviour.

To design a JTWPA, it is essential to build a theoretical framework that captures the amplification process based on the device's design parameters. We achieved this by expanding the previously established coupled-mode equations (CME) framework for kinetic inductance TWPA to include JTWPAs with various nonlinear elements. This generalised framework, outlined in Chapter 2, is used in Chapter 3 to analyse the impact of circuit parameters on a JTWPA's figures of merit. Additionally, it introduces a methodology for leveraging electromagnetic (EM) simulation software to assist in JTWPA design. While previous JTWPA design techniques based on the CME rely on knowing exacly the electrical parameters of the JTWPA, and only work for a single unit cell design, our new methodology provides the flexibility to use the output of any geometry implemented in an EM simulation software to estimate the gain performance of the device under development. I then applied this novel methodology to design JTWPAs with both parallel plate capacitors (PPCs) and interdigitated capacitors (IDCs), which were subsequently fabricated and tested in this thesis.

Before proceeding with the fabrication of the JTWPAs, I first fabricated a series of test devices to evaluate the limits of the fabrication process. These tests allowed us to determine the parameters necessary to achieve the low critical current densities required for our JTWPAs, specifically $J_c = 1.4\,\mathrm{kA/cm^2}$. Additionally, this process revealed potential issues with undersized junctions, which became apparent during

data re-analysis for this manuscript. The tests also uncovered a problem with pin-holes in the dielectric layer, leading to numerous PPCs being shorted to ground — critical in JTWPA implementation. To address this issue, we explored two mitigation techniques and concluded that depositing a 20 nm Al_2O_3 protective layer would help reduce the number of pin-holes, resulting in an estimated fabrication yield of $\sim 15\,\%$ for a 2,000-junctions JTWPA design with PPCs.

Although small, the estimated fabrication yield was judged sufficient to proceed with fabricating a batch of microwave JTWPAs with PPCs. This resulted in one working device that allowed us to assess the dielectric losses and demonstrated broadband gain when pumped at various frequencies. However, the gain was highly inconsistent, with significant dips and peaks, suggesting issues with impedance mismatch and/or variation in the I_c of the junctions. Additionally, the instability in gain highlighted the importance of shielding the JTWPA from magnetic flux, which could otherwise degrade the device's performance by introducing trapped magnetic fluxes

To improve the fabrication yield of the JTWPA, I designed and fabricated an updated version with interdigitated capacitors (IDCs) replacing the parallel-plate capacitors (PPCs), optimised for operation in the DC3WM regime, instead of DP4WM. While the RF characterisation showed an expected reduction in frequency-dependent losses and higher fabrication yield, it also revealed a significant reduction in junction size of $\sim 34.1\,\%$. Additionally, this batch displayed indications of possible outlier junctions with $I_c < 65\,\mathrm{nA}$, which restricted the application of DC current through the device, limiting its functionality in the DC3WM regime. Despite this, I attempted to measure 4WM gain but observed only narrow-band gain around the pump frequency. However, noise measurements indicated an 8.4 dB improvement in SNR for a specific frequency configuration. With further resolution of the fabrication and design challenges, this device could potentially be viable for practical quantum-limited amplification.

During my DPhil, I have also explored a 500-junction array forming a Fabry-Pérot cavity, which exhibited intriguing RF properties. This device, termed the Standing Wave Parametric Amplifier (SWPA), serves as a middle ground between a JTWPA and a JPA. In this device, I observed a $\sim 30.6\,\%$ reduction in junction size, similar to the JTWPA with IDCs. When pumped, the SWPA demonstrated 4WM gain up to $\sim 20\,\mathrm{dB}$ over a moderate bandwidth of $\sim 600\,\mathrm{MHz}$, with a measured compression point of $P_{1\mathrm{dB}} = -106.2\,\mathrm{dBm}$ at 20 dB gain. These RF characteristics match or exceed those of conventional JPAs. However, at high gain, the SWPA degraded the SNR, which merits further investigation to fully understand its behaviour. Additionally,

the device showed clear signs of efficient phase-sensitive amplification. Further study is required to fully understand and optimise the SWPA's performance.

Finally, I designed, fabricated, and tested a small number of JTWPAs for operation in the W-band (70-115 GHz). The fabricated devices exhibited a $\sim 50.4\,\%$ reduction in junction size; however, upon further analysis, this unexpected fabrication error did not render the devices impractical. RF characterisation of the device revealed a 30 dB transmission loss, likely due to poor grounding, misalignment of the chip, and potential imperfections in the block. Despite these losses, we observed nonlinear effects in the RF transmission during pumping, with clear evidence of 4WM idler generation. Therefore, we believe that with design improvements to address these issues, JTWPAs have the potential to operate effectively in the W-band.

Overall, the thesis demonstrates significant progress in developing JTWPAs, introducing novel design ideas and characterisation techniques. Despite the design-specific issues that limited the performance of the devices presented in this thesis, we consistently observed indications of I_c spread and a $\sim 30-50\,\%$ reduction of the junctions' size. Therefore, further efforts are needed to refine the fabrication techniques to ensure the successful fabrication of the devices.

Future work

General — Given the large number of junctions required for a JTWPA, it is essential to master their fabrication techniques. This thesis identified undersized junctions as a major problem in our designs, likely due to the oxidation of the side-walls or overetching during the fabrication. However, recent SEM observations by Samuel Wood at IRAM indicated a good match with expected dimensions for $0.5\,\mu m^2$ junctions, suggesting the undersizing is most likely caused by to the oxidation of the side-walls. If this size reduction is systematic, we should incorporate it into future designs to improve performance and yield. Additionally, a systematic study of the I_c spread across junctions on a single chip would be beneficial.

The microwave designs presented here would also improve with a more refined sample holder and mounting technique. Designing the PCB to include filtering structures in the CPW could help mitigate bond wire reflections. Moreover, reducing the residual magnetic field in the sample holder is critical; using paramagnetic materials for the SMA connectors and the screws will help improve the device's performance. Addressing these areas will strengthen future JTWPA implementations.

Microwave JTWPAs — The microwave JTWPA designs presented in this thesis utilised a straight-line geometry, resulting in a rectangular chip approximately 2.12 cm long. Therefore, during the e-beam lithography, cumulative beam alignment errors caused junction shifts that were occasionally critical. This issue was addressed by adding additional alignment crosses on each device and recalibrating the beam multiple times during the patterning process. However, a more compact design, such as a meandered line geometry creating a square chip, could also resolve this issue. A compact squared chip could benefit from using a smaller sample holder, reducing the device volume and facilitating the operation at higher microwave frequencies (where big sample holders may result in unwanted cavity modes).

Further design improvements could include adding holes to the CPW ground trilayer plane to trap magnetic fluxes, thereby reducing their negative effects on the device's performance. Finally, the IDCs size in the JTWPA design discussed in Chapter 7 was limited by the minimum CPW gap achievable with photolithography. By using e-beam lithography, the gap could be further reduced, increasing capacitance and allowing for smaller stubs. This would enable the implementation of a unit cell design similar to the W-band JTWPA, which includes ground bridges ensuring ground continuity, and addresses the dielectric window misalignment issue.

SWPA — One of the most intriguing and limiting factors in these devices is the degradation of SNR at high gain levels. We believe this could result from the generation of higher harmonics and mixing products. To investigate this further, I would focus on measuring the amplitude of these harmonics and mixing products when the device is operated at high gain. This would require precise calibration of the system's losses, as well as a setup capable of broadband observation without significantly impacting the device's gain — a challenging but essential task.

Additionally, during my last visit to IRAM, I included SWPA devices with varying numbers of junctions ($N_{\mathrm{jj}} = 300$, 400, and 500) on the W-band JTWPA and IDC-based JTWPA wafers, which remained untested due to time constraints. A thorough investigation of these devices could shed light on the fundamental mechanisms underlying the behaviour observed in our SWPA, potentially revealing an optimal cavity length that enhances the performance.

W-band JTWPA — To further improve this device, it is essential to understand the mechanisms behind the observed 30 dB tranmission losses. I propose fabricating a test sample identical to the W-band JTWPA, but replacing the line with a

$Z_0 = 70\,\Omega$ CPW. This would allow for testing of the probe antenna design, grounding technique, and the possible issues with the block design and/or fabrication. If similar losses are observed, further analysis would be needed to identify the limiting factor. If the probe antennas are the issue, we could explore using a feedline geometry instead. If grounding proves problematic, beam-leads could be an alternative, although this would complicate the fabrication. In the case of block-related issues, a more thorough analysis would be required to consider redesign options. Additionally, like the microwave JTWPA, the W-band design would benefit from incorporating holes in the ground plane to trap magnetic fluxes.

Despite all these challenges, this thesis reports on our effort in developing novel JTWPA devices starting from scratch and using non-optimised fabrication facilities, which were not initially designed for such superconducting devices. These progresses are significant, we have formulated a new theoretical framework, we have built several experimental setups from the ground up, discovered novel parametric devices and attempted for the first time to push the operation of JTWPAs into the millimetre-wave range. The insights gained, alongside the experience and expertise acquired, will be invaluable for future projects, paving the way for high-quality quantum-limited JTWPA devices for astronomy, quantum computing, dark matter search and other fundamental physics experiments requiring such ultra-sensitive amplification.

Appendix A

Fabrication recipe

Step	**Parameters**
Deposition 1	SiO_2, sputtered Ar 1 Pa Target power: 600 W (30 s) Wait (2 min 30 sec) # of cycles: 10
Resist Spin Baking	AZ5214 JP 4000 rpm (60 s) + 6000 rpm (2 s) 110 °C (1 min)
Exposure 1	UV photolitography wavelength: 250-350 nm (1 s)
Baking	115 °C (2 min)
Exposure 2	UV photolitography, flood wavelength: 250-350 nm (15 s)
Development	MF26A (25 s) DI water flushing ($\sim$ 30 s)
Deposition 2	Niobium, sputtered Ar 40 sccm Target DC power: 600 W (9 s) Wait (5 min) # of cycles: 4
Deposition 3	Aluminum, sputtered while rotating Ar 40 sccm Target DC power: 200 W (1 min)
Oxidation	Parameters 1: O_2 1.6 Pa (120 min) Parameters 2: O_2 1.6 Pa (180 min) Parameters 3: O_2 2.0 Pa (180 min) Parameters 4: O_2 4.0 Pa (300 min)
Deposition 4	Niobium, sputtered Ar 40 sccm Target DC power: 600 W (9 s) Wait (5 min) # of cycles: 5
Liftoff	Acetone + ultrasounds (3-4 h)

Table A.1: Recipe for the trilayer deposition.

Step	**Parameters**
Resist Spin Baking	Ma-N 2405 1800 rpm (30 s) + 5000 rpm (3 s) 90 °C (2 min)
Exposure 1	Ebeam litography Area Dose: 200 µC/cm^2
Exposure 2	UV photolitography wavelength: 250-350 nm (20 s)
Development	MF26A (20 s) DI water flushing ($\sim$ 30 s)
Etching	ICP-RIE SF6 30 sccm, C4F8 30 sccm Target power: 700 W, Substrate power: 100 W (2 min)
Deposition 1	Aluminum, evaporated 20 nm @ 0.25 nm·s^{-1} O_2 8 sccm
Deposition 2	SiO_2, sputtered Ar 1 Pa Target power: 600 W, Substrate power: 8 W (30 s) Wait (2 min 30 sec) # of cycles: 48
Liftoff	Acetone + ultrasounds (10 h)

Table A.2: Recipe for the junction definition and dielectric growth.

Step	**Parameters**
Resist Spin Baking	AZ5214 JP 4000 rpm (60 s) + 6000 rpm (2 s) 110 °C (1 min)
Exposure 1	UV photolitography wavelength: 250-350 nm (1 s)
Baking	115 °C (2 min)
Exposure 2	UV photolitography, flood wavelength: 250-350 nm (15 s)
Development	MF26A (25 s) DI water flushing ($\sim$ 30 s)
Deposition 2	Niobium, sputtered Ar 40 sccm Target DC power: 600 W (9 s) Wait (5 min) # of cycles: 12
Liftoff	Acetone + ultrasounds (1 h)

Table A.3: Recipe for the second metallisation layer deposition.

Step	**Parameters**
Resist Spin Baking	AZ5214 JP 4000 rpm (60 s) + 6000 rpm (2 s) 110 °C (1 min)
Exposure 1	UV photolitography wavelength: 250-350 nm (3 s)
Development	MF26A (25 s) DI water flushing ($\sim$ 30 s)
Deposition 1	Titanium, sputtered Ar 2 Pa Target DC power: 600 W (6 s)
Deposition 2	Gold, sputtered Ar 2 Pa Target DC power: 300 W (30 s)
Liftoff	Acetone + ultrasounds (1 h)

Table A.4: Recipe for the titanium-gold layer deposition.

Appendix B

Test devices masks

The photolithography masks used for the fabrication of the devices presented in this thesis were designed using custom Python codes developed in-house. I used the Python package `gdspy`, which provides an extensive set of functions to generate basic geometries in a `.gds` file. Since each chip design featured a unique geometry, the codes had to be extensively rewritten to accommodate these variations. Once finalised, the chip design could be easily replicated to populate the wafer area. Alignment crosses were incorporated at the chip level to assist with electron beam alignment, as well as wafer-scale alignment markers for the photolithography steps.

Once the mask designs were completed, they were sent to Compugraphics, a company specialising in photolithography mask fabrication. The masks were then produced according to our designs, with the specified resolution. Fig. B.1 shows an image of the `.gds` file created for the photolithography mask of the test devices presented in Chapter 5. Each colour represents a different material layer, and hence a different photolithography mask. A total of four lithography maks were required for these designs.

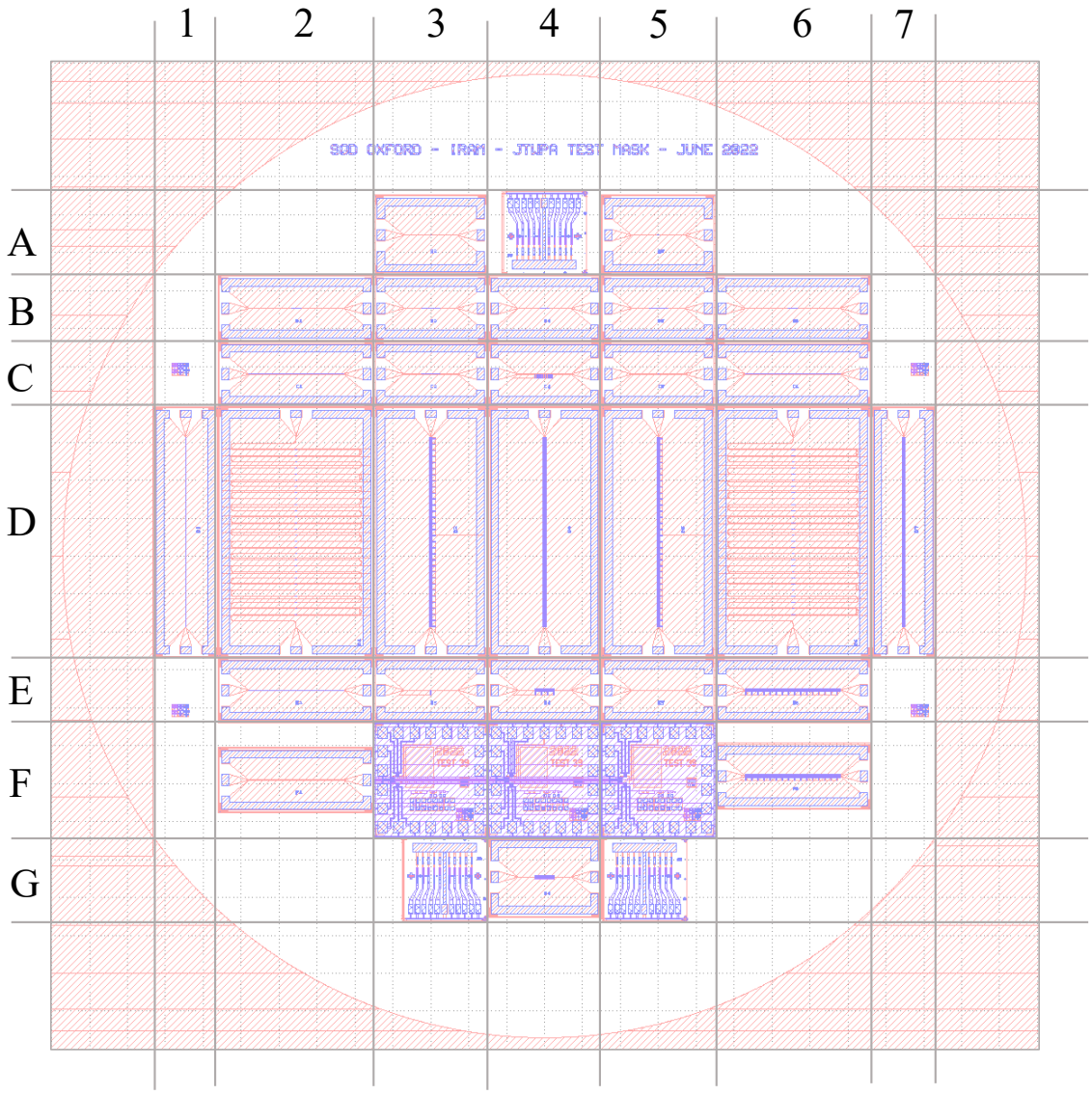

Figure B.1: Photolithography masks layout of the test devices presented in Chapter 5.

ID	Description
A3	CPW 4:2 µm, 1 JJ, $A_{jj} = 0.5\,\mu m^2$
A4	Chip test Oxford
A5	CPW 4:2 µm, 10 JJ (packed together), $A_{jj} = 0.5\,\mu m^2$
B2	CPW 4:2 µm, 50 JJ (packed together), $A_{jj} = 0.5\,\mu m^2$
B3	CPW 4:2 µm, 100 JJ (packed together), $A_{jj} = 0.5\,\mu m^2$
B4	CPW 4:2 µm, 50 JJ (packed together), $A_{jj} = 0.25\,\mu m^2$
B5	CPW 4:2 µm, 100 JJ (packed together), $A_{jj} = 0.25\,\mu m^2$
B6	CPW 4:2 µm, 50 JJ (packed together), $A_{jj} = 1\,\mu m^2$
C2	CPW 4:2 µm, 500 JJ (packed together), $A_{jj} = 0.5\,\mu m^2$
C3	CPW 4:2 µm, 100 JJ (packed together), $A_{jj} = 1\,\mu m^2$
C4	CPW 4:2 µm, 10 resonators
C5	CPW 4:2 µm, 5 JJ, $A_{jj} = 0.5\,\mu m^2$ capacitively coupled to the ports
C6	CPW 4:2 µm, 500 JJ (packed together), $A_{jj} = 0.25\,\mu m^2$
D1	CPW 4:2 µm, 1000 JJ (packed together), $A_{jj} = 0.5\,\mu m^2$
D2	CPW 4:2 µm, PL structure 5x10JJ, 3x5JJ (total 65 JJ), $A_{jj} = 0.5\,\mu m^2$
D3	CPW 4:2 µm, 1000 JJ, 1000 PPC, $A_{jj} = 0.5\,\mu m^2$ and 32 resonator
D4	CPW 4:2 µm, 1000 JJ (packed together), $A_{jj} = 0.5\,\mu m^2$ with PPC
D5	CPW 4:2 µm, 1000 JJ, 1000 PPC, $A_{jj} = 0.5\,\mu m^2$ and resonator
D6	CPW 4:2 µm, PL structure 5x20JJ, 3x10JJ (total 130 JJ), $A_{jj} = 0.5\,\mu m^2$
D7	CPW 4:2 µm, 1000 PPC
E2	CPW 4:2, 500 JJ (packed together), $A_{jj} = 1\,\mu m^2$
E3	CPW 4:2 µm, 1 resonator (JJ in the meander)
E4	CPW 4:2 µm, 100 JJ (packed together), $A_{jj} = 0.5\,\mu m^2$ with PPC and resonator
E5	CPW 4:2 µm
E6	CPW 4:2 µm, 500 JJ, 500 PPC, $A_{jj} = 0.5\,\mu m^2$ and 16 resonator
F2	CPW 8:4 µm
F3	Chip test IRAM
F4	Chip test IRAM
F5	Chip test IRAM
F6	CPW 4:2 µm, 500 JJ, 500 PPC, $A_{jj} = 0.5\,\mu m^2$ and resonator
G3	Chip test Oxford
G4	CPW 4:2 µm, 100 JJ (packed together), $A_{jj} = 0.5\,\mu m^2$, 100 PPC
G5	Chip test Oxford

Table B.1: Design description of the devices included on the masks.

Appendix C

JTWPA with PPCs masks

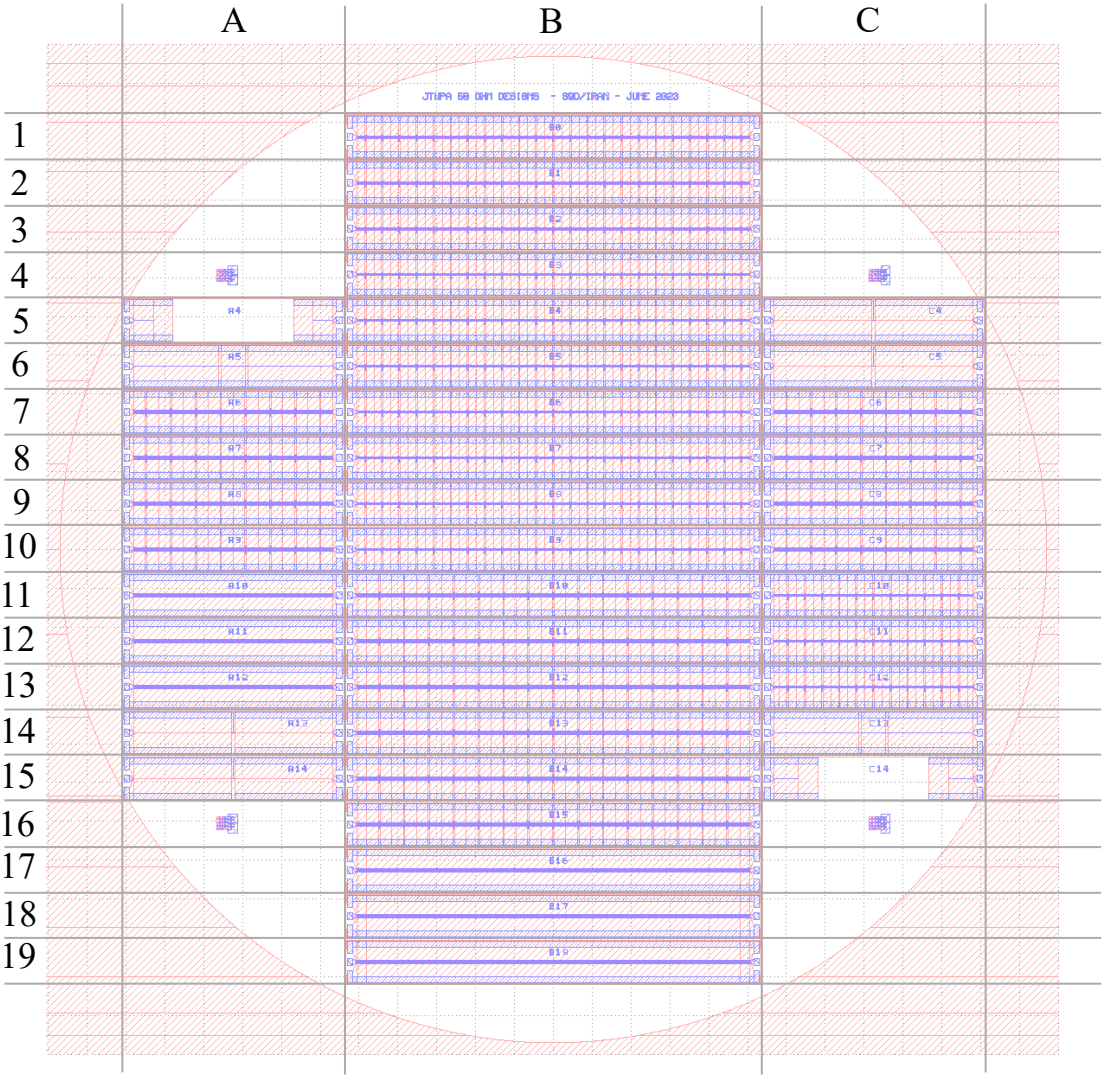

Figure C.1: Photolithography masks layout of the JTWPA with PPCs presented in Chapter 6.

ID	Description
A4	Reflective JPA, $J_c = 0.9\,\mathrm{kA/cm^2}$, 100 JJ ($f_r = 7\,\mathrm{GHz}$)
A5	Cavity-mode JPA, $J_c = 1.4\,\mathrm{kA/cm^2}$, 124 JJ ($f_r = 7\,\mathrm{GHz}$)
A6	JTWPA, $J_c = 0.9\,\mathrm{kA/cm^2}$, RPM, $N_{jj} = 1022$ ($f_r = 7.404\,\mathrm{GHz}$)
A7	JTWPA, $J_c = 0.9\,\mathrm{kA/cm^2}$, RPM, $N_{jj} = 1022$ ($f_r = 7.404\,\mathrm{GHz}$)
A8	JTWPA, $J_c = 0.9\,\mathrm{kA/cm^2}$, RPM, $N_{jj} = 1022$ ($f_r = 7.404\,\mathrm{GHz}$)
A9	JTWPA, $J_c = 0.9\,\mathrm{kA/cm^2}$, RPM, $N_{jj} = 1022$ ($f_r = 7.404\,\mathrm{GHz}$)
A10	JTWPA, $J_c = 0.9\,\mathrm{kA/cm^2}$, no RPM
A11	JTWPA, $J_c = 0.9\,\mathrm{kA/cm^2}$, no RPM
A12	JTWPA, $J_c = 0.9\,\mathrm{kA/cm^2}$, no RPM
A13	Transmission JPA, $J_c = 0.9\,\mathrm{kA/cm^2}$, 100 JJ ($f_r = 7\,\mathrm{GHz}$)
A14	Transmission JPA, $J_c = 0.9\,\mathrm{kA/cm^2}$, 100 JJ ($f_r = 7\,\mathrm{GHz}$)
B0	JTWPA, $J_c = 1.4\,\mathrm{kA/cm^2}$, RPM, $N_{jj} = 2024$ ($f_r = 7.404\,\mathrm{GHz}$)
B1	JTWPA, $J_c = 1.4\,\mathrm{kA/cm^2}$, RPM, $N_{jj} = 2024$ ($f_r = 7.404\,\mathrm{GHz}$)
B2	JTWPA, $J_c = 1.4\,\mathrm{kA/cm^2}$, RPM, $N_{jj} = 2024$ ($f_r = 7.404\,\mathrm{GHz}$)
B3	JTWPA, $J_c = 1.4\,\mathrm{kA/cm^2}$, RPM, $N_{jj} = 2024$ ($f_r = 7.404\,\mathrm{GHz}$)
B4	JTWPA, $J_c = 1.4\,\mathrm{kA/cm^2}$, RPM, $N_{jj} = 2024$ ($f_r = 7.404\,\mathrm{GHz}$)
B5	JTWPA, $J_c = 1.4\,\mathrm{kA/cm^2}$, RPM, $N_{jj} = 2024$ ($f_r = 7.404\,\mathrm{GHz}$)
B6	JTWPA, $J_c = 1.4\,\mathrm{kA/cm^2}$, RPM, $N_{jj} = 2024$ ($f_r = 7.404\,\mathrm{GHz}$)
B7	JTWPA, $J_c = 1.4\,\mathrm{kA/cm^2}$, RPM, $N_{jj} = 2024$ ($f_r = 7.404\,\mathrm{GHz}$)
B8	JTWPA, $J_c = 1.4\,\mathrm{kA/cm^2}$, RPM, $N_{jj} = 2024$ ($f_r = 7.404\,\mathrm{GHz}$)
B9	JTWPA, $J_c = 1.4\,\mathrm{kA/cm^2}$, RPM, $N_{jj} = 2024$ ($f_r = 7.404\,\mathrm{GHz}$)
B10	JTWPA, $J_c = 0.9\,\mathrm{kA/cm^2}$, RPM, $N_{jj} = 2024$ ($f_r = 7.404\,\mathrm{GHz}$)
B11	JTWPA, $J_c = 0.9\,\mathrm{kA/cm^2}$, RPM, $N_{jj} = 2024$ ($f_r = 7.404\,\mathrm{GHz}$)
B12	JTWPA, $J_c = 0.9\,\mathrm{kA/cm^2}$, RPM, $N_{jj} = 2024$ ($f_r = 7.404\,\mathrm{GHz}$)
B13	JTWPA, $J_c = 0.9\,\mathrm{kA/cm^2}$, RPM, $N_{jj} = 2024$ ($f_r = 7.404\,\mathrm{GHz}$)
B14	JTWPA, $J_c = 0.9\,\mathrm{kA/cm^2}$, RPM, $N_{jj} = 2024$ ($f_r = 7.404\,\mathrm{GHz}$)
B15	JTWPA, $J_c = 0.9\,\mathrm{kA/cm^2}$, RPM, $N_{jj} = 2024$ ($f_r = 7.404\,\mathrm{GHz}$)
B16	JTWPA, $J_c = 0.9\,\mathrm{kA/cm^2}$, no RPM, $N_{jj} = 2024$
B17	JTWPA, $J_c = 0.9\,\mathrm{kA/cm^2}$, no RPM, $N_{jj} = 2024$
B18	JTWPA, $J_c = 0.9\,\mathrm{kA/cm^2}$, no RPM, $N_{jj} = 2024$
C4	Transmission JPA, $J_c = 0.9\,\mathrm{kA/cm^2}$, 100 JJ ($f_r = 7\,\mathrm{GHz}$)
C5	Transmission JPA, $J_c = 0.9\,\mathrm{kA/cm^2}$, 100 JJ ($f_r = 7\,\mathrm{GHz}$)
C6	JTWPA, $J_c = 0.9\,\mathrm{kA/cm^2}$, RPM, $N_{jj} = 1022$ ($f_r = 7.404\,\mathrm{GHz}$)
C7	JTWPA, $J_c = 0.9\,\mathrm{kA/cm^2}$, RPM, $N_{jj} = 1022$ ($f_r = 7.404\,\mathrm{GHz}$)
C8	JTWPA, $J_c = 0.9\,\mathrm{kA/cm^2}$, RPM, $N_{jj} = 1022$ ($f_r = 7.404\,\mathrm{GHz}$)
C9	JTWPA, $J_c = 0.9\,\mathrm{kA/cm^2}$, RPM, $N_{jj} = 1022$ ($f_r = 7.404\,\mathrm{GHz}$)
C10	JTWPA, $J_c = 1.4\,\mathrm{kA/cm^2}$, RPM, $N_{jj} = 1022$ ($f_r = 7.404\,\mathrm{GHz}$)
C11	JTWPA, $J_c = 1.4\,\mathrm{kA/cm^2}$, RPM, $N_{jj} = 1022$ ($f_r = 7.404\,\mathrm{GHz}$)
C12	JTWPA, $J_c = 1.4\,\mathrm{kA/cm^2}$, RPM, $N_{jj} = 1022$ ($f_r = 7.404\,\mathrm{GHz}$)
C13	Cavity-mode JPA, $J_c = 1.4\,\mathrm{kA/cm^2}$, 124 JJ ($f_r = 7\,\mathrm{GHz}$)
C14	Reflective JPA, $J_c = 1.4\,\mathrm{kA/cm^2}$, 124 JJ (Rsonance 7 GHz)

Table C.1: Designs description of the devices included on the masks.

Appendix D

JTWPA with IDCs masks

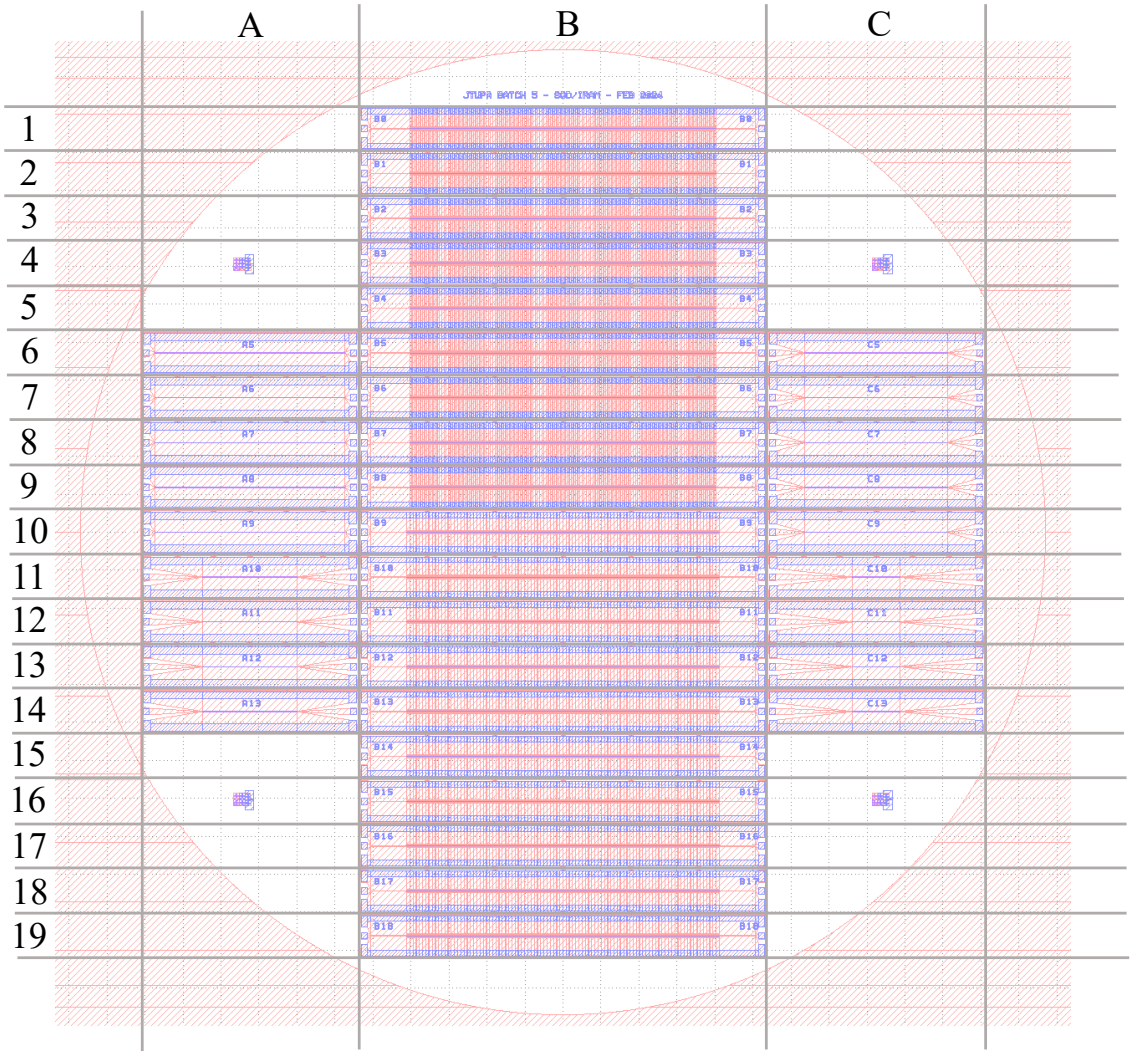

Figure D.1: Photolithography masks layout of the JTWPA with IDCs.

ID	Description
A5	SWPA, $N_{\mathrm{jj}} = 1000$
A6	SWPA, $N_{\mathrm{jj}} = 1000$
A7	SWPA, $N_{\mathrm{jj}} = 1000$
A8	SWPA, $N_{\mathrm{jj}} = 1000$
A9	SWPA, $N_{\mathrm{jj}} = 1000$
A10	SWPA, $N_{\mathrm{jj}} = 500$
A11	SWPA, $N_{\mathrm{jj}} = 500$
A12	SWPA, $N_{\mathrm{jj}} = 500$
A13	SWPA, $N_{\mathrm{jj}} = 500$
B0	JTWPA Design D
B1	JTWPA Design D
B2	JTWPA Design D
B3	JTWPA Design D
B4	JTWPA Design D
B5	JTWPA Design D
B6	JTWPA Design D
B7	JTWPA Design D
B8	JTWPA Design D
B9	JTWPA Design C
B10	JTWPA Design C
B11	JTWPA Design C
B12	JTWPA Design C
B13	JTWPA Design C
B14	JTWPA Design C
B15	JTWPA Design C
B16	JTWPA Design C
B17	JTWPA Design C
B18	JTWPA Design C
C4	SWPA, $N_{\mathrm{jj}} = 750$
C5	SWPA, $N_{\mathrm{jj}} = 500$
C6	SWPA, $N_{\mathrm{jj}} = 500$
C7	SWPA, $N_{\mathrm{jj}} = 500$
C8	SWPA, $N_{\mathrm{jj}} = 500$
C9	SWPA, $N_{\mathrm{jj}} = 500$
C10	SWPA, $N_{\mathrm{jj}} = 250$
C11	SWPA, $N_{\mathrm{jj}} = 250$
C12	SWPA, $N_{\mathrm{jj}} = 250$
C13	SWPA, $N_{\mathrm{jj}} = 250$
C14	SWPA, $N_{\mathrm{jj}} = 250$

Table D.1: Design description of the different devices included on the masks.

Appendix E

W-band JTWPA masks

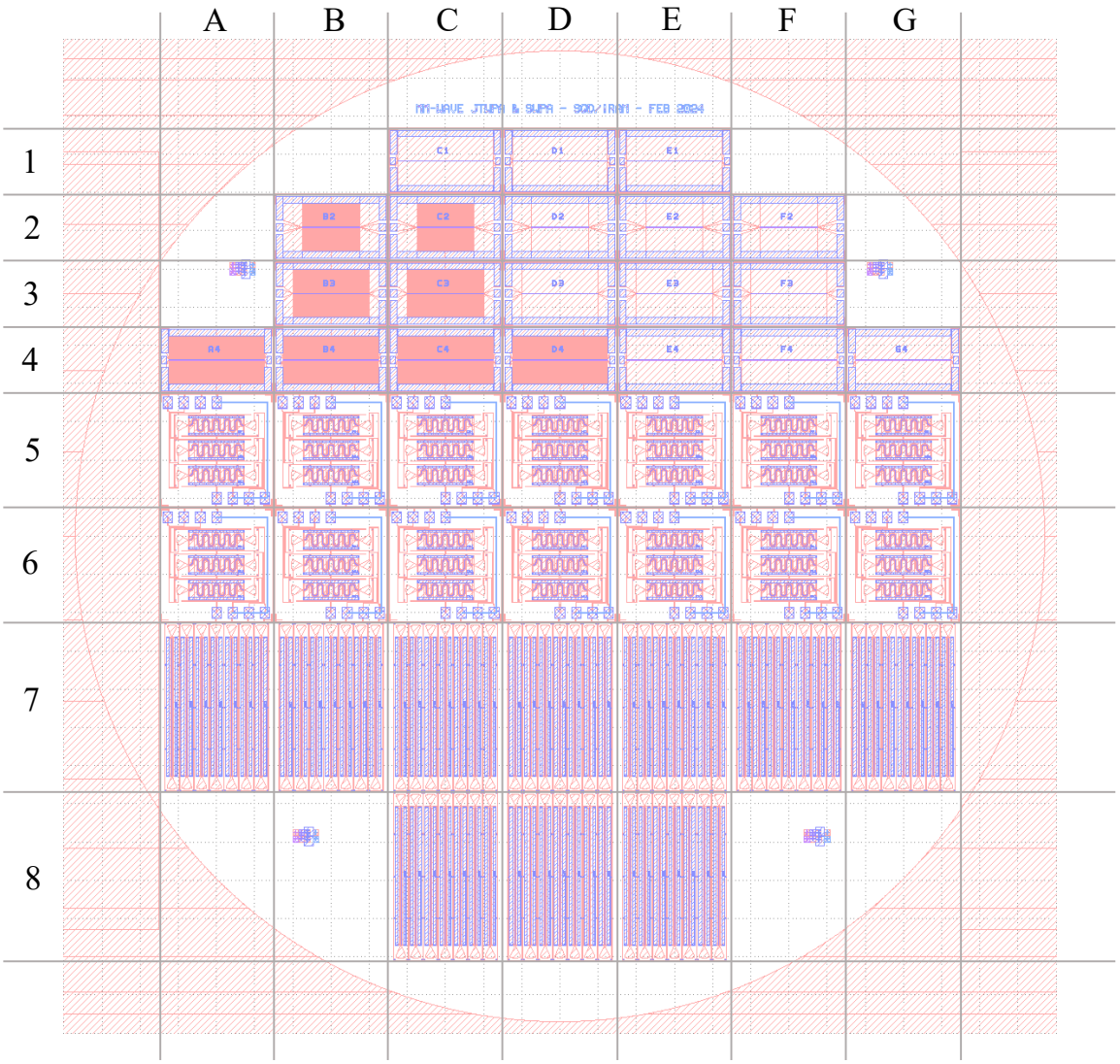

Figure E.1: Photolithography masks layout of the W-band JTWPAs presented in Chapter 9.

ID	Description
C1 - E1	SWPA $N_{\mathrm{jj}} = 500$
B2 - F2	SWPA $N_{\mathrm{jj}} = 300$
B3 - F3	SWPA $N_{\mathrm{jj}} = 400$
A4 - G4	SWPA $N_{\mathrm{jj}} = 500$
A5 - G5	W-band JTWPA Unloaded Design (3x chip)
A6 - G6	W-band JTWPA Unloaded Design (3x chip)
A7 - G7	W-band JTWPA Loaded Design (7x chip)
C8 - E8	W-band JTWPA Loaded Design (7x chip)

Table E.1: Design description of the different devices included on the masks.

References

[1] J Navarro Montilla et al. "Exploring the limits of the tunnel junction fabrication technique for Josephson junctions TWPA and the preliminary characterisation results". In: 2022.

[2] J Navarro Montilla et al. "Investigating pin-holes issues in Josephson junction travelling wave parametric amplifiers requiring large area of dielectric layer". In: 2024.

[3] J Navarro Montilla et al. "Design considerations for a W-band Josephson junction travelling wave parametric amplifier". In: 2024.

[4] The Event Horizon Telescope Collaboration. "First M87 Event Horizon Telescope Results. I. The Shadow of the Supermassive Black Hole". In: *The Astrophysical Journal Letters* 875.1 (2019), p. L1. DOI: 10.3847/2041-8213/ab0ec7. URL: https://dx.doi.org/10.3847/2041-8213/ab0ec7.

[5] A Richard Thompson, James M Moran, and George W Swenson. *Interferometry and synthesis in radio astronomy*. Springer Nature, 2017.

[6] Frank Arute et al. "Quantum supremacy using a programmable superconducting processor". In: *Nature* 574.7779 (2019), pp. 505–510. DOI: 10.1038/s41586-019-1666-5. URL: https://doi.org/10.1038/s41586-019-1666-5.

[7] Jay Gambetta Edwin Pednault John Gunnels. *Quantum Supremacy? A Case for Classical Computation*. Accessed: 2024-09-27. 2019. URL: https://www.ibm.com/quantum/blog/on-quantum-supremacy.

[8] Akihiko Hirota et al. "ALMA 12CO (J= 1–0) imaging of the nearby galaxy M 83: Variations in the efficiency of star formation in giant molecular clouds". In: *Publications of the Astronomical Society of Japan* 70.4 (2018), p. 73.

[9] Mélanie Chevance et al. "The lifecycle of molecular clouds in nearby star-forming disc galaxies". In: *Monthly Notices of the Royal Astronomical Society* 493.2 (Dec. 2019), pp. 2872–2909. ISSN: 0035-8711. DOI: 10.1093/mnras/stz3525. eprint: https://academic.oup.com/mnras/article-pdf/493/2/2872/32891502/stz3525.pdf. URL: https://doi.org/10.1093/mnras/stz3525.

[10] James G. Bartlett. "The standard cosmological model and CMB anisotropies". In: *New Astronomy Reviews* 43.2 (1999), pp. 83–109. ISSN: 1387-6473. DOI: https://doi.org/10.1016/S1387-6473(99)00007-X. URL: https://www.sciencedirect.com/science/article/pii/S138764739900007X.

[11] Rita K. Mann et al. "ALMA OBSERVATIONS OF THE ORION PROPLYDS". In: *The Astrophysical Journal* 784.1 (2014), p. 82. DOI: 10.1088/0004-637X/784/1/82. URL: https://dx.doi.org/10.1088/0004-637X/784/1/82.

[12] Snellen, I. A. G. et al. “Re-analysis of the 267 GHz ALMA observations of Venus - No statistically significant detection of phosphine”. In: *AA* 644 (2020), p. L2. DOI: 10.1051/0004-6361/202039717. URL: https://doi.org/10.1051/0004-6361/202039717.

[13] Jane S. Greaves et al. “Phosphine gas in the cloud decks of Venus”. In: *Nature Astronomy* 5.7 (2021), pp. 655–664. DOI: 10.1038/s41550-020-1174-4. URL: https://doi.org/10.1038/s41550-020-1174-4.

[14] Baes, M. et al. “Herschel-ATLAS: The dust energy balance in the edge-on spiral galaxy UGC4754 *”. In: *AA* 518 (2010), p. L39. DOI: 10.1051/0004-6361/201014644. URL: https://doi.org/10.1051/0004-6361/201014644.

[15] Benjamin D. Boizelle et al. “A Precision Measurement of the Mass of the Black Hole in NGC 3258 from High-resolution ALMA Observations of Its Circumnuclear Disk*”. In: *The Astrophysical Journal* 881.1 (2019), p. 10. DOI: 10.3847/1538-4357/ab2a0a. URL: https://dx.doi.org/10.3847/1538-4357/ab2a0a.

[16] Samuel E. Gralla, Alexandru Lupsasca, and Daniel P. Marrone. “The shape of the black hole photon ring: A precise test of strong-field general relativity”. In: *Phys. Rev. D* 102 (12 2020), p. 124004. DOI: 10.1103/PhysRevD.102.124004. URL: https://link.aps.org/doi/10.1103/PhysRevD.102.124004.

[17] H.T. Friis. “Noise Figures of Radio Receivers”. In: *Proceedings of the IRE* 32.7 (1944), pp. 419–422. DOI: 10.1109/JRPROC.1944.232049.

[18] Chau-Ching Chiong et al. “Low-Noise Amplifier for Next-Generation Radio Astronomy Telescopes: Review of the State-of-the-Art Cryogenic LNAs in the Most Challenging Applications”. In: *IEEE Microwave Magazine* 23.1 (2022), pp. 31–47. DOI: 10.1109/MMM.2021.3117318.

[19] Anthony J. Ardizzi et al. “Self-heating of cryogenic high electron-mobility transistor amplifiers and the limits of microwave noise performance”. In: *Journal of Applied Physics* 132.8 (Aug. 2022), p. 084501. ISSN: 0021-8979. DOI: 10.1063/5.0103156. eprint: https://pubs.aip.org/aip/jap/article-pdf/doi/10.1063/5.0103156/16513774/084501_1_online.pdf. URL: https://doi.org/10.1063/5.0103156.

[20] Christopher Groppi et al. *First Generation Heterodyne Instrumentation Concepts for the Atacama Large Aperture Submillimeter Telescope*. 2019. arXiv: 1907.03479 [astro-ph.IM]. URL: https://arxiv.org/abs/1907.03479.

[21] Yagoubov, P. et al. “Wideband 67116 GHz receiver development for ALMA Band 2”. In: *AA* 634 (2020), A46. DOI: 10.1051/0004-6361/201936777. URL: https://doi.org/10.1051/0004-6361/201936777.

[22] O.Noroozian. *Cycle 5 NRAO ALMA Development Study Report Technology Development of Quantum-Limited, Ultra-Wideband RF Amplifiers for ALMA: A 65-150 GHz Test Case*. Tech. rep. 2020.

[23] Peter W. Shor. "Polynomial-Time Algorithms for Prime Factorization and Discrete Logarithms on a Quantum Computer". In: *SIAM Journal on Computing* 26.5 (1997), pp. 1484–1509. DOI: 10.1137/S0097539795293172. eprint: https://doi.org/10.1137/S0097539795293172. URL: https://doi.org/10.1137/S0097539795293172.

[24] Y. Cao, J. Romero, and A. Aspuru-Guzik. "Potential of quantum computing for drug discovery". In: *IBM Journal of Research and Development* 62.6 (2018), 6:1–6:20. DOI: 10.1147/JRD.2018.2888987.

[25] Yudong Cao et al. "Quantum Chemistry in the Age of Quantum Computing". In: *Chemical Reviews* 119.19 (Oct. 2019), pp. 10856–10915. DOI: 10.1021/acs.chemrev.8b00803. URL: https://doi.org/10.1021/acs.chemrev.8b00803.

[26] Jacob Biamonte et al. "Quantum machine learning". In: *Nature* 549.7671 (2017), pp. 195–202. DOI: 10.1038/nature23474. URL: https://doi.org/10.1038/nature23474.

[27] U.S. Congress. *H.R.6227 - National Quantum Initiative Act*. Accessed: 2024-09-28. 2018. URL: https://www.congress.gov/bill/115th-congress/house-bill/6227.

[28] UK Government. *National Quantum Strategy*. Accessed: 2024-09-28. 2023. URL: https://assets.publishing.service.gov.uk/media/6411a602e90e0776996a4ade/national_quantum_strategy.pdf.

[29] G7 Cyber Expert Group. *G7 Cyber Expert Group Statement on Quantum Computing: Planning for Opportunities and Managing Risks*. Accessed: 2024-09-28. 2023. URL: https://home.treasury.gov/system/files/136/G7-CYBER-EXPERT-GROUP-STATEMENT-PLANNING-OPPORTUNITIES-RISKS-QUANTUM-COMPUTING.pdf.

[30] A. Wallraff et al. "Strong coupling of a single photon to a superconducting qubit using circuit quantum electrodynamics". In: *Nature* 431.7005 (2004), pp. 162–167. DOI: 10.1038/nature02851. URL: https://doi.org/10.1038/nature02851.

[31] J. Stehlik et al. "Fast Charge Sensing of a Cavity-Coupled Double Quantum Dot Using a Josephson Parametric Amplifier". In: *Phys. Rev. Appl.* 4 (1 2015), p. 014018. DOI: 10.1103/PhysRevApplied.4.014018. URL: https://link.aps.org/doi/10.1103/PhysRevApplied.4.014018.

[32] J. D. Teufel et al. "Sideband cooling of micromechanical motion to the quantum ground state". In: *Nature* 475.7356 (2011), pp. 359–363. DOI: 10.1038/nature10261. URL: https://doi.org/10.1038/nature10261.

[33] A. Bienfait et al. "Reaching the quantum limit of sensitivity in electron spin resonance". In: *Nature Nanotechnology* 11.3 (2016), pp. 253–257. DOI: 10.1038/nnano.2015.282. URL: https://doi.org/10.1038/nnano.2015.282.

[34] Dorian Fraudet et al. *Direct detection of down-converted photons spontaneously produced at a single Josephson junction*. 2024. arXiv: 2405.00411 [cond-mat.mes-hall].

[35] K. Ramanathan et al. “Wideband Direct Detection Constraints on Hidden Photon Dark Matter with the QUALIPHIDE Experiment”. In: *Phys. Rev. Lett.* 130 (23 2023), p. 231001. DOI: 10.1103/PhysRevLett.130.231001. URL: https://link.aps.org/doi/10.1103/PhysRevLett.130.231001.

[36] H. A. Haus and J. A. Mullen. “Quantum Noise in Linear Amplifiers”. In: *Phys. Rev.* 128 (5 1962), pp. 2407–2413. DOI: 10.1103/PhysRev.128.2407. URL: https://link.aps.org/doi/10.1103/PhysRev.128.2407.

[37] H. Heffner. “The Fundamental Noise Limit of Linear Amplifiers”. In: *Proceedings of the IRE* 50.7 (1962), pp. 1604–1608. DOI: 10.1109/JRPROC.1962.288130.

[38] Carlton M. Caves. “Quantum limits on noise in linear amplifiers”. In: *Phys. Rev. D* 26 (8 1982), pp. 1817–1839. DOI: 10.1103/PhysRevD.26.1817. URL: https://link.aps.org/doi/10.1103/PhysRevD.26.1817.

[39] D. F. Walls. “Squeezed states of light”. In: *Nature* 306.5939 (1983), pp. 141–146. DOI: 10.1038/306141a0. URL: https://doi.org/10.1038/306141a0.

[40] Ulrik L Andersen et al. “30 years of squeezed light generation”. In: *Physica Scripta* 91.5 (2016), p. 053001. DOI: 10.1088/0031-8949/91/5/053001. URL: https://dx.doi.org/10.1088/0031-8949/91/5/053001.

[41] M. Tse et al. “Quantum-Enhanced Advanced LIGO Detectors in the Era of Gravitational-Wave Astronomy”. In: *Phys. Rev. Lett.* 123 (23 2019), p. 231107. DOI: 10.1103/PhysRevLett.123.231107. URL: https://link.aps.org/doi/10.1103/PhysRevLett.123.231107.

[42] Jose Aumentado. “Superconducting Parametric Amplifiers: The State of the Art in Josephson Parametric Amplifiers”. In: *IEEE Microwave Magazine* 21.8 (2020), pp. 45–59. DOI: 10.1109/MMM.2020.2993476.

[43] E.F.W. Alexanderson and S.P. Nixdorff. “A Magnetic Amplifier for Radio Telephony”. In: *Proceedings of the Institute of Radio Engineers* 4.2 (1916), pp. 101–120. DOI: 10.1109/JRPROC.1916.217224.

[44] John William Planinac. “An investigation of the junction diode parametric amplifiers at medioum radio frequencies”. Master’s thesis. Oklahoma State University, 1959. URL: https://research-solution.com/uplode/book/book-89371.pdf.

[45] B.M. Albrecht, J. Kliphuis, and D. Neuf. “Single parametric amplifier for operation at either 16 Gc or 35 Gc”. In: *Proceedings of the IEEE* 53.8 (1965), pp. 1163–1163. DOI: 10.1109/PROC.1965.4147.

[46] Ronald E. Burgess. “Low noise possibilities of certain semiconductor amplifying systems”. In: *Solid-State Electronics* 4 (1962), pp. 25–30. ISSN: 0038-1101. DOI: https://doi.org/10.1016/0038-1101(62)90068-0. URL: https://www.sciencedirect.com/science/article/pii/0038110162900680.

[47] H. Zimmer. "PARAMETRIC AMPLIFICATION OF MICROWAVES IN SUPERCONDUCTING JOSEPHSON TUNNEL JUNCTIONS". In: *Applied Physics Letters* 10.7 (Apr. 1967), pp. 193–195. ISSN: 0003-6951. DOI: 10.1063/1.1754906. eprint: https://pubs.aip.org/aip/apl/article-pdf/10/7/193/18419865/193_1_online.pdf. URL: https://doi.org/10.1063/1.1754906.

[48] H. Kanter and A. H. Silver. "Self-Pumped Josephson Parametric Amplification". In: *Applied Physics Letters* 19.12 (Dec. 1971), pp. 515–517. ISSN: 0003-6951. DOI: 10.1063/1.1653795. eprint: https://pubs.aip.org/aip/apl/article-pdf/19/12/515/18425630/515_1_online.pdf. URL: https://doi.org/10.1063/1.1653795.

[49] M. J. Feldman, P. T. Parrish, and R. Y. Chiao. "Parametric amplification by unbiased Josephson junctions". In: *Journal of Applied Physics* 46.9 (Sept. 1975), pp. 4031–4042. ISSN: 0021-8979. DOI: 10.1063/1.322157. eprint: https://pubs.aip.org/aip/jap/article-pdf/46/9/4031/18371268/4031_1_online.pdf. URL: https://doi.org/10.1063/1.322157.

[50] B. Yurke et al. "Observation of parametric amplification and deamplification in a Josephson parametric amplifier". In: *Phys. Rev. A* 39 (5 1989), pp. 2519–2533. DOI: 10.1103/PhysRevA.39.2519. URL: https://link.aps.org/doi/10.1103/PhysRevA.39.2519.

[51] B. Yurke et al. "Observation of 4.2-K equilibrium-noise squeezing via a Josephson-parametric amplifier". In: *Phys. Rev. Lett.* 60 (9 1988), pp. 764–767. DOI: 10.1103/PhysRevLett.60.764. URL: https://link.aps.org/doi/10.1103/PhysRevLett.60.764.

[52] R. Movshovich et al. "Observation of zero-point noise squeezing via a Josephson-parametric amplifier". In: *Phys. Rev. Lett.* 65 (12 1990), pp. 1419–1422. DOI: 10.1103/PhysRevLett.65.1419. URL: https://link.aps.org/doi/10.1103/PhysRevLett.65.1419.

[53] M. A. Castellanos-Beltran and K. W. Lehnert. "Widely tunable parametric amplifier based on a superconducting quantum interference device array resonator". In: *Applied Physics Letters* 91.8 (Aug. 2007), p. 083509. ISSN: 0003-6951. DOI: 10.1063/1.2773988. eprint: https://pubs.aip.org/aip/apl/article-pdf/doi/10.1063/1.2773988/13979299/083509_1_online.pdf. URL: https://doi.org/10.1063/1.2773988.

[54] M. A. Castellanos-Beltran et al. "Amplification and squeezing of quantum noise with a tunable Josephson metamaterial". In: *Nature Physics* 4.12 (2008), pp. 929–931. DOI: 10.1038/nphys1090. URL: https://doi.org/10.1038/nphys1090.

[55] Ananda Roy and Michel Devoret. "Quantum-limited parametric amplification with Josephson circuits in the regime of pump depletion". In: *Phys. Rev. B* 98 (4 2018), p. 045405. DOI: 10.1103/PhysRevB.98.045405. URL: https://link.aps.org/doi/10.1103/PhysRevB.98.045405.

[56] Daniel Huber Slichter. "Quantum Jumps and Measurement Backaction in a Superconducting Qubit". PhD thesis. University of California Berkeley, 2011. URL: https://escholarship.org/uc/item/6r4482rq.

[57] Luca Planat. "Resonant and traveling-wave parametric amplification near the quantum limit". PhD thesis. University of Grenoble Alpes, 2020.

[58] N. Bergeal et al. "Phase-preserving amplification near the quantum limit with a Josephson ring modulator". In: *Nature* 465.7294 (2010), pp. 64–68. DOI: 10.1038/nature09035. URL: https://doi.org/10.1038/nature09035.

[59] M. Hatridge et al. "Dispersive magnetometry with a quantum limited SQUID parametric amplifier". In: *Phys. Rev. B* 83 (13 2011), p. 134501. DOI: 10.1103/PhysRevB.83.134501. URL: https://link.aps.org/doi/10.1103/PhysRevB.83.134501.

[60] J. Y. Mutus et al. "Strong environmental coupling in a Josephson parametric amplifier". In: *Applied Physics Letters* 104.26 (July 2014), p. 263513. ISSN: 0003-6951. DOI: 10.1063/1.4886408. eprint: https://pubs.aip.org/aip/apl/article-pdf/doi/10.1063/1.4886408/14301463/263513_1_online.pdf. URL: https://doi.org/10.1063/1.4886408.

[61] Ananda Roy and Michel Devoret. "Introduction to parametric amplification of quantum signals with Josephson circuits". In: *Comptes Rendus Physique* 17.7 (2016), pp. 740–755. DOI: 10.1016/j.crhy.2016.07.012.

[62] J. Grebel et al. "Flux-pumped impedance-engineered broadband Josephson parametric amplifier". In: *Applied Physics Letters* 118.14 (Apr. 2021), p. 142601. ISSN: 0003-6951. DOI: 10.1063/5.0035945. eprint: https://pubs.aip.org/aip/apl/article-pdf/doi/10.1063/5.0035945/14546990/142601_1_online.pdf. URL: https://doi.org/10.1063/5.0035945.

[63] X. Zhou et al. "High-gain weakly nonlinear flux-modulated Josephson parametric amplifier using a SQUID array". In: *Phys. Rev. B* 89 (21 2014), p. 214517. DOI: 10.1103/PhysRevB.89.214517. URL: https://link.aps.org/doi/10.1103/PhysRevB.89.214517.

[64] G. Liu et al. "Josephson parametric converter saturation and higher order effects". In: *Applied Physics Letters* 111.20 (Nov. 2017), p. 202603. ISSN: 0003-6951. DOI: 10.1063/1.5003032. eprint: https://pubs.aip.org/aip/apl/article-pdf/doi/10.1063/1.5003032/13454231/202603_1_online.pdf. URL: https://doi.org/10.1063/1.5003032.

[65] R. Vijay, D. H. Slichter, and I. Siddiqi. "Observation of Quantum Jumps in a Superconducting Artificial Atom". In: *Phys. Rev. Lett.* 106 (11 2011), p. 110502. DOI: 10.1103/PhysRevLett.106.110502. URL: https://link.aps.org/doi/10.1103/PhysRevLett.106.110502.

[66] K. M. Backes et al. "A quantum enhanced search for dark matter axions". In: *Nature* 590.7845 (2021), pp. 238–242. DOI: 10.1038/s41586-021-03226-7. URL: https://doi.org/10.1038/s41586-021-03226-7.

[67] A. L. Cullen. “A Travelling-Wave Parametric Amplifier”. In: *Nature* 181.4605 (1958), pp. 332–332. DOI: 10.1038/181332a0. URL: https://doi.org/10.1038/181332a0.

[68] Honey R. C. and Jones E. M. T. “A Wide-Band UHF Traveling-Wave Variable Reactance Amplifier”. In: *IRE Transactions on Microwave Theory and Techniques* 8.3 (1960), pp. 351–361. DOI: 10.1109/TMTT.1960.1125245.

[69] T. H. Mainan. “Stimulated Optical Radiation in Ruby”. In: *Nature* 187.4736 (1960), pp. 493–494. DOI: 10.1038/187493a0. URL: https://doi.org/10.1038/187493a0.

[70] J. A. Giordmaine and Robert C. Miller. “Tunable Coherent Parametric Oscillation in $LiNbO_3$ at Optical Frequencies”. In: *Phys. Rev. Lett.* 14 (24 1965), pp. 973–976. DOI: 10.1103/PhysRevLett.14.973. URL: https://link.aps.org/doi/10.1103/PhysRevLett.14.973.

[71] J. Hansryd and P.A. Andrekson. “Broad-band continuous-wave-pumped fiber optical parametric amplifier with 49-dB gain and wavelength-conversion efficiency”. In: *IEEE Photonics Technology Letters* 13.3 (2001), pp. 194–196. DOI: 10.1109/68.914318.

[72] J. Hansryd et al. “Fiber-based optical parametric amplifiers and their applications”. In: *IEEE Journal of Selected Topics in Quantum Electronics* 8.3 (2002), pp. 506–520. DOI: 10.1109/JSTQE.2002.1016354.

[73] Byeong Ho Eom et al. “A wideband, low-noise superconducting amplifier with high dynamic range”. In: *Nature Physics* 8.8 (2012), pp. 623–627. DOI: 10.1038/nphys2356. URL: https://doi.org/10.1038/nphys2356.

[74] A. Giachero et al. “Kinetic Inductance Traveling Wave Amplifier Designs for Practical Microwave Readout Applications”. In: *Journal of Low Temperature Physics* 215.3 (2024), pp. 152–160. DOI: 10.1007/s10909-024-03078-1. URL: https://doi.org/10.1007/s10909-024-03078-1.

[75] Farzad Faramarzi et al. *A 4-8 GHz Kinetic Inductance Travelling-Wave Parametric Amplifier Using Four-Wave Mixing with Near Quantum-Limit Noise Performance*. 2024. arXiv: 2402.11751 [quant-ph]. URL: https://arxiv.org/abs/2402.11751.

[76] Nikita Klimovich et al. *Demonstration of a Quantum Noise Limited Travelling-Wave Parametric Amplifier*. 2023. arXiv: 2306.11028 [quant-ph]. URL: https://arxiv.org/abs/2306.11028.

[77] S. Shu et al. “Nonlinearity and wide-band parametric amplification in a (Nb,Ti)N microstrip transmission line”. In: *Phys. Rev. Res.* 3 (2 2021), p. 023184. DOI: 10.1103/PhysRevResearch.3.023184. URL: https://link.aps.org/doi/10.1103/PhysRevResearch.3.023184.

[78] M. Sweeny and R. Mahler. “A travelling-wave parametric amplifier utilizing Josephson junctions”. In: *IEEE Transactions on Magnetics* 21.2 (1985), pp. 654–655. DOI: 10.1109/TMAG.1985.1063777.

[79] C. Macklin et al. “A near–quantum-limited Josephson traveling-wave parametric amplifier”. In: *Science* 350.6258 (2015), pp. 307–310. DOI: 10.1126/science.aaa8525. eprint: https://www.science.org/doi/pdf/10.1126/science.aaa8525. URL: https://www.science.org/doi/abs/10.1126/science.aaa8525.

[80] Luca Planat et al. “Photonic-Crystal Josephson Traveling-Wave Parametric Amplifier”. In: *Phys. Rev. X* 10 (2 2020), p. 021021. DOI: 10.1103/PhysRevX.10.021021. URL: https://link.aps.org/doi/10.1103/PhysRevX.10.021021.

[81] Arpit Ranadive et al. “Kerr reversal in Josephson meta-material and traveling wave parametric amplification”. In: *Nature Communications* 13.1 (2022), p. 1737. DOI: 10.1038/s41467-022-29375-5. URL: https://doi.org/10.1038/s41467-022-29375-5.

[82] Anita Fadavi Roudsari et al. “Three-wave mixing traveling-wave parametric amplifier with periodic variation of the circuit parameters”. In: *Applied Physics Letters* 122.5 (Jan. 2023), p. 052601. ISSN: 0003-6951. DOI: 10.1063/5.0127690. eprint: https://pubs.aip.org/aip/apl/article-pdf/doi/10.1063/5.0127690/18103561/052601_1_5.0127690.pdf. URL: https://doi.org/10.1063/5.0127690.

[83] J C Longden, J Navarro Montilla, and B-K Tan. “Balanced travelling-wave parametric amplifiers for practical applications”. In: *Physica Scripta* 99.6 (2024), p. 065046. DOI: 10.1088/1402-4896/ad492a. URL: https://dx.doi.org/10.1088/1402-4896/ad492a.

[84] Hampus Renberg Nilsson et al. “Peripheral circuits for ideal performance of a traveling-wave parametric amplifier”. In: *Phys. Rev. Appl.* 21 (6 2024), p. 064062. DOI: 10.1103/PhysRevApplied.21.064062. URL: https://link.aps.org/doi/10.1103/PhysRevApplied.21.064062.

[85] Arpit Ranadive et al. *A Traveling Wave Parametric Amplifier Isolator*. 2024. arXiv: 2406.19752 [quant-ph]. URL: https://arxiv.org/abs/2406.19752.

[86] M. Malnou et al. *A Traveling-Wave Parametric Amplifier and Converter*. 2024. arXiv: 2406.19476 [quant-ph]. URL: https://arxiv.org/abs/2406.19476.

[87] Javier Navarro Montilla and Boon-Kok Tan. “Design of high compression point Josephson junction travelling wave parametric amplifiers for readout of millimetre and sub-millimetre astronomical receivers”. In: *Millimeter, Submillimeter, and Far-Infrared Detectors and Instrumentation for Astronomy XI*. Ed. by Jonas Zmuidzinas and Jian-Rong Gao. Vol. 12190. International Society for Optics and Photonics. SPIE, 2022, p. 1219030. DOI: 10.1117/12.2628992. URL: https://doi.org/10.1117/12.2628992.

[88] Kaidong Peng et al. “Floquet-Mode Traveling-Wave Parametric Amplifiers”. In: *PRX Quantum* 3 (2 2022), p. 020306. DOI: 10.1103/PRXQuantum.3.020306. URL: https://link.aps.org/doi/10.1103/PRXQuantum.3.020306.

[89] H. Kamerlingh Onnes. "The Superconductivity of Mercury". In: *Comm. Phys. Lab. Univ., Leiden* (1911), pp. 122–124.

[90] J. Bardeen, L. N. Cooper, and J. R. Schrieffer. "Microscopic Theory of Superconductivity". In: *Phys. Rev.* 106 (1 1957), pp. 162–164. DOI: 10.1103/PhysRev.106.162. URL: https://link.aps.org/doi/10.1103/PhysRev.106.162.

[91] R. Meservey and P. M. Tedrow. "Measurements of the Kinetic Inductance of Superconducting Linear Structures". In: *Journal of Applied Physics* 40.5 (Apr. 1969), pp. 2028–2034. ISSN: 0021-8979. DOI: 10.1063/1.1657905. eprint: https://pubs.aip.org/aip/jap/article-pdf/40/5/2028/18350463/2028_1_online.pdf. URL: https://doi.org/10.1063/1.1657905.

[92] Daria Kalacheva et al. "Coplanar superconducting resonators with nonlinear kinetic inductance bridge". In: *Superconductor Science and Technology* 36.5 (2023), p. 055011. DOI: 10.1088/1361-6668/acbc53. URL: https://dx.doi.org/10.1088/1361-6668/acbc53.

[93] L. J. Swenson et al. "Operation of a titanium nitride superconducting microresonator detector in the nonlinear regime". In: *Journal of Applied Physics* 113.10 (Mar. 2013), p. 104501.

[94] B.D. Josephson. "Possible new effects in superconductive tunnelling". In: *Physics Letters* 1.7 (1962), pp. 251–253. ISSN: 0031-9163. DOI: https://doi.org/10.1016/0031-9163(62)91369-0. URL: https://www.sciencedirect.com/science/article/pii/0031916362913690.

[95] Michael Tinkham. *Introduction to superconductivity*. Courier Corporation, 2004.

[96] Clark A Hamilton, Charles Burroughs, and Kao Chieh. "Operation of NIST Josephson Array Voltage Standards." eng. In: *J Res Natl Inst Stand Technol* 95.3 (1990), pp. 219–235. ISSN: 1044-677X (Print); 2165-7254 (Electronic); 1044-677X (Linking). DOI: 10.6028/jres.095.026.

[97] J Wenninger. "A dual-polarization receiver for multi-beam interferometry". PhD thesis. University of Oxford, 2023.

[98] A. B. Zorin. "Josephson Traveling-Wave Parametric Amplifier with Three-Wave Mixing". In: *Phys. Rev. Appl.* 6 (3 2016), p. 034006. DOI: 10.1103/PhysRevApplied.6.034006. URL: https://link.aps.org/doi/10.1103/PhysRevApplied.6.034006.

[99] Nikita Klimovich et al. *Demonstration of a Quantum Noise Limited Travelling-Wave Parametric Amplifier*. 2023. arXiv: 2306.11028 [quant-ph].

[100] D.M. Pozar. *Microwave Engineering, 4th Edition*. Wiley, 2011. ISBN: 9781118213636. URL: https://books.google.fr/books?id=JegbAAAAQBAJ.

[101] JC Longden. "Development of superconducting thin film travelling wave parametric amplifiers". PhD thesis. University of Oxford, 2023.

[102] R. Stolen and J. Bjorkholm. "Parametric amplification and frequency conversion in optical fibers". In: *IEEE Journal of Quantum Electronics* 18.7 (1982), pp. 1062–1072. DOI: 10.1109/JQE.1982.1071660.

[103] Kevin O'Brien et al. "Resonant Phase Matching of Josephson Junction Traveling Wave Parametric Amplifiers". In: *Phys. Rev. Lett.* 113 (15 2014), p. 157001. DOI: 10.1103/PhysRevLett.113.157001. URL: https://link.aps.org/doi/10.1103/PhysRevLett.113.157001.

[104] O. Yaakobi et al. "Parametric amplification in Josephson junction embedded transmission lines". In: *Phys. Rev. B* 87 (14 2013), p. 144301. DOI: 10.1103/PhysRevB.87.144301. URL: https://link.aps.org/doi/10.1103/PhysRevB.87.144301.

[105] Rowan J. Gilmore and Michael B. Steer. "Nonlinear circuit analysis using the method of harmonic balance—A review of the art. Part I. Introductory concepts". In: *International Journal of Microwave and Millimeter-Wave Computer-Aided Engineering* 1.1 (1991), pp. 22–37. DOI: https://doi.org/10.1002/mmce.4570010104. eprint: https://onlinelibrary.wiley.com/doi/pdf/10.1002/mmce.4570010104. URL: https://onlinelibrary.wiley.com/doi/abs/10.1002/mmce.4570010104.

[106] T Sweetnam et al. "Simulating the behaviour of travelling wave superconducting parametric amplifiers using a commercial circuit simulator". In: *Superconductor Science and Technology* 35.9 (2022), p. 095011. DOI: 10.1088/1361-6668/ac850b. URL: https://dx.doi.org/10.1088/1361-6668/ac850b.

[107] Daryoush Shiri et al. *Modeling and Harmonic Balance Analysis of Parametric Amplifiers for Qubit Read-out*. 2024. arXiv: 2306.05177 [quant-ph]. URL: https://arxiv.org/abs/2306.05177.

[108] K. Peng et al. "X-parameter based design and simulation of Josephson traveling-wave parametric amplifiers for quantum computing applications". In: *2022 IEEE International Conference on Quantum Computing and Engineering (QCE)*. Los Alamitos, CA, USA: IEEE Computer Society, 2022, pp. 331–340. DOI: 10.1109/QCE53715.2022.00054. URL: https://doi.ieeecomputersociety.org/10.1109/QCE53715.2022.00054.

[109] Saptarshi Chaudhuri, Jiansong Gao, and Kent Irwin. "Simulation and Analysis of Superconducting Traveling-Wave Parametric Amplifiers". In: *IEEE Transactions on Applied Superconductivity* 25.3 (2015), pp. 1–5. DOI: 10.1109/TASC.2014.2378059.

[110] A. Yu. Levochkina et al. "Numerical Simulations of Josephson Traveling Wave Parametric Amplifiers (JTWPAs): Comparative Study of Open-Source Tools". In: *IEEE Transactions on Applied Superconductivity* 34.3 (2024), pp. 1–6. DOI: 10.1109/TASC.2024.3364125.

[111] Boon-Kok Tan et al. "Engineering the thin film characteristics for optimal performance of superconducting kinetic inductance amplifiers using a rigorous modelling technique." eng. In: *Open Res Eur* 2 (2022), p. 88. ISSN: 2732-5121 (Electronic); 2732-5121 (Linking). DOI: 10.12688/openreseurope.14860.2.

[112] Jack Y. Qiu et al. "Broadband squeezed microwaves and amplification with a Josephson travelling-wave parametric amplifier". In: *Nature Physics* 19.5 (2023), pp. 706–713. DOI: 10.1038/s41567-022-01929-w. URL: https://doi.org/10.1038/s41567-022-01929-w.

[113] Hampus Renberg Nilsson et al. *A small footprint travelling-wave parametric amplifier with a high Signal-to-Noise Ratio improvement in a wide band*. 2024. arXiv: 2408.16366 [physics.app-ph]. URL: https://arxiv.org/abs/2408.16366.

[114] Sylvain Mahieu et al. "The ALMA Band-7 Cartridge". In: *IEEE Transactions on Terahertz Science and Technology* 2.1 (2012), pp. 29–39. DOI: 10.1109/TTHZ.2011.2177734.

[115] Morvan Salez et al. "30sensitivity for Herschel/HIFI band 1". In: *Millimeter and Submillimeter Detectors for Astronomy*. Ed. by Thomas G. Phillips and Jonas Zmuidzinas. Vol. 4855. International Society for Optics and Photonics. SPIE, 2003, pp. 402 –414. DOI: 10.1117/12.459365. URL: https://doi.org/10.1117/12.459365.

[116] P. W. Anderson and J. M. Rowell. "Probable Observation of the Josephson Superconducting Tunneling Effect". In: *Physical Review Letters* 10.6 (Mar. 1963), pp. 230–232. DOI: 10.1103/PhysRevLett.10.230. URL: https://link.aps.org/doi/10.1103/PhysRevLett.10.230.

[117] G. J. Dolan. "Offset masks for lift-off photoprocessing". In: *Applied Physics Letters* 31.5 (Sept. 1977), pp. 337–339. ISSN: 0003-6951. DOI: 10.1063/1.89690. eprint: https://pubs.aip.org/aip/apl/article-pdf/31/5/337/18435275/337_1_online.pdf. URL: https://doi.org/10.1063/1.89690.

[118] Yuzhen Zheng et al. "Fabrication of Al/AlOx/Al junctions with high uniformity and stability on sapphire substrates". In: *Scientific Reports* 13.1 (2023), p. 11874. DOI: 10.1038/s41598-023-39052-2. URL: https://doi.org/10.1038/s41598-023-39052-2.

[119] Anastasiya A. Pishchimova et al. "Improving Josephson junction reproducibility for superconducting quantum circuits: junction area fluctuation". In: *Scientific Reports* 13.1 (2023), p. 6772. DOI: 10.1038/s41598-023-34051-9. URL: https://doi.org/10.1038/s41598-023-34051-9.

[120] R. B. Laibowitz and A. F. Mayadas. "Josephson Junctions with Nb/Al Composite Electrodes". In: *Applied Physics Letters* 20.7 (Apr. 1972), pp. 254–256. ISSN: 0003-6951. DOI: 10.1063/1.1654136. eprint: https://pubs.aip.org/aip/apl/article-pdf/20/7/254/18425939/254_1_online.pdf. URL: https://doi.org/10.1063/1.1654136.

[121] R.F. Broom et al. “Niobium oxide-barrier tunnel junction”. In: *IEEE Transactions on Electron Devices* 27.10 (1980), pp. 1998–2008. DOI: 10.1109/T-ED.1980.20137.

[122] G. Albrecht, J. Richter, and P. Weber. “Properties of niobium-based Josephson tunneling elements in junction microstructures”. In: *Journal of Low Temperature Physics* 48.1 (1982), pp. 61–83. DOI: 10.1007/BF00681718. URL: https://doi.org/10.1007/BF00681718.

[123] M. Gurvitch, M. A. Washington, and H. A. Huggins. “High quality refractory Josephson tunnel junctions utilizing thin aluminum layers”. In: *Applied Physics Letters* 42.5 (Mar. 1983), pp. 472–474. ISSN: 0003-6951. DOI: 10.1063/1.93974. eprint: https://pubs.aip.org/aip/apl/article-pdf/42/5/472/18448144/472_1_online.pdf. URL: https://doi.org/10.1063/1.93974.

[124] SK Tolpygo et al. “A 150-nm process node of an eight-Nb-layer fully planarized process for superconductor electronics”. In: *Proceedings of the Applied Superconductivity Conference, ASC 2020 Virtual Conference. Superconductivity News Forum (SNF), Virtual*. Vol. 14. 2020.

[125] Sergey K Tolpygo et al. “Deep sub-micron stud-via technology of superconductor VLSI circuits”. In: *Superconductor Science and Technology* 27.2 (2014), p. 025016. DOI: 10.1088/0953-2048/27/2/025016. URL: https://dx.doi.org/10.1088/0953-2048/27/2/025016.

[126] S Anders et al. “Sub-micrometer-sized, cross-type Nb–AlOx–Nb tunnel junctions with low parasitic capacitance”. In: *Superconductor Science and Technology* 22.6 (2009), p. 064012. DOI: 10.1088/0953-2048/22/6/064012. URL: https://dx.doi.org/10.1088/0953-2048/22/6/064012.

[127] Leif Grönberg et al. “Side-wall spacer passivated sub-m Josephson junction fabrication process”. In: *Superconductor Science and Technology* 30.12 (2017), p. 125016. DOI: 10.1088/1361-6668/aa9411. URL: https://dx.doi.org/10.1088/1361-6668/aa9411.

[128] Dennis C. Feng et al. “Design and Measurement Of A Josephson Traveling Wave Parametric Amplifier Fabricated In A Superconducting Qubit Process”. In: *2020 IEEE/MTT-S International Microwave Symposium (IMS)*. 2020, pp. 940–943. DOI: 10.1109/IMS30576.2020.9223912.

[129] S Ó Peatáin et al. “Simulating the effects of fabrication tolerance on the performance of Josephson travelling wave parametric amplifiers”. In: *Superconductor Science and Technology* 36.4 (2023), p. 045017. DOI: 10.1088/1361-6668/acba4e. URL: https://dx.doi.org/10.1088/1361-6668/acba4e.

[130] C. Kissling et al. “Vulnerability to Parameter Spread in Josephson Traveling-Wave Parametric Amplifiers”. In: *IEEE Transactions on Applied Superconductivity* 33.5 (2023), pp. 1–6. DOI: 10.1109/TASC.2023.3242927.

[131] Samuel T. Elkin, Michael Haider, and Thomas E. Roth. "Multiphysics Numerical Method for Modeling Josephson Traveling-Wave Parametric Amplifiers". In: *IEEE Journal on Multiscale and Multiphysics Computational Techniques* 9 (2024), pp. 247–257. URL: https://api.semanticscholar.org/CorpusID:268667577.

[132] T. C. White et al. "Traveling wave parametric amplifier with Josephson junctions using minimal resonator phase matching". In: *Applied Physics Letters* 106.24 (June 2015), p. 242601. ISSN: 0003-6951. DOI: 10.1063/1.4922348. eprint: https://pubs.aip.org/aip/apl/article-pdf/doi/10.1063/1.4922348/13280556/242601_1_online.pdf. URL: https://doi.org/10.1063/1.4922348.

[133] Slawomir Simbierowicz et al. "Characterizing cryogenic amplifiers with a matched temperature-variable noise source". In: *Review of Scientific Instruments* 92.3 (Mar. 2021), p. 034708. ISSN: 0034-6748. DOI: 10.1063/5.0028951. eprint: https://pubs.aip.org/aip/rsi/article-pdf/doi/10.1063/5.0028951/13865090/034708_1_online.pdf. URL: https://doi.org/10.1063/5.0028951.

[134] Takeo Watanabe. "Current status and prospect for EUV lithography". In: *2017 7th International Conference on Integrated Circuits, Design, and Verification (ICDV)*. 2017, pp. 2–7. DOI: 10.1109/ICDV.2017.8188625.

[135] M. M. T. M. Dierichs et al. "Submicron niobium junctions for submillimeter-wave mixers using optical lithography". In: *Applied Physics Letters* 62.7 (Feb. 1993), pp. 774–776. ISSN: 0003-6951. DOI: 10.1063/1.108575. eprint: https://pubs.aip.org/aip/apl/article-pdf/62/7/774/7794057/774_1_online.pdf. URL: https://doi.org/10.1063/1.108575.

[136] H. Kamerlingh Onnes. "The liquefaction of helium". In: *KNAW, Proceedings* 11 (1909), pp. 168–185.

[137] A. T. A. M. de Waele. "Basic Operation of Cryocoolers and Related Thermal Machines". In: *Journal of Low Temperature Physics* 164.5 (2011), pp. 179–236. DOI: 10.1007/s10909-011-0373-x. URL: https://doi.org/10.1007/s10909-011-0373-x.

[138] Xiaotong Xi et al. "Progress and Challenges of Sub-Kelvin Sorption Cooler and Its Prospects for Space Application". In: *Journal of Low Temperature Physics* 199.5 (2020), pp. 1363–1381. DOI: 10.1007/s10909-020-02442-1. URL: https://doi.org/10.1007/s10909-020-02442-1.

[139] Chase Research Cryogenics. *Product Range, GL7*. [Online; accessed August 28, 2024]. 2024. URL: https://www.chasecryogenics.com/products.

[140] Blufors. *BF-LD-SERIES Cryogen-Free Dilution Refrigerator System, User Manual*. English. Version 1.5.0. Blufors. 76 pp.

[141] A.W. Kleinsasser, R.E. Miller, and W.H. Mallison. "Dependence of critical current density on oxygen exposure in Nb-AlO/sub x/-Nb tunnel junctions". In: *IEEE Transactions on Applied Superconductivity* 5.1 (1995), pp. 26–30. DOI: 10.1109/77.384565.

[142] Sergey K. Tolpygo et al. "Properties of Unshunted and Resistively Shunted Nb/AlOx-Al/Nb Josephson Junctions With Critical Current Densities From 0.1 to 1 mA/m2". In: *IEEE Transactions on Applied Superconductivity* 27.4 (2017), pp. 1–15. DOI: 10.1109/TASC.2017.2667403.

[143] T. Shiota, T. Imamura, and S. Hasuo. "Fabrication of high quality Nb/AlO/-sub /x-Al/Nb Josephson junctions. III. Annealing stability of AlO/sub /x tunneling barriers". In: *IEEE Transactions on Applied Superconductivity* 2.4 (1992), pp. 222–227. DOI: 10.1109/77.182734.

[144] J.V. Migacz and M.E. Huber. "Thermal annealing of Nb/Al-AlO/sub x//Nb Josephson junctions". In: *IEEE Transactions on Applied Superconductivity* 13.2 (2003), pp. 123–126. DOI: 10.1109/TASC.2003.813661.

[145] A. Oliva and R. Monaco. "Annealing properties of high quality Nb/Al-AlO/sub x//Nb tunnel junctions". In: *IEEE Transactions on Applied Superconductivity* 4.1 (1994), pp. 25–32. DOI: 10.1109/77.273061.

[146] James A. Oke and Tien-Chien Jen. "Atomic layer deposition and other thin film deposition techniques: from principles to film properties". In: *Journal of Materials Research and Technology* 21 (2022), pp. 2481–2514. ISSN: 2238-7854. DOI: https://doi.org/10.1016/j.jmrt.2022.10.064. URL: https://www.sciencedirect.com/science/article/pii/S2238785422016039.

[147] Takeo Hattori, Yutaka Utsugi, and Hiroshi Yamauchi. "Detection of pinholes in R.F.-diode-sputtered SiO2 films". In: *Thin Solid Films* 97.3 (1982), pp. 231–235. ISSN: 0040-6090. DOI: https://doi.org/10.1016/0040-6090(82)90457-6. URL: https://www.sciencedirect.com/science/article/pii/0040609082904576.

[148] Christopher Stewart Macklin. "Quantum Feedback and Traveling-wave Parametric Amplification in Superconducting Circuits". PhD thesis. UniversityofCalifornia,Berkeley, 2015.

[149] S. Wood, N. Klimovich, and B.-K. Tan. "Automated characterisation and operational insights of superconducting travelling wave parametric amplifiers: unveiling novel behaviours and enhancing tunability". In: *Journal of Instrumentation* 19.08 (2024), P08024. DOI: 10.1088/1748-0221/19/08/P08024. URL: https://dx.doi.org/10.1088/1748-0221/19/08/P08024.

[150] Victor Elhomsy et al. *Broadband parametric amplification for multiplexed SiMOS quantum dot signals*. 2023. arXiv: 2307.14717 [cond-mat.mes-hall]. URL: https://arxiv.org/abs/2307.14717.

[151] Chandrashekhar Gaikwad et al. "Observing parity-time symmetry breaking in a Josephson parametric amplifier". In: *Phys. Rev. Res.* 5 (4 2023), p. L042024. DOI: 10.1103/PhysRevResearch.5.L042024. URL: https://link.aps.org/doi/10.1103/PhysRevResearch.5.L042024.

[152] V. V. Sivak et al. "Josephson Array-Mode Parametric Amplifier". In: *Phys. Rev. Appl.* 13 (2 2020), p. 024014. DOI: 10.1103/PhysRevApplied.13.024014. URL: https://link.aps.org/doi/10.1103/PhysRevApplied.13.024014.

[153] C. Eichler et al. "Quantum-Limited Amplification and Entanglement in Coupled Nonlinear Resonators". In: *Phys. Rev. Lett.* 113 (11 2014), p. 110502. DOI: 10.1103/PhysRevLett.113.110502. URL: https://link.aps.org/doi/10.1103/PhysRevLett.113.110502.

[154] Luca Planat et al. "Understanding the Saturation Power of Josephson Parametric Amplifiers Made from SQUID Arrays". In: *Phys. Rev. Appl.* 11 (3 2019), p. 034014. DOI: 10.1103/PhysRevApplied.11.034014. URL: https://link.aps.org/doi/10.1103/PhysRevApplied.11.034014.

[155] Imran Mahboob et al. "A three-dimensional Josephson parametric amplifier". In: *Applied Physics Express* 15.6 (2022), p. 062005. DOI: 10.35848/1882-0786/ac702d. URL: https://dx.doi.org/10.35848/1882-0786/ac702d.

[156] Martina Esposito et al. "Observation of Two-Mode Squeezing in a Traveling Wave Parametric Amplifier". In: *Phys. Rev. Lett.* 128 (15 2022), p. 153603. DOI: 10.1103/PhysRevLett.128.153603. URL: https://link.aps.org/doi/10.1103/PhysRevLett.128.153603.

[157] R. Movshovich et al. "Vacuum noise squeezing at microwave frequencies using a Josephson parametric amplifier". In: *IEEE Transactions on Magnetics* 27.2 (1991), pp. 2658–2660. DOI: 10.1109/20.133758.

[158] L Zhong et al. "Squeezing with a flux-driven Josephson parametric amplifier". In: *New Journal of Physics* 15.12 (2013), p. 125013. DOI: 10.1088/1367-2630/15/12/125013. URL: https://dx.doi.org/10.1088/1367-2630/15/12/125013.

[159] A. Bienfait et al. "Magnetic Resonance with Squeezed Microwaves". In: *Phys. Rev. X* 7 (4 2017), p. 041011. DOI: 10.1103/PhysRevX.7.041011. URL: https://link.aps.org/doi/10.1103/PhysRevX.7.041011.

[160] O.Noroozian. *Cycle 5 NRAO ALMA Development Study Report Technology Development of Quantum-Limited, Ultra-Wideband RF Amplifiers for ALMA: A 65-150 GHz Test Case*. Tech. rep. 2020.

[161] Kevin K. S. Multani et al. *Quantum limits of superconducting-photonic links and their extension to mm-waves*. 2024. arXiv: 2406.14501 [id='quant-ph' $full_name =' Quantum Physics' is_active = True alt_name = None in_archive =' quant-ph' is_general = False description = None$].

[162] Farzad Faramarzi et al. “Initial Design of a W-Band Superconducting Kinetic Inductance Qubit”. In: *IEEE Transactions on Applied Superconductivity* 31.5 (2021), pp. 1–5. DOI: 10.1109/TASC.2021.3065304.

[163] Alexander Vladimir Anferov. “Millimeter-Wave Superconducting Quantum Devices”. PhD thesis. University of Chicago, 2024.

[164] Peter K. Day et al. “Millimeter-wave superconducting parametric amplifiers based on kinetic inductance”. In: *Millimeter, Submillimeter, and Far-Infrared Detectors and Instrumentation for Astronomy XI*. Ed. by Jonas Zmuidzinas and Jian-Rong Gao. Vol. PC12190. International Society for Optics and Photonics. SPIE, 2022, PC1219009. DOI: 10.1117/12.2629110. URL: https://doi.org/10.1117/12.2629110.

[165] B-K Tan et al. “Operation of kinetic-inductance travelling wave parametric amplifiers at millimetre wavelengths”. In: *Superconductor Science and Technology* 37.3 (2024), p. 035006. DOI: 10.1088/1361-6668/ad20fd. URL: https://dx.doi.org/10.1088/1361-6668/ad20fd.

[166] *Ansys HFSS*. https://www.ansys.com/products/electronics/ansys-hfss.

[167] M.P. Lepselter et al. “Beam-lead devices and integrated circuits”. In: *Proceedings of the IEEE* 53.4 (1965), pp. 405–405. DOI: 10.1109/PROC.1965.3772.

[168] R.B. Bass et al. “Beam Lead Fabrication for Submillimeter-wave Circuits Using Vacuum Planarization”. In: 2003.